THERMALLY ASSISTED AUTOFRETTAGE OF THICK CYLINDERS

A Thesis Submitted in partial fulfilment of the requirements for the degree of

DOCTOR OF PHILOSOPHY

by

Rajkumar Shufen
(Roll no 156103005)

Department of Mechanical Engineering
Indian Institute of Technology Guwahati
Guwahati-781039
INDIA
October 2019

DECLARATION

I declare that,

a. The work contained in this thesis is original and has been done by me under the guidance of my supervisor.
b. The work has not been submitted to any other institute for any degree or diploma.
c. I have followed the guidelines provided by the institute in preparing the thesis.
d. I have confirmed to the norms and guidelines given in the ethical code of conduct of the institute.
e. Whenever I used materials (data, theoretical analysis, figure and text) from other sources I have given due credit to them by citing them in the text of the thesis and giving their detail in references.

Signature of student

(Rajkumar Shufen)

Department of Mechanical Engineering,
Indian Institute of Technology Guwahati,
Guwahati-781039, INDIA

CERTIFICATE

It is certified that the work contained in the thesis entitled "**Thermally Assisted Autofrettage of Thick Cylinders**" is submitted by **Mr. Rajkumar Shufen** to the Indian Institute of Technology Guwahati for the award of the degree of Doctor of Philosophy has been carried out under my supervision in the Department of Mechanical Engineering, Indian Institute of Technology Guwahati. This work has not been submitted elsewhere for the award of any other degree or diploma.

Dr. Uday Shanker Dixit
Professor
Department of Mechanical Engineering,
Indian Institute of Technology Guwahati,
Guwahati-781039, INDIA

Date: 29/10/2019

Dedicated to the Almighty, my beloved parents Mr. Rajkumar Tikendra & Mrs. Hijam Soroma Devi, my sisters Mrs. Rajkumari Aruna, Mrs. Rajkumari Shivani & Dr. Rajkumari Diana, my brother Mr. Rajkumar Charles and My teachers

Acknowledgements

I would like to start by thanking the Almighty for keeping me healthy and well. I would like to express my sincere gratitude towards all those who have helped me directly and indirectly during the tenure of my PhD at IIT Guwahati. The present thesis has been the fruition of many people who supported me and have played important role. I am grateful to all of them.

I thank the Indian Institution of Technology Guwahati for facilitating all the infrastructure required in my research. Special thanks to the Central Workshop and Material Science Laboratory for providing the necessary instruments and workspace to carry out the research. The support provided by the Engineering and Physical Sciences Research Council (EPSRC) (UK) (through grant EP/K028316/1) and Department of Science and Technology (India) (through grant: DST/RC-UK/14-AM/2012) funded project entitled 'Modeling of Advanced Materials for Simulation of Transformative Manufacturing Processes' is gratefully acknowledged.

I express my sincere gratitude and appreciation to my supervisor, Prof. Uday Shanker Dixit, Department of Mechanical Engineering, IIT Guwahati, for his expert guidance, patience and encouragement. Without his support and advice, it would not have been possible for me to carry out this research work. I really feel privileged for having the opportunity to work under him as my PhD supervisor. I shall always be grateful to him.

I would like to thank my doctoral committee members, Prof. D. Chakraborty, Prof. S Natesan and Dr. P. Kumari, for their valuable suggestions and encouragement during the period of my research work. I would also like to thank my former doctoral committee late A.N Reddy for his valuable suggestions. I am also grateful to the former and present heads of the Department of Mechanical Engineering, Prof. A.K. Dass and Prof. S.K. Dwivedy for extending various facilities during the tenure of my doctoral program.

I express my deepest gratitude to my father Mr. Rajkumar Tikendra, my mother Mrs. Hijam Soroma Devi, my sisters Mrs. Rajkumari Aruna, Mrs. Rajkumari Shivani, Dr. Rajkumari Diana, my brother Mr. Rajkumar Charles, my brothers-in-law Mr. Soraisham Gunindro, Mr. Thokchom Athumba Meitei and Mr. Rakesh Moirangthem for their immense support during the course of my PhD program. I will be grateful to them for sharing every responsibility in my family during my PhD.

I express my sincere thanks to my friends Mr. Sanasam Sunderlal, Mr. Krishnananda Moirangthem, Mr. Tekcham Gishan, Mr. Haobam Kisan, Mr. Gyanendro Loitongbam, Mr. Hijam Jiten, Mr. Lenin Laitonjam, Mr. Somorjit Ningthoujam, Mr. Nilkamal Mahanta, Dr.

Besufekad Negesh Fetene, Dr. Seikh Mustafa Kamal, Dr. Vinod Yadav, Dr. Polash Pratim Dutta, Mr. Vikash Vanik, Mr. Faladrum Sharma, Mr. Amit Raj, Mr. Kaustabh, Mr. Nitish Bharadwaj and last but not the least Mr. Shyaman Saloi.

Abstract

Autofrettage is a classical metal working technique for increasing the pressure bearing capacity, fatigue life, creep and stress-corrosion cracking resistance of thick-walled cylindrical and spherical vessels. Autofrettage is carried out by applying a load to the thick-walled cylinder or sphere that causes a partial or full plastic deformation. When the vessel is subsequently unloaded, compressive residual stresses are induced in the vicinity of the inner wall whereas tensile residual stresses are induced in the vicinity of the outer wall. On the basis of the type of load used for the plastic deformation, autofrettage can be classified into five types such as hydraulic, swage, explosive, thermal and rotational autofrettage.

Literature review indicates that hydraulic autofrettage is one of the two most popular and widely accepted type of autofrettage processes, together with swage autofrettage. However, the requirement of very high pressure makes the process costly. On the other hand, the thermal autofrettage is very simple although the achievable maximum increase in the pressure carrying capacity is limited due to the restriction on the maximum allowable temperature difference. Another detrimental feature that is common in any autofrettage processes is that the tensile residual stresses in the vicinity of the outer wall weakens the autofrettaged cylinder or sphere, a condition that is further aggravated in the presence of external surface flaws like cracks or wears as the tensile stresses causes the cracks to open up.

The focus of the thesis is the design of a special class of autofrettage processes that could be called as “thermally assisted autofrettage processes” where a conventional autofrettage process is augmented by a thermal load. The scope of the thesis is limited to hydraulic and thermal autofrettage processes. The first objective of the study is to explore the feasibility of economizing a hydraulic autofrettage process and increasing the efficacy of a thermal autofrettage by combining them in a single process. A finite element method (FEM) modeling of a combined hydraulic and thermal autofrettage of a thick cylinder was carried out by applying the hydraulic pressure and temperature gradient simultaneously using an FEM package ABAQUS® for aluminum and SS304 steel cylinders. These type of cylinders are widely used for several applications and represent two widely different sets of material properties. The aluminum has high coefficient of thermal expansion and low yield strength. On the other hand, SS304 steel has relatively low coefficient of thermal expansion and high yield strength. Moreover, for these materials, some analytical and experimental results are available in the literature, which are helpful for validating FEM model. A series of combinations of temperature difference and hydraulic pressure were explored for the two materials, for

achieving the maximum increase in the pressure capacity. The results showed that the combined autofrettage can achieve desired increase in the pressure capacity of thick-walled cylinders with a relatively small autofrettage pressure.

The next objective was the design of a thermal autofrettage coupled with heat treatment. In the proposed method, the conventional thermal autofrettage of a cylinder was followed by a thermally reloading step where the outer wall was heated above the lower critical temperature to cause local austenization. The inner wall temperature was lower and was governed by the criterion that the corresponding temperature difference did not yield the cylinder. This was followed by a quenching process in which the cylinder from both the walls after which compressive residual stresses were induced in the vicinity of the inner and the outer wall. An FEM analysis was carried out considering temperature and microstructure dependent material properties of AISI 1080 steel. Phase transformation kinetics was incorporated through the user defined subroutine UMATHT in ABAQUS®. The results indicated that the technique mitigated the harmful autofrettage-induced tensile residual stresses in the vicinity of the outer wall.

In a follow up study, thermal autofrettage of thick-walled cylinder coupled with heat treatment was carried out experimentally on thick-walled cylinder made of AH36 mild steel. An experimental setup was developed to carry out the proposed thermal autofrettage process and the heat treatment procedure for inducing compressive residual stresses to the walls of a thermally autofrettaged cylinder. The cylinder subjected to the procedure was inspected for the presence of residual stresses using two approaches— one based on the measurement of microhardness and another based on the measurement of the opening angle due to a radial cut in the heat treated autofrettaged cylinder. Based on measurements taken before the autofrettage, after the thermal autofrettage and after the heat treatment of the autofrettaged specimens, the presence of residual stresses at the vicinity of the outer as well as the inner wall of the thermally autofrettaged cylinder was ascertained.

The heat treatment design of the thermally autofrettaged cylinder was also simulated for a hydraulic autofrettaged cylinder also. An FEM based analysis is carried out in ABAQUS®. The results indicated that the heat treatment design proposed for the thermally autofrettaged cylinder to induce compressive residual stresses at the outer wall was also applicable for a hydraulic autofrettaged cylinder. However, for the cylinders subjected to high percentage of autofrettage, heating of the outer wall was needed to be carried out well-below the lower critical temperature. In fact, this was an advantage in terms of energy saving and could be implemented even for cylinders subjected to a low percentage of autofrettage.

Overall, the hydraulic autofrettage process was economized by combining it with a temperature gradient due to a lower inner wall temperature. The harmful effects of the tensile residual stresses in the vicinity of the outer wall of a hydraulically or thermally autofrettaged cylinder was also mitigated by proposing a novel heat treatment procedure. This procedure was supported by experiments carried out in a thermally autofrettaged cylinder.

Table of Contents

List of Figures

भारतीय प्रौद्योगिकी संस्थान गुवाहाटी
Indian Institute of Technology Guwahati

List of Tables

Nomenclature

Roman letters

$(K_I)_A$	Opening mode (mode I) stress intensity factor
$\{f_i\}_{ex}^{b}$	Elemental external force vector
$\{f_i\}_{in}^{e}$	Elemental internal force vector
$[B_L]$	Components of the gradient of the shape function
$[K]^{(i-1)}$	Global stiffness matrix
$\{F_{in}\}$	Global internal force vector
$\{R\}^{(i-1)}$	Unbalanced force between the external force vector
$\{U\}^{i}$	Global incremental displacement vector in the current iteration
a	Inner radius
Ac_1	Lower critical temperature
Ac_3	Upper critical temperature
b	Outer radius
b_k and n_k	Temperature dependent rate constants in the Johnson-Mehl-Avrami-Kolmogorov equation
c	Radius of elastic-plastic interface
C	Kinematic hardening modulus
c	Specific heat energy at constant volume
dT	Change in temperature
du	Internal energy change per unit mass
E	Young's modulus and
e_T	Thermal emissivity
f	Von Mises yield function
k	Thermal conductivity
K and n	Strain hardening parameters
l	Length of parallel section of swage mandrel

M	Locked bending moment
N	Number of constituents present in steel alloy
N_e	Total number of finite elements
N_i^b	Shape functions for the boundary
p	Autofrettage pressure
P	Aggregate property of material
P_k	Property of the k^{th} constituent
p_{max}	Maximum autofrettage pressure applicable at the inner wall without causing reverse yielding
Q	Rate of internal heat generated per unit volume
q_a	Heat flux at the inner wall
q_b	Heat flux at the outer wall
r	Radial coordinate in cylindrical coordinate space
t	Time
$T(r, t)$	Temperature as a function of spatial coordinate r and time t
T_0	Temperature at which the volume fraction of the k^{th} constituent reaches 1% of the maximum obtainable volume fraction
T_∞	Ambient temperature at steady state
T_a	Temperature of the inner wall of cylinder
T_b	Temperature of the outer wall of cylinder
t_f	Finish time
T_j	Temperature at current time
T_{MS}	Temperature below which the transformation of austenite to martensite commences
t_o	Datum time corresponding to the temperature T_0 at which the volume fraction of the k^{th} constituent has reached 1% of the maximum obtainable volume fraction
T_{Room}	Room temperature
t_s	Start time

T_s	Surface temperature
tol	Tolerance factor
u_z	Axial displacement
X_{AUS}	Volume fractions of austenite
X_{BN}	Volume fractions of bainite
X_{FER}	Volume fractions of ferrite
X_k	Volume fraction of a particular kth constituent
X_{MAR}	Volume fraction of martensite
X_{MS}	Volume fraction of martensite
X_{PER}	Volume fractions of pearlite
z	Axial coordinate in cylindrical coordinate space
A	Back stress tensor
β	Stefan-Boltzmann constant
E	Is the equivalent strain
ρ	Density
X_k^{max}	Maximum volume fraction of the k^{th} constituent that can be obtained
X_k^{eq}	Equilibrium volume fraction of proeutectoid ferrite or cementite

Greek letters

$[\phi]$	Shape function matrix
$[\phi]^b$	Shape function matrix for an area element
$\{\delta u\}^b$	Virtual displacement vector at the specific nodes of a surface element
$\{\Delta u\}$	Incremental displacement vector
$\{\Delta\delta u\}_e$	Virtual displacement vector at the specific nodes for an *n*-noded element *e*
∇	Gradient operator
μ	Coefficient of friction
$d\alpha_{ij}$	Incremental back stress tensor

$d\varepsilon^{pl}$	Incremental plastic strain tensor
$d\lambda$	Plastic multiplier
$d\varepsilon_{ij}^{e}$	Incremental elastic strain
$d\varepsilon_{eq}^{p}$	Incremental equivalent plastic strain
$d\varepsilon_{ij}^{p}$	Incremental plastic strain
$d\varepsilon_{ij}^{th}$	Incremental thermal strain
T_{∞}	Ambient temperature at steady state
u_{θ}	Angular displacement
$X\gamma$	Volume fraction of austenite that was available at the beginning of the transformation of a constituent
α	Opening angle due to a radial cut in an autofrettaged ring sample
α_T	Coefficient of thermal expansion
β	Stefan-Boltzmann constant
β_B	Bauschinger effect factor
δ	Overstrain
ΔH	Enthalpy of formation
δ_{ij}	Dirac-delta function
δU	Total internal work
δu	Virtual displacement field in a domain
δu_i	Components of the virtual displacement tensor
δW	External work done due to the virtual displacement
$\delta\varepsilon_{ij}$	Virtual strain field tensor
Δt	Increment of time
ΔT	Temperature difference
ΔX_k	Incremental change in volume fraction of the k^{th} constituent
ε_p	Plastic strain
ε_Y	Is the strain at the start of yielding

θ	Angular coordinate in cylindrical coordinate space
θ_F	Front taper of swage mandrel
θ_R	Rear taper of swage mandrel
ν	Poisson's ratio
ρ	Density
σ	Flow stress
$\boldsymbol{\sigma'}$	Deviatoric part of the current stress tensor
Σ	Assembling operation of finite elements
σ_{cY}	Compressive yield strength of material
σ_{ij}	Stress tensor
σ'_{ij}	Deviatoric stress tensor
σ_{θ}^{res}	Compressive hoop residual stress induced at the inner wall
σ_Y	Yield stress
τ	Fictitious time parameter
φ	Angular position of the state of stress in a 12-sided polygonal yield locus
ψ	Parameter with value either 0 or –1

List of abbreviations

AC	Alternating current
ASME	American Society of Mechanical Engineers
BEF	Bauschinger effect factor
CPU	Central processing unit
DC	Direct current
EMF	Electromotive force
EP	Extra pressure
FDM	Finite difference method
FEM	Finite element method
GUI	Graphical user interface
HPP	High pressure processing
JMAK	Johnson-Mehl-Avrami-Kolmogorov
PWD	Pressurized water reactor
SMP	Safe minimum pressure
TTT	Time temperature transformation
VMP	Variable method property
ZVS	Zero volt switching

भारतीय प्रौद्योगिकी संस्थान गुवाहाटी
Indian Institute of Technology Guwahati

Chapter 1

Background and Scope

1.1 Beginning of a Process Called Autofrettage

The mid-19th century marked the influence of the industrial revolution in military engineering when military engineers were assigned the task of enhancing the performance of small arms and heavy artillery. During this period, the 'built up' method of fabricating gun barrels was introduced which was performed by shrink-fitting layers of wrought iron around an inner core that formed the barrel of the firearm [1]. Similar concepts were also applied for fabricating barrels from direct casting using a differential cooling technique that was performed by heating the outer surface, while cooling the bore with cold water [1]. In principle, the basis of these techniques was to increase the overall strength of the gun barrel by imparting a compressive stress field to the inner wall where the impact of the forces exerted due to expansion of hot gases was the maximum. With the further modifications on the basis of this principle and evolution of a series of efforts made in the design of gun barrels, the concept of autofrettage was born. The concept was pioneered in the year 1907 by Jacob, a French artillery officer, for pre-stressing monobloc gun barrels who gave the term 'autofrettage' which means "self-hooping" in French. The idea of autofrettage was revolutionary because the gun barrel was strengthened without any external components but by plastic deformation. Since its inception, the technique has gradually gained popularity and has evolved from originally being a military application to various other applications.

1.2 General Concept of Autofrettage

The process is based on the application of a uniform load to the inner wall of a cylindrical or spherical vessel to cause a partial or full plastic deformation. In case of partial plastic deformation, the applied load partially yields the vessel resulting in two deformed zones *viz*., an inner plastic zone from the inner wall to an intermediate radius and an outer elastic zone till the outer wall. When the vessel is unloaded, the outer elastic zone contracts due to its tendency to regain its original position whereas the inner plastic zone remains permanently deformed. This exerts internal forces on the inner plastic zone generating compressive residual stress in the vicinity of the inner wall. However, tensile residual stresses are induced in the vicinity of the outer wall due to the reaction forces exerted by the plastic zone on the elastic zone. In the case of autofrettage with full plastic deformation, the applied load completely yields the vessel up to the outer wall. However, the material at inner wall is more strained than

that at the outer wall and therefore tensile stresses are larger at the inner wall surface than those at the outer wall surface. After unloading, compressive residual stresses are induced at the inner wall due to non-uniform straining. At the same time tensile residual stresses are induced in the vicinity of the outer wall. The induced compressive residual stresses are beneficial and enhance the pressure carrying capacity, fatigue life and stress corrosion resistance of the vessel.

The schematic of a typical autofrettage process for a thick cylinder or sphere is shown in Fig.1.1. In the loading step, a typical deforming load that is an internal pressure *p* in this case is applied to the inner surface of the cylinder, which creates two deformed zones, *viz*., an inner plastic zone from the inner surface to a certain intermediate radius and an outer elastic zone from the intermediate radius to the outer wall. The displacement of the inner surface of the cylinder with respect to the original inner surface (shown by dotted lines) is apparent in an exaggerated way. When the load is removed in the unloading step, elastic recovery takes place in the cylinder. The contraction of the elastic zone applies pressure to the inner plastic zone. At this stage, the cylinder has compressive stresses in the inner plastic zone and tensile stresses in the outer elastic zone.

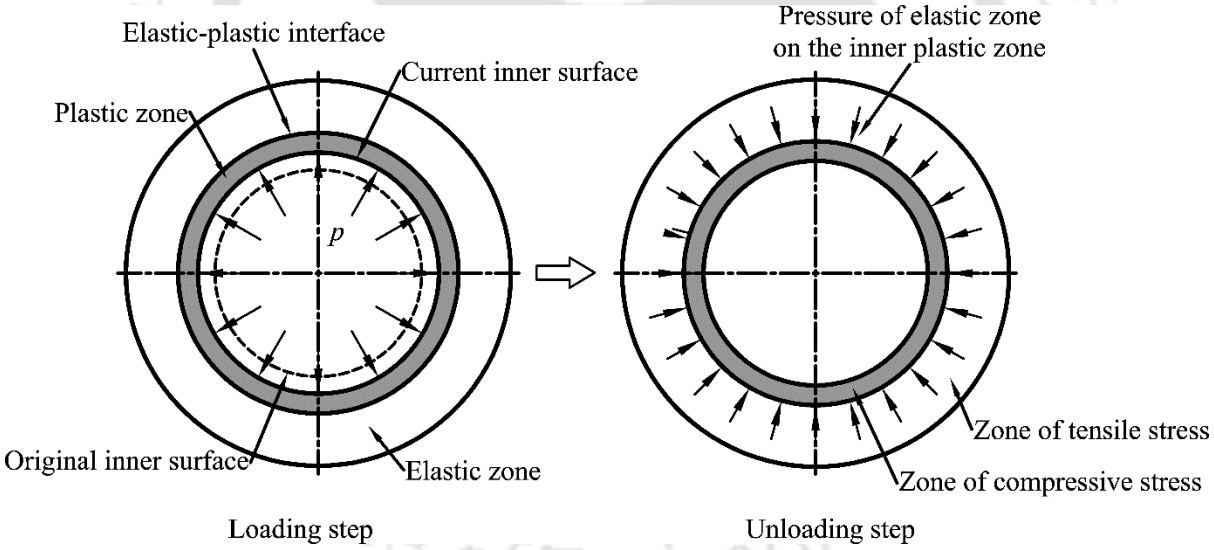

Figure 1.1 Working principle of a typical autofrettage process

The amount of autofrettage in a cylinder or sphere can be quantified in terms of overstrain or percentage of autofrettage. Overstrain is the percentage of the thickness of the cylinder/sphere that has to be plastically deformed and is expressed as

$$\delta = \left(\frac{c-a}{b-a} \right) \times 100\%, \tag{1.1}$$

where *a* is the inner radius, *b* is the outer radius and *c* is the radius of elastic-plastic interface. A 100% overstrain means that the cylinder or sphere is completely plastic. On the other hand,

percentage of autofrettage signifies the fraction of the maximum possible compressive hoop residual stress that can be achieved in an autofrettage process for a particular cylinder or sphere with the given material and dimensions [2]. As a thumb rule, the maximum autofrettage pressure that can be applied at the inner wall is limited to the magnitude that does not cause reverse yielding due to the induced compressive residual stresses during the unloading. The percentage of autofrettage is computed as

$$Autofrettage\,\% = \frac{\sigma_\theta^{res} \text{ achieved with autofrettage pressure } p}{\sigma_\theta^{res} \text{ achieved with autofrettage pressure } p_{\max}} \times 100, \tag{1.2}$$

where σ_θ^{res} is the compressive hoop residual stress induced at the inner wall, p is a particular autofrettage pressure and p_{max} is the maximum autofrettage pressure applicable at the inner wall without causing reverse yielding. A 100% autofrettage means that the cylindrical or spherical vessel has been autofrettaged using p_{max} and the maximum possible magnitude of the residual stress has been achieved.

1.3 Applications of Autofrettage

Autofrettage is widely practiced and incorporated in the design and manufacture of thick cylindrical and spherical vessels or containers that are subjected to static/pulsating high magnitude load or corrosive medium. Some important applications of autofrettage are listed as follows:

- high pressure processing (HPP) equipment in food industry,
- pressure carrying components of water jet cutting system,
- pressurized water reactor (PWR) in nuclear power plants,
- automobile combustion chambers and steam/chemical pipelines,
- Gun barrels of small and heavy artillery,
- strengthening double-layered combined die in forging as proposed by Hu *et al*. [3].

The American Society of Mechanical Engineers (ASME) has cited the importance of autofrettage and has documented standard procedures for the design of thick-walled cylindrical pressure vessels with the incorporation of autofrettage in article KD-5 of the ASME Boiler & Pressure Vessel Code, Section VIII Division 3 [4].

1.4 Types of Autofrettage Processes

On the basis of the type of the load used for the process, autofrettage can be classified into various types— hydraulic, swage, explosive, thermal and rotational. A brief description for each autofrettage process is provided in the following subsections.

1.4.1 Hydraulic Autofrettage

Hydraulic autofrettage is the earliest concept of autofrettage that was originally conceived by Jacob [5]. In this process, the bore of the thick-walled cylinder is filled with a hydraulic oil and pressurized with ultra-high pressure. The cylinder starts yielding at the inner surface on reaching a particular pressure called yield pressure, which is the original pressure carrying capacity of the cylinder with the specific material and dimensions. As the pressure is slightly increased beyond the yield pressure, further yielding takes place in the cylinder creating an inner plastic zone that extends from the inner surface to an intermediate radius and an outer elastic zone that extends from the intermediate radius to the outer surface. At this point, if the cylinder is depressurized, the outer elastic zone recovers and compressive residual stresses are induced in the vicinity of the inner surface of the cylinder. The amount of plastic-overstrain desired in the cylinder is controlled by increasing the pressure beyond the yield pressure. Care must be taken while applying the large pressure during hydraulic autofrettage because the cylinder can undergo reyielding due to the compressive residual stresses. For cylinders having wall thickness ratios (ratio of outer to inner diameters) greater than 2.22, the reyielding occurs when the applied pressure is greater than twice the yield pressure of the cylinder [6].

A schematic of a hydraulic autofrettage process is shown in Fig. 1.2. The autofrettage pressure is delivered to the cylinder by injecting the hydraulic fluid through an inlet using a powerful hydraulic pump. Seal plugs are provided at the ends of the cylinder for preventing oil leakage. To conserve the volume of the oil used in the process, a core is inserted inside the cylinder [7]. The process is very effective in terms of the maximum increase in pressure carrying capacity that can be achieved. To reach its full potential, the process requires a very large magnitude of pressure to be applied at the inner wall of the cylinder and this increases with the increase in the wall thickness ratio. For example, in a typical 10 mm thick ring sample made of steel alloy 4333 M4 (yield strength 1070 MPa) with an inner radius of 15 mm and an outer radius of 31 mm, the pressure required for yielding through 50% of the ring thickness is 662 MPa. The requirement of high pressure makes the process costly.

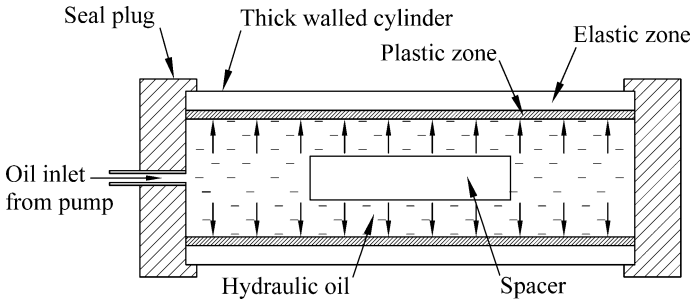

Figure 1.2 A schematic of hydraulic autofrettage process

1.4.2 Swage Autofrettage

The swage autofrettage process was proposed by Davidson *et al*. [8] as an economical alternative to conventional hydraulic autofrettage process. In this method, the inner wall of the cylinder is plastically deformed by the interference of an oversized mandrel called 'swage' that is mechanically forced through the bore of the cylinder by means of the ram of a hydraulic/mechanical press. Davidson *et al*. [8] used three types of set ups, *viz*. mechanical push swaging, mechanical pull swaging and hydraulic push swaging. The mechanical push swaging used a ram that was pushed by a hydraulic press, the mechanical pull swaging used an overhead crane to pull up the mandrel vertically and the hydraulic push swaging used hydraulic pressure applied at the end of the mandrel. The mechanical pull swaging and hydraulic push swaging along with a typical swage mandrel geometry are shown in Fig. 1.3. The hydraulic fluid for swaging was a mixture of water and glycerin.

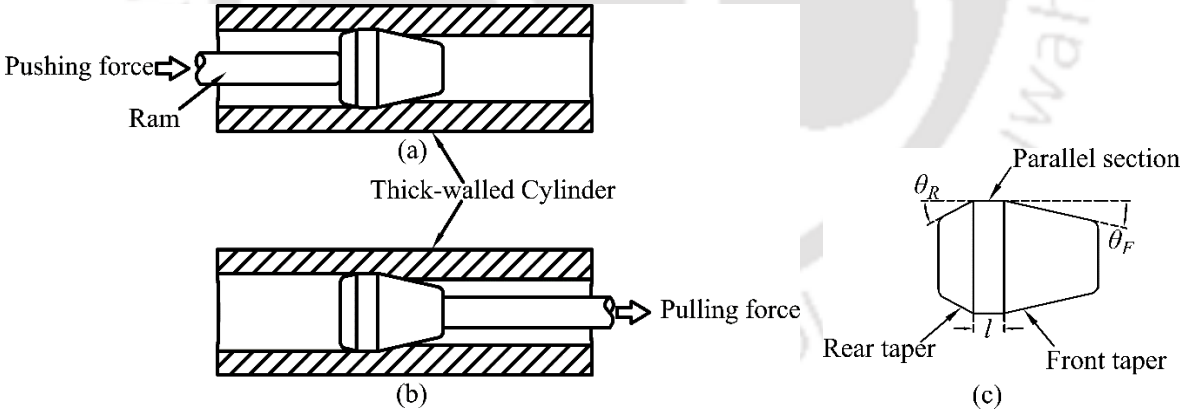

Figure 1.3 Schematic of (a) push (b) pull swaging and (c) swage mandrel geometry

The mandrel has three main geometrical specifications— a front taper of θ_F, a rear taper θ_R and a parallel section of length l as shown in Fig. 1.3(c). The front taper provides the angle of approach for gradual application of the autofrettage load, the parallel section ensures uniform plastic deformation of the inner wall of the cylinder and the rear taper enables elastic unloading of the cylinder. The swage mandrel used in the process is usually made of a material which has a higher strength than the material of the cylinder specimen. Chen [9] used tungsten

carbide as the material of the mandrel whose elastic modulus was 610 GPa which is about three times the elastic modulus of a typical steel alloy. The process involves a lot of friction between the bore and the mandrel surface and hence requires a highly polished surface finish of the mandrel and use of lubricants. Davidson *et al.* [8] used a centerline average surface roughness of 0.05–0.38 μm for the mandrel A molybdenum disulfide suspension in oil and copper plating used in combination provided the best lubrication performance. For a particular tube specimen and the same level of plastic overstrain, the fatigue lifetime of a swage autofrettaged tube is significantly higher than that for the hydraulic autofrettage. On reapplication of the working pressure, the reyielding of the autofrettaged tubes occurs at the same level of pressure implying that swage autofrettage can also achieve the same increase in the pressure carrying capacity as given by hydraulic autofrettage [10]. The method is suitable only for tube specimen and is generally used in the autofrettage of gun barrels. Spherical vessels cannot be autofrettaged by this process.

1.4.3 Explosive Autofrettage

Autofrettage can also be performed by using an explosive charge detonated inside the cylinder in a pressure propagating medium like air or water [11]. This method is called explosive autofrettage. Because of the use of explosive, the process is difficult to control and dangerous for practical implementations. A typical set up of the apparatus for the explosive autofrettage is shown in Fig. 1.4.

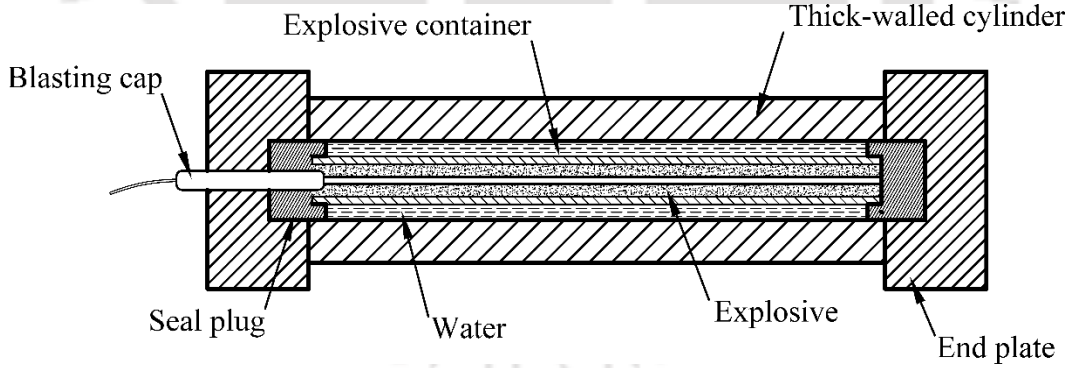

Figure 1.4 Schematic of a typical set up of explosive autofrettage process. Modified figure from Ref. **[12]**

1.4.4 Thermal Autofrettage

In this method, the autofrettage is carried out by using thermally induced stresses by subjecting the cylinder to a temperature gradient across its thickness. When the cylinder is cooled to room temperature, compressive residual stresses are induced in the inner wall of the cylinder due to elastic unloading of the thermal stresses. The term ‘thermal autofrettage’ was first used by Wen *et al*. [13] as an alternative method for autofrettage of internal metal liner of

a cryogenic composite feed line. However, a rigorous elastoplastic analysis of thermal autofrettage was first carried out by Kamal and Dixit [14] for a long thick walled cylinder with open ends based on Tresca yield criterion and non-hardening material. Thermal autofrettage is a very simple technique and does not require any complex machinery or special equipment for the practical implementation [15]. Despite its simplicity, the efficiency of the process in terms of the achievable maximum increase in the pressure carrying capacity is limited to only about 40%. This is mainly because the maximum temperature difference that can be used in the process for a particular cylinder dimension is limited to the maximum range beyond which material properties start to change [16]. Nevertheless, the economic advantage of the process can still be utilized and the performance of the thermally autofrettaged cylinder can be improved by shrink fitting [18]. A schematic of a setup for thermal autofrettage is shown in Fig. 1.5 [15]. Here, the outer surface of the cylinder is heated by an electric heater and the inner surface is cooled by the flowing cold water. This creates the required temperature gradient for causing the plastic deformation of a portion of cylinder. When the cylinder is brought back to the room temperature, the residual stresses are generated.

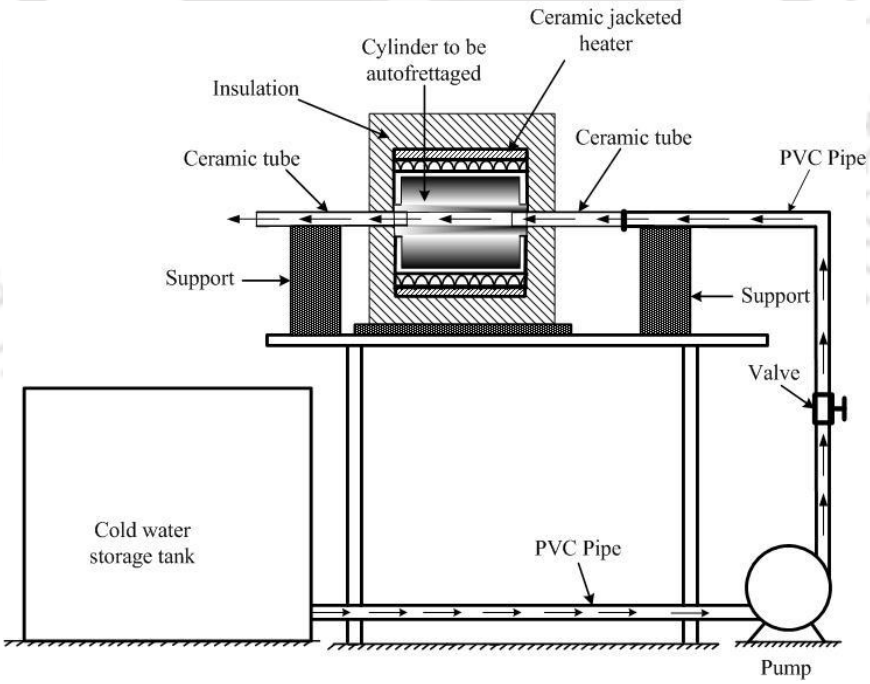

Figure 1.5 A schematic of thermal autofrettage process **[15]**

1.4.5 Rotational Autofrettage

In this method of autofrettage, the cylinder is applied with a centrifugal force due to rotation of the cylinder at a high angular velocity in the loading phase. In the unloading phase, the angular velocity is decreased and the cylinder is gradually brought to rest that induces the residual compressive stress field in the cylinder. The method was proposed by Zare and

Darijani [17]. A schematic of the process is shown in Fig. 1.6. The rotation of the cylinder is provided by mounting it on a bearing support. The output rotation of the motor is transmitted to the cylinder through a transmission system. For a typical 1 m long cylinder having inner radius of 0.1 m and outer radius of 0.3 m, made of ASTM-A709 steel, the speed required for the autofrettage of the cylinder was 9780 revolutions per minute.

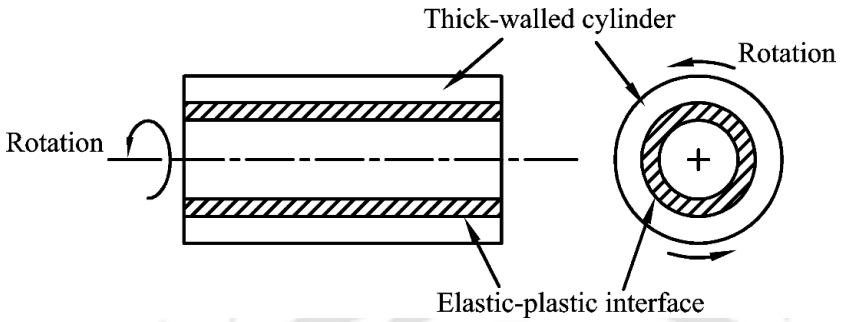

Figure 1.6 A schematic of rotational autofrettage process

The advantages and disadvantages associated with each type of autofrettage process are summarized and compared in Table 1.1.

Table 1.1 Comparison of the advantages and disadvantages of the different types of autofrettage processes

Autofrettage	Advantages	Disadvantages
Hydraulic autofrettage	• Efficient in terms of the maximum achievable increase in the pressure carrying capacity • Suitable for all types of vessels such as cylinders and spheres	• Requires large magnitude of pressure • Process is costly
Swage autofrettage	• More economical than hydraulic autofrettage • Simple for practical implementation and energy efficient	• It is not applicable in thick spheres or closed ended cylinders
Explosive autofrettage	• May be applicable in all types of vessels such as cylinders and spheres	• Involves explosives • Process is difficult to control and dangerous for practical implementations • Require legal permission
Thermal autofrettage	• May be applicable in all types of vessels such as cylinders and spheres • Very simple for practical implementation • Cost effective	• Limited efficiency in terms of the achievable maximum increase in the pressure carrying capacity
Rotational autofrettage	• Very simple for practical implementation • Cost effective	• Not a properly established type of autofrettage • May not be applicable in thick-walled spheres as it will cause shape distortion at high angular speed

1.5 Scope of the Present Thesis

In the previous section, various types of autofrettage processes have been explained. A comparison of the types of autofrettage processes reveals that the hydraulic autofrettage is the most popular and widely accepted type of autofrettage process. However, the requirement of very high pressure makes the process costly. On the other hand, the thermal autofrettage is very simple although the achievable maximum increase in the pressure carrying capacity is limited due to the restriction on the maximum allowable temperature difference. Another detrimental feature that is common in any autofrettage processes is that while the compressive residual stresses induced in the vicinity of the inner wall is beneficial for strengthening, the tensile residual stresses the tensile residual stresses in the vicinity of the outer wall weaken the autofrettaged cylinder or sphere. This condition is aggravated in the presence of external surface flaws like cracks or wears [18] as the tensile stresses cause the cracks to open up.

The focus of the present thesis is to design a special class of autofrettage processes that may be called a thermally assisted autofrettage process where a conventional autofrettage process is carried out by combining with a thermal load. The emphasis shall be on hydraulic and thermal autofrettage processes and the overall objectives are broadly into two categories that are explained in the following Subsections.

1.5.1 Design of a Combined Hydraulic and Thermal Autofrettage Process in Thick Cylinders

This objective explores the feasibility of economizing a hydraulic autofrettage process or increasing the efficiency of a thermal autofrettage by combining them in a single process. The schematic of such an autofrettage is shown in Fig. 1.7. In the loading step, the vessel is pressurized using an internal pressure p in the presence of a temperature gradient that exists across the thickness of the vessel by heating the outer wall at a temperature T_b while maintaining the inner wall at a lower temperature T_a ($< T_b$). The combined loading causes the elastic-plastic deformation in the cylinder creating the inner plastic and outer elastic zones. In the unloading step, the vessel is simultaneously depressurized and gradually cooled to room temperature T_{Room} and compressive residual stresses are induced in the vicinity of the inner wall. For a particular autofrettage vessel and a desirable level of the increase in pressure capacity, it may be possible to design an autofrettage process that complements the relative advantages of both the hydraulic and thermal autofrettage processes.

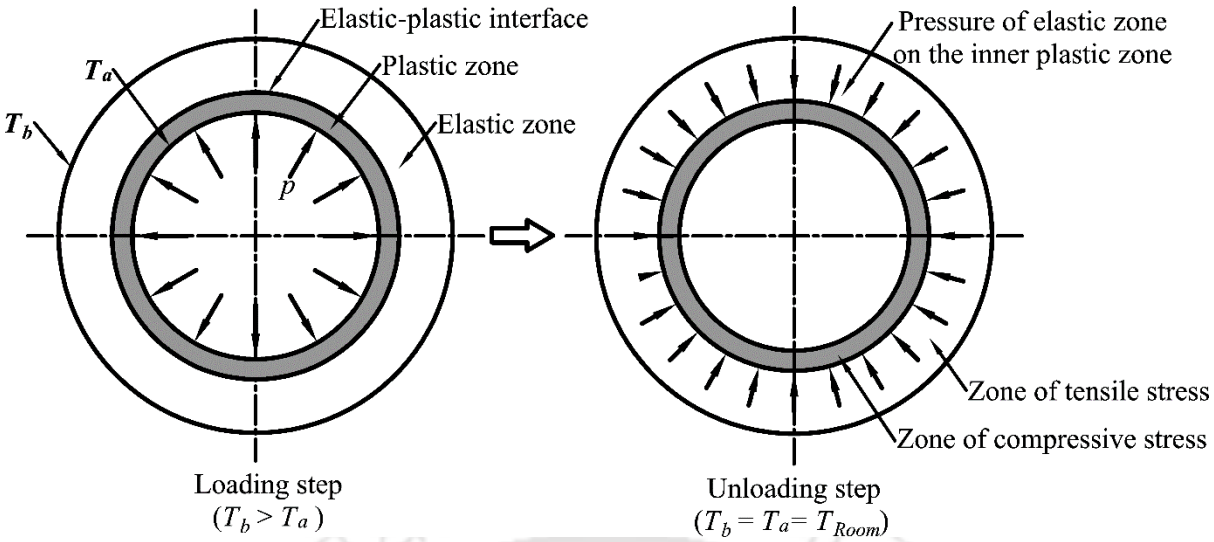

Figure 1.7 Schematic of the combined hydraulic and thermal autofrettage process

1.5.2 Design of a Hydraulic and Thermal Autofrettage Process Coupled with Heat Treatment in Thick Cylinders

This objective is directed towards the design of a heat treatment procedure that can be incorporated in a conventional thermal and hydraulic autofrettage process to mitigate the autofrettaged-induced outer wall tensile residual stresses. In the heat treatment procedure, the cylinder autofrettaged by thermal or hydraulic method is again subjected to two subsequent steps viz., a thermal reloading and a quenching step. A schematic of the process is shown in Fig. 1.8. Figure 1.8(a) shows the initially autofrettaged cylinder with the induced residual stress fields. This is thermally reloaded by heating the outer wall at a temperature T_b while the inner wall is kept at a much lower temperature T_a as shown in Fig. 1.8(b). In the quenching step, the cylinder is subsequently quenched till the room temperature T_{Room} as shown in Fig. 1.8(c). When the cylinder come into contact with the quenchant, the temperature of the walls decrease suddenly leading to rapid contraction. The underlying material having not commenced the contraction at this point resists the contraction of the inner and outer wall, generating very large tensile stresses at the surfaces. If the equivalent stress of these tensile stresses exceeds the local yield stress, yielding occurs creating an outer plastic zone in the autofrettaged cylinder. With gradual cooling, the remaining portion of the material contracts and exerts an inward pull force on the outer plastic zone. As a result, compressive residual stresses are induced in the vicinity of the outer wall.

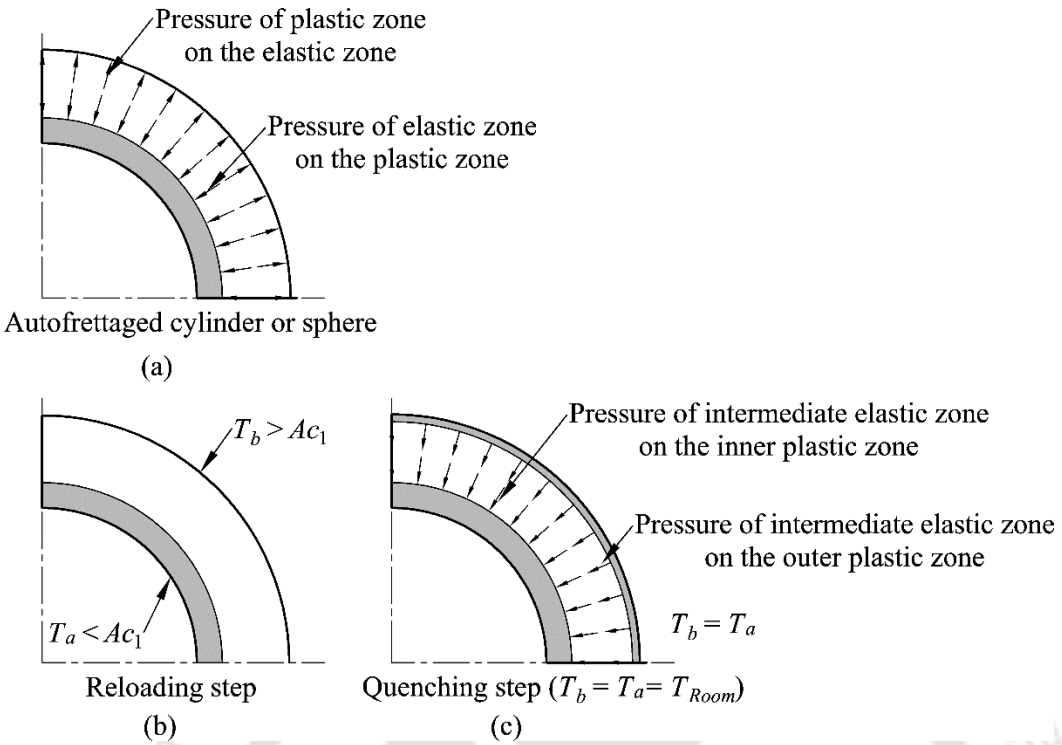

Figure 1.8 Schematic of the heat treatment coupled autofrettage process

1.6 Organization of thesis

The present thesis contains seven chapters. The present chapter introduces the general concept of autofrettage along with its classification into hydraulic, mechanical or swage, explosive, thermal and rotational variant. The remainder of the thesis is organized as follows: Chapter 2 presents the survey of literature and states the detailed objective of this thesis. Chapter 3 presents a combined hydraulic and thermal autofrettage process of a thick-walled cylinder. Chapter 4 presents a heat treatment design of thermally autofrettaged cylinder. Chapter 5 presents the construction and working of an experimental set up for thermal autofrettage coupled with heat treatment in a cylinder. Chapter 6 presents a heat treatment design of a hydraulically autofrettaged cylinder. Chapter 7 identifies future challenges and scope for further work.

Chapter 2

Literature Review and Detailed Objectives

2.1 Introduction

Autofrettage is a metal working process carried out for inducing beneficial compressive residual stresses in the thick walled cylindrical or spherical pressure vessels. In this process, the thick-walled cylinder or sphere is subjected to a state of partial or full plastic deformation. In case of partial plastic deformation, the autofrettaged specimen comprises an inner plastic zone that restrains the tendency of an outer elastic zone to contract internally to regain its original undeformed position. This induces compressive residual stresses in the vicinity of the inner wall. In case of full plastic deformation, the material at inner wall suffers larger strain hardening than that at the outer wall. Here, the inner wall compressive residual stresses are induced due to non-uniform straining. The induced compressive residual stresses enhance the pressure carrying capacity, fatigue life and stress corrosion resistance of the vessel.

On the basis of the type of the load used for the process, autofrettage can be classified into various types— hydraulic, swage, explosive, thermal and rotational. Since the last eight decades, autofrettage has captured significant attention of researchers and engineers. Numerous researchers have proposed various theoretical models and carried out experimental studies for the elastic-plastic analysis of autofrettage and its types. In spite of a lot of research activities in the field of autofrettage, there has been a lack of review papers on this subject. Crossland and Bones [7] presented a review on internally pressurized thick-walled cylinders in the year 1958, which emphasized mainly on determining the strength of autofrettaged cylinders. Malik *et al*. [19] presented a review of hydraulic autofrettage process in 2008 and Malik and Khusnood [20] presented a review for swage autofrettage process in 2003. Although these reviews are based on adequate surveys, significant amount of works have been further carried out in the two aforementioned as well as the other types of autofrettage processes. Autofrettage of thick-walled spherical vessels has also not been reviewed by researchers. Hence, a review to supplement these advancements has been long overdue. The objective of this chapter is to compile and present an extensive review of autofrettage with its various types encompassing all types of applicable vessels. Based on the review, some challenging issues and key areas for future research are identified.

The review presented is based on a classification according to the research aspects rather than the chronology on how the works have progressed. The chapter is organized into

different sections as follows— Section 2.2 presents the modeling issues common to various autofrettage processes, Sections 2.3 and 2.4 present the mathematical models and experimental studies, respectively, of hydraulic autofrettage. Sections 2.5, 2.6, 2.7 and 2.8 discuss swage, explosive, thermal and rotational autofrettage, respectively. Section 2.9 presents the issues related to optimization of autofrettage. Section 2.10 briefly describes the ASME code related to autofrettage, Section 2.11 presents the challenging issues and directions for future research and Section 2.12 concludes the chapter.

2.2 Modeling Issues Common to Various Autofrettage Processes

Like most problems in plasticity, the general basis for mathematical modeling of a typical autofrettage process consists of formulating a set of governing differential equations, which are essentially the stress equilibrium equations, stress-strain constitutive equations and the strain-displacement compatibility equations that must be solved by invoking certain boundary conditions. The elastic limit of the cylinder is governed by a yield criterion. The stress response in the cylinder due to the evolution of plastic strain after yielding is described by a strain hardening function. Since the loading cycle in an autofrettage process includes an unloading stage, the Bauschinger effect also becomes an important factor. Therefore, three common issues arise while modeling a typical autofrettage process *viz*. (i) boundary conditions (ii) yield criterion and (iii) incorporation of the material behavior for the plastic deformation. These are discussed in the following subsections.

2.2.1 Boundary Conditions

The mechanical boundary conditions for solving the governing differential equations vary according to the type of vessel that is being studied. For cylinders, the formulation may be based on either a plane stress or a generalized plane strain assumption. In the plane stress assumption, the axial stress is taken as zero as in the analysis of thin rings or discs [21–24]. In the generalized plane strain assumption, the axial displacement of the cylinder is assumed to remain constant throughout the length of the cylinder as in the analysis of long tubes [25–60]. Again based on the type of the axial constraints, the long cylinder satisfying the generalized plane strain assumption may have one of the three end conditions— open end, closed end and plane strain. In the open end condition, the ends of the cylinder remain free [25–41]. In the closed end condition, the cylinder has structurally sealed ends [42–48]. Finally, in the plane strain condition, the ends of the cylinder are rigidly constrained and the axial displacement is zero [21,48–60]. For hydraulic autofrettage, the analyses of the plane stress and the open end conditions have been considered equivalent by some researchers [21,25] because the ends of

the cylinder remain traction-free in both the cases. This was also shown by Gibson *et al*. [61] using results based on a finite element method (FEM) study. Gibson *et al*. [61] also showed that the results provided by closed end and plane strain conditions were similar. In the case of a thick-walled sphere, the mechanical boundary conditions only consist of whether the outer wall remains traction-free or constrained.

2.2.2 Yield Criteria

The yield criterion is commonly based on either Tresca or von Mises criterion. The Tresca yield criterion leads to comparatively less complicated formulation but is independent of the end condition of cylinder. This drawback is most evident in the case of an open ended cylinder with wall-thickness ratios (ratio of outer diameter to inner diameter) more than 2.96 [25]. The von Mises yield criterion gives a more accurate prediction of the real material behavior and is more convenient because of the normality rule. Some researchers utilized the simplicity of the Tresca criterion and the accuracy of the von Mises criterion in a single model. Hill *et al*. [49] carried out a rigorous elastic-plastic analysis of a thick-walled cylinder subjected to internal pressure under plane strain condition. They discussed the applicability of von Mises as well as Tresca criteria; the Tresca criterion was referred by them as Mohr criterion. Li *et al*. [26] and Zeng *et al*. [27] used a yield criterion based on a twelve sided polygonal yield locus that was inscribed in the von Mises yield locus as shown in Fig. 2.1 Li *et al*. [26] used this criterion for the elastic-plastic analysis of an internally pressurized open ended cylinder. The solution was linear and simple but more accurate than one based on the Tresca yield criterion. For the open ended case where the axial stress σ_z is zero, this criterion exploits the fact that the states of stress at all stages of deformation in an internally pressurized cylinder or sphere remain confined in the fourth quadrant of the biaxial stress space because the radial stress σ_r is always compressive whereas the hoop stress σ_θ is always tensile. The yield criterion for a point P in the yield locus was defined by two linear functions depending on whether it was located on the MN or the MH line. The transition of P from MN to MH was based on the angle φ becoming –45°. Zeng *et al*. [27] further extended this study to the case of closed ended cylinder, sphere, conic shell and ellipsoidal vessels. In the case of a sphere, both Tresca and von Mises yield criteria reduce to a single identical form. Hence, the preference of a yield criterion becomes inconsequential.

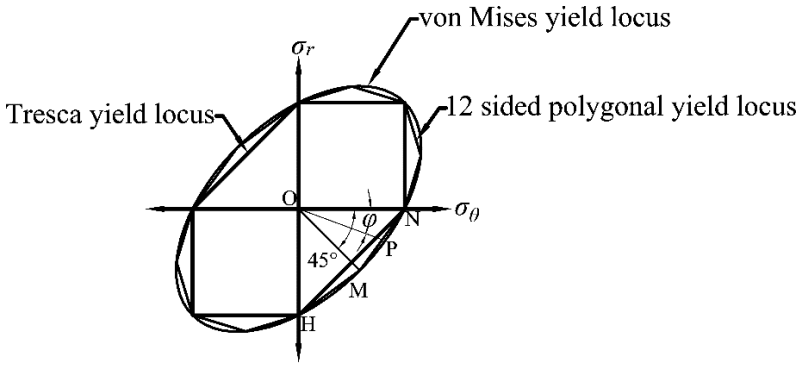

Figure 2.1 Yield locus based on a 12 sided polygon under plane stress

2.2.3 Material Behavior During Elastic-Plastic Deformation

The incorporation of the material behavior for plastic deformation requires the selection of a particular strain hardening model and the consideration of the Bauschinger effect for the unloading stage. Some of the strain hardening models that have been commonly used in the analysis of autofrettage process of thick-walled cylinders and sphere are as follows [62]:

(i) Hollomon's law:

$$\sigma = K\left(\varepsilon^p\right)^n, \tag{2.1}$$

(ii) Ludwik's law:

$$\sigma = \sigma_Y + K\left(\varepsilon^p\right)^n, \tag{2.2}$$

(iii) Swift's law:

$$\sigma = \sigma_Y\left(1+K\varepsilon^p\right)^n, \tag{2.3}$$

(iv) Ramberg-Osgood law:

$$\varepsilon_{eq}^p = \frac{\sigma}{E}\left\{1+K\left(\frac{\sigma}{\sigma_Y}\right)^{n-1}\right\}. \tag{2.4}$$

where σ is the flow stress, σ_Y is the yield stress, ε^p is the plastic strain, E is the Young's modulus and K & n are strain hardening parameters. When n=1 in Eqns. (2–3), the hardening law is called linear hardening law. Other specialized hardening functions exclusive to a particular model are mentioned wherever necessary.

The Bauschinger effect is generally incorporated by following two approaches. The first and the most common approach is to define the reverse loading yield criterion by using the Bauschinger effect factor (*BEF*), which is defined as follows [63]:

$$\beta_B = \frac{\sigma_{cY}}{\sigma}, \tag{2.5}$$

where β_B is the Bauschinger effect factor and σ_{cY} is the compressive yield strength of the material. The yield criterion for the unloading stage is defined by replacing the flow stress σ with $\beta_B\sigma$ in the same yield function used for the loading stage. If β_B =1, the hardening is isotropic whereas if β_B < 1, then the hardening is kinematic. If hardening is neglected in the loading stage then $\sigma = \sigma_Y$. Bastun and Podil'chuk [64] carried out a study to predict the Bauschinger effect factor in a complex state of loading based on a graphical-analytical approach. By considering a case study of hydraulic autofrettage of a thick-walled cylinder, the method was demonstrated with open and closed end conditions.

The second approach for incorporating the Bauschinger effect is by using a kinematic hardening model. Kinematic hardening models based on Prager [65] and Ziegler [66] have been commonly used by researchers for modeling autofrettage of thick-walled cylinders. The Bauschinger effect reduces the maximum residual stress in an autofrettage process. Parker [28] suggested a thumb-rule that the Bauschinger effect reduces the maximum residual hoop stress at the inner wall of a typical hydraulically autofrettaged cylinder by about 30% compared to a case based on ideal material behavior.

2.3 Mathematical Models of Hydraulic Autofrettage

In hydraulic autofrettage, the induced residual stresses are caused by ultra-high pressurization and subsequent depressurization of the thick-walled cylinder or sphere using hydraulic oil. The hydraulic autofrettage has been described in detail in Section 1.4.1. The mathematical modeling for the elastic-plastic analysis of hydraulic autofrettage process has been carried out for both cylindrical [21–60] and [67–81] as well as spherical [82–97] vessels.

All the end conditions in the case of cylinders have been considered in a variety of models. Most of the theoretical models of hydraulic autofrettage have been formulated based on deformation [98] or incremental [99] theory of plasticity. The deformation theory of plasticity considers total strain as function of stress whereas the incremental theory of plasticity considers incremental strain as a function of stress. The deformation theory of plasticity leads to inaccuracies in the analysis of hydraulic autofrettage process. Thomas [29] showed that the use of deformation theory introduces an error of as large as 21% in the distribution of axial stress and strain for an open ended cylinder. In the case of a sphere, formulations based on deformation and incremental theories lead to results that are in complete agreement [82]. This is because of the spherical symmetry of the applied load, which creates a state of proportional loading, a condition where both theories of plasticity coincide [100]. A few models have also

been developed based on the flow theory of plasticity using strain rate formulation [60,70,95,96]. The type of formulation along with the various modeling issues discussed in Section 2.2 affect the complexity of the model and the particular solution method. This leads to a classification of the general class of the theoretical models into three types— analytical, numerical and FEM model that are reviewed in the following subsections.

2.3.1 Analytical Models

An analytical model with a closed form solution is generally obtainable when the formulation is based on the deformation theory of plasticity [22]. Literature includes Refs. [26,27,30,33,42,50–59] for cylinders and Refs. [27,83,84] for sphere. All these models, except those in Refs. [26,27] have used the von Mises yield criterion. Nadai [51] assumed a rigid-plastic material behavior resulting in a discontinuous stress distribution at the elastic-plastic interface. In the absence of Bauschinger effect, Gao [42], Huang [52] and Gao [83] used a linear hardening law. Gao [30] used the following hardening model:

$$\sigma = E\varepsilon\left(\frac{\varepsilon}{\varepsilon_Y}\right)^{n-1}, \tag{2.6}$$

where ε is the equivalent strain and ε_Y is the strain at the start of yielding. For the cases incorporating Bauschinger effect using the *BEF* parameter, Hosseinian *et al.* [56] used the linear hardening law and Wang [50] used a hardening law modified from the Ramberg Osgood law (Eq. 2.3) as follows:

$$\varepsilon^p = \frac{\sigma}{E}\left(\frac{\sigma}{\sigma_Y}\right)^{n-1}. \tag{2.7}$$

Another class of analytical models with closed form solution using Hencky's total deformation theory is a formulation based on the theory of strain gradient plasticity. Strain gradient plasticity is an extension of the classical theory of plasticity where the equivalent stress due to the current state of stress not only involves the Cauchy's stress tensor but also a spatial gradient of the effective plastic strain. The strain gradient term, which is inversely proportional to a length scale gives higher flow stress at spatial gradient predominantly found in the deformation of miniature components. Models based on strain gradient plasticity can capture the strengthening effect of size. For hydraulic autofrettage analysis, analytical models based on this approach include the works of Gao [45, 46] and Gao *et al*. [59] for a cylinder and Gao [84] and Wen *et al*. [85] for sphere. A plane strain condition was assumed in all the models [57–59] for the analysis of the cylinder. For the material behavior, the Bauschinger effect was also neglected in all these models. Gao [57] used Hollomon's hardening law; Gao [58,84] used a

linear hardening law. Gao *et al*. [59] and Wen *et al*. [85] considered a linear hardening behavior as well as a case of Holloman's hardening law. These models predicted that for a given wall-thickness ratio, the yield pressure of the thick-walled cylinder or sphere increased as the inner radius approached an order of 10 micrometers. With the gradual increase in the size of the inner radius, the increasing trend became less and finally vanished at about 100 micrometers. Beyond 100 micrometers, the result became identical to that obtained from a formulation based on the classical theory of plasticity.

A few researchers developed analytical models using the incremental theory of plasticity, which is generally possible when the formulation is based on the Tresca yield criterion using an elastic-perfectly plastic or linear isotropic or kinematic hardening material behavior. Examples are solutions provided by Koiter [34], Mendelson [35], Chen [36] and Alexandrov *et al*. [48] for cylinders and Chadwick [86] and Adibi and Livieri [87] for a sphere. Koiter [34] provided an analytical solution for the open and closed ended cylinders of non-hardening material. Mendelson [35] provided solution for the case of linear hardening. Chen [36] applied the solution provided by Koiter [34] considering Bauschinger effect using the *BEF* parameter. Alexandrov *et al*. [48] used Prager's linear kinematic hardening rule in their analytical model.

The incremental formulation approach for an analytical solution may also be possible by using the von Mises yield criterion but only for plane strain or closed end condition. This is because in either of the end conditions, the axial stress is equal to the mean of radial and hoop stresses [37]. Therefore, upon substitution in the yield function, the von Mises criterion reduces to a linear form that is similar to the Tresca yield function given by

$$\left(\sigma_\theta - \sigma_r\right) = \frac{2}{\sqrt{3}}\sigma, \tag{2.8}$$

The analytical model of Livieri and Lazzarin [43] was based on this approach for a closed end cylinder. The Bauschinger effect was incorporated using the *BEF* parameter considering two hardening laws *viz*., a linear hardening law and a modified Ramberg-Osgood law given by Eq. (2.7).

For sphere, the analytical model of Chadwick [86] used a linear hardening behavior without the Bauschinger effect. Adibi and Livieri [87] considered the Bauschinger effect and studied two cases of hardening— a linear hardening behavior and a modified form of Ramberg Osgood law that was suitable for a closed form expression, which is given as

$$\varepsilon^p = \frac{\sigma_Y}{E}\left(\frac{\sigma}{\sigma_Y}\right)^n - \frac{\sigma}{E}. \tag{2.9}$$

Besides the analytical models discussed till now, another type of approach for obtaining closed form solution exists. This is based on a direct approach in which the elastoplastic problem of an internally pressurized cylinder or sphere is formulated as a statically determinate problem. This approach does not rely on either the deformation or incremental theory of plasticity as no constitutive stress strain relation appear anywhere. The stress equilibrium equation is solved using the traction boundary conditions and the condition of force equilibrium at the elastic-plastic interface. Models based on this approach are the studies of Avitzur [21] for cylinder and Mendelson [35] for sphere. This method is applicable only with stress boundary conditions and cannot be used when displacement boundary conditions are prescribed. Davidson *et al*. [38] developed an analytical solution for elastoplastic stresses and displacement components based on simple empirical equations where the constants were obtained from experiments.

2.3.2 Numerical Models (Other than FEM)

A numerical model of hydraulic autofrettage is mostly observed for formulations based on the incremental theory of plasticity using a non-linear isotropic or kinematic hardening material model. Literature includes the models in Refs. [12, 13, 20, 25, 27–29, 37, 38, 48, 89] for cylinders and Refs. [70, 76–79] for sphere. Rees [101] proposed an incremental formulation for the closed ended cylinder with different cases of using the Tresca and von Mises yield criterion and different material behaviors, *viz*. elastic-perfectly plastic isotropic hardening and kinematic hardening. Rees [25] further extended the study to the case of an open ended cylinder. Lazzarin and Livieri [44] applied the method formulated by Rees [101] considering a linear hardening as well as a modified form of Ramberg-Osgood law (Eq. 2.7) and incorporated the Bauschinger effect using the *BEF* parameter. Bland [37] developed a general model for a cylinder acted by internal pressure, external pressure and a temperature gradient with multiple end conditions (plane strain, open end and closed end). Loghman and Wahab [45] developed a numerical model based on the solution procedure proposed by Mendelson [31] for a cylinder loaded by a combination of internal hydraulic pressure and temperature gradient. The model used the following hardening function proposed by Niitsu and Ikegami [102]:

$$\sigma = \sigma_Y\left\{1 + \frac{K}{E}\left(\varepsilon^p\right)^n\right\}. \tag{2.10}$$

Numerical models have also been developed based on the finite difference method (FDM). Literature includes the models of Perry and Aboudi [24], Thomas [29], Chen [31], Chu [39], Elder *et al*. [40], Perl and Perry [46] and Hill *et al*. [49]. All these models except by Thomas [29] and Hill *et al*. [49] were based on the von Mises yield criterion and its associated flow rule. Hardening and Bauschinger effect were neglected in some of these models [17, 28, 37]. A linear hardening material was used in the model of Ref. [39] and the power law was used in the models of Refs. [12, 19]. The material behavior in the model by Perl and Perry [46] was modeled using cubic spline approximation.

Marcal [47] developed a numerical model based on the stiffness method. Here, the von Mises yield function was first converted in the form of an implicit differential resulting in an expression where the incremental equivalent stress was a function of incremental principal stresses. The expression for the incremental equivalent stress from this function and that for the equivalent plastic strain was then substituted in a linear strain hardening function. This resulted in a final expression that related the incremental principal stresses to the principal plastic strain increments through the hardening function. The final expression along with the incremental Prandtl-Reuss equations yielded a system of linear equations relating the plastic strain increments to the stress increments. When arranged in a matrix form, it gave a coefficient matrix that was symmetric about the principal diagonal. This method was applied for the autofrettage analysis of a thick-walled cylinder with plane strain condition. The results were compared with those of Hill [49] and were found to be in good agreement. The method was simpler than that of Hill [49] as it did not require continuous tracking of the elastoplastic interface radius for subsequent solution in the plastic zone. Marcal [41] also applied this method for the case of an open ended cylinder.

Another type of numerical model, which is based on the deformation theory of plasticity is the variable method property (VMP) method. The method was originally proposed by Jahed *et al*. [67] for determining stresses during the elastoplastic deformation in an internally pressurized thick-walled cylinder. In this method, the cylinder was divided into finite domains or strips within which the material properties, *viz*. E and v (Poisson's ratio) were treated as field variables. The deformation in each domain was treated as pseudo-elastic. The inelastic solution was obtained from the elastic constitutive equations using the value of E and v determined using a numerical procedure. The method was versatile and could accurately simulate analytical results based on Tresca as well as von Mises yield criterion. It could also incorporate linear as well as non-linear hardening properties. The numerical model was further amenable for reduction to an analytical model for a case of non-hardening material based on Tresca

criterion. Jahed and Dubey [68] further extended this method for the determination of residual stresses. Sedighi and Jabbari [69] used this method to study residual stresses in a cylinder due to a combination of hydraulic autofrettage and wire winding. It was shown that the wire winding of the cylinder decreased the residual tensile stress induced at the outer surface of the cylinder due to autofrettage. Jahromi *et al*. [103] used this method to study residual stresses in an autofrettaged thick-walled cylinder made of functionally graded metal-ceramic composite. The VMP formulation was based on von Mises yield criterion assuming plane strain condition. The ceramic particles were distributed in a proportion that increased from inner to outer wall. It was found that inclusion of ceramic particles in the thick-walled cylinder increased the compressive residual stress induced due to autofrettage compared to a case without ceramic particles. The presence of high ceramic content at the outer region of the cylinder also improved the corrosion resistance of the cylinder. Parker and Huang [92,93] and Maleki *et al*. [94] applied this method for hydraulic autofrettage analysis in spherical vessels.

A few numerical models have also been proposed based on the flow theory of plasticity using strain rate formulations. Durban and Kubi [60] proposed a model for a plane strain thick-walled cylinder using Tresca yield criterion and its associated flow rule. An isotropic hardening material based on the Ramberg Osgood law was used. Durban and Baruch [95,96] also proposed a similar model for sphere. Song *et al*. [70] carried out uniaxial cyclic loading experiments on medium carbon steel to investigate the effect of loading speed on the elastic modulus, yield strength and strain hardening behavior using two different strain rates, *viz*., $\pm 4.8\times10^{-4}$ /s and $\pm 1.2\times10^{-2}$ /s. The effect of strain rate was found to be significant on the tensile yield strength and the reverse strain hardening; both increased with increase in strain rate. A case study was presented for a visco-elastoplastic model of hydraulic autofrettage using Tresca yield criterion based on two different loading-unloading speeds of $\pm10^{-4}$ /s and $\pm10^{-2}$ /s. It was found that the increased rate of loading was counterproductive and led to the decrease of maximum residual hoop stress by 15% and the size of the residual stress field zone by 35% for a given autofrettage pressure. The autofrettage pressure required for complete plastic deformation of the cylinder also increased by 15% in the case of the higher loading speed.

2.3.3 Finite Element Method (FEM) Models

Researchers have used the FEM to simulate accurate material behavior [72–78,97] or validate newly developed numerical models [79–81]. All the FEM models reported in the literature are based on the von Mises yield criterion. Marcal [71] extended the stiffness method [29, 35] for an axisymmetric FEM formulation and applied it for the elastic-plastic analysis of

an internally pressurized thick-walled cylinder. Chen [72] carried out an FEM simulation using ADINA® and used a piecewise linear hardening curve defined by 6 points and used Prager's kinematic hardening law. Alegre *et al*. [73] performed a simulation using an elastic-perfectly plastic behavior for the loading stage but used the Ramberg Osgood law for the unloading stage through ANSYS®. Gibson *et al.* [74] carried out an FEM simulation by incorporating real material behavior by using USERMAT subroutine in ANSYS®. Feng *et al*. [75] carried out an FEM analysis to study a process of cold temperature autofrettage. The cylinder was subjected to a particular ambient temperature during the autofrettage and effect on the residual stresses due to the variation of the ambient temperature was investigated. Out of various cases of temperature ranging from –170 °C to room temperature, it was found that, better residual stress distribution can be obtained when the autofrettage was carried out at low temperatures. For a typical case of a thick-walled cylinder with wall-thickness ratio 3 made of AISI 304 L stainless steel, it was found that an optimum temperature pressure combination of –90 °C and 400 MPa gave the most beneficial hoop compressive stress at the bore of the cylinder. Feng *et al*. [76] further extended it to the case of a cylinder with cross bore. A cross bore is a hole made in a cylinder for side-channeling.

2.4 Experimental Studies on Hydraulic Autofrettage Process

This section presents a review of some experimental studies that have been carried out for hydraulic autofrettage process. Experimental studies for hydraulic autofrettage have been generally carried out for one or more of the following objectives— identifying the presence of residual stresses, measuring the level of autofrettage or obtaining the distribution of residual stresses. The various techniques that have been utilized by researchers for these objectives are reviewed below.

The simplest method of identifying the presence of hoop residual stress is the split-ring method [104] of measuring the opening angle due to a longitudinal through-cut made on a ring sample of the autofrettaged specimen. The theoretical basis of the method was first explained by Parker and Farrow [105]. In this method, a through-cut is made on a ring sample of the autofrettaged specimen. The ring sample opens due to release of locked bending moment caused by residual hoop stresses in the ring. The method is shown in Fig. 2.2. An autofrettage ring sample is shown in Fig. 2.2(a) with the radial through-cut to be made along the line CC'. In Fig. 2.2(b), locked bending moment M is released and the cylinder opens symmetrically about the line NN'. In Fig. 2.2(c) the final configuration of the opened ring is obtained with an opening angle α. Here, the measurement of opening angle was carried out in two types of

cylinder samples viz. autofrettaged and post heat treated autofrettaged cylinder to inspect the presence of residual stresses. For experimental purpose, each sample was cut radially using power hacksaw and the measurement of opening angle was carried out using profile projector. The experimentally measured opening angles were compared with those obtained from FEM simulations.

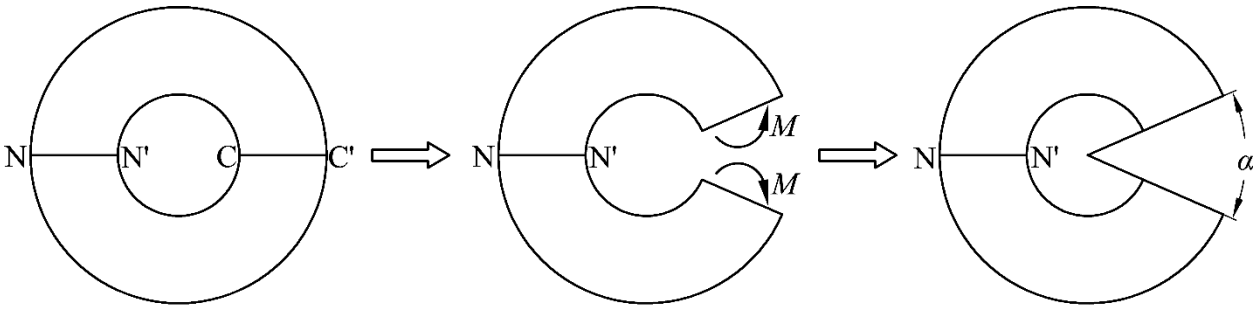

Figure 2.2 The split ring method: (a) saw cut to be made along CC (b) releasing of locked bending moment and (c) the final bend angle

Perl [106] proposed an improved version of the split-ring method to make it suitable for measurement of level of autofrettage. In this method, two strain gages each of which was attached at the inner and outer surfaces of the autofrettaged ring sample measures the relaxation of hoop strain at the diametrically opposite positions of the cut line. The strain measurements and the opening angle were inserted in an approximate formula for the determination of the level of autofrettage that was derived from the analytical solution for hydraulic autofrettage by Hill [99]. A simple method called the axisymmetric stress release method for determining the level of autofrettage in a cylinder was also proposed by Perl and Arone [107]. This method was based on the measurement of relaxation of hoop strain due to an array of uniformly spaced multiple axial through-cuts made in the cylinder. The process was simulated using FEM and an empirical formula was obtained from the results that would enable the accurate determination of the autofrettage level from experimental measurements. Although the authors did not mention it, Prime [108] in a review suggested that the method was similar to the compliance method (explained later) for residual stress measurement. The experimental validation of this method was shown by Perl and Arone [109] on a swage autofrettaged thick-walled cylinder.

For a quantitative determination of the residual stresses, preparation of both the autofrettage specimen and the measurement sample affect the accuracy of the results because the fabrication process induces additional residual stresses and interfere with the residual stresses due to autofrettage. Faupel [2] subjected the initial specimen to a mild heat treatment

before performing autofrettage. Stacey and Webster [110] did not do heat treatment but subtracted the pre-autofrettage residual stresses from the corresponding post-autofrettage residual stresses measured at identical radial positions in the cylinder specimen. Jahed *et al*. [111] showed experimentally that due to cutting of the sample, the residual hoop and radial stress distributions can vary up to 11% and 45%, respectively. Some of the commonly used methods for quantitative determination of residual stresses in hydraulic autofrettage studies are the hole drilling technique [112], Sachs boring technique [113], compliance method [114], X-ray diffraction [115] and neutron diffraction method [116]. The studies using these techniques are reviewed as follows.

The hole drilling technique is a destructive method in which the specimen is first gun-drilled through the wall thickness of the specimen and a core containing this hole is extracted by trepanning operation. The trepanning operation is generally carried out by electric discharge machining (EDM). This causes enlargement of the initial gun-drilled hole due to stress relaxation whose variation is measured by a probe and the residual stress distribution is obtained by suitable calibration. This technique has been used in a hydraulically autofrettaged cylinder by Jahed *et al*. [111] and George and Smith [112]. Using an FEM simulation, George and Smith [112] predicted that a smaller core diameter would result in more accurate experimental values. A simplified schematic of the process is shown Fig. 2.3.

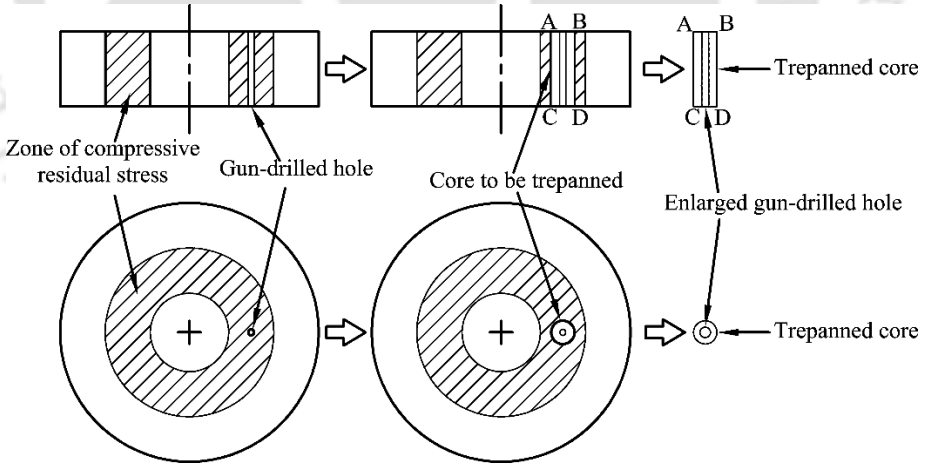

Figure 2.3 Schematic of the hole drilling technique

The Sachs boring technique for measurement of residual stress induced in a hydraulically autofrettaged cylinder has been reported in the works of Franklin and Morrison [117], Faupel [2], Stacey and Webster [110] and Stacey *et al*. [118]. The Sachs boring technique involves layer-wise removal of the inner surface of the autofrettaged cylinder through boring operation causing surface strain fluctuation, which is measured by strain gauges

attached to the outer surface. The corresponding stresses are calculated from the basic equations of elasticity. The calculation is based on the assumption that the unloading process is completely elastic. Parker [119,120] stated that this assumption is invalid because of the Bauschinger effect. A numerical model simulating the Sachs method was developed and it was shown that the omission of the Bauschinger effect led to the Sachs method overestimating the residual radial stress by 24% and residual hoop stress by 43%. Hence, it was not recommended as a reliable or conservative technique. The boring process also induces further residual stresses near the outer surface of the cylinder.

The compliance method suggested by Cheng and Fannie [121] is a simpler method for measuring the residual stresses. Cheng and Fannie [121] applied this technique to measure residual stresses induced in a hydraulically autofrettaged cylinder. In this technique, a slot is initially cut at the outer surface of the thin ring sample of an autofrettaged specimen. This cut is extended incrementally and the change in strain due to relaxation of residual stress is measured by an array of strain gauges attached at the outer surface of the sample. The schematic of this technique is demonstrated in Fig. 2.4. An axial through-cut is made for relaxation and measurement of the hoop residual stress in a ring sample A of the autofrettaged specimen as shown in Fig. 2.4(a). Similarly, in another fresh sample B of the same autofrettaged specimen, a circumferential through-cut is made used for measuring the axial residual stress as shown in Fig. 2.4(b). Detailed discussion of this technique is available in the review paper by Prime [108]. Venter *et al.* [122] used this technique for measuring residual stresses in a hydraulically autofrettaged cylinder.

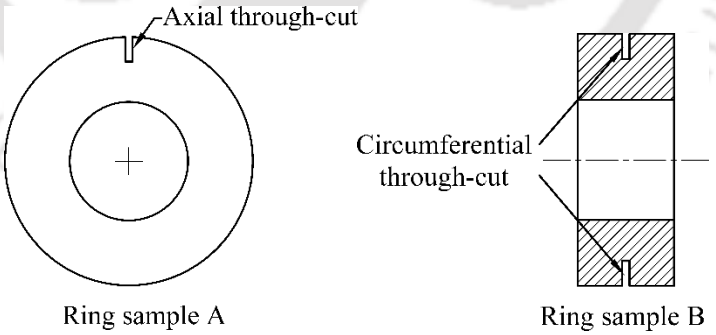

Figure 2.4 Schematic of the compliance method with (a) axial through-cut for measuring hoop residual stress and (b) circumferential through-cut for measuring axial residual stress

Researchers also used non-destructive techniques in the experimental studies of hydraulic autofrettage, e.g. the X-ray diffraction and neutron diffraction techniques. These techniques are based on the principle of coherent scattering of an X-ray or a monochromatic neutron beam incident on a polycrystalline solid. The strain is determined by calibrating the

angle of scattering calculated from Bragg's law. In the experimental study of hydraulic autofrettage, the X-ray diffraction technique has been used by Zerari *et al*. [123] and Candar and Filiz [124]. X-ray diffraction technique is suitable only for surface measurements because X-rays interact with electrons and get absorbed in the material after moving a few micrometers. This problem does not arise in the neutron diffraction technique because the charge-less neutrons do not interact with any particle. This method has been used by Stacey and Webster [110], Stacey *et al*. [118], Underwood *et al*. [125] and Ma *et al*. [126]. Stacey and Webster [110] showed that the experimentally measured residual hoop stress lies between the values predicted by a Tresca yield criterion and von Mises yield criterion. This agrees with the statement proposed by Avitzur [21] that the Tresca yield criterion and the von Mises yield criterion may be used as a lower bound and an upper bound solution, respectively. Stacey *et al*. [118] compared the residual stress distributions obtained from the neutron diffraction technique with those obtained from Sachs boring technique and found good agreement between the two. It was stated that the method can be problematic for thick samples due to impenetrability of the neutrons and showed that satisfactory results can be obtained up to only 10 mm thick steel samples. Venter *et al.* [122] carried out a comparative study of the Sachs boring technique, compliance method and the neutron diffraction technique for measuring residual stresses in a hydraulically autofrettaged cylinder and found good agreements among them. The relative merits and demerits of the various methods and techniques for the experimental studies of hydraulic autofrettage are compared and summarized in Table 2.1.

Table 2.1 Comparison of various experimental techniques used in the study of hydraulic autofrettage

Technique	Merits	Demerits
Split-ring	Quick and simple	Destructive and unable to provide detailed distribution of residual stresses
Compliance	Simple and accurate	Destructive and time consuming
Hole drilling	Simple and accurate	Time consuming
Sachs boring	Simple and accurate	Destructive and time consuming. The boring operation induces additional residual stresses in the sample
X-ray diffraction	Non-destructive and accurate	Method useful only for surface measurements due to low penetrability of X-rays
Neutron diffraction	Non-destructive, accurate and better penetrability than X-ray diffraction technique	Expensive and need a lot of safety measures

Some researchers have also carried out experiments to study the effect of autofrettage on the bursting pressure of the cylinder. The bursting pressure is the pressure where the cylinder

fails structurally. The design for static load of a thick-walled cylinder or sphere is based on an assigned factor of safety of the vessel, which is the ratio of the bursting pressure to the design pressure [127]. Autofrettage improves the static life of a thick-walled vessel by offsetting this limit load. Majzoobi *et al*. [128] carried out experiments validated by FEM simulations to study the effect of autofrettage on the bursting pressure of a thick-walled cylinder of aluminum alloy with wall-thickness ratio of 2.2. It was found that partial autofrettage increased the bursting pressure of the cylinder. Further, it was shown that autofrettage carried out in multiple stages did not improve the bursting pressure of the cylinder. Seifi and Babalhavaeji [129] also carried out numerical modeling with experimental validation to study the reduction of bursting pressure in an autofrettage thick-walled cylinder due to the presence of an inclined external surface crack. It was shown that external axial cracks and circumferential cracks reduced the bursting pressure by more than 30% and 6%, respectively. Also for some particular two cracks of the same length, the deeper crack was found to have a more detrimental effect.

2.5 Swage Autofrettage

The swage autofrettage process was proposed by Davidson *et al*. [8] as an economical alternative to conventional hydraulic autofrettage process. In this method, the inner wall of the cylinder is plastically deformed by the interference of an oversized mandrel called 'swage' that is mechanically forced through the bore of the cylinder by means of the ram of a hydraulic/mechanical press. Davidson *et al*. [8] used three types of set ups, *viz*. mechanical push swaging, mechanical pull swaging and hydraulic push swaging. The detailed description of the process has been presented in Section 1.4.2. This section presents a review of swage autofrettage process. Unless mentioned, all subsequent discussions of swage autofrettage from here on will mean the mechanical push swaging. First, the theoretical models are reviewed, which is followed by a discussion on the experimental studies.

2.5.1 Theoretical Models of Swage Autofrettage Process

Exact solution is complicated because the deformation is localized and dynamic along the length of the cylinder. A few researchers have proposed analytical closed form solution [130,131] based on simplified assumptions such as Tresca yield criterion and elastic perfectly plastic material. For a rigorous elastic-plastic analysis of the process, researchers relied on numerical [46,132–136] or FEM [137–145] approach for modeling the process. Literature survey suggests that a review of swage autofrettage is convenient following a classification based on the objectives of the studies. Studies of swage autofrettage have been generally carried out for the calculation of two quantities— mandrel driving force and residual stress

distribution. These quantities are dependent on various factors such as the mandrel geometry, mandrel material behavior, friction coefficient between mandrel and cylinder, number of passes of the swage mandrel. These aspects are discussed in detail in the following subsections.

2.5.1.1 Mandrel Geometry

The mandrel, which has three main geometrical specifications— front angle θ_F, rear angle θ_R and length of parallel section l as shown in Fig. 1.3(c) affects the driving force quite significantly. The front angle may be taken smaller [8], greater [134] or equal to the rear angle [135]. Based on an explicit finite difference method (FDM) model, Iremonger and Kalsi [134] carried out a parametric study and showed that an increase in the front angle from 3° to 6° resulted in 24% increase in the predicted driving force, when other dimensions were kept constant. Similarly, increasing the rear angle from 1.5 to 4.5 resulted in 18.4% increase and reducing the length of the parallel section from 9.9 mm to 6.6 mm resulted in 6.4% decrease in the mandrel driving force. Bihamata *et al*. [136] and Gibson *et al*. [137] observed the same by considering kinematic hardening and effect of friction in the cylinder using FEM models. Bihamata *et al*. [136] also showed that the mandrel driving force can be reduced using a mandrel with straight or helical grooves. Gibson *et al*. [138] showed that residual stresses increased with increase in both the angles although the variation due to the rear angle was more sensitive. Increase in the length of the parallel section beyond an optimum value equal to 0.12 times of the inner radius led to a drop in the hoop residual stresses.

2.5.1.2 Mandrel Material Behavior

Most studies have taken tungsten carbide as the material of the mandrel whose elastic modulus is three times greater than a typical steel alloy. Recently, Jin and Yuan [144] suggested a design of a tungsten carbide swage mandrel with a center hole shrunk fitted on a Steel shaft. The design reduced the difficulty in manufacturing a tungsten carbide swage mandrel with large volume. In general, the theoretical models of swage autofrettage have assumed the material behavior of the mandrel as either rigid or elastic. Literature based on the rigid material include Refs. [140,141] whereas those based on the elastic material include Refs. [130,133,137–143]. Based on an FEM model neglecting hardening and effect of friction, Chen [140] showed that elasticity of the mandrel reduces overstrain in the cylinder from 70% to 60% that also led to the reduction of hoop residual stresses. A more rigorous FEM based analysis was carried out by Barbechano *et al*. [141] using Chaboche's kinematic hardening model [146] without the effect of friction. It was shown that while the radial and hoop residual stresses remained the least affected, the maximum compressive axial residual stress at the inner surface

of the cylinder decreased by 19% due to the elasticity of the mandrel. Iremonger and Kalsi [134] suggested that for an explicit analysis, the elastic behavior of the mandrel posed numerical difficulties due to elastic stress waves in the mandrel and assumed it an elastic-perfectly plastic material.

2.5.1.3 Friction Between Mandrel and Cylinder

Swage autofrettage process involves the surface interaction of two bodies (mandrel and cylinder) and the effect of friction affects the mandrel driving load significantly. Friction is incorporated by using the coefficient of friction μ according to the Coulomb's law. O'Hara [139] and Hua and Penumarthy [142] carried out FEM based studies using μ value of 0.015. According to an FEM based parametric study, Gibson *et al*. [137] showed that the driving force increased in almost the same proportion as the friction coefficient. A similar result was shown in the experimentally validated FEM model by Bihamta *et al*. [136]. The FEM based parametric studies of Gibson *et al*. [138] and Chang *et al*. [143] showed that the effect of friction was very small.

2.5.1.4 Number of Passes of the Swage Mandrel

For a very large interference, it may be suitable to perform the swage autofrettage in more than one pass to reduce the overall requirement of the mandrel driving force [138]. Usually, the first pass uses a lesser interference and the final pass uses the desired interference that would have been in the case of a single pass operation. The effect of multistage pass swage autofrettage on the mandrel driving force and the residual stresses has been investigated by some researchers [134,137,138,141,145]. Iremonger and Kalsi [134] observed that a double pass swage autofrettage process reduced the mandrel driving force by 22% compared to that of a single pass process, when the interference used in the first pass was 70% of the desired final interference. A double pass also increased the residual stresses marginally. Gibson *et al*. [137] carried out a similar study by considering kinematic hardening in the cylinder material. The role of Bauschinger effect for the first pass was insignificant; it had a moderate effect in the force required and the residual stresses in the second pass due to strain hardening and reduced compressive yield stress at the inner wall due to plastic deformation in the first pass. Barbechano *et al*. [141] improved a double pass swage autofrettage process by reversing the directions of mandrel passage in the two consecutive passes ; it resulted in greater compressive stresses and reduction of edge effect. Edge effect is a phenomenon where the maximum hoop residual stresses at the inner surface of the cylinder are lesser at the edges compared to those at the inner regions. Hu [145] also carried out FEM modeling of a two-pass swage process of

a cylinder and observed 30–35% reduction in the average and peak mandrel driving forces in the two-pass process.

2.5.2 Experimental Studies on Swage Autofrettage Process

Experimental studies on swage autofrettage process have been carried out for measuring the mandrel driving force and the residual stresses. For the mandrel driving force, literature includes studies by Davidson *et al*. [147], Perry and Perl [133] and Bihamata *et al*. [136]. As explained by Perry and Perl [133], the axial strain in the tube during the passage of the mandrel was measured by using four strain gauges attached along the length of the tube. The average reading of the four strain gauges were then multiplied by the Young's modulus of the mandrel and its cross-sectional area, which gave the required mandrel driving force. Bihamata *et al*. [136] carried out an extensive study of the effect of friction on the mandrel driving force. The authors performed ring compression test of the cylinder material in the presence of various lubricants, *viz*. RATAK, extra pressure (EP) grease, cutting oil and natural oil, out of which RATAK gave the best performance. A thin layer of electrochemically deposited copper at the inner surface of the cylinder in combination with extra pressure grease further decreased the mandrel driving force; the same copper lining when used with RATAK increased the required force.

Perl and Arone [109] applied the axisymmetric stress release method discussed earlier to measure the level of overstrain in 25 mm ring sample of a swage autofrettaged thick-walled specimen. The detailed instrumentation of the sample is available in the literature. The experiments for the quantitative determination of the residual stresses have been performed by Davidson *et al*. [8,147], Clark [148,149], Lee *et al*. [150] and Chang *et al*. [143]. Davidson *et al*. [8,147] used the Sachs boring technique. Clark [148,149] and Lee *et al*. [150] used the X-ray diffraction technique.

2.6 Explosive Autofrettage Process

In explosive autofrettage, the process is carried out by detonating an explosive charge inside the thick-walled cylinder filled with a pressure propagating medium like air or water. This process has not been actively studied by researchers perhaps because the method involves explosives and requires legal permission for experimental implementation. A schematic of a typical set up of explosive autofrettage is shown in Fig. 1.4. The earliest analytical model for the feasibility analysis of explosive autofrettage was reported by Mote *et al*. [11] based on a strain rate formulation of plasticity using von Mises yield criterion and its associated flow rule assuming a material behavior without any strain or strain rate hardening. A rigorous

experimental analysis was also carried out along with the theoretical formulations. Explosive autofrettage was carried out a 152 mm (bore diameter) cannon barrel model M81 made up of steel alloy 4340. A preliminary experiment was first carried out on 40% of the breech section (where canon shell is loaded) and the entire barrel. The scaled models gave acceptable results and the experiment was extended to a full model of 105 mm gun barrel. A simple apparatus of the experimental set up consisted of an array of explosive charges lined up along the axis of the barrel that was held in place by end plugs. The residual stresses were measured by using Sachs boring technique.

2.7 Thermal Autofrettage

In this method, the autofrettage is carried out by using thermally induced stresses by subjecting the cylinder to a temperature gradient across its thickness. When the cylinder is cooled to room temperature, compressive residual stresses are induced in the inner wall of the cylinder due to elastic unloading of the thermal stresses. The term 'thermal autofrettage' was first used by Wen *et al*. [13] as an alternative method for autofrettage of internal metal liner of a cryogenic composite feed line. However, a rigorous elastic-plastic analysis of thermal autofrettage was first carried out by Kamal and Dixit [14] for a long thick walled cylinder with open ends based on Tresca yield criterion and non-hardening material. Thermal autofrettage is a very simple technique and does not require any complex machinery or special equipment for the practical implementation [15]. Despite its simplicity, the efficiency of the process in terms of the achievable maximum increase in the pressure carrying capacity is limited to only about 40%. This is mainly because the maximum temperature difference that can be used in the process for a particular cylinder dimension is limited to the maximum range beyond which material properties start to change [16]. Nevertheless, the economic advantage of the process can still be utilized and the performance of the thermally autofrettaged cylinder can be improved by shrink fitting [18]. A schematic of a setup for thermal autofrettage is shown in Fig. 1.5 [15]. Here, the outer surface of the cylinder is heated by an electric heater and the inner surface is cooled by the flowing cold water. This creates the required temperature gradient for causing the plastic deformation of a portion of cylinder. When the cylinder is brought back to the room temperature, the residual stresses are generated.

2.8 Rotational Autofrettage

In this method of autofrettage, the cylinder is applied with a centrifugal force due to rotation of the cylinder at a high angular velocity in the loading phase. In the unloading phase, the angular velocity is decreased and the cylinder is gradually brought to rest that induces the

residual compressive stress field in the cylinder. A schematic of the process is shown in Fig. 1.6. The method was proposed by Zare and Darijani [17] who carried out a rigorous mathematical analysis based on an analytical model. An elastic perfectly plastic material behavior was assumed using Tresca yield criterion with its associated flow rule. The Bauschinger effect was considered in the unloading phase by using the *BEF* parameter. Zare and Darijani [151] extended this study for a linear kinematic hardening material. Kamal [152,153] studied the rotational autofrettage of a thick-walled disc based on Tresca yield criterion without hardening and Bauschinger effect using plane stress assumption. Kamal *et al*. [154] developed an analytical closed form model using Tresca yield criterion and its associated flow rule. The feasibility of the proposed model was presented in [155].

2.9 Optimization of Autofrettage

Among all the autofrettage processes, hydraulic and swage autofrettage are the most popular and widely used methods in industries. Swage autofrettage is more energy efficient and cost effective but it is used only for autofrettage of tubes and gun barrels. For large vessels like pressure vessels, hydraulic autofrettage must be used. Hydraulic autofrettage requires a very high magnitude of pressure that makes it costly. For applications with very high working pressure a 100% autofrettage will be necessary for getting the maximum residual stresses while for some applications, lesser autofrettage might suffice. Therefore, optimizing an autofrettage process for a particular application and vessel geometry is important to economize the process.

Rees [101] stated that the optimum autofrettage pressure that can give the maximum benefit of autofrettage, i.e., 100% autofrettage is the pressure that just avoids the reverse yielding in the cylinder due to compressive residual stresses during the unloading stage. This optimum pressure depends on three factors— cylinder dimensions, strain hardening behavior and Bauschinger effect. Based on the Tresca yield criterion and assuming ideal material behavior, the optimum autofrettage pressure in cylinders with wall-thickness ratios greater than 2.22, is equal to twice the yield pressure of the cylinder [156]. In terms of overstrain, a rough but quick estimate was proposed [157] to keep the elastic-plastic interface radius corresponding to the optimum autofrettage pressure equal to the geometric mean of the inner and outer radii of the cylinder. Reverse yielding is not necessarily detrimental to the cylinder, however, it implies that the autofrettage has been performed with a pressure redundantly greater than an optimum magnitude. With the consideration of the Bauschinger effect, the optimum autofrettage pressure will be lesser because of reduced compressive yield strength that affects the maximum achievable autofrettage compared to a case with ideal material behavior.

Although not based on an optimization study, Parker [158] suggested that the loss of compressive residual stresses due to Bauschinger effect can be mitigated by carrying out the autofrettage in multiple stages where an initial autofrettage is followed by a mild heat treatment and a subsequent autofrettage with a second overstrain. For a typical cylinder with wall-thickness ratio of 2 made up of A723 steel and 70% overstrain, the procedure with a double and a triple autofrettage increased the fatigue life by 5.7 and 30.2 times, respectively compared to that in a single autofrettage case. However, the method was not validated with experimental results.

Varga [159] carried out an optimization study to minimize the weight of a cylindrical vessel closed with hemi-spherical ends subjected to hydraulic autofrettage. Based on an analytical procedure, the maximum equivalent stress at the elastic-plastic interface due to application of working pressure in the autofrettaged cylinder was minimized to obtain an optimum autofrettage pressure. The optimum autofrettage pressure gave the corresponding optimum wall-thickness ratio; the weight of the vessel being a function of the wall-thickness ratio was automatically optimized.

Zhu and Yang [160] carried out an analytical study to determine the optimum elastic-plastic interface radius that minimizes the maximum equivalent stress in a hydraulically autofrettaged cylinder during application of the working pressure. Stress distribution in the cylinder was based on a pre-existing analytical solution available in the literature. Material hardening was neglected in the study. Two cases of optimum elastic-plastic interface radii, one based on the Tresca yield criterion and another based on plane strain von Mises yield criterion, were obtained. On comparison, the optimum elastic-plastic interface radius obtained from the latter was lesser. Darijani *et al*. [161] applied the analytical solution by Mendelson [35] and carried out a study for the optimization of the hoop stress, equivalent stress and the cylinder wall thickness in a hydraulically autofrettaged cylinder. The optimization procedures for the hoop stress and equivalent stress were based on a graphical method whereas that of the cylinder wall thickness was based on a simple analytical procedure.

Hojjati and Hassani [79] applied the analytical solution developed by Gao [30] for plane stress and Gao [57] for plane strain condition to determine the optimum elastic-plastic interface radius and autofrettage pressure. Both the base models [30,57] were used with Hollomon's hardening law. A simple analytical optimization procedure was possible for the plane strain condition whereas a numerical iterative procedure was required for the plane stress condition. The optimum autofrettage pressures obtained for both the end conditions were almost the same and the optimum autofrettage pressures increased with the increase in the wall-thickness ratio

and the hardening exponent. Candar and Filiz [162] also carried out a similar study to find out the optimum autofrettage pressure for the cylinder of a waterjet intensifier pump using the elastic-plastic interface radius as the design variable. The stress analysis was based on an analytical model using von Mises yield criterion with linear kinematic hardening. The optimization procedure was implemented in the optimization toolbox available in MATLAB®. For a 160 mm long AISI 4340 alloy steel cylinder of inner radius 14 mm and outer radius 38 mm, the optimum autofrettage pressure came out as 936 MPa.

Maleki *et al*. [94] applied the variable material property (VMP) method in a spherical vessel to determine the optimum autofrettage at which the compressive residual hoop stress at the inner wall was the maximum while the tensile residual hoop stress at the outer wall was the minimum. The material behavior in the VMP model was based on actual non-linear hardening curve for loading and unloading stages. Two case of spherical vessels made of materials A723 and HB7 steels with a common wall-thickness ratio of 2 were investigated. For the sphere made of A723 steel, 40% was the recommended percentage of autofrettage. However, for HB7 steel, the criterion could not be applied due to considerable strain hardening behavior of the material.

Perl and Perry [163] carried out a study based on FDM to optimize the weight of a thick-walled spherical vessel. The model was based on real material behavior incorporating kinematic hardening and was validated using the VMP method. The minimum pressure at which the autofrettaged spherical vessel yielded during application of a working pressure was termed the safe minimum pressure (SMP) and the optimization was aimed at maximizing the specific SMP, which was the ratio of the SMP and the weight of the vessel. For a typical vessel with wall-thickness ratio of 1.5 with a prescribed SMP, it was shown that 60% autofrettage resulted in 57% reduction of the total weight of the vessel compared to the case without autofrettage designed to withstand a pressure equal to the SMP.

2.10 Autofrettage Design in American Society of Mechanical Engineers (ASME) Code

The standard procedures for the design of thick-walled cylindrical pressure vessels with the incorporation of autofrettage are documented in article KD-5 of the ASME Boiler & Pressure Vessel Code, Section VIII Division 3 [4]. The article is documented on the basis of hydraulic autofrettage of a thick-walled cylinder without any discontinuities or cross-bores. The calculation of the residual stresses is based on the Tresca yield criterion. Hence, it is based on a conservative design. The maximum allowable autofrettage in the cylinder is limited to a partial plastic deformation where the permanent tangential strain at the bore does not exceed 2%. This limits the validity of the code to about 40% overstrain [28]. A design procedure to

extend the Code's validity has been suggested by Parker [28]. Prediction of the elastic-plastic interface given on the basis of the known values of the following three parameters— tangential strain on the outer surface of the cylinder, residual tangential strain on the inner surface and autofrettage pressure. The yield stress term appearing in the formulae is scaled by a factor of 1.15 to approximately match the elastic-plastic interface radius predicted by using von Mises yield criterion. The article provides formulae for calculating residual stresses in the inner plastic and outer elastic zone of the autofrettaged cylinder. A procedure to account for the Bauschinger effect in calculating the compressive residual stresses for the case of reverse yielding is also given. The code needs to be updated considering various types of newer autofrettage processes and newer materials.

2.11 Gaps in the Literature

The hydraulic autofrettage is the most efficient for but costly whereas the thermal autofrettage is less efficient but cost friendly. In hindsight, it may be possible to combine both the processes to utilize the advantages of both. The design approach can economize the hydraulic autofrettage process while increasing the efficiency of the thermal autofrettage process. This work has not been attempted by any researcher so far. Bland [37] developed an analytical solution for elastoplastic stress distribution in thick walled cylinders subjected to both internal and external pressurization and temperature gradients based on Tresca yield criterion and its associated flow rule for both non hardening and linearly hardening materials. However, the variation of the residual stresses due to various combination of pressure and temperature was not shown and the results were shown mostly for a cylinder with closed ends. Loghman and Wahab [26] also obtained numerical solutions of loading and unloading of thick-walled cylindrical pressure vessel subjected combined pressure and temperature gradient. However, they considered only the cases in which the inner surface of the cylinder was at higher temperature than the outer surface, which does not help in reducing the required autofrettage pressure.

In any type of autofrettage, the compressive residual stresses at the inner wall are beneficial as they strengthen the autofrettaged cylinder/sphere against internal loads. On the other hand, the tensile residual stresses at the outer wall weaken the autofrettaged cylinder or sphere. This condition is aggravated in the presence of external surface flaws like cracks or wears [18] as the tensile stresses cause the cracks to open up. Seifi and Babalhavaeji [129] carried out a theoretical analysis and experimental study to demonstrate that the tensile residual stress reduced the bursting pressure of an externally cracked autofrettaged thick-walled

cylinder. The authors considered four types of surface crack configurations— an axial crack, a circumferential crack and two angular cracks inclined at 30° and 60°, respectively, with the axis of the cylinder. The effect of the axial crack was the most significant and reduced the bursting pressure by about 30%. The circumferential crack caused the least reduction by about 6%. Some researchers suggested techniques to mitigate the effect of the outer wall tensile residual stresses in hydraulically autofrettaged cylinders. Franklin and Morrison [117] subjected a hydraulically autofrettaged cylinder to a mild heat treatment by soaking it at 250 °C for an hour. Although, the process reduced the outer wall tensile residual stresses, a rigorous analysis is still required.

Sedighi and Jabbari [69] proposed wire winding of an autofrettaged thick-walled cylinder. The technique not only eliminated the outer wall tensile residual stresses but also increased the inner wall compressive residual stresses. Koh and Stephens [164] subjected an externally grooved autofrettaged thick-walled cylinder to shot peening. This induced compressive residual stresses at the outer wall and increased the fatigue life of the cylinder by about 3.5 to 13 times. However, these techniques have some drawbacks. The depth of the compressive residual stresses field achievable by mechanical shot peening is limited up to about 0.25 mm in soft materials like aluminum [165]. The process is also likely to result in a rough surface finish at the outer wall. The wire winding arrangement increases the outer diameter and weight of the pressure vessel [69]. Hence, an improved technique is still required.

2.12 Objectives of the Present Thesis

On the basis of the literature survey and the gaps in research identified, the following objectives are decided.

- **Design of a combined thermal and hydraulic autofrettage of a thick cylinder**

  The first objective of the study is to explore the feasibility of combining a hydraulic autofrettage process with thermal autofrettage. FEM modeling is developed and carried out by applying the hydraulic pressure and temperature gradient simultaneously in the autofrettage vessel. A series of combinations of temperature difference and hydraulic pressure are formed for different case of materials for achieving the maximum increase in the pressure capacity.

- **Heat treatment design of thermally autofrettaged cylinder**

  The second objective is the design of a thermal autofrettage process coupled with heat treatment to induce beneficial compressive stresses on the outer as well as inner walls of a pressure vessel with. In the proposed method, after thermal autofrettage, the outer wall of

the vessel is heated above the lower critical temperature to cause local austenization of the cylinder in its vicinity. Then the cylinder is quenched to room temperature after which beneficial compressive residual stresses are induced at both the inner and outer walls. A user defined material model is developed for incorporating the phase transformation kinetics in the commercial FEM package ABAQUS®.

- **An experimental set up for thermal autofrettage with heat treatment in cylinder**

  The third objective is developing an experimental setup to carry out the proposed heat treatment coupled thermal autofrettage process. Experiments are carried out on AH36 mild steel cylinders to assess the presence of the compressive residual stresses. The cylinder subjected to the procedure is inspected for the presence of residual stresses using two approaches— one based on the measurement of microhardness and another based on the split ring test that involves measurement of the opening angle due to a radial cut in the heat treated autofrettaged cylinder. A FEM technique is also presented to simulate split ring test for predicting the opening angle due to the release of moment locked generated by the residual stresses in an autofrettaged cylinder.

- **Heat treatment design of hydraulically autofrettaged cylinder**

  The fourth objective is to investigate the feasibility of the heat treatment coupled autofrettage process for a hydraulic autofrettaged cylinder. This is based on the FEM model used for the study in the third objective.

The objectives are executed in a sequence and the research plan is outlined in a flowchart shown in Fig. 2.5

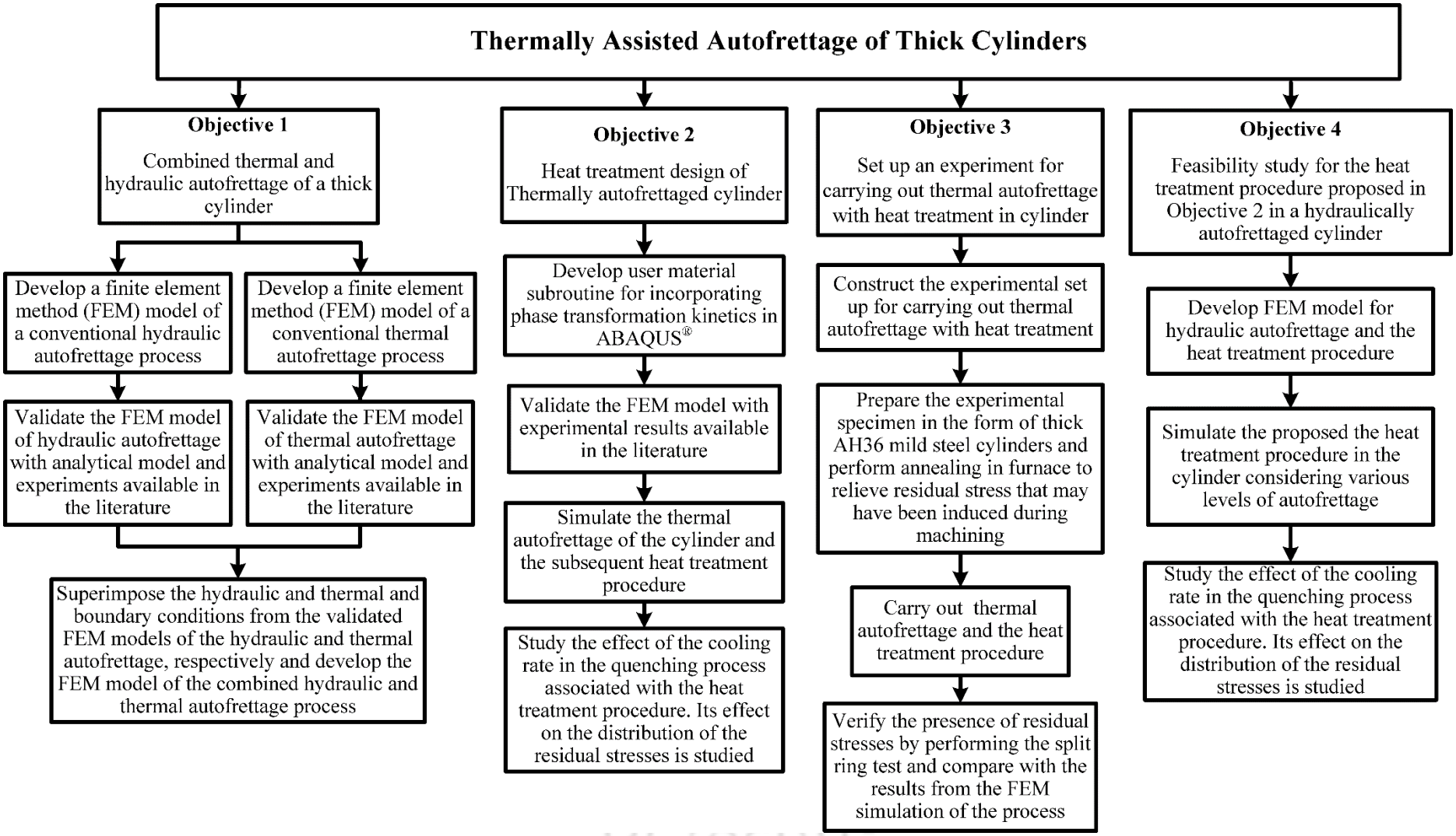

Figure 2.5 Flowchart of the research plan

Chapter 3

Combined Thermal and Hydraulic Autofrettage of a Thick Cylinder

3.1 Introduction

Autofrettage is a metal working process generally carried out in thick cylindrical or spherical vessels for inducing compressive residual stresses in the vicinity of the inner wall. The induced compressive residual stresses nullify the effect of generated tensile stresses when the vessel is reloaded with pressure in its application, thus enhancing the pressure carrying capacity, fatigue life and creep-resistance. The process is carried out by applying a plastically deforming load such as pressure to the inner wall of the vessel to cause a partial or full plastic deformation. Depending on the type of the load applied at the inner wall, autofrettage can be classified into hydraulic, swage, explosive, thermal and rotational. Among these, the hydraulic autofrettage is the most popular and widely used method in industries. Despite its effectiveness and wide acceptability in industries, the hydraulic autofrettage is a costly process. To achieve the maximum increase in the pressure carrying capacity of the cylinder, the process requires the application of very high pressure. On the other hand, the thermal autofrettage is a very simple technique. As described by Kamal *et al*. [15], the experimental set up of thermal autofrettage does not require any complex or moving machine parts. However, despite its simplicity and economic aspect, the maximum increase in the pressure bearing capacity of a thermally autofrettaged specimen is lesser than that of a hydraulically autofrettage specimen. There is also a restriction on the maximum allowable temperature difference to which the specimen can be subjected during the loading step because at elevated temperatures, the property of the material begins to change. It may be possible to combine both the hydraulic and thermal autofrettage procedures in a single process to economize the requirement of hydraulic pressure. Existing literature on the elastic-plastic analysis of thick cylinders subjected to both hydraulic pressure and temperature gradient includes that of Bland [37] and Loghman and Wahab [45]. Bland [37] developed an analytical solution for elastic-plastic analysis of thick cylinders subjected to both internal and external pressurization and temperature gradients. The solution was based on Tresca yield criterion and its associated flow rule. Loghman and Wahab [45] obtained numerical solution of loading and unloading of a thick cylindrical pressure vessel subjected to both internal pressure and temperature gradient by neglecting the Bauschinger effect. The authors considered only the cases in which the inner surface of the cylinder was at higher temperature than the outer surface, which did not help in reducing the required

autofrettage pressure. Both these studies focused mainly on mathematical modeling of the process and did not carry out a detailed study of the variation of the residual stresses due to various combination of pressure and temperature.

The objective of the present chapter is to study a combined hydraulic and thermal autofrettage process. In this process, the cylinder is internally pressurized in the presence of a radial temperature gradient that exists across the thickness due to a higher temperature at the outer wall. The combined loading causes the elastic-plastic deformation in the cylinder creating the inner plastic and outer elastic zones. The cylinder is then subsequently depressurized and gradually cooled to room temperature that causes inducement of the beneficial compressive residual stresses in the vicinity of the inner wall. The schematic of the proposed autofrettage method is depicted in Fig. 1.7. An FEM analysis is carried out in commercial package ABAQUS® to study the proposed combined autofrettage process in a thick cylinder. The salient basic concepts of FEM related to ABAQUS® is provided in Appendix A. FEM models of the two individual autofrettage processes, *viz*., hydraulic and thermal, are first developed separately. The two models are validated after which the FEM model of the combined hydraulic-thermal autofrettage is developed by superimposing the thermal and mechanical boundary conditions used in the previous individual models. The pressure carrying capacities in the cylinder autofrettaged using combinations of hydraulic pressure and temperature difference are obtained.

The rest of the chapter is organized as follows. Section 3.2 presents the procedure for FEM modeling of the combined hydraulic and thermal autofrettage processes. Section 3.3 discusses the results and Section 3.4 concludes the chapter.

3.2 FEM Modeling of Autofrettage Processes

This section presents the procedure for modeling followed in the ABAQUS® environment. This includes the part modeling, selection of material model, basis for load increment sizing and the convergence study for optimum mesh sizes. FEM models of hydraulic and thermal autofrettage processes are first developed and validated after which the combined autofrettage process is modelled by superimposing the load and boundary conditions used in the individual models.

3.2.1 Model Set-Up for the Autofrettage Analysis

The part considered for the FEM analysis is a thick cylinder with open ends. An axisymmetric part model is used as shown in Fig. 3.1 where *a*, *b* and *r* represent the inner radius, outer radius and any radial position in the cylinder, respectively. A generalized plane

strain condition is considered, which is ensured by taking a sufficiently long cylinder compared to its radial dimensions.

3.2.2 Material Properties

Kamal and Dixit [14] had developed the closed form analytical model of thermal autofrettage for open ended cylinders and presented the results of analysis based on the materials aluminum and steel SS304. The experimental study of Kamal *et al*. [15] for the quantitative determination of compressive residual stresses in a thermally autofrettaged cylinder was also carried out in SS304 cylinders. These type of cylinders are widely used for several applications and represent two widely different sets of material properties. The aluminum has high coefficient of thermal expansion and low yield strength. On the other hand, SS304 steel has relatively low coefficient of thermal expansion and high yield strength. The results of the FEM models in this chapter are also investigated based on these two materials with the respective radial dimensions identical to those taken in Ref. [14]. In addition, the results of Stacey *et al*. [118] for high strength low alloy steel, 4333 M4, are used for the experimental validation of the hydraulic autofrettage model,. The mechanical and thermal properties of aluminium and steel SS304 are given in Table 3.1. It is assumed that the material properties remain unaffected by the temperature variations in the cylinder during the thermal autofrettage process. Bland [37] also assumed the temperature-independence of the properties in his analytical model. The assumption is valid as the temperatures are well-below the recrystallization temperature [16]. A rough estimate is that Young's modulus of elasticity and yield stress change by less than 5%, which is of the usual order of uncertainty in the mechanical properties.

Table 3.1 Material properties for aluminum and steel SS304 **[12]**

Material	Young's Modulus (GPa)	Yield strength (MPa)	Coefficient of expansion (/°C)	Thermal conductivity (W/mK)	Kinematic hardening modulus (MPa)
Aluminum	69	50.3	22.2×10^{-6}	205	2388
SS304	193	205	17.2×10^{-6}	16.2	10504

A kinematic hardening model is considered to incorporate Bauschinger effect in the material. The hardening behavior is based on Ziegler's linear hardening law which is mathematically expressed as [166]:

$$\left(\boldsymbol{\sigma}' - \mathrm{d}\boldsymbol{\alpha}\right)\left(\boldsymbol{\sigma}' - \mathrm{d}\boldsymbol{\alpha}\right) - \frac{2}{3}\sigma_Y^2 = 0, \tag{3.1}$$

$$d\boldsymbol{\alpha} = C\frac{1}{\sigma_Y}(\boldsymbol{\sigma} - \boldsymbol{\alpha})d\boldsymbol{\varepsilon}^{pl}, \tag{3.2}$$

$$C = \frac{(\sigma - \sigma_Y)}{\varepsilon^{pl}}, \tag{3.3}$$

where $\boldsymbol{\sigma}'$ is the deviatoric part of the current stress tensor, $d\boldsymbol{\varepsilon}^{pl}$ is incremental plastic strain tensor and C is the kinematic hardening modulus. The tensor $\boldsymbol{\alpha}$ is called the back stress.

3.2.3 Analysis steps, Loading and Boundary Conditions

A steady state thermal displacement coupled analysis procedure is selected for modeling the autofrettage processes. The model comprises three analysis steps, *viz*., the loading and unloading steps of the autofrettage process and a pressure reloading step for determining the increase in the pressure carrying capacity of the autofrettaged cylinder. The total load is applied incrementally using a suitable load step size whose maximum values is the 1 in which the entire load gets applied in a single increment. The convergence of the problem was tested at various sizes of load increments— 0.01, 0.05, 0.1, 0.2, 0.5 and 1. A very small variation was observed in the results obtained by using the different load increments although computational time increased with the decrease in the load step size. However, the load step size was taken as 0.01 to accurately determine the onset of the yielding in the cylinder in a particular analysis step. At the end of the simulation, the equivalent plastic strain was checked at each load increment. When the equivalent plastic strain becomes greater than zero, the cumulative load at that incremental step provided the minimum load for yielding the cylinder within 1% tolerance. The boundary and loading conditions in the cylinder are shown in Fig. 3.1 where AD and BC represents the inner and outer walls, respectively. In the hydraulic autofrettage model, autofrettage pressure p is applied to AD in the loading step. In the thermal autofrettage model, wall temperatures T_a and T_b are assigned to AD and BC, respectively in the loading step. In the unloading step, ΔT is brought down to zero. In the combined hydraulic and thermal autofrettage model, the loading and boundary conditions from the models of hydraulic and thermal autofrettage are superimposed. In all the cases, the ends of the cylinder AB and CD remain insulated and traction-free.

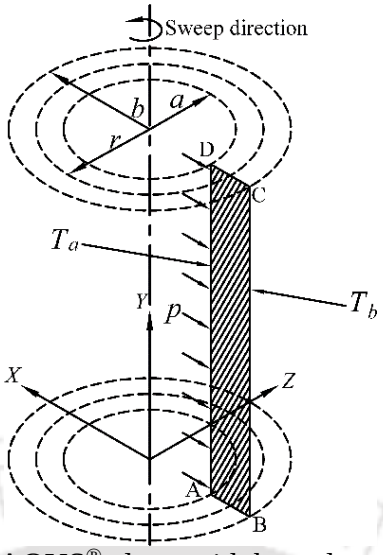

Figure 3.1 Schematic of part in ABAQUS® along with boundary conditions

3.2.3 Element Type and Mesh Sensitivity Analysis

The 8-noded axisymmetric thermally coupled quadrilateral element, CAX8T, is used for the analysis. The mesh sensitivity analysis for the autofrettage models is carried out based on the convergence of the maximum values of the radial, hoop and axial stresses towards an approximate stationary value on increasing the number of elements during the loading step. As in autofrettage process, the yielding of the cylinder starts from the inner wall, a finer mesh is used in the vicinity of the inner wall to accurately model the elastic-plastic transition during loading. This is achieved by partitioning the geometry in the ratio of 1:4 along the radial dimension. For each material, the mesh sensitivity analysis is first carried out in the hydraulic autofrettage model. After obtaining the optimum mesh in the hydraulic model, the mesh sensitivity analysis in continued in the thermal autofrettage model by starting from the current optimum mesh. If convergence is observed in the thermal autofrettage model with the same mesh, then it is taken as the optimum mesh for the thermal as well as the combined autofrettage model. If convergence is not satisfactory in the thermal autofrettage model, then the mesh is further refined. Based on this strategy, the mesh sensitivity analysis for SS304 was initially carried out in the hydraulic autofrettage model using a typical pressure of 110 MPa. The optimum mesh was obtained using 17500 elements comprising 50 divisions in the radial direction and 350 divisions in the axial direction. Again the 50 divisions in the radial direction comprise 20 divisions in the inner $1/4^{th}$ partition and 30 divisions in the outer $3/4^{th}$ partition. The mesh is shown in Fig. 3.2(a). This mesh was also sufficient for the thermal autofrettage model. The results of the mesh convergence study for SS304 based on the hydraulic autofrettage model are shown in Table 3.2 with the optimum mesh highlighted in bold. For aluminum, the optimum mesh size was for a typical pressure of 25 MPa was not sufficient for

thermal autofrettage with a temperature difference of 45 °C. The optimum mesh for thermal autofrettage was obtained using 12000 elements comprising of 40 divisions in the radial direction and 300 divisions along the axial direction. The 40 divisions in the radial direction comprise 15 divisions in the inner 1/4th partition and 25 divisions in the outer 3/4th partition. The mesh is shown in Fig. 3.2(b). The results are shown for aluminum in Table 3.3 with the optimum mesh highlighted in bold.

Table 3.2 Results of mesh sensitivity analysis for SS304 based on the hydraulic autofrettage model (Mesh 6 is the optimum mesh)

	Number of elemental divisions			Maximum stress (MPa)			CPU time
Mesh	**Radial**	**Axial**	**Total**	**Radial**	**Hoop**	**Axial**	**(s)**
Mesh 1	10	100	1000	–106.94	138.75	1.35	1
Mesh 2	15	150	2250	–107.16	130.15	0.7	2.6
Mesh 2	20	200	4000	–107.16	130.15	0.75032	4.7
Mesh 3	30	250	7500	–108.59	130.40	0.708	8.9
Mesh 4	40	300	12000	–110.04	132.07	0.691	18.40
Mesh 5	50	300	15000	–109.98	131.55	0.422	18.6
Mesh 6	**50**	**350**	**17500**	**–109.97**	**131.57**	**0.423**	**21.8**
Mesh 7	50	400	20000	–109.96	131.58	0.422	25.6

Table 3.3 Results of mesh sensitivity analysis for aluminum based on the thermal autofrettage model (Mesh 5 is the optimum mesh)

Mesh	Number of elemental divisions			Maximum stress (MPa)			CPU time
	Radial	**Axial**	**Total**	**Radial**	**Hoop**	**Axial**	**(s)**
Mesh 1	10	100	1000	8.82	60.53	52.62	1.7
Mesh 2	15	150	2250	8.80	59.03	53.91	3.5
Mesh 3	20	200	4000	8.76	59.01	53.91	6
Mesh 4	30	250	7500	8.74	58.59	54.53	11.9
Mesh 5	**40**	**300**	**12000**	**8.73**	**58.45**	**54.51**	**22.5**
Mesh 6	50	300	15000	8.73	58.46	54.31	24.7

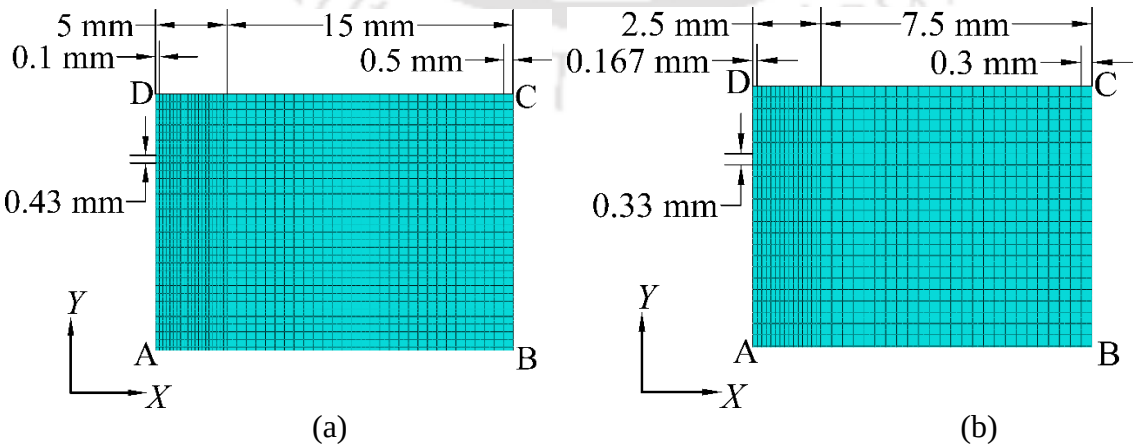

Figure 3.2 A typical FEM mesh for (a) SS304 and (b) aluminum cylinders

3.3 Results and discussion

In this section, the results from the FEM analyses of hydraulic, thermal and the combined autofrettage processes are presented. The validation results of the FEM models of the hydraulic autofrettage and thermal autofrettage are first shown. Then the results of the combined autofrettage are shown.

3.3.1 Validation of Hydraulic Autofrettage

The FEM model of hydraulic autofrettage is validated using analytical as well as experimental results. The analytical model for the validation is based on the solution developed by Avitzur [21] for an open-ended cylinder considering von Mises yield criterion and elastic perfectly plastic material behavior. The experimental validation of the FEM model is based on the study carried out by Stacey *et al*. [118] who performed measurement of residual stresses in a hydraulically autofrettaged disk using neutron diffraction. The material considered for the experimental investigation was 4333 M4, a high strength low alloy steel having yield strength of 1070 MPa, ultimate tensile strength of 1150 MPa and Young's modulus of 207 GPa. The test specimen was a 5 mm thick ring having a nominal bore diameter 30 mm and outside diameter 62 mm. This specimen was autofrettaged using a pressure of 662 MPa. The kinematic hardening modulus of 4333 M4 is 7530 MPa. The value is taken from the stress strain curve of the same material used by Stacey and Webster [110]. The disk and the autofrettage pressure used in [110] is used as the basis for the analytical as well as experimental validation.

The results of validation of the FEM model of hydraulic autofrettage based on the analytical model are shown in Fig 3.3 and Fig. 3.4. Figure 3.3 shows the comparison of the distribution of stresses across the thickness of the cylinder obtained from the FEM and analytical models during the loading step. The elastic-plastic interface radii from the analytical and FEM models are obtained as 18.87 mm and 18.79 mm respectively, with a deviation of about 0.42%. Since, the positions of the elastic-plastic interface obtained from the two models almost coincide, it is represented by a single vertical dotted line that demarcates the inner plastic zone I and outer elastic zone II as shown in Fig. 3.3. The yield pressure of the cylinder is obtained as 468.86 MPa based on the analytical model whereas that based on the FEM model is obtained as 470.02 MPa, which is a deviation of about 0.24%. The (Central Processing Unit) CPU time for solving the analytical model was recorded as 104.34 seconds while that for solving the FEM model was recorded as 34 seconds. The comparison of the distribution of the residual stresses across the thickness of the cylinder after the unloading step between the FEM and analytical results also indicate a good agreement as shown in Fig 3.5.

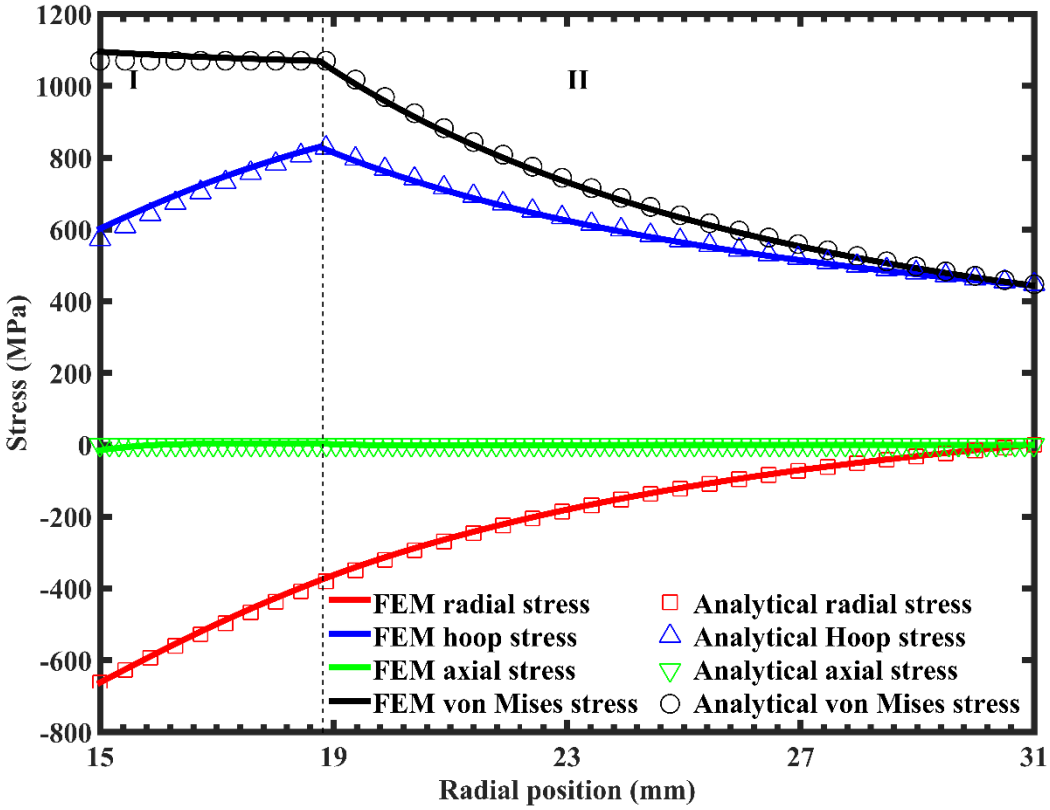

Figure 3.3 Distribution of stresses due to elastic-plastic deformation during the loading step of the hydraulic autofrettage of 4333 M4 cylinder based on FEM and analytical [21] models

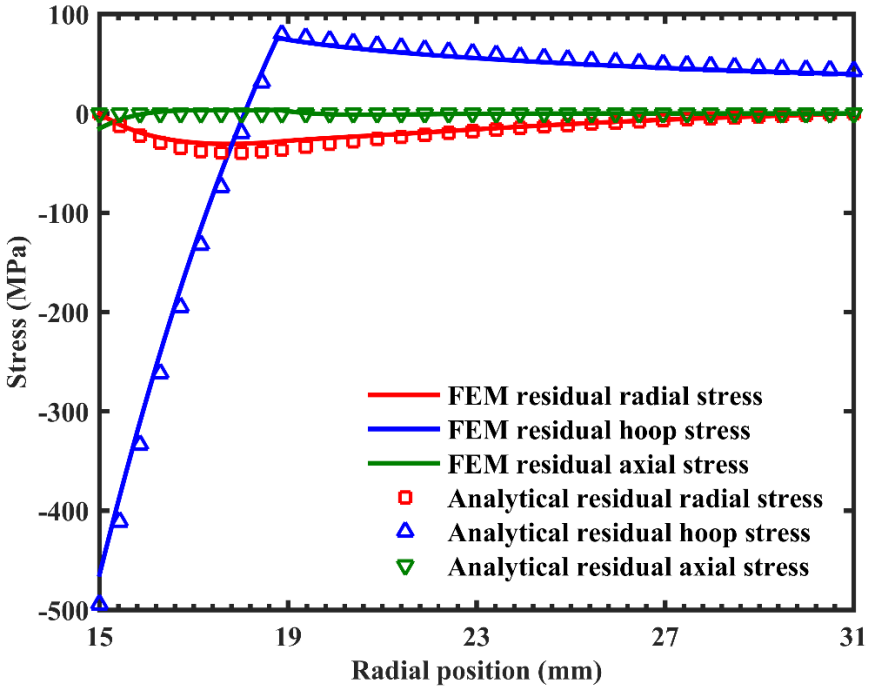

Figure 3.4 Distribution of residual stresses due to elastic recovery after the unloading step of the hydraulic autofrettage of 4333 M4 cylinder based on FEM and analytical [21] results

The results of validation of the FEM with the experimental study of Stacey *et al*. [118] are shown in Fig. 3.5. Stacey *et al*. [118] did not show the distribution of the residual axial stress in their study and has been omitted from the comparison. Referring to Fig. 3.5(a), a good

match can be observed at the majority of the radial positions in the distribution of the radial residual stress with a maximum deviation of about 7.16%. The hoop residual stress distribution from the FEM model also matches well with those from the experiments. Compared to the experimental result, the FEM overestimates the maximum compressive residual hoop stress at the inner wall by 162 MPa. In the comparison shown by Stacey *et al*. [118], the analytical solution based on Tresca yield criterion overestimated the maximum compressive stress by a much larger margin of 350 MPa. Thus, the consideration of von Mises yield criterion gives a better match with the experimental results than the Tresca yield criterion. Further, the incorporation of hardening and Bauschinger effect through kinematic hardening further improves the experimental matching.

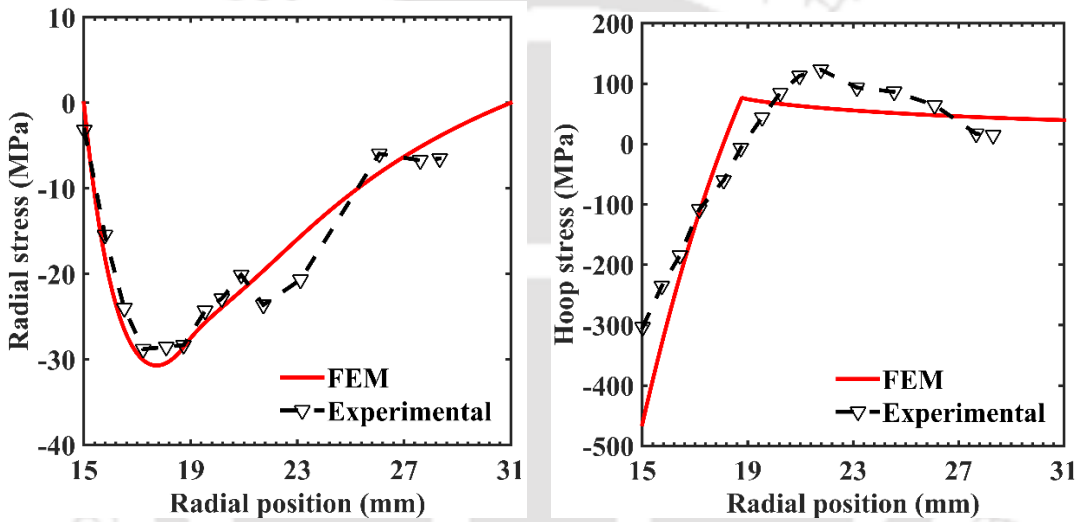

Figure 3.5 Comparison of the distribution of (a) radial residual stress (b) hoop residual stress and (c) axial residual stress across the thickness of a hydraulically autofrettaged M4 4333 cylinder based on FEM and experimental results [118]

3.3.2 Validation of thermal autofrettage

The FEM model of thermal autofrettage is also validated using analytical as well as experimental results. The analytical model for the validation is based on the solution developed by Kamal and Dixit [14] that was based on Tresca yield criterion for generalized plane strain case condition and assuming elastic perfectly plastic material behavior. The validation with experimental results is based on the study carried out by Kamal *et al*. [15] who performed measurement of residual stresses in a thermally autofrettaged cylinder using Sachs boring technique. The material considered for the experimental investigation was steel SS304 whose properties are given in Table 3.1. The test specimen was a cylinder having inner radius 10 mm and outer radius 25 mm and length 90 mm. The specimen was thermally autofrettaged using a

temperature difference of 120 °C. The cylinder and the autofrettage temperature difference used in [15] is used as the basis for the analytical as well as experimental validation.

The results of validation of the FEM model of thermal autofrettage based on the analytical model are shown in Fig. 3.6 and Fig. 3.7. Figure 3.6 shows the comparison of the distribution of stresses across the thickness of the cylinder obtained from the FEM and analytical models during the loading step. The elastic-plastic interface radii obtained from the analytical and FEM models are 12.37 mm and 12.20 mm, respectively with a deviation of about 1.37%. The position of the elastic-plastic interface obtained from the analytical model is shown by the vertical dashed line and that obtained from the FEM model is shown by the vertical dotted line that demarcates the inner plastic zone I and outer elastic zone II as shown in Fig. 3.6. The distributions of the has a slight deviation in the plastic zone I. A maximum deviation of 13.44 % is observed in the hoop stress at the inner wall whereas the maximum deviation in the axial stress distribution is about 7.57% at the inner wall. The deviation is due to the difference in the yield criteria adopted, which is Tresca in analytical model and von Mises in the FEM model. Moreover, kinematic hardening is incorporated in the FEM model that is omitted in the analytical model. The matching is good in the rest of the elastic zone II. The yield temperature difference based on the analytical model 66.50 °C whereas that based on the FEM model is 66 °C. The CPU time for the analytical solution was recorded as 285.06 seconds, whereas the FEM solution recorded 172.30 seconds. The comparison of the distribution of the residual stresses across the thickness of the cylinder after the unloading step between the FEM and analytical results is shown in Fig. 3.7. Here a good agreement is observed with some minor deviations in the distributions of the hoop and axial residual stresses mainly in the plastic zone due to different material model in FEM.

The results of validation of the FEM with the experimental study of Kamal *et al*. [15] are shown in Fig. 3.8. Some minor deviations are observed in the distributions of the hoop and axial residual stresses in the plastic region of the cylinder due to different material model in FEM. Referring to Fig. 3.8(a), the distribution of the radial residual stress based on the FEM is in good agreement with that obtained from the experiment. The distributions of the hoop and axial residual stresses obtained from the FEM model also match well with those from the experiments as shown in Figs. 3.8(b) and 3.8(c), respectively.

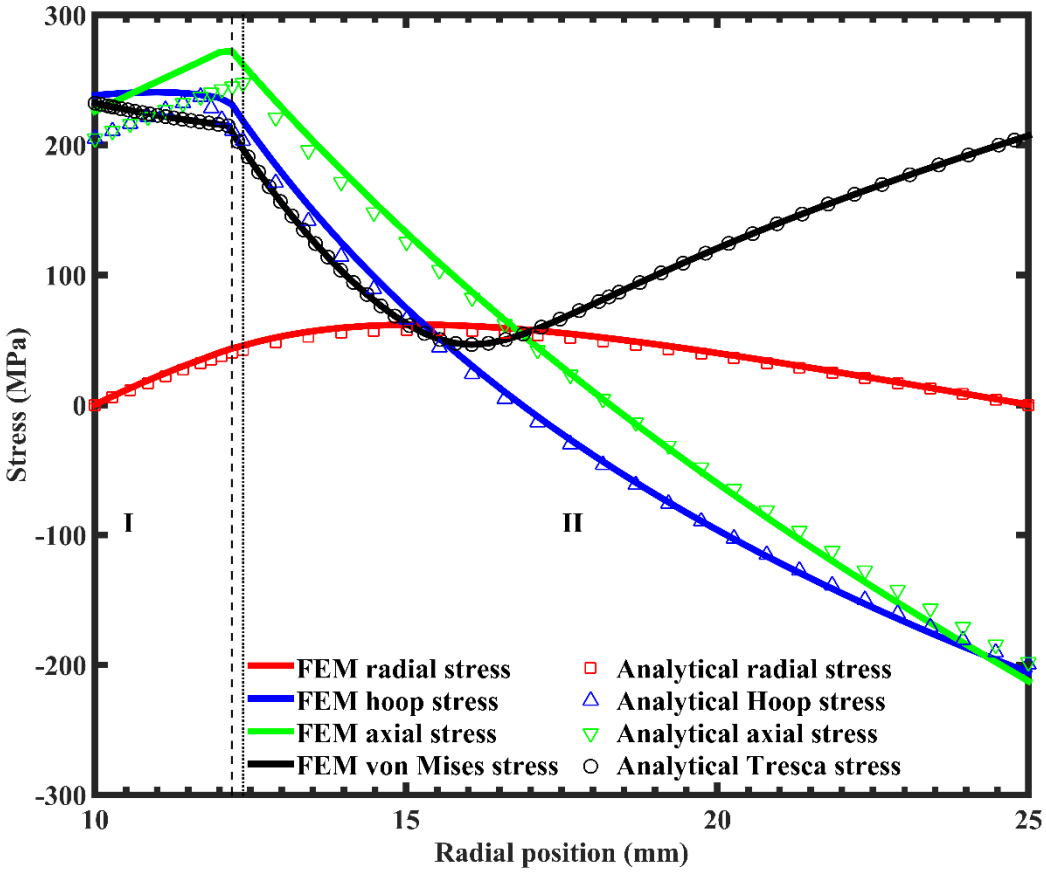

Figure 3.6 Distribution of stresses due to elastic-plastic deformation during the loading step of the thermal autofrettage of SS304 cylinder based on FEM and analytical [14] results

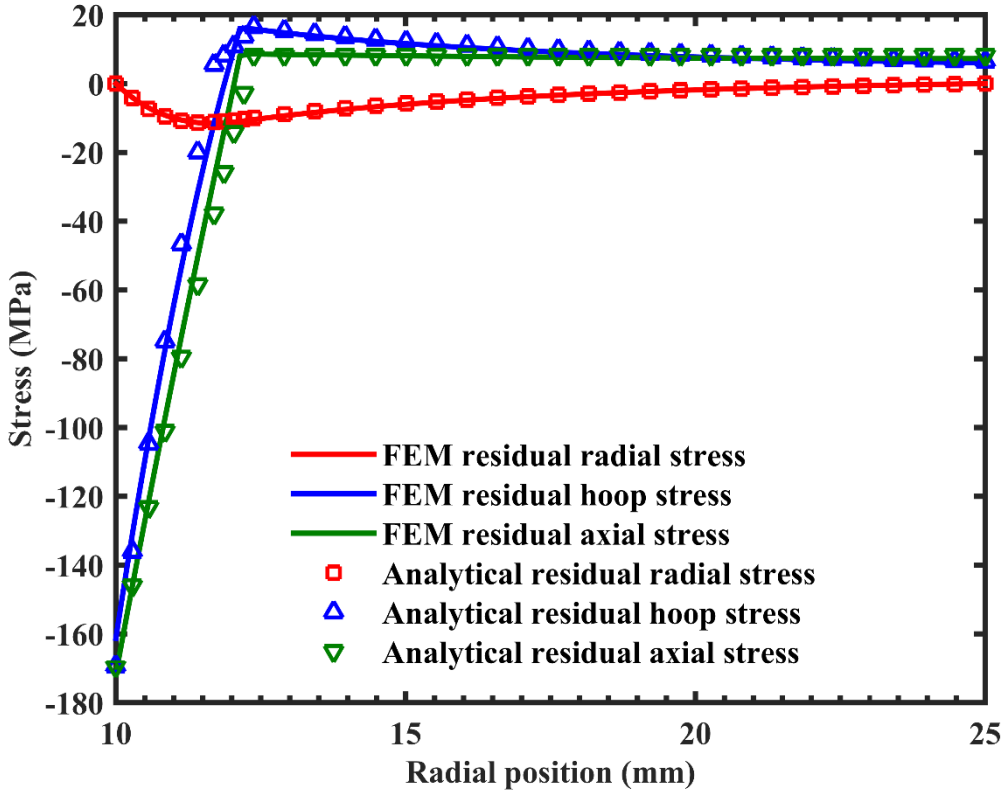

Figure 3.7 Distribution of residual stresses due to elastic recovery after the unloading step of the thermal autofrettage of SS304 cylinder based on FEM and analytical [14] results

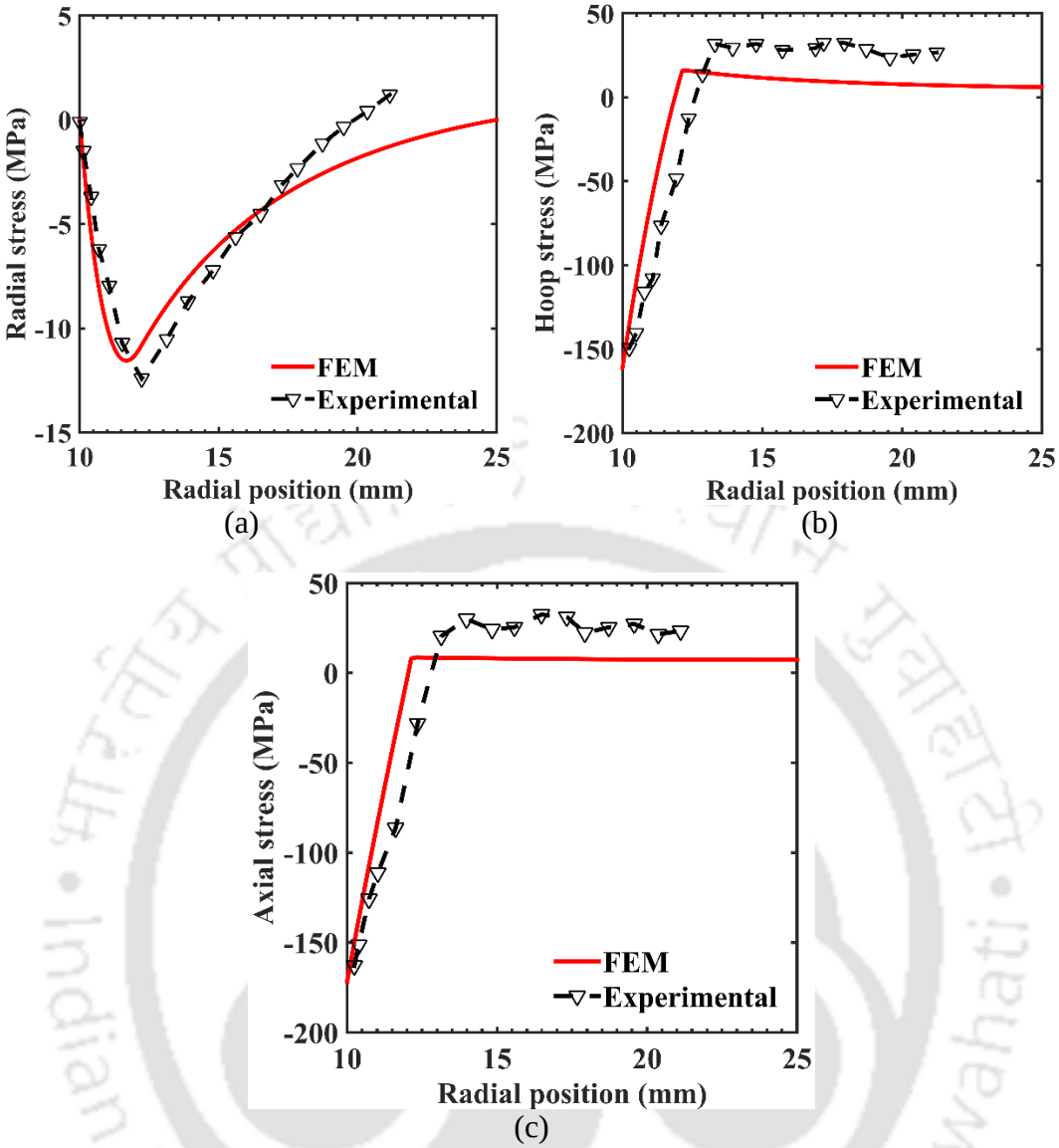

Figure 3.8 Comparison of the distribution of (a) radial residual stress (b) hoop residual stress and (c) axial residual stress across the thickness of a thermally autofrettaged SS304 cylinder based on FEM and experimental results [15]

3.3.3 Results of the Combined Thermal and Hydraulic Autofrettage

After the validation of the FEM model of hydraulic and thermal autofrettage, a new FEM model is developed for the study of the combined autofrettage process. The distribution of stresses due to elastic-plastic deformation during the loading step and that of the residual stresses due to elastic recovery after the unloading step for various cases of the combination of pressure and temperature difference are shown for cases of SS304 and aluminum.

3.3.3.1 Case of SS304

For SS304, a 150 mm long cylinder with inner radius 10 mm and outer radius 30 mm was considered. The radial dimensions were taken identical to that considered in Ref. [14] for the ease of validation and the length was taken to suffice to the requirement for the condition

of a generalized plane strain condition i.e., (length ≥ six times the thickness of the cylinder). Based on the FEM model of hydraulic autofrettage, the yield pressure of the cylinder was obtained as 105 MPa whereas the yield temperature difference based on the FEM model of the thermal autofrettage was obtained as 65 °C. The cylinder was loaded by combining the two threshold loads i.e., an internal pressurization of 105 MPa in presence of a radial temperature difference of 65 °C due to a lower inner wall temperature. The simulation was carried out in a computer with CPU processor Intel® core™ i5 7500 with a speed of 3.41 Giga Hertz and a Random Access Memory 8 Giga Bytes running Windows 10 Professional. The CPU time required to complete the simulation was recorded as 263 seconds.

The distribution of stresses during the loading step and that of the residual stresses after the unloading step for the combined autofrettage of SS304 are shown in Figs. 3.9(a) and 3.9(b) respectively. The position of the elastic-plastic interface radius at 13.39 mm is shown by the dashed line demarcating the inner plastic zone and the outer elastic zone II. When the autofrettaged cylinder was reloaded with a working pressure of 160 MPa at room temperature, the cylinder started yielding at a pressure of 153.6 MPa. This means an increase of 46.28% in the pressure carrying capacity. At this condition, the compressive hoop residual stress at the inner wall is 182 MPa, which is 89% of the yield stress. This will help in preventing stress corrosion cracking.

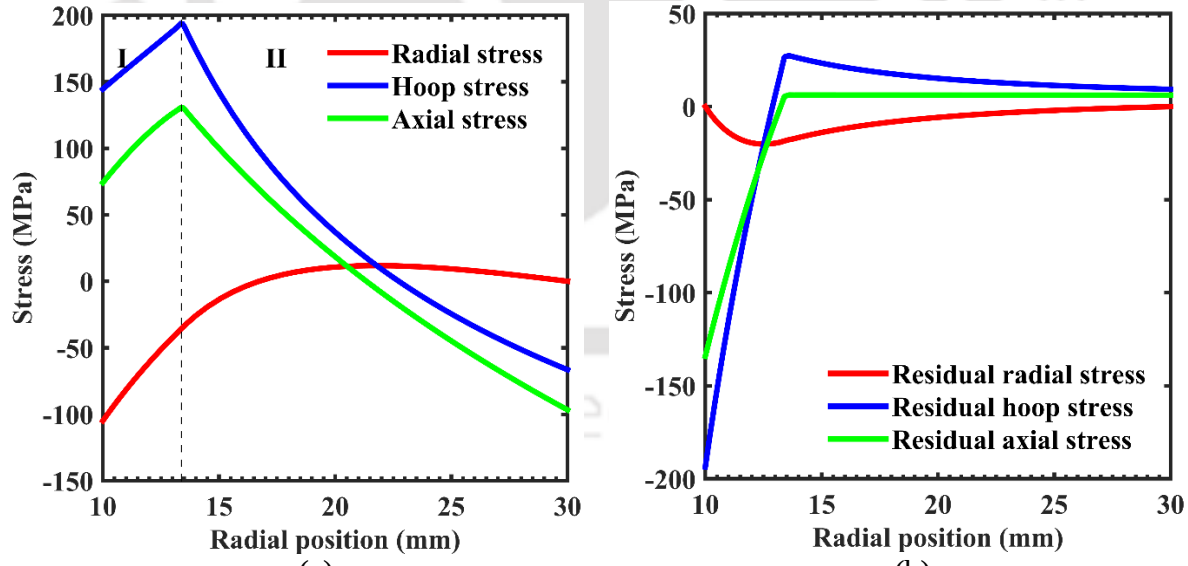

(a) (b)

Figure 3.9 Distribution of (a) stresses during the loading step and (b) residual stresses after unloading step of the combined autofrettage of SS304 cylinder with a pressure of 105 MPa and temperature difference of 65 °C

3.3.3.2 Case of Aluminum

For aluminum, the 100 mm long cylinder with inner radius 10 mm and outer radius 20 mm is considered. The dimensions were taken on a basis similar to that described in the case of the SS304 cylinder. A pressure and temperature-difference combination of 21 MPa and 35 °C is used for the combined autofrettage. Like in the case for SS304, the chosen pressure and temperature difference were the yield pressure and the yield temperature difference at which loading the cylinder started yielding in the hydraulic and thermal autofrettage processes, respectively. The CPU time required to complete the simulation carried out in the same computer as that described in Section 3.3.3.2 was recorded as 270 seconds.

The distribution of stresses during the loading step and that of the residual stresses after the unloading step for the combined autofrettage of SS304 are shown in Figs. 3.10(a) and 3.10(b), respectively. The position of the elastic-plastic interface radius at 12.57 mm is shown by the dashed line demarcating the inner plastic zone and the outer elastic zone II.

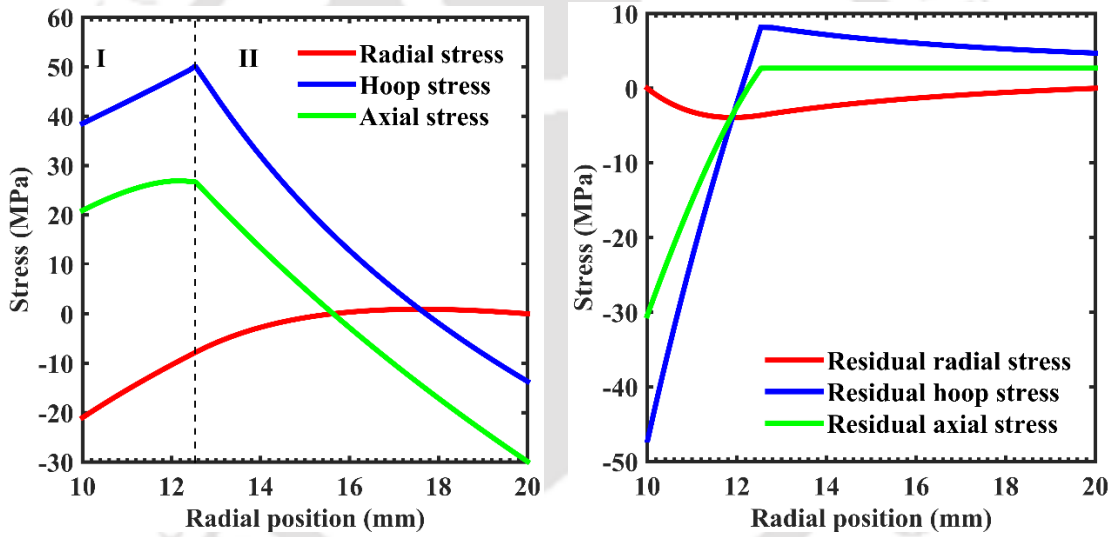

Figure 3.10 Distribution of (a) stresses during the loading step and (b) residual stresses after unloading step of the combined autofrettage of aluminum cylinder with a pressure of 21 MPa and temperature difference of 35 °C

The autofrettaged cylinder was reloaded with working a pressure of 35 MPa. It was observed that, cylinder commenced yielding at 26.95 MPa. This means a 28.33% increase in the pressure carrying capacity. The maximum compressive hoop stress is 48.23 MPa at the inner wall, 96% of the yield stress. This will be very helpful in preventing the stress corrosion cracking, although the gain in pressure carrying capacity is just 28.33%. The result indicates that the yield pressure is sufficient to achieve autofrettage when augmented by the thermal load hence the significant role.

3.3.4 Increase in Pressure Carrying Capacity with Combined Autofrettage Using Various Load Combinations

In this subsection, the increase in the pressure carrying capacities achievable by combined autofrettage for various combinations of pressure and temperature difference is studied. A series of combinations for temperature difference and hydraulic pressure are formed by gradually decreasing the pressure from its maximum allowable value to 0 while the temperature difference is increased from zero to its maximum allowable limit at a particular pressure. The maximum allowable limit of the autofrettage load is defined as the load that can be applied without the occurrence of reverse yielding during the unloading stage. For hydraulic autofrettage, the maximum pressure is about 208 MPa in SS304 whereas it is 38 MPa in aluminum at room temperature. For thermal autofrettage, the maximum allowable temperature difference is 127 °C in SS304 and 74 °C in aluminum without the application of any pressure. With the increase in the pressure, the maximum allowable temperature difference decreases. In a non-hardening material, the compressive yielding can be easily identified in the FEM model. When Bauschinger effect is incorporated in the FEM model, the compressive yield strength will be lesser than the tensile yield strength. It is therefore necessary to first determine the compressive yield strength of the materials to ensure the correct selection of hydraulic pressure and temperature difference. To achieve this, a technique similar to the one used by Barbachano *et al*. [167] is followed. Although, the technique was used for swage autofrettage in their case, it can also be applied to other autofrettage processes. For the present study, the same procedure is followed by using the hydraulic autofrettage model. By assuming isotropic hardening, FEM simulation of hydraulic autofrettage is carried out at the maximum allowable autofrettage pressure. From this simulation, the maximum plastic strain in the cylinder is obtained. The maximum plastic strains for SS304 and aluminum are obtained as 0.00216 and 0.00183, respectively. By applying these values of maximum plastic strains, the FEM simulation of uniaxial cyclic loading is carried out by considering kinematic hardening. The compressive yield stress for SS304 and aluminum are obtained as 190.3 MPa and 48.7 MPa, respectively, which are lower than the tensile yield stresses of 205 MPa and 50.3 MPa, respectively. Once the compressive yield stresses have been found, FEM simulation of combined autofrettage is carried such that the yielding is avoided during unloading. Figure 3.11 shows the increase in pressure carrying capacity for a combination of the autofrettage pressure and temperature difference for SS304. Figure 3.11(a) shows the results neglecting hardening whilst the

kinematic hardening is incorporated in the results of Fig. 3.11(b). Similar results are shown for aluminum in Figs. 3.12(a) and (b).

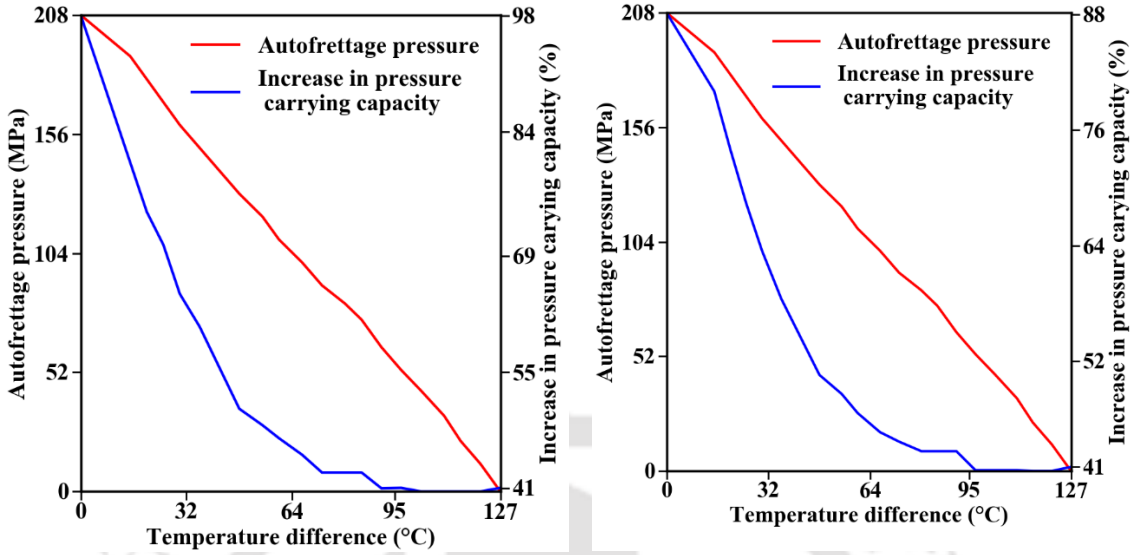

(a) (b)

Figure 3.11 Variation of the increase in pressure carrying capacity with autofrettage pressure and temperature difference in combined autofrettage of SS304 cylinder for (a) non-hardening and (b) hardening material

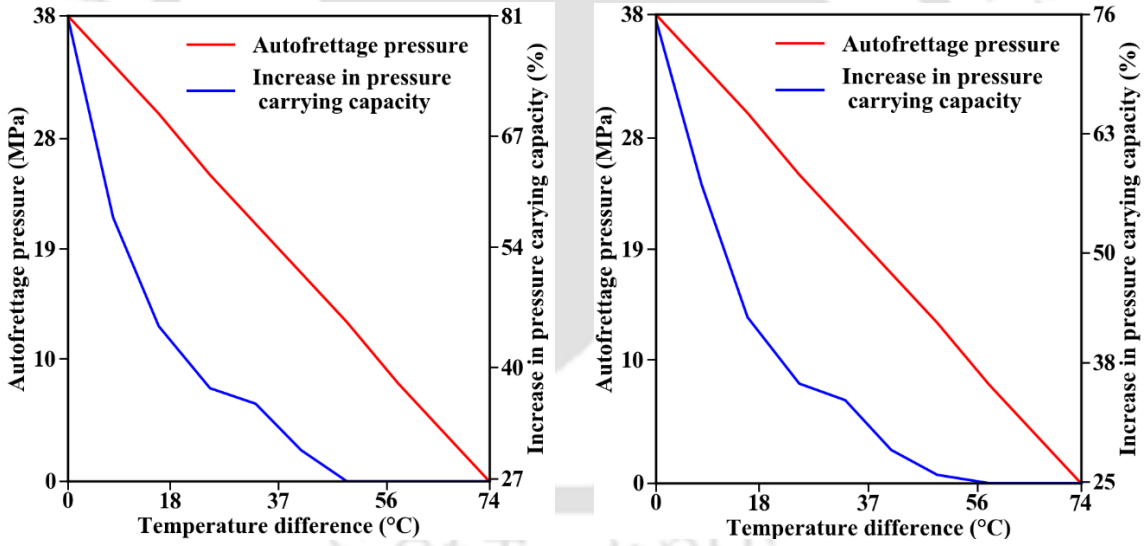

(a) (b)

Figure 3.12 Variation of the increase in pressure carrying capacity with autofrettage pressure and temperature difference in combined autofrettage of aluminum cylinder for (a) non-hardening and (b) hardening material

It is observed from Figs. 3.11 and 3.12 that when hardening is considered, the increase in pressure capacity is lower than the ones predicted from a non-hardening material model. This difference is much larger at high hydraulic pressure. In SS304, a 98% increase in pressure capacity is predicted at the maximum autofrettage pressure when hardening is not considered. Whereas, it is only 88% when hardening is considered. In the combined autofrettage dominated by thermal loading, the difference is very small. For SS304, the increase in pressure capacities

of thermally autofrettaged cylinder with and without hardening are 40% and 41% respectively. A similar behavior is observed for aluminum.

Considering the cases of hardening shown in Figs. 3.11(b) and 3.12(b), the maximum increase in the pressure capacities are 88% in SS304 and 75% in aluminum when the hydraulic autofrettage is carried out at the room temperature. The hydraulic autofrettage will require the application of the pressures of 208 MPa for SS304 and 38 MPa in aluminum, respectively. The distributions plotted in Figs. 3.11 and 3.12 are useful for predicting the increase in the pressure carrying capacity for a combination of pressure. Let us take an example of the SS304 cylinder, with the maximum rating of the hydraulic power pack as 150 MPa. This much amount of autofrettage pressure at room temperature can enhance the pressure capacity only by 40.64% over the pressure capacity of 105 MPa for the non autofrettaged case. However, if this autofrettage pressure is applied along with a temperature difference of 36 °C between the inner and the outer wall, the pressure capacity increases by 60%. Thus, combined autofrettage can be used for achieving higher increase in the pressure capacity when the autofrettage pressure is limited due to the capacity of the hydraulic power pack.

3.4 Conclusion

FEM modeling of a combined hydraulic and thermal autofrettage of a thick cylinder was carried out by applying the hydraulic pressure and temperature gradient simultaneously. For a realistic prediction of the elastoplastic and residual stress distributions in the cylinder, strain hardening and Bauschinger effects were considered. FEM models of the hydraulic autofrettage and thermal autofrettage were individually developed and validated using results available in the literature. After the validation, the load and boundary conditions from the individual models were combined for the simulation of a combined hydraulic and thermal autofrettage process. A series of combinations of temperature difference and hydraulic pressure were formed for two materials, *viz*., SS304 and aluminum, for achieving the maximum increase in the pressure capacity. Following major conclusions are drawn:

- Consideration of von Mises criterion along with strain-hardening and Bauschinger effect in FEM model provides realistic prediction of thermal and hydraulic autofrettage.
- The combined autofrettage can produce desirable levels of increase in pressure capacity which otherwise would have required a higher pressure in a conventional hydraulic autofrettage process. For example, in an SS304 cylinder of wall-thickness ratio of 3, an autofrettage pressure of 150 MPa enhances the pressure capacity by 41%, but the same pressure with a 36 °C higher outer wall temperature than inner wall enhances the pressure

capacity by 60%. Hence, combined autofrettage can be a potential autofrettage process in the industries where there is a limitation on the pressure due to available power pack.

Chapter 4

Heat Treatment Design of Thermally Autofrettaged Cylinder

4.1 Introduction

The fundamental objective of any type of autofrettage process is to subject a thick-walled cylindrical or spherical vessel to a state of partial or full plastic deformation. In the case of partial plastic deformation, the autofrettaged specimen comprises an inner plastic zone that restrains the tendency of an outer elastic zone to contract internally to regain its original undeformed position. This induces compressive residual stresses in the vicinity of the inner wall. In case of full plastic deformation, the material at inner wall suffers larger strain hardening than that at the outer wall. Here, at the inner wall, compressive residual stresses are induced due to non-uniform straining. In both the cases, tensile residual stresses are induced at the vicinity of the outer wall to attain a state of equilibrium. The compressive residual stresses internally strengthen the autofrettaged cylinder against static/pulsating high magnitude load. On the contrary, the tensile residual stresses at the outer wall weaken the cylinder when there are external flaws like surface cracks at the outer wall of the cylinder [18]. Seifi and Babalhavaeji [129] carried out a rigorous FEM and experimental analysis to study the reduction of bursting pressure of a thick-walled autofrettaged cylinder due to the presence of surface cracks. Four types of surface crack configurations *viz*., an axial crack, a 30° inclined crack, a 60° inclined crack and a circumferential crack were considered. Out of all these crack configurations, it was shown that the axial crack caused maximum reduction in the bursting pressure by about 30% whereas the circumferential crack had the least effect causing about 6% reduction.

A few researchers have proposed some techniques to reduce the tensile residual stresses or induce compressive residual stresses at the outer surface of autofrettaged cylinders. Based on an experimental study, Franklin and Morrison [117] subjected an autofrettaged thick-walled cylinder with wall-thickness ratio of 2.39 to a mild heat treatment of 250 °C for 1 hour. This reduced the tensile residual stress shown by a decrease in the measured radial strain from 32.5×10^{-5} to 30.6×10^{-5}. Koh and Jabbari [69] proposed a combination of autofrettage and wire winding of the thick-walled cylinder. It was shown that with sufficient layers, the wire winding arrangement eliminated the outer tensile residual stresses and also increased the inner compressive residual stresses. Koh and Stephens [164] mechanically induced compressive residual stresses around an external groove in a thick-walled autofrettaged cylinder by shot

peening. This increased the fatigue life of the cylinder by about 3.5 to 13 times. Although these techniques are effective, there are still some drawbacks that need to be addressed. The compressive residual stresses field imparted by mechanical shot peening may not be uniform. The process may also lead to a rough surface finish of the outer wall. The wire winding arrangement also required sufficient turns of the windings and increased the outer diameter and weight of the cylinder [69]. Hence, there is still a need to develop a better technique for mitigating the tensile residual stresses at the outer wall.

The proposed model is described with a background of thermal autofrettage in the following subsection. The objective of the present chapter is to study a thermal autofrettage process wherein a heat treatment is incorporated that induces beneficial compressive stresses at the inner as well as outer wall of the cylinder. An FEM analysis is carried out in commercial package ABAQUS®. The FEM model considers temperature and microstructure dependent material properties. Phase transformation kinetics is incorporated in the model through user defined subroutine UMATHT. The rest of the chapter is organized as follows. Section 4.2 presents the concept of the proposed heat treatment design coupled in a thermal autofrettage process. Section 4.3 describes the mathematical modeling of the phase transformation kinetics. Section 4.4 describes details of the FEM analysis. Section 4.5 discusses the results and Section 4.6 concludes the chapter.

4.2 Concept of Heat Treatment-Coupled Thermal Autofrettage Process

A thermal autofrettage process for a thick cylinder comprises two steps— a loading step in which the cylinder is subjected to a radial temperature gradient and an unloading step where the cylinder is slowly cooled down to room temperature. In the proposed heat treatment technique, the thermally autofrettaged cylinder is subjected to the following two additional steps— a reloading step in which the cylinder is again subjected to a radial temperature gradient that results in partial recrystallization of the cylinder and a quenching step where the cylinder is rapidly cooled. The whole process comprising the four steps, *viz*., loading, unloading, reloading and quenching, is depicted in Fig. 4.1 on a quarter-section of a cylinder. In the loading step shown in Fig. 4.1(a), a radial temperature gradient is setup by maintaining the inner wall at a temperature T_a and heating the outer wall to a higher temperature T_b. The loading step creates an inner plastic zone and an outer elastic zone in the cylinder. In the unloading step, the cylinder is cooled down and the temperature gradient is removed. The induced internal material pressure field after autofrettage is shown in Fig. 4.1(b). In the reloading step, the outer wall of the thermally autofrettaged cylinder is heated to a temperature T_b that is greater than the lower

critical temperature Ac_1 and the inner wall is kept at a temperature T_a that is less than Ac_1 as shown in Fig. 4.1(c). This step causes austenization in the vicinity of the outer wall. In the quenching step, the cylinder is cooled rapidly from both the inner and outer walls to room temperature T_{Room}. This causes a sudden contraction of the outer wall surface and causes plastic deformation creating an outer plastic zone from the outer surface up to an intermediate radius. With further cooling, the gradual contraction of the underlying material commences. Because of a larger volume of the contracting material, the underlying material pulls the plastically deformed outer wall surface reducing the initial tensile residual stress at the vicinity of the outer wall with temperature approaching room temperature. Eventually the outer surface attains compressive residual stresses.

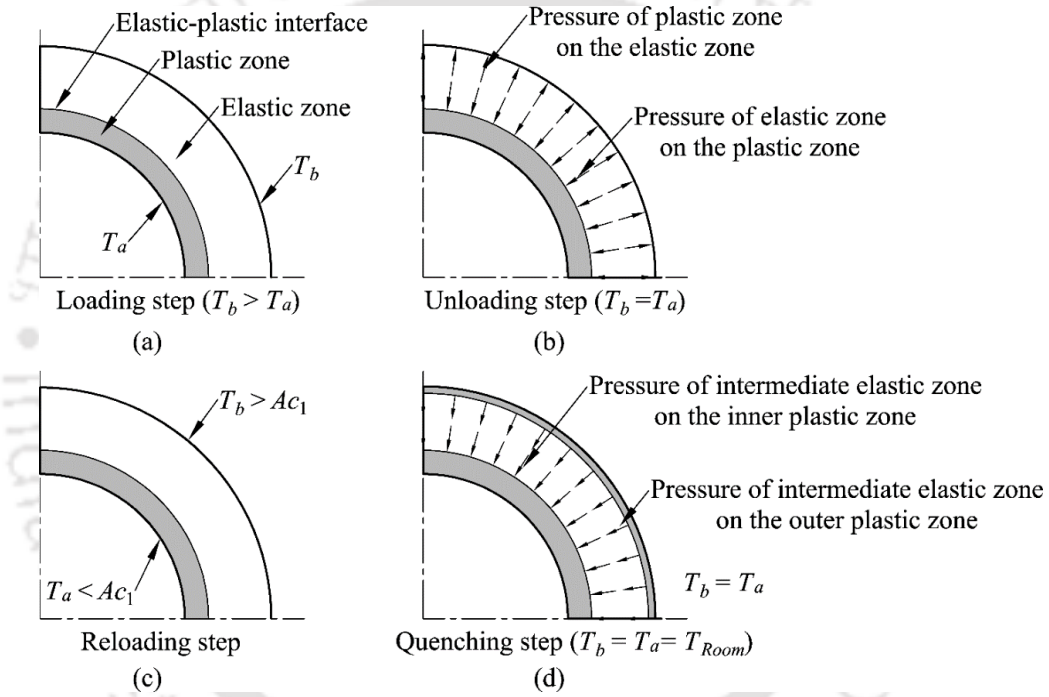

Figure 4.1 A typical heat treatment coupled thermal autofrettage process and the concept of the heat treatment design

4.3 Mathematical Modeling of Phase Transformation Kinetics

Phase transformation kinetics describes the rate of transformation of a parent phase into its microstructural constituents at different temperatures. In typical steels, based on the type of the movement of the atoms, the transformation may be diffusional or displacive. The brief description of these two types of transformation and their mathematical models are presented in the following subsections.

4.3.1 Kinetics of Diffusional Phase Transformation

In diffusional transformation, the atomic bonds break and individual atoms move and rearrange themselves to form new microstructures whereas in displacive transformation,

ordered groups of atoms displace without actually breaking the bonds. In steels, austenite undergoes diffusional transformation to give one or more of the following constituents: pearlite, bainite, proeutectoid ferrite (in hypoeutectoid steel) and proeutectoid cementite (in hypereutectoid steel). Depending on the variation of temperature with time, transformation may be isothermal or anisothermal. First, the case of isothermal transformation is introduced briefly and its extension to the case of non-isothermal transformation is explained in detail.

The kinetics of diffusion based transformation under isothermal condition is governed by the classical Johnson-Mehl-Avrami-Kolmogorov (JMAK) equation that is given as follows [168]:

$$X_k(t) = X_k^{\max}\left\{1-\exp(-b_k t^{n_k})\right\}, \tag{4.1}$$

where X_k is the volume fraction of a particular kth constituent that grows with time t at a rate defined by the temperature dependent constants b_k and n_k and X_k^{max} is the maximum volume fraction of the k^{th} constituent that can be obtained. For all types of steel with varying carbon content *viz*., hypoeutectoid (carbon less than 0.76%), eutectoid (carbon equal to 0.76%) and hypereutectoid steel (carbon more than 0.76%), X_k^{max} for pearlite and bainite equal to unity. In case of hypoeutectoid steels, in addition to these three constituents, austenite decomposition may also give proeutectoid ferrite when the temperature is above the eutectoid isotherm but below the upper critical temperature. Here, the variation of X_k^{max} is computed as follows [169]:

$$X_k^{\max} = \begin{cases} 0, & T \geq Ac_3 \\ X_k^{eq}\dfrac{Ac_3 - T}{Ac_3 - Ac_1}, & Ac_1 > T > Ac_3 \\ X_k^{eq}, & T \leq Ac_1 \end{cases} \tag{4.2}$$

where Ac_3 is the upper critical temperature and X_k^{eq} is the equilibrium volume fraction of the proeutectoid phase. The value of X_k^{eq} below Ac_1 is decided by the lever rule as follows [170]:

$$X_k^{eq} = \begin{cases} \left(\dfrac{0.76-C}{0.76-0.022}\right), & \text{for proeutectoid ferrite} \\ \left(\dfrac{2.1-C}{2.1-0.76}\right), & \text{for proeutectoid cementite} \end{cases} \tag{4.3}$$

where C is the percentage of carbon content. The start and finish of each k^{th} constituent that undergoes diffusional transformation at a constant temperature is defined when the transformed volume fraction has reached 1% and 99%, respectively, of the maximum transformable volume fraction X_k^{max}. For each isothermal transformation, the start and finish

times when plotted for a range of different temperatures traces the time-temperature-transformation (TTT) curve of the material.

Under anisothermal condition, the kinetics of transformation is governed by a slightly modified version of the original JMAK equation, which is derived based on the assumption that the overall anisothermal transformation comprises a series of small incremental isothermal transformations. To incorporate this, the time variable t in Eqn. (1) is replaced by a fictitious time parameter τ, which is calculated as follows [168]:

$$\tau = \left\{ \frac{-1}{b_k} \ln\left(1 - X_k\right) \right\}^{\frac{1}{n_k}}. \tag{4.4}$$

This is a rearranged form of Eqn. (1) and provides the time required to achieve a known volume fraction X_k. The temperature dependent constants b_k and n_k are determined from Eq. (4.1) by substituting the volume fractions $X_k = 0.01$ and $X_k = 0.99$ corresponding to the start and finish of the transformation. Therefore,

$$n_k = \frac{6.127}{\ln\left(\frac{t_f}{t_s}\right)}, \tag{4.5}$$

$$b_k = \frac{0.01}{t_s^{n_k}} \quad \text{or} \quad b_k = \frac{4.60}{t_f^{n_k}}. \tag{4.6}$$

where t_s and t_f are the start and finish times, respectively whose values are taken from the TTT diagram of the material.

The schematic of an anisothermal transformation considering a k^{th} constituent is depicted in Fig. 4.2. In Fig. 4.2(a), the continuous variation of temperature has been approximated as a series of small isotherms each of duration Δt. Each temperature point is obtained on the TTT diagram and the projection of the end points of the TTT diagram on the time-volume fraction Cartesian plane provides the JMAK curve governing the isothermal transformation at the temperature. The time t_o is the datum time at the temperature T_0 at which the volume fraction of the k^{th} constituent has reached 1% of the maximum obtainable volume fraction. For temperature T_0, the isothermal transformation in the increment Δt occurs along the JMAK curve traced by *1-2* resulting in volume fraction X_k^0. When the temperature changes to T_1, the rate constants n_k and b_k are calculated using the t_s and t_f for T_2 in Eq. (4.5) and (4.6), respectively. Then Eq. (4.4) is applied to calculate the fictitious time τ_1 required to attain the volume fraction X_k^1. The volume fraction can now be computed by adding the increment Δt over τ_1; the transformation occurs along the JMAK curve for T_1 traced by the path *1'-2'-3*

resulting in the volume fraction X_2 as depicted in Fig. 4.2(c). Likewise, when the temperature reaches T_2 in the next increment, the fictitious time τ_2 is first calculated and the volume fraction is computed defined by the path *1''-3'-4* resulting in the volume fraction X_2. The computation of the volume fraction in the next increment at the temperature of T_3 along the path *1'''-4'-5* is also computed using a similar approach. The JMAK equation for anisothermal condition can thus be written as follows:

$$X_k\left(t+\Delta t\right)=X_k^{\max}X_\gamma\left[1-\exp\left\{b_k\left(\tau+\Delta t\right)^{n_k}\right\}\right], \tag{4.7}$$

where the volume fraction of a k^{th} constituent $X_k(t + \Delta t)$ is computed as a function of time at the end of each time increment Δt. The symbol X_γ denotes the volume fraction of austenite that was available at the beginning of the transformation of the k^{th} constituent. This value is updated at the beginning of the transformation of each subsequent k^{th} constituent as follows:

$$X_\gamma=1-\sum_{i\neq k}X_i, \tag{4.8}$$

where X_i is the volume fraction of each preceding i^{th} constituent whose transformation has already occurred.

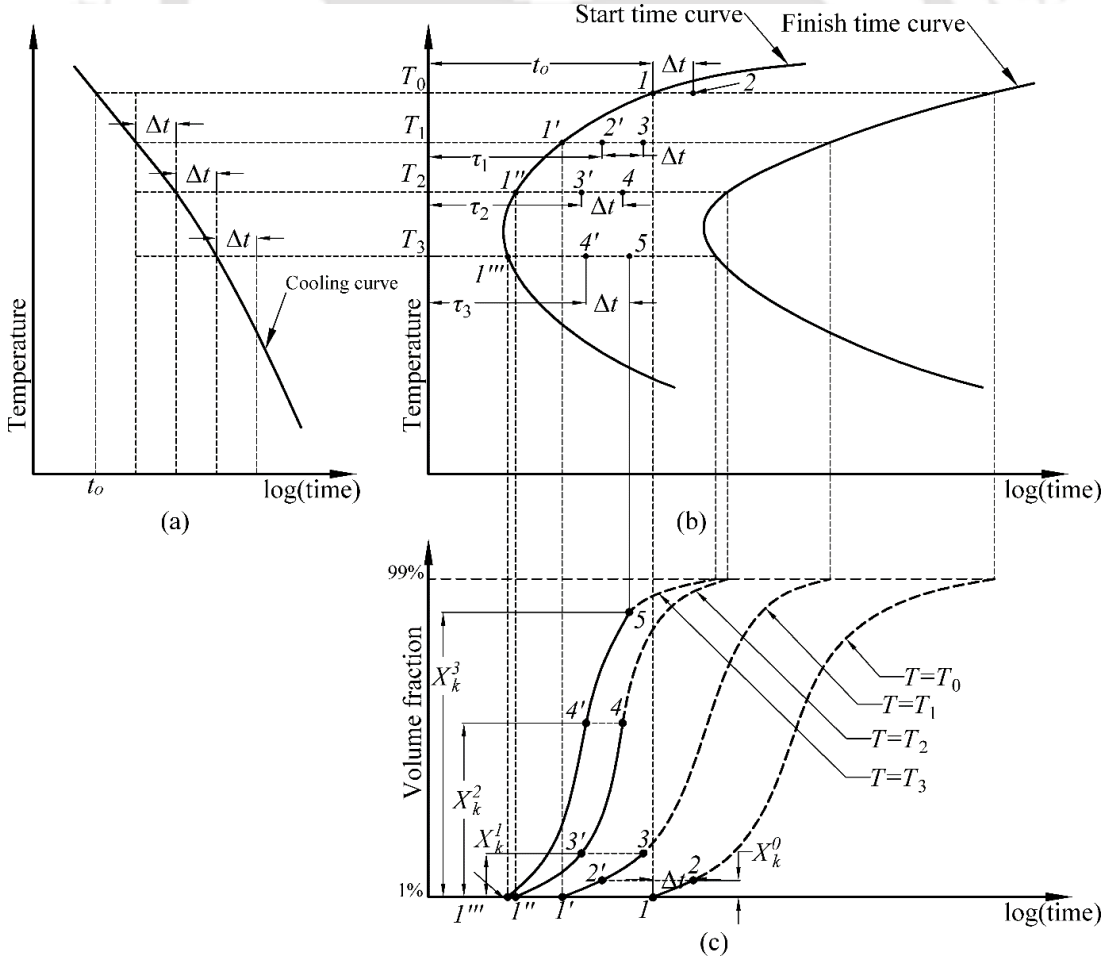

Figure 4.2 Schematic of anisothermal cooling curve and the projected temperature points on the TTT diagram with the incremental transformation along different JMAK curves

4.3.2 Kinetics of Displacive Phase Transformation

In typical steels, austenite undergoes displacive transformation to give martensite. The mathematical formula for computing the volume fraction of martensite is expressed only as a function of temperature. Once the temperature reaches the threshold for martensitic transformation, which is generally about 225 °C [170], all the available austenite transforms into martensite until reaching the room temperature.

$$X_k = X_\gamma \left[1 - \exp\left\{-0.011\left(T_{MS} - T_j\right)\right\}\right], \tag{4.9}$$

where T_{MS} is the temperature below which the transformation of austenite to martensite commences and T_j is the temperature at current time.

4.4 FEM Modeling of Coupled Thermal Autofrettage and Heat Treatment Process

This section presents the procedure for FEM modeling of the coupled thermal autofrettage and heat treatment process. This includes the part modeling, basis for load increment sizing, selection of material model, implementation of the phase transformation kinetics in the FEM code and the convergence study for optimum mesh sizes.

4.4.1 Model Description

The autofrettage specimen considered in this study is a thick-walled, open ended cylinder with free ends considering a generalized plane strain condition. The generalized plane strain condition is achieved by taking the length of the cylinder sufficiently larger compared to the thickness (≥ 6 times wall thickness) [171]. A 120 mm long cylinder having an inner and outer radius of 10 mm and 30 mm respectively, was taken for the analysis. The analysis was carried out using an axisymmetric model with a planar 2D shell as shown in Fig 4.3.

4.4.2 Analysis Steps, Loading and Boundary Conditions

The FEM model consists of four successive analysis steps— thermal loading, thermal unloading, thermal reloading and quenching. The first two steps comprise the steps of a conventional thermal autofrettage process. In the thermal reloading step, the outer wall cylinder is heated above Ac_1 and the inner wall is kept at a temperature below Ac_1. Finally, in the quenching step, the cylinder is cooled simultaneously from the inner and outer walls. Since a time dependent phase transformation phenomenon is studied only in the quenching step, the analysis of the first three steps were carried out using steady state condition and a transient analysis was performed only in the quenching step. The temperature boundary conditions in the first three analysis steps were applied incrementally by using a fixed increment size of 0.01 to accurately determine the minimum temperature difference for causing the initial yield. In the quenching step, a minimum increment of 10^{-6} s and a maximum increment of 1 s was used.

The duration of cooling was set till the cylinder attains the room temperature 20 °C. The loading and boundary conditions assigned to the axisymmetric model is depicted in Fig. 4.3 in cylindrical coordinate space with r, θ and z representing the radial, angular and axial coordinates, respectively. The inner wall is represented by AD whereas the outer wall is represented by BC. In the first three steps, AD is assigned a temperature T_a and BC is assigned a higher temperature T_b. In the quenching step, a combined convective or radiation boundary condition is assigned to the walls that is defined as follows:

$$q_a = h\left(T_a - T_\infty\right) + \beta e_T \left(T_a^4 - T_\infty^4\right), \tag{4.10}$$

$$q_b = h\left(T_b - T_\infty\right) + \beta e_T \left(T_b^4 - T_\infty^4\right), \tag{4.11}$$

where q_a, q_b are the heat fluxes at the inner and outer cylinder walls, respectively, h is the convective heat transfer coefficient, T_∞=20°C is the ambient temperature at steady state, e_T is the thermal emissivity and β=5.67×10^{-8} W/m^2 is the Stefan-Boltzmann constant. In all the analysis steps, the ends of the cylinder represented by AB and CD remain insulated. Due to the axial symmetry of the cylinder, the model was further simplified by reducing the analysis cylinder to half of its length. This condition was invoked using the mechanical boundary condition u_z=0 at the mid section (represented by AB in Fig. 4.3) of the cylinder where u_z is the displacement in the axial direction.

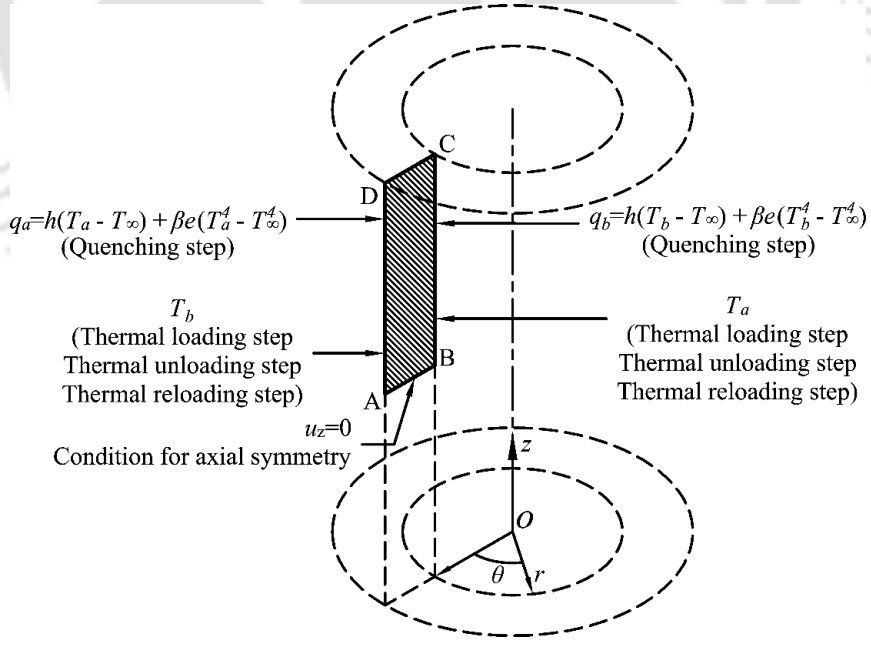

Figure 4.3 Schematic of the axisymmetric part in ABAQUS® along with boundary conditions

4.4.3 Definition of the Material Behavior

The material used in the study is 1080 steel, which has a eutectoid composition with a carbon content of 0.8%. The TTT diagram of 1080 steel is shown in Fig. 4 where TBN is the

temperature for the start of bainite formation and $M_{50\%}$ & $M_{90\%}$ are the temperatures at which the volume fraction of martensite reaches 50% and 90%, respectively. The start and end curves are approximated using piecewise polynomial interpolation. As evident from the nature of the start curve in Fig. 4.4, the start time t_s tends to a very large value (infinity) as the temperature approaches 725 °C. This becomes a problem during the computation of the rate constant n_k defined by Eqn. (4.5) at temperatures near 725 °C. This is because the denominator term in Eqn. (4.5) becomes very small at the corresponding temperatures. To overcome this, the upper critical temperature was slightly offset to a lower value. A stable and convergent solution was found at 715 °C. Hence, the upper critical temperature was considered as 715 °C.

The temperature and microstructure dependent properties taken from [172] are shown in Tables 4.1–4.6. The Poisson's ratio was taken as 0.3. Since the material is composed of various microstructural constituents, the magnitude of a particular type of property is computed as an aggregate of the values contributed by each constituent at the particular temperature using the linear mixture law, which is expressed as follows:

$$P = \sum_{k=1}^{N} X_k P_k, \tag{4.12}$$

where P represents the aggregate property, P_k is the property of the kth constituent and N is the number of constituents present in the alloy. The thermal, metallurgical and mechanical behavior of the material incorporated in the FEM model are explained in the following subsections.

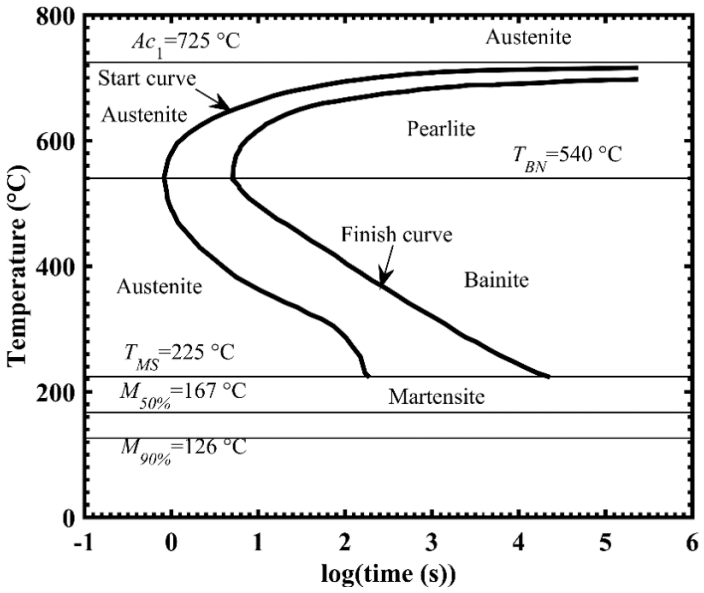

Figure 4.4 Time temperature transformation (TTT) diagram of 1080 steel. Data taken from **[172]**

Table 4.1 Temperature dependent Young's modulus of elasticity

Temperature (°C)	Young's modulus of elasticity (GPa)
12	221
461	165
522	153
570	136
695	62
883	20.45
947	11.5
1000	10

Table 4.2 Temperature dependent yield stress and hardening modulus

Temperature (°C)	σ_Y (MPa)	Hardening modulus (MPa)
10	714	25323
554	291	10937
600	215	9010
645	129	6013
720	59	3433
850	40	2231
1000	40	1403

Table 4.3 Temperature and microstructure dependent specific heat

Temperature (°C)	Specific heat (J/kg°C)		
	Austenite	Pearlite	Martensite
10	560	479	560
242	564	556	564
388	568	617	568
626	574	738	574
690	585	774	585
1200	679	774	679

Table 4.4 Temperature and microstructure dependent thermal conductivity

Temperature (°C)	Thermal conductivity (W/m°C)		
	Austenite	Pearlite	Martensite
15	11.25	50	41
520	19.5	35	41
790	24	30.5	41
1200	31		

Table 4.5 Temperature dependent coefficient of thermal expansion

Temperature (°C)	Coefficient of thermal expansion (/°C)×10^{-6}
10	15.2
557	15.8
750	21

Table 4.6 Temperature and microstructure dependent density

Temperature (°C)	Density (kg/m^3)	
	Austenite/Martensite	Pearlite
10	8005	7853
438	7788	7725
783	7618	7592
1200	7405	7592

4.4.3.1 Metallurgical Behavior

The mathematical model for the phase transformation kinetics explained in Section 4.3 was implemented through the user subroutine UMATHT in ABAQUS®, which is written in FORTRAN. The main code in ABAQUS® calls the UMATHT subroutine at each integration point for each increment. The subroutine is provided in Appendix B.

The volume fractions of each constituent were stored as solution dependent variables (SDVs), which are a set of global variables in the ABAQUS® main code stored in the state variable (STATEV) array. For 1080 steel, 4 SDVs were specified and the volume fractions of austenite, pearlite, bainite and martensite were stored as SDV 1, SDV2, SDV 3 and SDV 4, respectively. The material is assumed to be initially composed of 55% Pearlite and 45% Bainite. This condition was invoked through the SDVINI user subroutine. The SDVINI subroutine, which is called only at the first increment of the analysis allows initial values to be assigned to the SDVs. The SDVs that store the initial volume fractions of pearlite and bainite are then passed into the UMATHT subroutine, where the algorithm for phase transformation is implemented. For a particular node, the algorithm is depicted in the flowchart shown in Fig. 4.5, where X_{AUS}, X_{FER}, X_{PER}, X_{BN} and X_{MAR} symbolize the volume fractions of austenite, ferrite, pearlite, bainite and martensite, respectively. The steps are explained as follows:

Step 1. The SDVINI subroutine is called at the node to initialize a microstructural state comprising 55% Pearlite and 45% Bainite. The SDVs representing these volume fractions are passed into the UMATHT subroutine in the step 2.

Step 2. Nodal temperature T is checked. If T is greater than Ac_1, then assuming that the node remains at the temperature for more than 10 s, a fully austenitic microstructure with X_{AUS} = 1 is assigned at the particular node. Else Step 8 is executed.

Step 3. The available volume fraction of austenite X_{AUS} is checked. If it is greater than 1%, Step 4 is executed. Else the austenite decomposition is considered complete and Step 8 is executed.

Step 4. If nodal temperature T is less than lower critical temperature Ac_1 but greater than T_{BN}, X_{PER} is calculated using Eq. (4.7) and the current volume fraction of X_{AUS} is updated by

subtracting X_{BN} from that in the previous increment using Eq. (4.8) and Step 8 is executed. Else Step 5 is executed.

Step 5. If nodal temperature T is less than T_{BN} but greater than T_{MS}, X_{BN} is calculated using Eq. (4.7) and the current volume fraction of X_{AUS} is updated by subtracting X_{BN} from that in the previous increment using Eq. (4.8) and Step 8 is executed. Else Step 6 is executed.

Step 6. If nodal temperature T is less than T_{MS} but greater than room temperature, X_{MAR} is calculated using Eq. (4.9) and the current volume fraction of X_{AUS} is updated by subtracting X_{MAR} from that in the previous increment using Eq. (4.8) and Step 8 is executed.

Step 7. If nodal temperature T has reached the room temperature T_{Room}, the microstructure has reached a metastable state and Step 9 is executed. Else Step 8 is executed.

Step 8. Thermal properties at the particular node are calculated by applying mixture rule given by Eq. (4.12) on the basis of the resulting microstructural composition and UMATHT subroutine for thermal analysis is executed. Execute the elastic-plastic analysis by incrementing the time and go to Step 3.

Step 9. Stop simulation by calling the exit command XIT in the subroutine

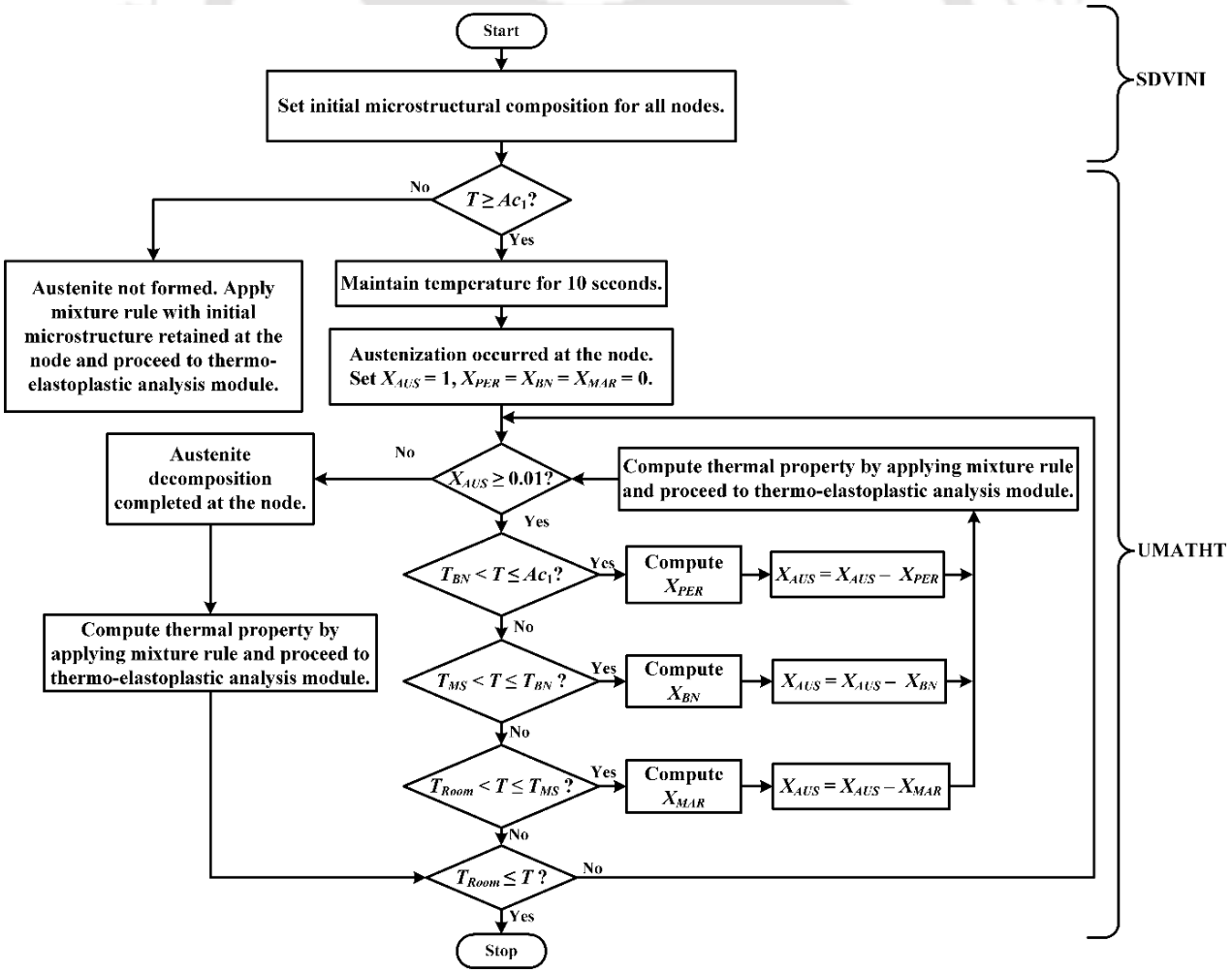

Figure 4.5 Flowchart of the algorithm applied for phase transformation kinetics

4.4.3.2 Thermal behavior

The thermal behavior was also defined in the UMATHT subroutine after the instructions for the computation of the volume fractions of the microstructural constituents. The resulting volume fractions are used to calculate the aggregate thermal properties *viz*., specific heat and thermal conductivity by applying Eqn. (4.8). The governing thermal constitutive equations is based on Fourier's law of conduction, which is as follows:

$$\rho c \frac{\partial T(r,t)}{\partial t} = \nabla.\{k \nabla T(r,t)\} + Q(r,t) \tag{4.13}$$

where c is the specific heat energy, ∇ is the gradient operator, ρ is the density, $T(r, t)$ is the temperature as a function of spatial coordinates r and time t, k is the thermal conductivity and Q is the rate of internal heat generated per unit volume. The material properties are defined in the following sets of equations:

$$\frac{\partial u}{\partial T} = c, \tag{4.14}$$

where u is the internal energy per unit mass. The latent heat due to phase transformation is incorporated in the equation for the change in internal energy as follows:

$$\mathrm{d}u = \frac{\partial u}{\partial T}\mathrm{d}T + \psi \frac{\Delta H}{\rho} \Delta X_k, \tag{4.15}$$

where du is the internal energy change per unit mass, dT is the change in temperature, ΔX_k is the incremental change in volume fraction of the k^{th} constituent, ΔH is the enthalpy of formation per unit volume whose values for austenite-martensite and austenite-pearlite transformations were taken as 640×10^6 J/m^3 and $(1.56\times10^9 - 1.5\times10^6\, T)$ J/m^3, respectively [173] and ψ is a parameter defined as

$$\psi = \begin{cases} -1 & \text{if } \mathrm{d}T \le 0, \\ 1 & \text{if } \mathrm{d}T > 0. \end{cases} \tag{4.16}$$

4.4.3.3 Mechanical behavior

The material model for the plasticity is based on the von Mises yield criterion and the flow stress is governed by Ziegler's linear kinematic hardening rule, which is expressed as follows [166]:

$$\sigma_Y = \sqrt{\frac{2}{3}\left(\sigma'_{ij} - \mathrm{d}\alpha_{ij}\right)\left(\sigma'_{ij} - \mathrm{d}\alpha_{ij}\right)}, \tag{4.17}$$

$$\alpha_{ij} = \frac{H}{\sigma_Y}\left(\sigma_{ij} - \alpha_{ij}\right)\mathrm{d}\varepsilon^p_{eq}, \tag{4.18}$$

where σ'_{ij} is the deviatoric stress tensor, $\mathrm{d}\alpha_{ij}$ is the incremental back stress tensor, σ_{ij} is the stress tensor and $\mathrm{d}\varepsilon^p_{eq}$ is the incremental equivalent plastic strain, which is defined as

$$\mathrm{d}\varepsilon_{eq}^{p} = \sqrt{\frac{2}{3}\mathrm{d}\varepsilon_{ij}^{p}\mathrm{d}\varepsilon_{ij}^{p}}\,. \tag{4.19}$$

The total strain increment is defined as the sum of the following components:

$$\mathrm{d}\varepsilon_{ij} = \mathrm{d}\varepsilon_{ij}^{e} + \mathrm{d}\varepsilon_{ij}^{p} + \mathrm{d}\varepsilon_{ij}^{th}, \tag{4.20}$$

where $\mathrm{d}\varepsilon_{ij}^{e}$ is the incremental elastic strain, $\mathrm{d}\varepsilon_{ij}^{p}$ is the incremental plastic strain and $\mathrm{d}\varepsilon_{ij}^{th}$ is the incremental thermal strain, which are expressed as follows:

$$\begin{cases} \mathrm{d}\varepsilon_{ij}^{e} = \dfrac{1}{E}\left\{(1+\nu)\sigma_{ij} - \nu\sigma_{kk}\delta_{ij}\right\} \\ \mathrm{d}\varepsilon_{ij}^{p} = \mathrm{d}\lambda\dfrac{\partial f}{\partial\sigma_{ij}}, \\ \mathrm{d}\varepsilon_{ij}^{th} = (\alpha_T \mathrm{d}T)\delta_{ij}, \end{cases} \tag{4.21}$$

where ν is the poisson's ratio, δ_{ij} is the Dirac-delta function, $\mathrm{d}\lambda$ is the plastic multiplier, f is the von Mises yield function and α_T is the coefficient of thermal expansion.

4.4.4 Mesh sensitivity analysis

The element type CAX8T, which is an axisymmetric, 8-noded temperature-displacement coupled quadratic element was used for the FEM analysis. The 20 mm thickness of the cylinder was divided into three partitions in the ratio of 1:3:1 as shown in Fig. 4.6. Identical fine meshes were used in the outer two partitions whereas a comparatively coarse mesh was used in the intermediate partition. This was to ensure accurate prediction of stresses at the inner and outer wall of the cylinder where the plastic deformation takes place. The optimum mesh in the model was decided by a mesh sensitivity analysis that was carried out on the basis of the convergence of the maximum values of the radial, hoop and axial stresses during the loading step in a thermal autofrettage process towards an approximate constant value. A typical thermal autofrettage process was carried out for a temperature gradient of 330 °C by setting the temperatures of the inner wall and outer wall to 20 °C and 350 °C, respectively. The optimum mesh was obtained with 600 elements that 60 elements along the thickness and 10 elements along the length dimension. The 60 elements along thickness comprised 15 elements in each of the inner and outer partitions and 30 elements in the intermediate partition. The results of the mesh sensitivity analysis are shown in Table 4.7 where the optimum mesh is shown in bold and the typical mesh used is shown in Fig. 4.6.

Table 4.7 Result of the mesh sensitivity analysis

Mesh	Elemental divisions			Maximum stress (MPa)			CPU time (secs)
	Inner/outer partition	Intermediate partition	Axial	Radial	Hoop	Axial	
1	5	15	3	193.24	832.58	826.45	4.2
2	10	20	5	191.4	841.13	823.29	6.5
3	10	30	5	191.07	841.11	823.29	7.7
4	10	30	6	193.21	846.96	823.22	9
5	10	30	7	192.47	848.71	823.02	10.2
6	**15**	**30**	**10**	**192.51**	**848.53**	**822.46**	**16.2**

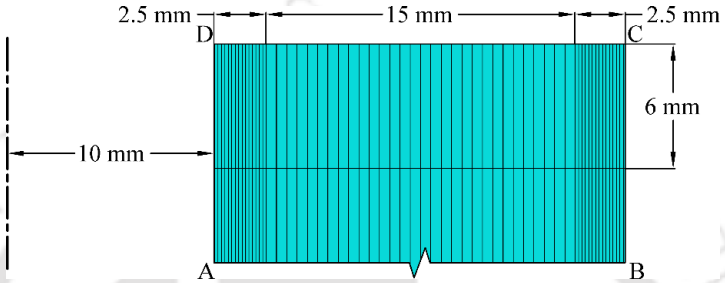

Figure 4.6 Typical mesh used in the current FEM model

4.5 Results and Discussion

This section presents the results of the FEM analysis. First the results of the validation of the FEM model using experimental results of thermal autofrettage and heat treatment are shown. Then the results of the coupled heat treatment and thermal autofrettage processes are shown.

4.5.1 Validation of the Model

Since the heat treatment coupled thermal autofrettage process has been analyzed for the first time, the validation of the overall model is carried out individually for the thermal autofrettage and the heat treatment modules. The validation of the FEM model based on thermal autofrettage has been already shown in Section 3.3.2 and will not be repeated. The calculation of the volume fractions of the microstructural constituents on the basis of the phase transformation kinetics incorporated in the FEM model is validated using the experimental results of Wang *et al*. [172]. The authors presented an FEM model of quenching of carbon steel and that was validated using experimental results. The experimental specimen was a 76.2 mm long solid cylinder of diameter 38.1 mm of material 1080 steel, which is the same as used in the present study. In the experiment, the cylinder was heated above the upper critical temperature at 850 °C and then quenched. Three types of quenchants were considered in the study, which were water, a 6% aqueous solution of UCON-A and a 14% aqueous solution of UCON-E. The latter two were non-flammable polymeric quenchants. After quenching, the quenched samples were sectioned and hardness measurements (Rockwell-C) were taken along

various radial positions. These were compared with the results predicted by the FEM. The measured surface temperatures given for each sample in the experiments were used as the temperature boundary conditions in the FEM model. The overall hardness at a material point was computed as a linear combination of the hardness values of each microstructural constituent. The hardness values of Pearlite and Martensite were taken as 39 RC and 66 RC respectively, and the hardness of the retained austenite (if any) was included as the hardness contributed by the Martensite as per ref. [171]. Based on a same strategy, quenching simulations were carried out using the present FEM model. The results of the validation are shown in Figs. 4.7(a–c).

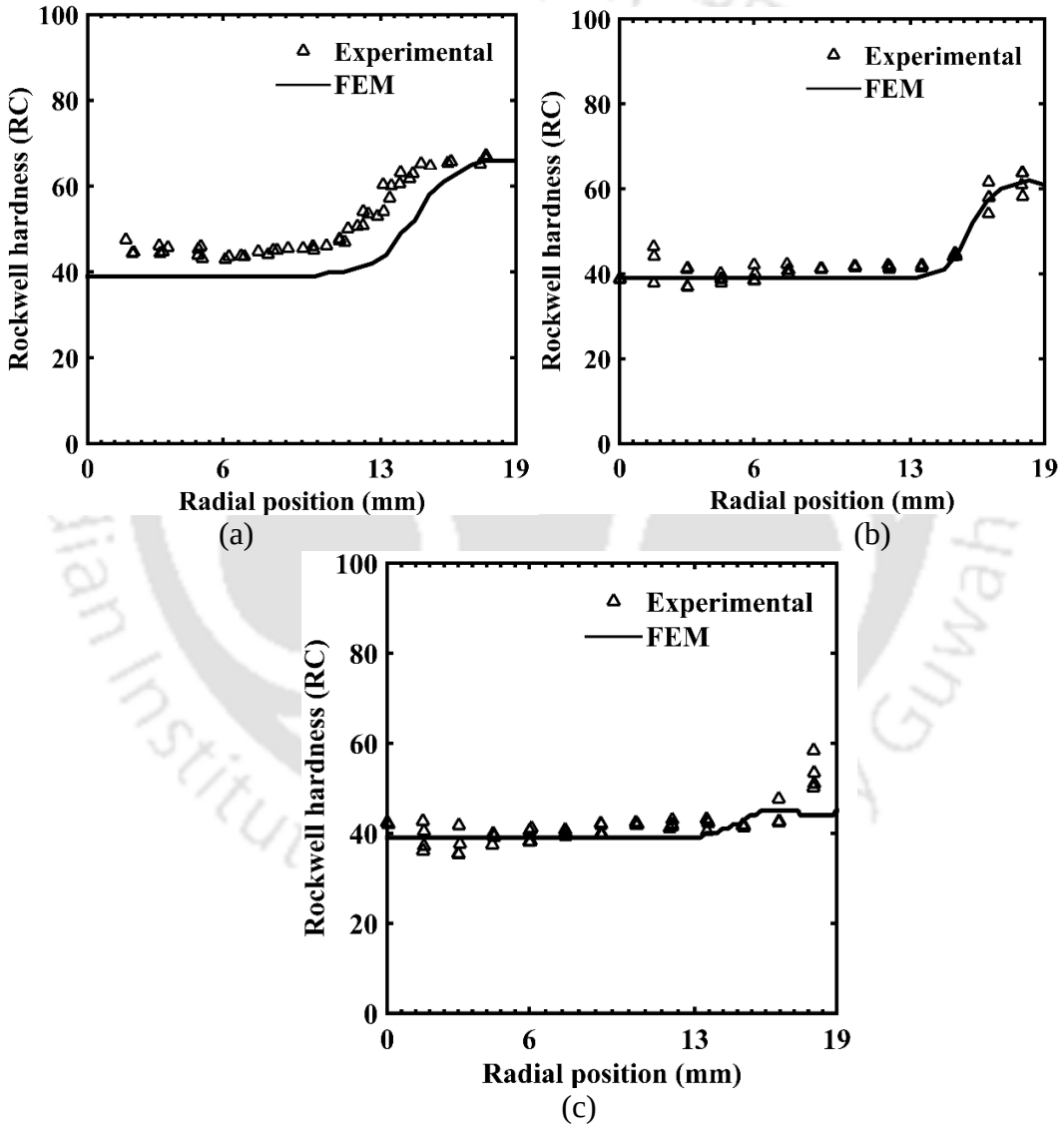

Figure 4.7 Comparison of the Rockwell hardness variation at various radial positions for the cylinder samples quenched in (a) water (b) 6% aqueous solution of UCON-A and (c) 14% aqueous solution of UCON-E based on the experimental results of **[172]**

4.5.2 Results of Thermal Autofrettage Coupled with Heat Treatment

This section presents the results of the proposed thermal autofrettage with heat treatment. The distribution of stresses in the initial thermal autofrettage process are first shown. This is followed by the discussion of results from the heat treatment process. The initial thermal autofrettage was carried out using a temperature difference of 350 °C with inner and outer wall temperatures 20 °C and 370 °C, respectively. The cylinder initially yielded at the inner wall at a temperature difference of 229 °C beyond which the yielding continues and a plastic zone spread outwards. On reaching a temperature difference of 323 °C, a second yielding occurred due to compressive stresses at the outer wall, which spreads inwards with further increase in the temperature difference. The distribution of stresses in the cylinder due to elastoplastic deformation and residual stresses due to elastic recovery are shown in Figs. 4.8(a) and 4.8(b), respectively. The cylinder comprises three deformed zones— an inner plastic zone I up to a radius of 11.75 mm, an outer plastic zone III from a radius of 28.34 mm to the outer wall and an intermediate elastic zone II. The maximum hoop and axial compressive residual stresses induced at the inner wall of the cylinder are 288.91 MPa and 324.75 MPa, respectively.

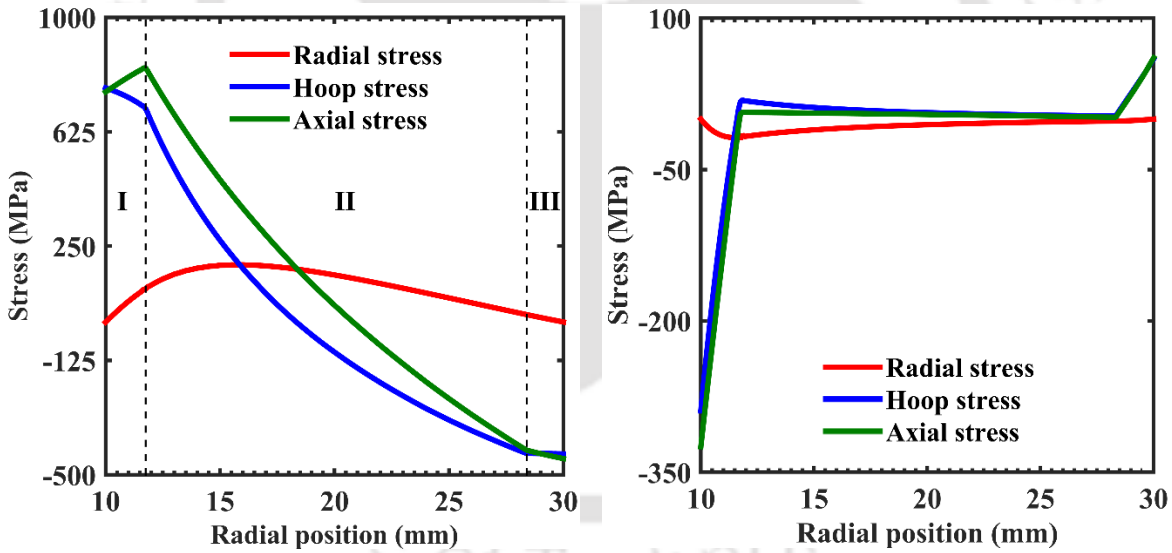

Figure 4.8 Distribution of (a) stresses due to elastoplastic deformation in the loading step and (b) residual stresses in the unloading step of thermal autofrettage with wall temperatures T_a = 20 °C and T_b = 370 °C

After the thermal autofrettage, the cylinder was again subjected to a temperature gradient across the wall thickness that involved austenization of the outer wall. Hence, the outer wall of the cylinder was kept at 725 °C (> Ac_1). The temperature to be kept at the inner wall was decided by the criterion that the resulting temperature gradient did not cause any additional yielding in the cylinder. This minimum temperature difference was obtained as about 60 °C i.e., a permissible temperature of 665 °C at the inner wall below which the autofrettaged

cylinder would undergo yielding at the inner wall due to thermal stresses. Hence, the inner wall was kept at 665 °C. The distribution of stresses during the thermal reloading step for the two cases are shown in Fig. 4.9. No additional plastic deformation occurs and the cylinder remains in the same deformed state obtained from the preceding thermal autofrettage process.

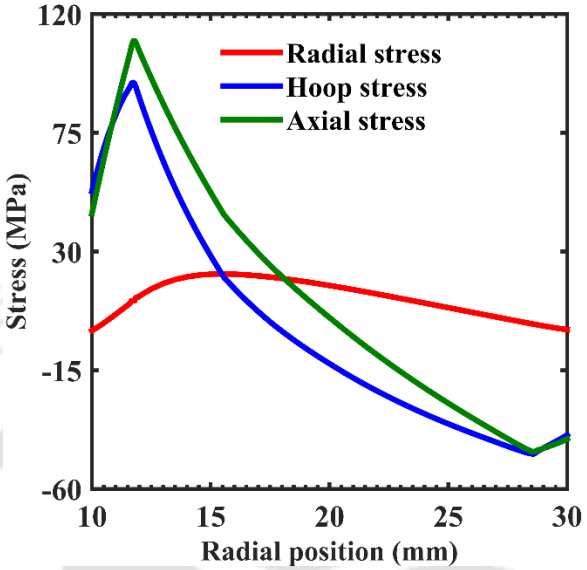

Figure 4.9 Distribution of stresses at the end of the reloading step with the temperature boundary conditions T_a = 665 °C, T_b = 725 °C

In the quenching step, the cylinder was cooled simultaneously from both the inner and outer walls by using the heat transfer boundary conditions shown in Eqns. (4.10) and (4.11). The thermal emissivity was taken as β_T as 0.3, which is typical in most steels [174] and two types of cooling rates defined by convective heat transfer coefficients viz., h = 300 W/(m^{2}K) and h = 500 W/(m^{2}K) were studied. The evolution of the hoop residual stresses at the outer wall with temperature and time during the quenching step for each of the cooling rates are shown in Fig. 4.10. Also shown in the variation of the yield stress of the material with the temperature. When the austenized outer wall is exposed to the quenchant, the surface temperature drops instantaneously leading to a sudden contraction. The underlying material just beneath the outer surface resists this contraction and generates large tensile stresses at the outer wall. When the equivalent von Mises stress exceeds the local yield stress as shown in the figure, the outer wall yields. When the temperature reaches the upper critical temperature 715 °C, pearlite formation occurs that releases latent and causes an increase in temperature that leads to expansion of the outer wall surface. The expansion slows down the contraction and causes a decrease in the stresses at the outer wall. With time, the rate of pearlite transformation decreases and hence the release in latent heat. The contraction of the outer surface continues and the tensile stresses again start to increase. As the temperature further drops, the rest of the

cylinder other than the outer surface continues to contract. This pulls the already plastically deformed surface and starts to nullify the initially tensile residual stresses at the outer surface. Due to a larger volume of the contracting material, the outer initial tensile residual stresses slowly begin to transit to a compressive behavior. The stresses further decrease until the entire cylinder reaches the steady state room temperature 20 °C. The simulations were carried out in a computer with CPU processor Intel® core™ i5 7500 with a speed of 3.41 Giga Hertz and a Random Access Memory 8 Giga Bytes running Windows 10 Professional. The CPU time required to complete the simulations for h = 300 W/(m^{2}K) and h = 500 W/(m^{2}K), were 328.2 seconds and 332.30 seconds, respectively.

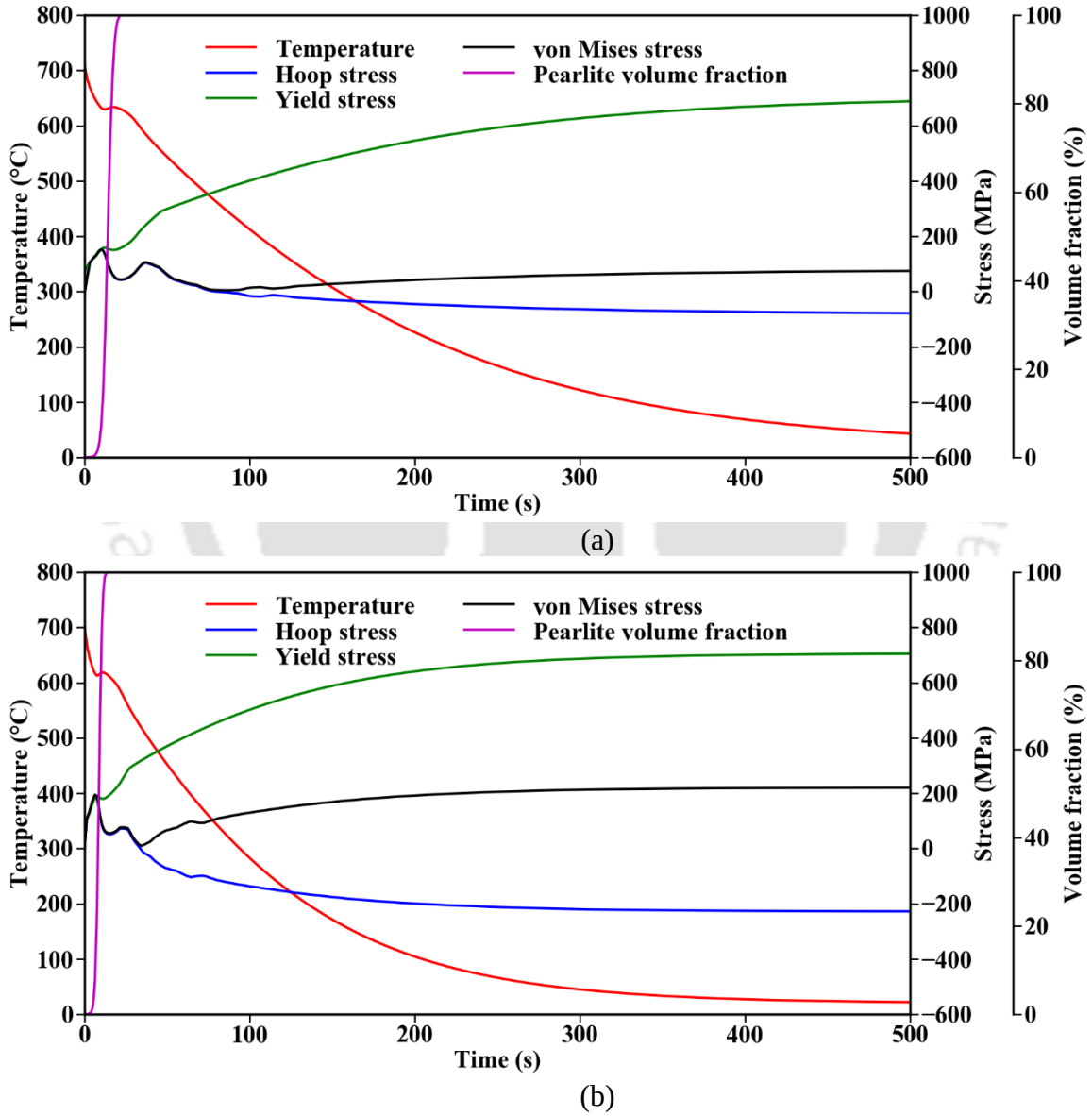

Figure 4.10 Variation of hoop residual stress, temperature and pearlite volume fraction with time at the outer wall of the cylinder quenched after thermally reloading with T_a = 665 °C, T_b = 725 °C considering the cooling rates provided by (a) h = 300 W/(m^{2}K) and (b) h = 500 W/(m^{2}K)

The distribution of residual stresses in the cylinder quenched after thermally reloading with T_a = 665 °C, T_b = 725 °C considering the cooling rates corresponding to h = 300 W/(m^{2}K) and h = 500 W/(m^{2}K) are shown in Figs. 4.11(a) and 4.11(b), respectively. In both the cases, residual stresses are induced, which are compressive at both the walls. The elastic-plastic interface radii due to the yielding in the vicinity of the outer wall during the quenching step provided by the cooling rates h = 300 W/(m^{2}K) and h = 500 W/(m^{2}K) are 28.75 mm and 27.92 mm, respectively. The position of the elastic-plastic interface is shown by dashed lines and demarcates the cylinder into an inner elastic zone I and an outer plastic zone II. The compressive residual stresses induced in the cylinder for the two cases are compared in Table 4.8. The maximum compressive hoop and axial residual stresses at the inner wall are lesser than those obtained at the end of the thermal autofrettage step. It is observed that the compressive residual stresses decrease at the inner wall but increases at the outer wall with increase in cooling rate of the outer surface.

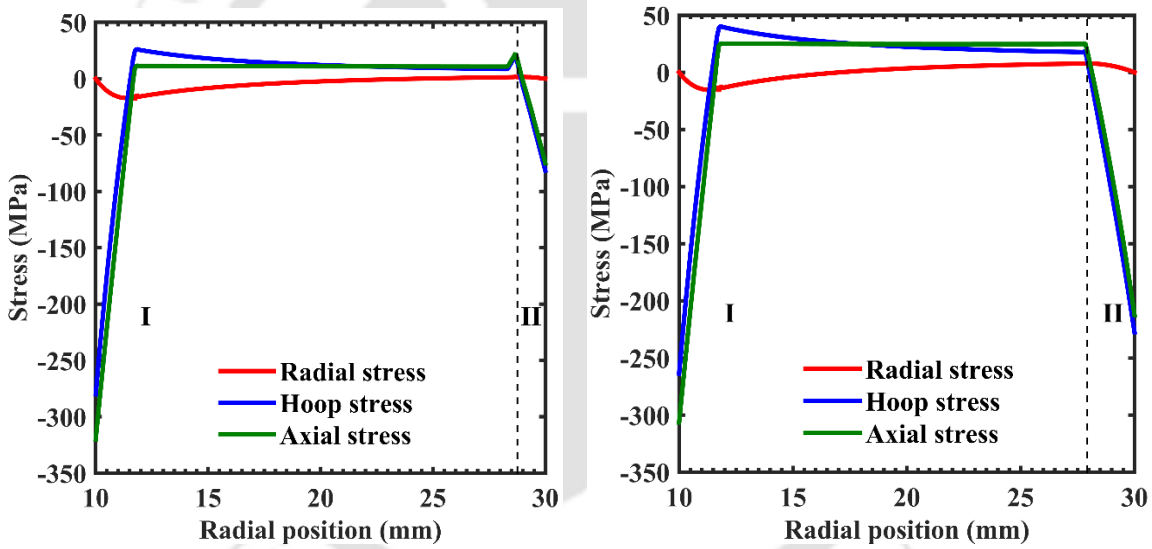

Figure 4.11 Distribution of residual stresses due to elastic recovery in the unloading step for various cases of cooling rates given by (a) h = 300 W/(m^{2}K) and (b) h = 500 W/(m^{2}K)

A pressure test was carried out to quantify the loss of the compressive residual stresses by subjecting the cylinder in each of the cases with a pressure of 600 MPa. It was found that the original pressure carrying capacity of the cylinder without autofrettage was 372 MPa. After thermal autofrettage the pressure carrying capacity was 492 MPa indicating a 24.39% increase. The decrease in the pressure carrying capacity of the cylinder after the heat treatment are shown in Table 4.8. The decrease in the pressure carrying capacity is small. In some practical situations the process may be useful against stress corrosion cracking because compressive

residual stresses cause closure of surface crack and retards the crack growth that leads to longer fatigue life without much loss in the pressure carrying capacity.

Table 4.8 Comparison of residual stresses at different cooling rates

h W/(m^{2}K)	Maximum compressive residual stress (MPa)				Increase in pressure carrying capacity (%)
	Inner wall		Outer wall		
	Hoop	Axial	Hoop	Axial	
300	280.19	320.35	81.85	85.27	23.46
500	263.76	306.54	227.75	212.81	22.5

The microstructural state of the cylinder is shown in Fig. 12. The microstructure in the vicinity of outer wall comprises of 100% Pearlite whereas the rest of the cylinder remains in the initial assumed state of 55% pearlite and 45% bainite.

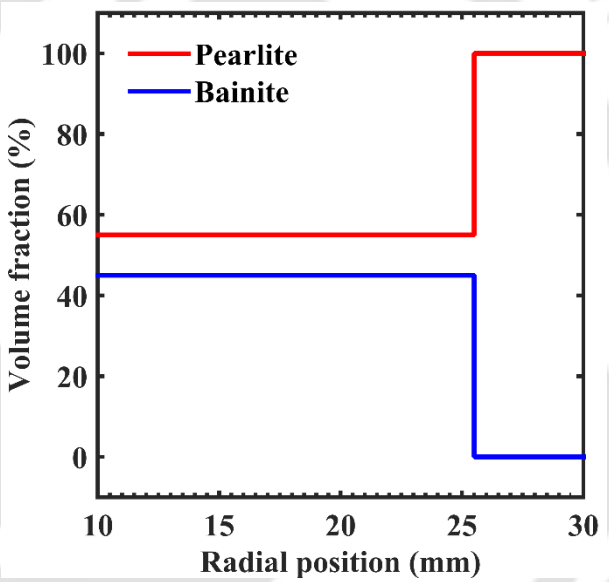

Figure 4.12 Distribution of microstructural constituents for the cooling rates corresponding to h = 300 W/(m^{2}K) and h = 500 W/(m^{2}K)

The results presented in this study shows that a thermal autofrettage process with a post heat treatment can induce compressive residual stresses in both the inner and outer walls of a cylinder. This can effectively eliminate the undesirable effect of the tensile residual stresses at the outer wall that is normally induced in a conventional autofrettage process. Compared to the earlier techniques such as shot peening or wire winding techniques, the present method presents the following advantages:

- The mode of inducing the residual stresses using thermally generated stresses ensures uniformity of in the compressive residual stress field at the outer wall. The method is also least likely to cause changes in the surface roughness of the outer wall. However, the process may need to be controlled to prevent oxidation during the quenching processes.

- Unlike the case in the wire winding technique present method is a mass controlled process with no increase in the weight of the cylinder.

4.6 Conclusion

In this study, an FEM based analysis of thermal autofrettage process with heat treatment was carried out. Here, the thick-walled cylinder was first thermally autofrettaged and then reloaded with a temperature gradient in which the outer wall of the cylinder was heated above the upper critical temperature at 725 °C while the inner wall was kept at a lower temperature 665 °C. This caused austenization only at vicinity of the outer wall. Finally, the cylinder was cooled to room temperature by simultaneously quenching from both the inner and outer walls. The cooling process induced beneficial compressive residual stresses at both the inner and outer walls of the cylinder. The FEM analysis was carried out in commercial package ABAQUS®. The FEM model considered temperature and microstructure dependent material properties. Phase transformation kinetics was incorporated in the model through user defined subroutine UMATHT to predict the microstructure in the thick-walled cylinder. The results show that the new technique can induce beneficial residual stresses at both inner and outer walls of the cylinder. However, the technique results in some loss of the inner wall compressive residual stresses than that can be achieved with only thermal autofrettage, although very small. This loss increases with the increase in the rate of the cooling rate applied in the quenching process. Nevertheless, the process can be useful in some practical situations, for example improving the stress corrosion resistance of the cylinder. Compressive residual stresses cause closure of a surface crack and retards the crack growth that leads to longer fatigue life.

The new method also offers better advantages than earlier proposed techniques like shot peening or wire winding for reducing outer surface tensile residual stresses in an autofrettaged cylinder in the following ways:

- The compressive residual stress field induced by the present method is uniform
- The present method does not increase the weight of the cylinder.

Chapter 5

Development of a Thermal Autofrettage Setup to Generate Compressive Residual Stresses on the Surfaces of a Cylinder

5.1 Introduction

A novel technique for inducing compressive residual stresses at the outer wall of a thermally autofrettaged cylinder has been proposed and analyzed in Chapter 4. In the technique, the initially thermally autofrettaged thick-walled cylinder is subjected to a temperature gradient; the outer wall is heated above the lower critical temperature while maintaining the temperature of inner wall below it. The cylinder is then quenched after which residual stresses are induced that is compressive in the vicinity of the inner as well as the outer wall. This Chapter presents the development of an experimental setup to perform the proposed thermal autofrettage process and the post heat treatment procedure. The cylinder subjected to the procedure is inspected for the presence of residual stresses using two approaches— one based on the measurement of microhardness and another based on the measurement of the opening angle due to a radial cut in the heat treated autofrettaged cylinder. Based on measurements taken before autofrettage, after thermal autofrettage and after heat treatment of the autofrettaged specimens, the presence of residual stresses in the vicinity of the walls of the thermally autofrettaged cylinder is ascertained. The Chapter is organized as follows. Section 5.2 describes a preliminary FEM analysis carried out to simulate the experiment. Section 5.3 describes the construction and working of the experimental setup. Section 5.4 discusses the results of the experiment and Section 5.5 concludes the Chapter.

5.2 Details of FEM Analysis for Simulating Experiments

The thermal autofrettage specimen used in this study is a 60 mm long cylinder with inner radius 14 mm and outer radius 24 mm. The material of the cylinder is AH36 mild steel. The weight percentage of carbon in AH36 is 0.18%, which falls in the hypoeutectoid (carbon content less than 0.76%) variant of steel. This means that the microstructure of the sample may comprise four phases *viz*. proeutectoid ferrite, pearlite, bainite and martensite. The maximum possible volume fraction of proeutectoid ferrite calculated on the basis of the lever rule given by Eq. (4.3) is 78.9%. The temperature dependent mechanical properties of AH36 steel are taken from Zhang *et al*. [175] and the thermal properties of each microstructural constituent are based on [172]. The thermal properties of proeutectoid ferrite, pearlite and bainite are

considered identical. The property of the sample existent at a particular temperature is computed using the linear mixture law given in Eq. (4.12).

The autofrettage samples were prepared from a 60 mm long solid cylindrical block of diameter 48 mm by boring a concentric hole of 28 mm diameter. The samples were subjected to a full annealing process by heating at 745 ºC followed by furnace cooling for 30-32 hours. The full annealing was carried out to remove any prior residual stresses that could have been induced due to the machining during sample preparation [2]. The full annealing process carried out on the experimental samples was simulated in an axisymmetric FEM model similar to that shown in Fig. 4.3 to predict the initial microstructural state in the cylinder. The FEM analysis comprised two steps. The entire cylinder was assigned a temperature of 745 °C in the first step. In the second step, the cylinder was cooled down slowly till room temperature. This was simulated by assigning the following radiation boundary condition to the edges AB, BC, CD and DA:

$$q = \beta e_T \left(T_s^4 - T_\infty^4\right), \tag{5.1}$$

where q is the heat flux at the cylinder surfaces, T_s is the surface temperature, T_∞ = 20 °C is the ambient temperature at steady state, e_T is the thermal emissivity whose value was taken as 0.3 typical for steel [174] and β=5.67×10^{-8} W/m^2 is the Stefan-Boltzmann constant. At the end of the simulation, a 78.6% ferrite and 21.4% bainite was obtained, which was taken as the initial microstructure of the sample for subsequent analysis.

Based on the dimensions of the cylinder and material properties (mechanical, thermal and microstructural), a finite element method (FEM) analysis of thermal autofrettage analysis was carried out to identify the thermal autofrettage parameters. The procedure of the FEM analysis is similar to that already explained in Section 4.4. In essence, the axisymmetric model used in the analysis is shown in Fig. 4.1. The analysis consists of four successive steps comprising thermal loading, thermal unloading, thermal reloading and quenching. In the first three steps, the inner wall of the cylinder represented by AD is assigned a temperature T_a and the outer wall represented by BC is assigned the temperature T_b as shown in Fig. 4.1. In the quenching step, a convective heat transfer boundary condition is applied at the edges AD and BC to simulate simultaneous cooling from both the inner and outer walls as follows:

$$\begin{cases} q_a = h\left(T_a - T_\infty\right), \\ q_b = h\left(T_b - T_\infty\right), \end{cases} \tag{5.2}$$

where q_a, q_b are the heat fluxes at the inner and outer cylinder walls, respectively and h is the convective heat transfer coefficient of the quenchant.

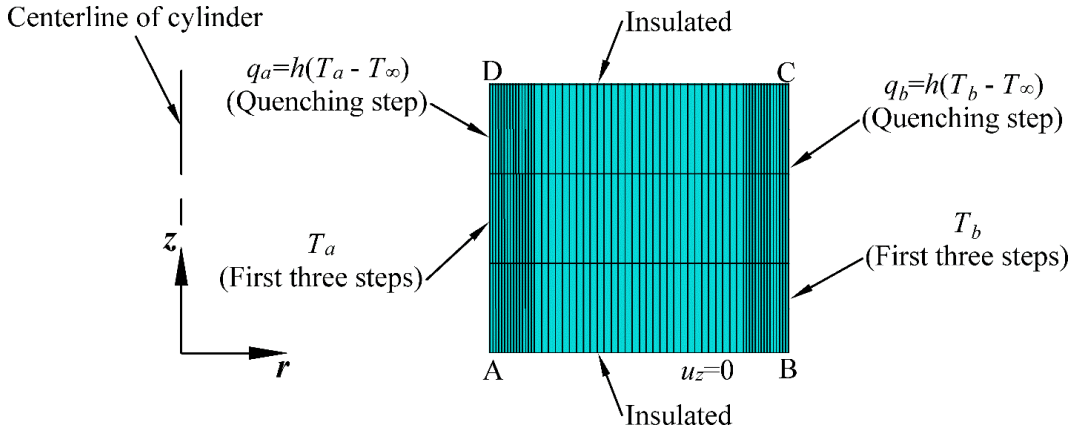

Figure 5.1 The meshed axisymmetric model with the boundary conditions

Based on the FEM analysis, the minimum temperature difference for initial yielding at the inner wall was 161 °C. The temperature difference for commencement of yielding at the outer wall was 180 °C. Beyond a temperature difference of 180 °C, the tensile residual stresses at the outer wall increased. The distribution of stresses after the loading step and that of the residual stresses after the unloading step due to a temperature difference of 180 °C (T_a = 20 °C and T_b= 200 °C) is shown in Fig. 5.2. Referring to Fig. 5.2(a), the cylinder comprises an inner plastic zone I from the inner wall to a radius of 14.5 mm and an outer elastic zone II up to the outer wall due to the elastic-plastic deformation caused by the thermal loading. After unloading, the residual stresses are induced in the cylinder as shown in Fig. 5.2(b). The maximum compressive hoop residual stress after the thermal autofrettage is 49 MPa and the tensile hoop residual stress at the outer wall is 0.24 MPa.

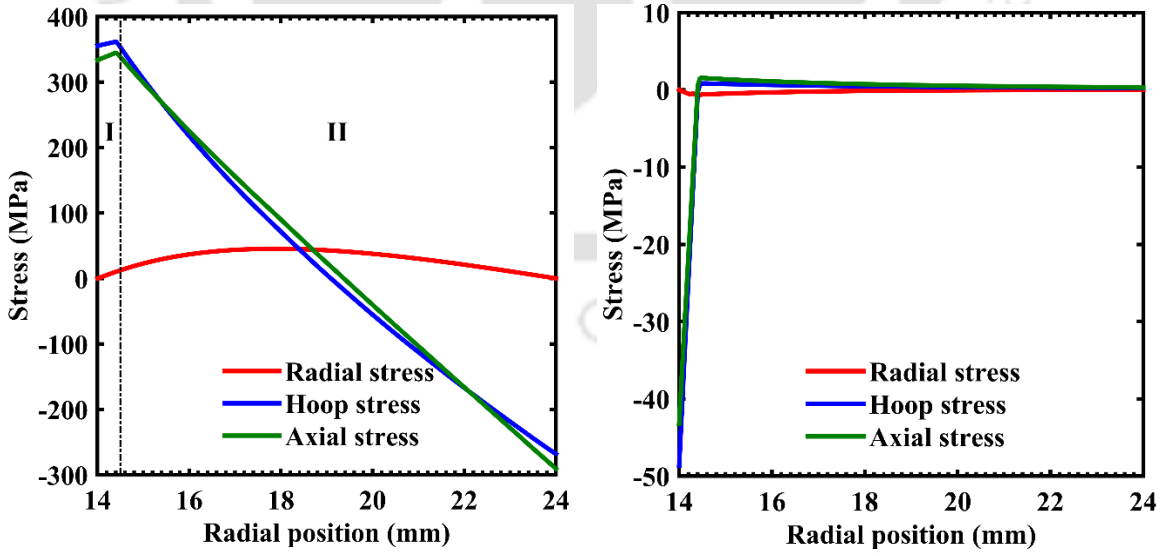

Figure 5.2 Distribution of (a) stresses after the loading step (T_a = 20 °C and T_b = 200 °C) and (b) residual stresses after the unloading step in AH36 steel cylinder with (T_a = T_b = 20 °C)

The thermally autofrettaged cylinder was again subjected to a temperature difference corresponding to an outer wall temperature greater than the lower critical temperature of AH36 (727 °C) and an inner wall temperature less than it. The temperature of the inner wall was decided by the criterion that the corresponding temperature gradient did not result in any additional yielding in the thermally autofrettaged cylinder. Thus, the outer wall of the thermally autofrettaged cylinder was subjected to a temperature of 735 °C. The minimum temperature of the inner wall that avoided additional yielding in the thermally autofrettaged cylinder came out to be 635 °C. After this, the inner and outer walls of the cylinder are subjected to the convection heat transfer boundary condition defined in Eq. (5.2) assuming a convective heat transfer coefficient of 2500 W/m^2.°C as per Ref. [176]. The distribution of stresses after the thermal reloading step is shown in Fig. 5.3(a) where no yielding takes place. The distribution of residual stresses in the cylinder after the final quenching step based on the FEM analysis is shown in Fig. 5.3(b). Due to the yielding in the vicinity of the outer wall during the quenching step, the cylinder comprises an inner elastic zone I and an outer plastic zone II. The position of the elastic-plastic interface at 23.4 mm is shown by dashed lines. The maximum compressive residual hoop stress at the inner wall after the quenching step slightly decreases to 48.6 MPa while that at the outer wall is 152.51 MPa.

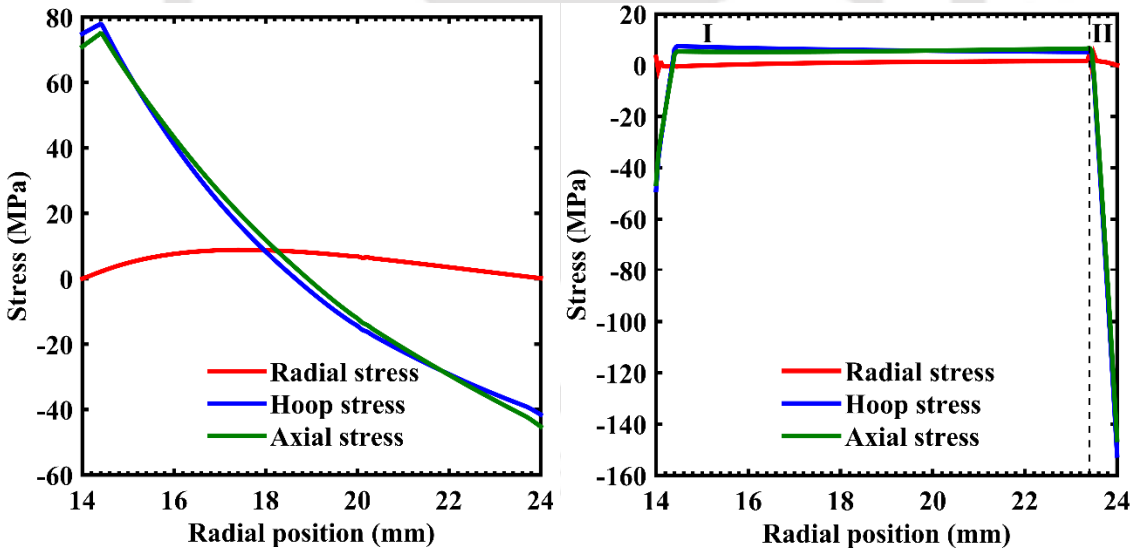

Figure 5.3 Distribution of (a) stresses after reloading step with T_a=635 °C and T_b=735 °C and (b) residual stresses after the quenching step

5.3 Details of the Experimental Setup

This section presents the experimental setup developed to implement the heat treatment coupled thermal autofrettage process. The experimental setup for carrying out the heat treatment coupled thermal autofrettage process mainly consists of three units. These are the

heating arrangement, the cooling arrangement and the control system. The heating arrangement is responsible for subjecting the specimen to the required temperature gradient during the thermal autofrettage process and heating the autofrettaged specimen to high temperature above the lower critical temperature, which is about 727 °C for a typical steel. The cooling arrangement maintains the temperature of the inner wall of the autofrettage specimen to achieve the desired temperature gradient. The control system regulates the temperature of the outer wall of the cylinder by switching on or off the power supply to the heating arrangement. The detailed description follows.

5.3.1 Heating Arrangement

The cylinder was heated by using a direct current (DC) powered zero volt switching (ZVS) driver induction heater (make Geekcreit®). The rated power of the device was 1000 W with a recommended supply of 20 A and a DC voltage of 36 V for continuous operation. The description of the device is available in [177]. The device converts the given input DC voltage into high frequency (60 to 80 kHz) oscillating pulsed DC, which is obtained across a helical copper tube coil. The oscillating voltage of the copper coil generates a varying magnetic field in the coil. When the steel cylinder is inserted and aligned concentric to the axis of the helix, an electromotive force (EMF) is induced in the steel cylinder due to Faraday's law of electromagnetic induction. This in turn generates eddy current in the cylinder and the cylinder is heated due to its electrical resistance. Induction heating ensures better efficiency of the energy since the heat is generated only in the cylinder material. This method also automatically ensures that induced eddy current is concentrated at the outer surface of the cylinder as a result of the skin effect [178] and hence the outer wall is heated more rapidly than the rest of the cylinder. Skin effect is a phenomenon in which the alternating current (AC) flowing in a conductor tends to concentrate at the surface of the conductor at high frequencies. The high frequency pulsed DC induced in the autofrettage cylinder specimen is also similar to an AC and exhibits a similar phenomenon and assists in setting up the required temperature gradient across the wall thickness in the thermal autofrettage process. This heating mechanism is more effective for materials like steel or cast iron. It is less effective for materials like copper or aluminum due to their relatively low resistance.

The ZVS driver was powered by a 24 V switch DC supply of rated power 480 W (24 V, 20 A). The supply voltage of 480 W, lesser than the maximum power rating of 720 W recommended for the ZVS driver, ensures a significant margin of the factor of safety for the circuit of the ZVS driver. The cylinder to be autofrettaged was first mounted in the base of a

fixture casted from mortar, which contained a through hole and a counter bored profile for seating of the cylinder. The other end of the cylinder was covered with a mortar-casted cap. The cap also had a through-hole in line with that of the base and the bore of the cylinder. The thermocouple to be attached to the outer wall of the cylinder was inserted through a small passage in the cap. The gap surrounding the base, cap and the outer wall of the cylinder were enclosed and filled with glass wool for insulation. This assemblage and the ZVS driver induction heater constitute the heating arrangement. The schematic of the entire assemblage is shown in Fig. 5.4 and the photograph of the actual setup is shown in Fig. 5.5.

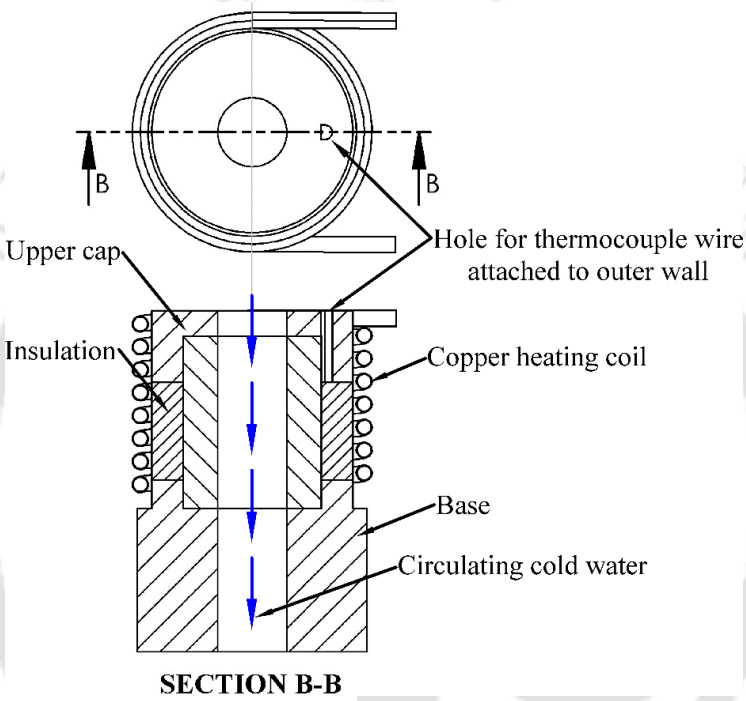

Figure 5.4 Schematic of heating arrangement

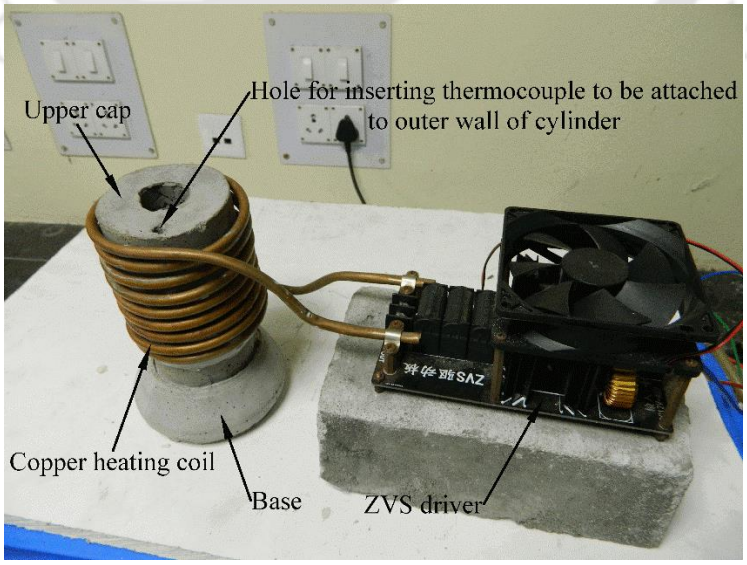

Figure 5.5 Photograph of the heating arrangement

5.3.2 Cooling Arrangement

The cooling arrangement comprised a system for circulation of cold water for cooling the inner wall of the cylinder and maintaining the temperature gradient across the wall of the cylinder. The cold water was pumped from a reservoir and flows through the hole passage as shown in Fig. 5.4. The pump used in the study was a submersible pump (make LAZER) with rated power of 18 W. The pump was submerged in a plastic tank reservoir and cooled the inner wall of the autofrettage specimen. After cooling the inner wall of the cylinder, the water was again collected in the same reservoir. The schematic of the heating and the cooling arrangements is shown in Fig 5.6.

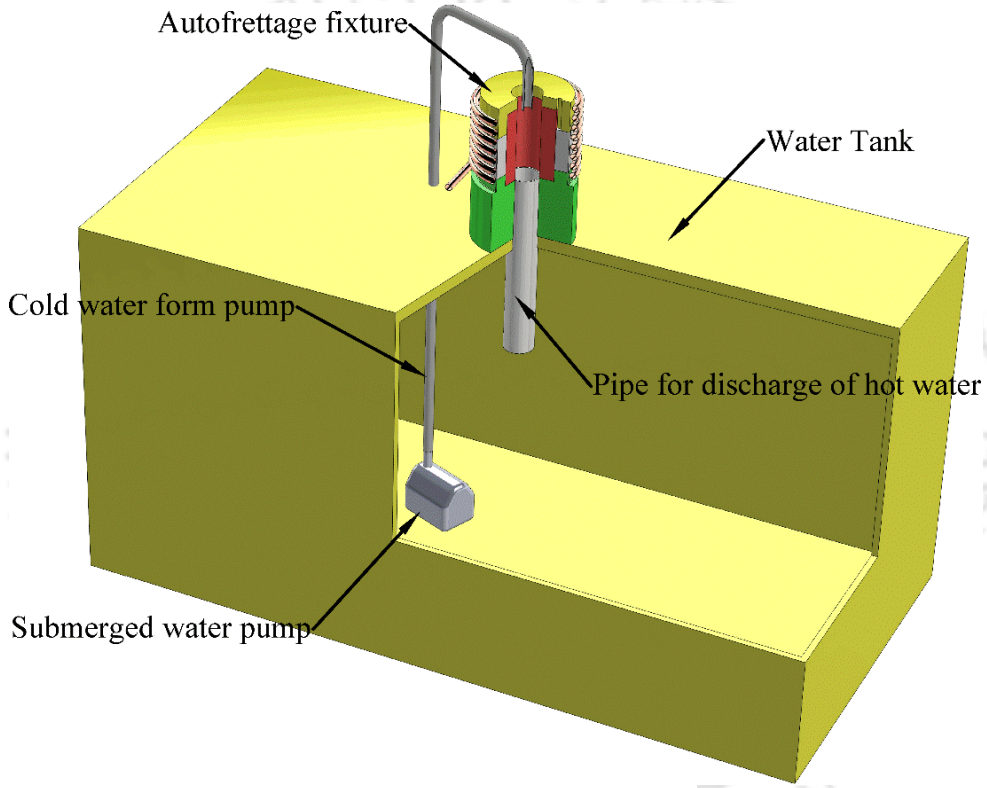

Figure 5.6 Schematic of the heating and cooling arrangements

5.3.3 Control System

The control system comprised arrangements for measuring the wall temperatures of the cylinder and controlling the amount of heat to be supplied to the cylinder depending on the required temperature gradient. The temperatures of the inner and outer walls of the cylinder were measured using K type thermocouples. The thermocouples were attached to the inner and outer walls of the cylinder through capacitive welding using the thermocouple attachment equipment Dyna Weld (make FABRICA). A thermocouple welded autofrettage specimen is shown in Fig. 5.7.

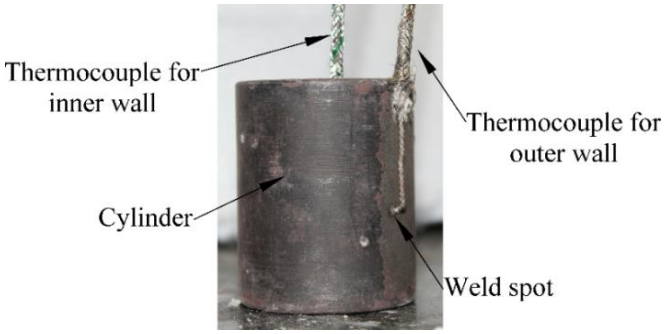

Figure 5.7 Thermocouple welded thermal autofrettage specimen

The signal obtained from each thermocouple was processed using the MAX6675 module (make Maxim Integrated). The MAX6675 module is a circuit that converts the analog voltage signal from the thermocouple into digital signals. The digital information was converted into temperature readings by interfacing the MAX6675 module with a microcontroller. The MAX6675 module provides a resolution of 0.25 °C with a measurable temperature range of 0 °C to 1024 °C. The datasheet for the MAX6675 module is provided in [179]. The microcontroller used in this study for interfacing with the MAX6675 was the Arduino MEGA 2560 microcontroller (make Arduino). The Arduino MEGA has 54 digital pins that can be set to either input or output mode to receive or transmit signals, respectively. The microcontroller is shown in Fig. 5.8(a). The MAX6675 module has five pins designated as GND, VCC, SCK, CS and SO as shown in Fig. 5.8(b). The GND and VCC are connected to the negative and positive ends, respectively, of a 5 V DC supply. The remaining three pins must be connected to any three digital pins of the Arduino microcontroller. For a particular MAX6675 module, the pins SO, CS and SCK were connected to the digital pins 5,6 and 7, respectively, of the microcontroller. Similarly, the pins SO, CS and SCK of the other MAX6675 module were connected to the digital pins 9, 10 and 11, respectively.

The absolute value of the difference between the measured temperatures of the inner and outer walls was computed and checked continuously. When the temperature difference exceeded the desired temperature difference during the thermal autofrettage loading step, the ZVS driver got turned off. When the temperature difference was lower than the desired temperature difference, the ZVS driver got turned on again. This switching action was achieved by using a relay. A relay is a device that comprises two circuits *viz.*, a trigger circuit and a load circuit. The load circuit is activated or deactivated by a current that flows in the trigger circuit. The relay used in this study was a solid-state relay (SSR) made by DMWD and is as shown in Fig. 5.8(c). The relay was controlled by a 5 V output signal from a digital pin of the Arduino microcontroller. The relay has two pairs of pins each for the input circuit and the output circuit. The pins designated "–" and "+" in the input circuit are connected to the GND pin and pin

number 3, respectively, of the Arduino microcontroller. After the pin connections were completed, the Arduino microcontroller was connected to a computer and uploaded with the program that contained instructions for measuring the temperature with the MAX6675 module and the feedback control with the relay. The Arduino program is provided in Appendix C. The arrangement of all the components in the control system is shown in Fig. 5.9. The complete setup of all the three modules is shown in Fig 5.10.

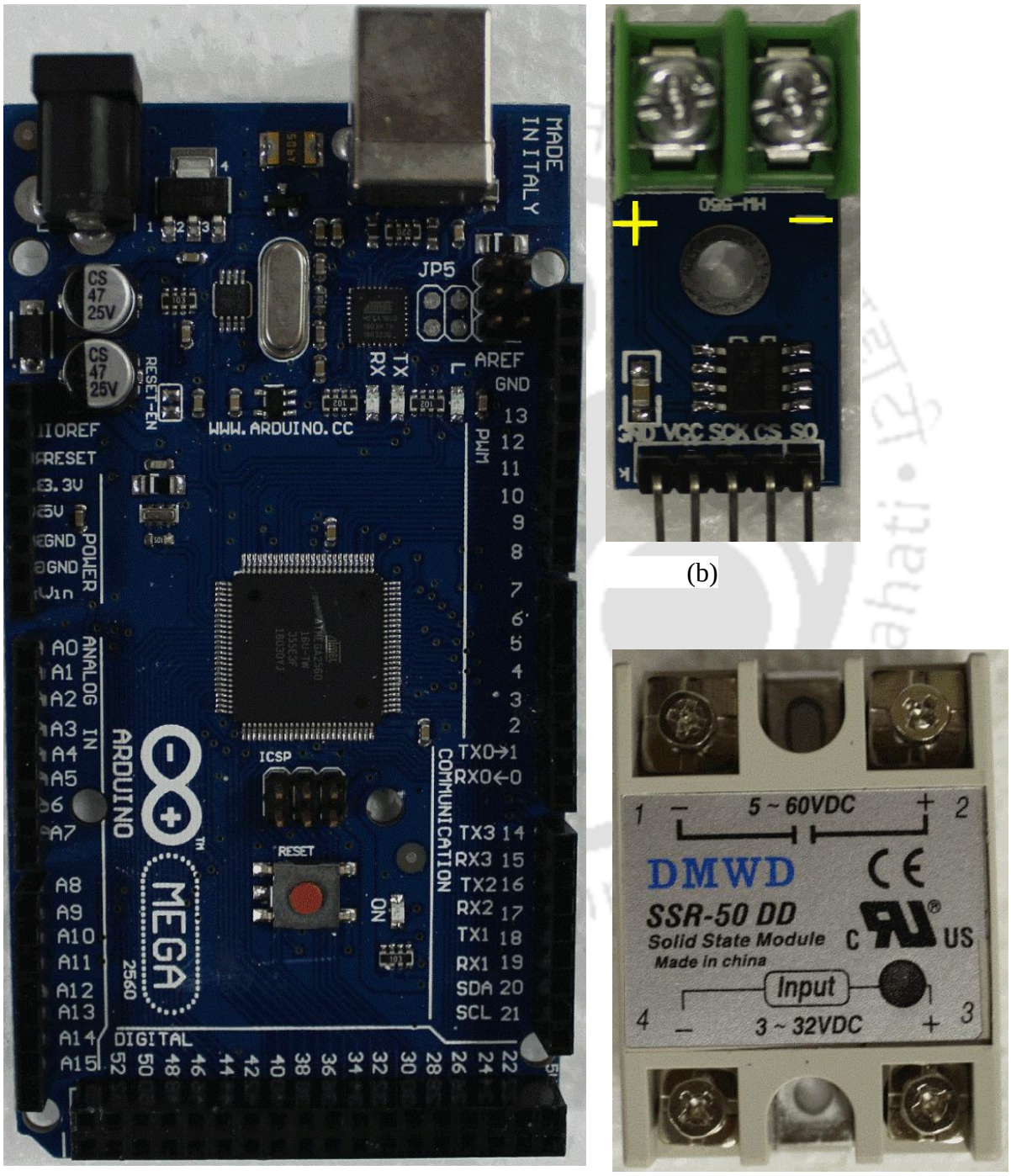

(a) (b) (c)

Figure 5.8 Pin configuration of the (a) Arduino microcontroller (b) MAX6675 module and (c) relay

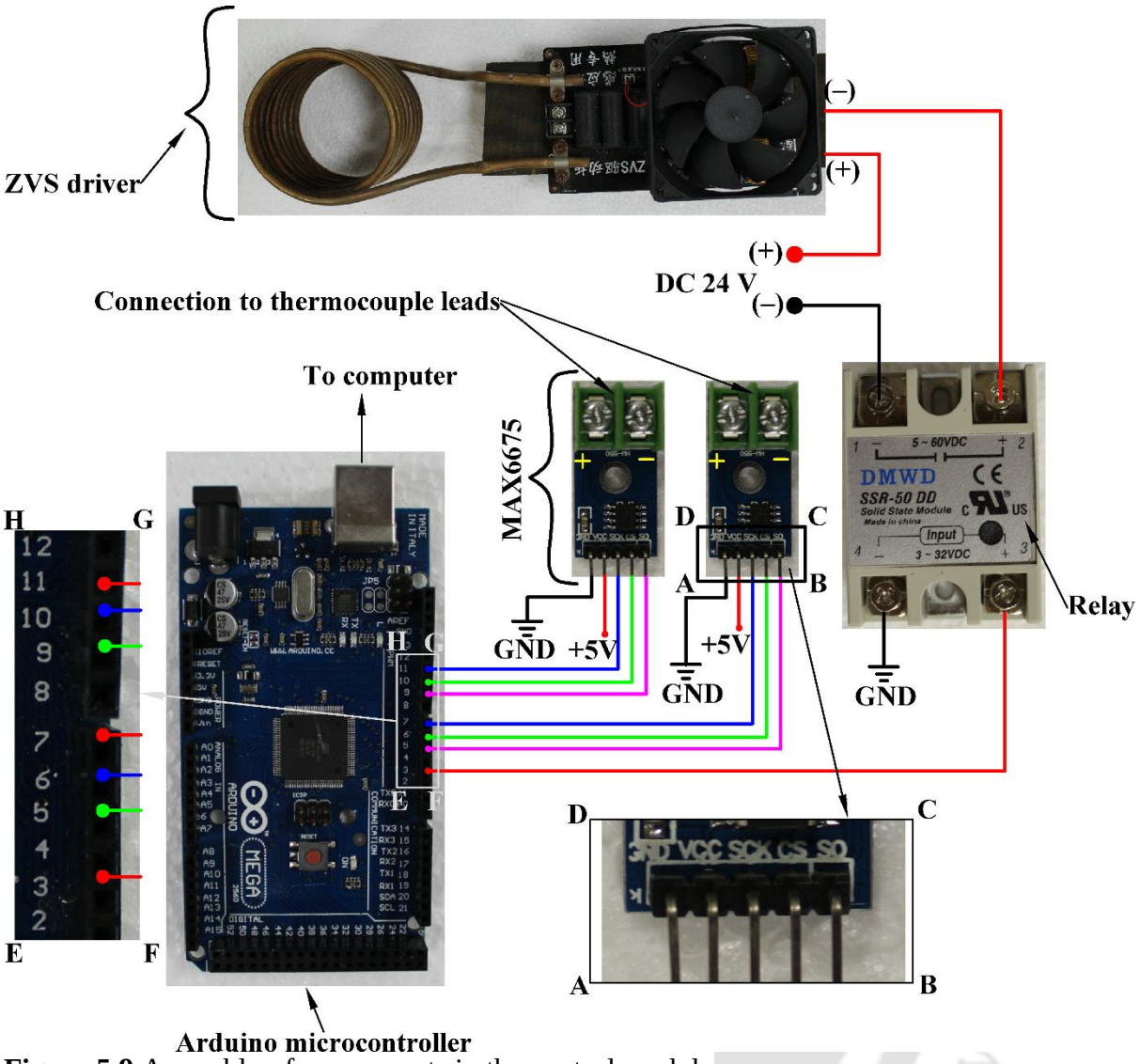

Figure 5.9 Assembly of components in the control module

Using the experimental setup, the initial thermal autofrettage was carried out using a temperature gradient of 180 ºC where the temperatures of outer and inner walls are 220 ºC and 40 ºC, respectively. For achieving this temperature difference, cold water was circulated through the bore of the cylinder while it was being heated. When the temperature difference exceeded the desired value, the ZVS driver induction heater was switched off to stop the heating. When the temperature difference was less than the desired value, the relay switched on the ZVS driver again. The temperature readings of the inner and outer wall from the thermocouples were taken at a frequency of 1 second using the Arduino microcontroller. After the thermal autofrettage, the cylinder was again subjected to an outer wall temperature of 735 ºC and an inner wall temperature of 635 ºC. This temperature gradient was maintained for one minute. After this, the cylinder was quenched to room temperature. Quenching was carried out simultaneously from both the inner and outer wall using cold water.

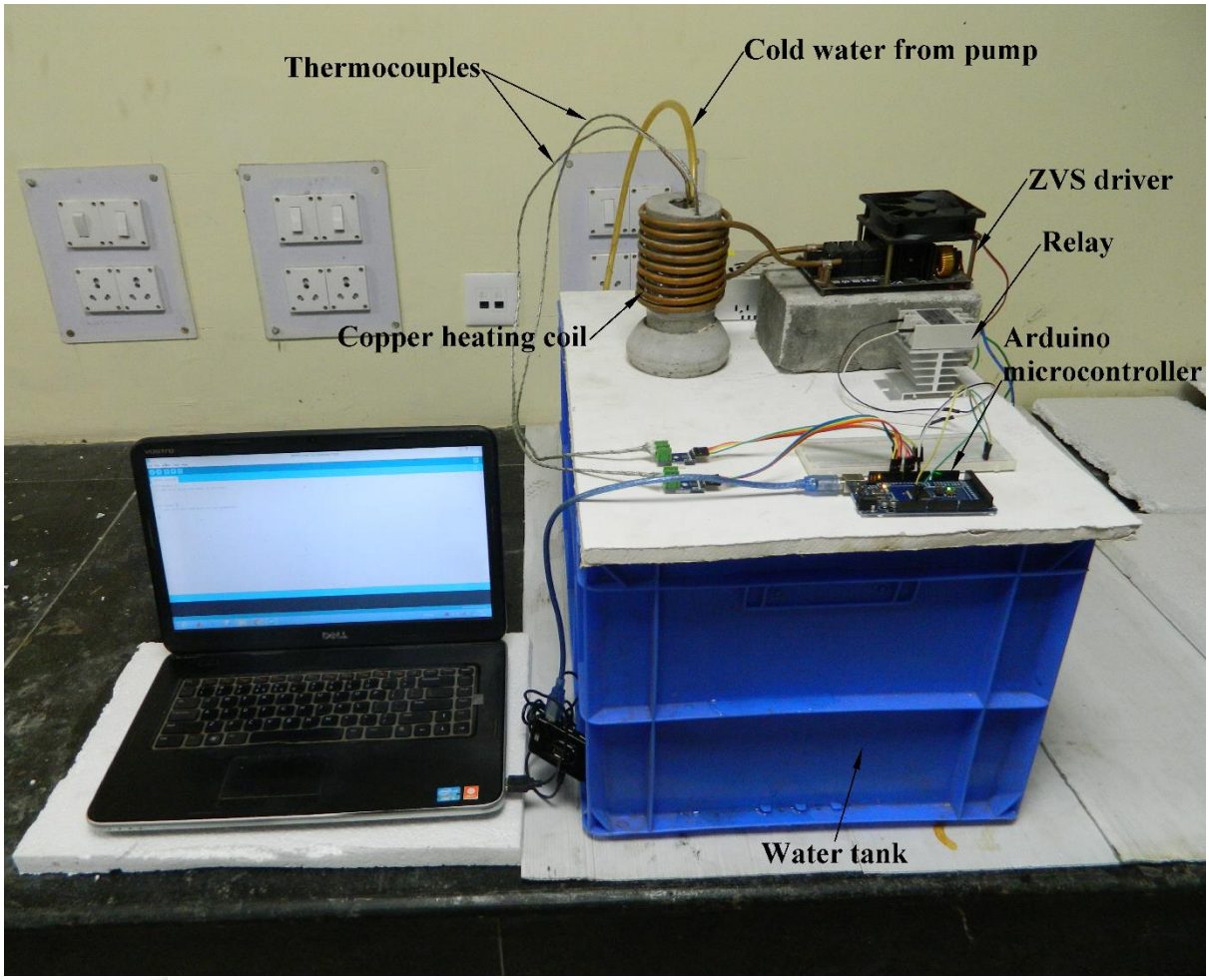

Figure 5.10 A photograph of the complete experimental setup for the heat treatment coupled thermal autofrettage process

5.4 Results and Discussion

This section presents the results of the thermal autofrettage and subsequent heat treatment on the experimental specimen (dimensions and material specified in Section 5.2). The assessment of the residual stress is based on two techniques— measurement of the microhardness of the inner and outer walls of the cylinder and measurement of the opening angle due to a radial cut in the cylinder. The results are explained in the following subsections.

5.4.1 Confirmation of Residual Stresses from Microhardness Test

Residual stresses have an impact on the surface microhardness. Researchers have used microhardness test to infer the existence of residual stresses. Pharr *et al*. (1994) reported that the surface hardness decreases in the presence of tensile residual stresses and increases in the presence of compressive residual stresses. Tosha (2002) observed that the hardness increases due to the presence of compressive residual stresses induced by shot peening. Tosha (2002) also showed that the hardness of the concave surface increases due to compressive residual

stresses and that of the convex surface decrease due to tensile residual stresses in the bent sheet. Kamal *et al*. [15] investigated the impact of residual stresses on surface hardness experimentally in the Vickers indentation test and observed similar results. In this work, microhardness was measured at the inner and outer wall on three samples viz., (i) non-autofrettaged cylinder, (ii) thermally autofrettaged cylinder and (iii) heat treated thermally autofrettaged cylinder. The measurement was carried out on a Vickers microhardness tester with 500 gf load. The distributions of the microhardness at the inner wall and outer wall in the three samples at 10 random locations are shown in Fig. 5.11(a) and 5.11(b), respectively.

Referring to Fig. 5.11(a), the microhardness of the inner wall after the heat treatment is more than that of the non-autofrettaged cylinder thanks to the presence of compressive residual stresses. However, autofrettaged cylinder without heat treatment has the greatest microhardness at the inner wall. This suggests that the heat treatment of the autofrettaged cylinder reduces the compressive stresses at the inner wall, albeit only slightly. This observation is in accordance with the computational results presented in Chapter 4. Referring to Fig. 5.11(b), the microhardness of the outer wall after thermal autofrettage is the lowest due to the induced tensile residual stresses at the outer wall. The microhardness increases after subjecting the thermally autofrettaged cylinder to the subsequent heat treatment process. This is due to the induced compressive residual stresses at the outer wall. This demonstrates the presence of tensile residual stresses at the outer wall of a thermally autofrettaged cylinder and compressive residual stress after the heat treatment procedure.

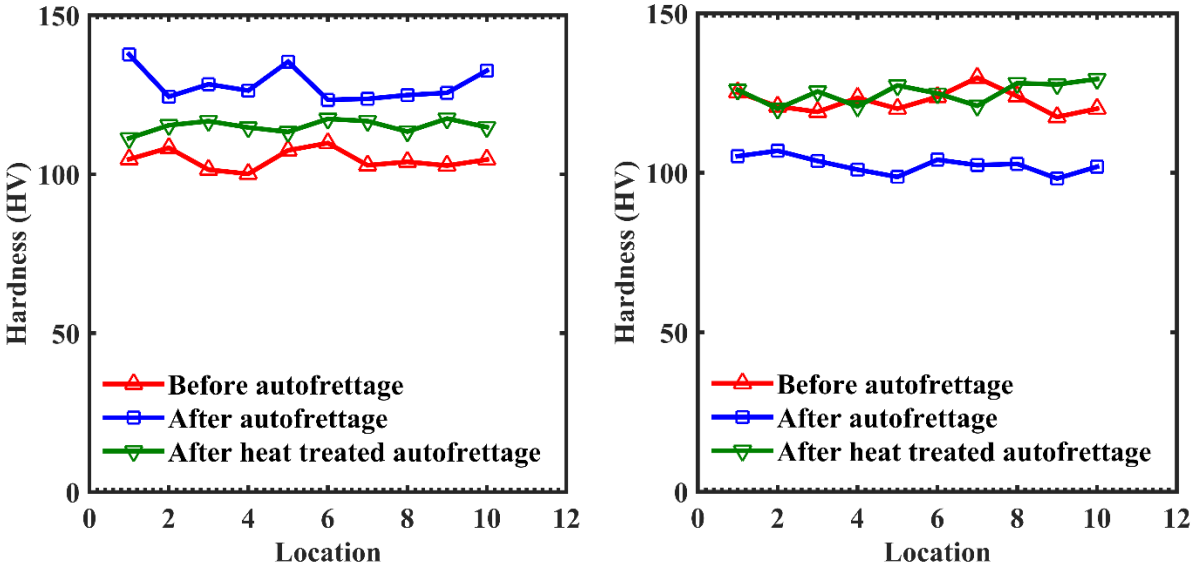

Figure 5.11 Variation of microhardness at the (a) inner wall and (b) outer wall measured before the autofrettage, after the thermal autofrettage and after the heat treatment of the autofrettaged specimens. Locations are random on the specimen

5.4.2 Demonstration of Residual Stresses by Using Split-Ring Method

The split-ring technique is one of the simplest methods for identifying the presence of residual stresses in a thick-walled cylinder. The method has been explained in Section 2.4. For the study in the present chapter, the measurement of opening angle was carried out in two types of cylinder samples viz. autofrettaged and post heat treated autofrettaged cylinder to inspect the presence of residual stresses. For experimental purpose, each sample was cut radially using power hacksaw and the measurement of opening angle was carried out using profile projector. The experimentally measured opening angles were compared with those obtained from FEM simulations.

A generalized plain strain two-dimensional model is developed with half of the circular section of the cylinder as shown in Fig. 5.12 with r and θ representing the radial and angular coordinates, respectively. The semicircular section of the cylinder is chosen for the split ring method on the basis that when the radial cut is made along the line AB, bending takes place due to release of residual stresses. The FEM analysis for the split ring method in the thermally autofrettaged cylinder is divided into three steps— thermal loading step, thermal unloading step and splitting step. A condition of zero angular displacement of the entire semicircular section was set as the initial condition of the entire analysis. In the thermal loading and unloading steps, the required temperature boundary conditions are assigned to the arcs AD (inner wall) and BC (outer wall) analogous to that shown in Fig. 5.1. In the splitting step, a new boundary condition of zero angular displacement was applied only at the edge CD and the initial boundary condition was removed. This means that all parts of the ABCD except the edge CD can displace. At the end of the splitting step, the opening angle is obtained. The activation and deactivation of the boundary and initial conditions is tabulated in Table 5.1. The angular displacement is represented by u_θ. Similarly, the FEM analysis for the split ring method in the heat treated thermally autofrettaged cylinder is carried out with two additional steps viz., thermal reloading step and quenching step. The activation and deactivation of the boundary and initial conditions in this cylinder are tabulated in Table 5.2.

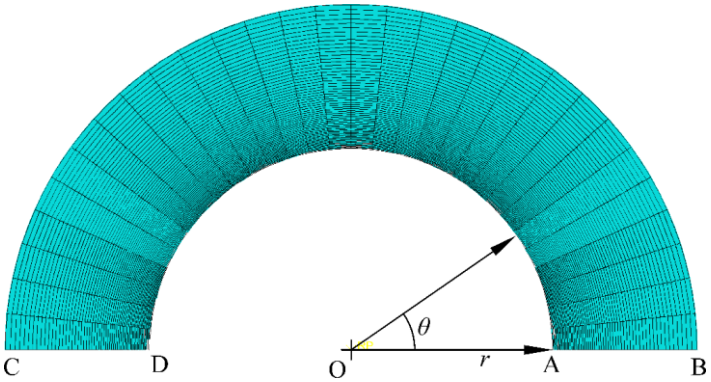

Figure 5. 12 Two-dimensional generalized plane strain model for analysis of split ring

Table 5.1 Activation and deactivation of the boundary and initial conditions for split ring method on the thermally autofrettaged cylinder

Boundary condition	Analysis steps		
	Load	Unload	Split ring
$u_\theta = 0$ on AB	Active	Active	Inactive
$u_\theta = 0$ on CD	Active	Active	Active
T_a on AD	Active	Active	Inactive
T_b on BC	Active	Inactive	–
$T_b = T_a$ on BC	–	Active	Inactive

Table 5.2 Activation and deactivation of the boundary and initial conditions for the split ring method on the heat treated autofrettaged cylinder

Boundary condition	Analysis steps				
	Load	Unload	Reload	Quench	Split ring
$u_\theta = 0$ on AB	Active	Active	Active	Active	Inactive
$u_\theta = 0$ on CD	Active	Active	Active	Active	Active
T_a on AD	Active	Active	Inactive	–	–
T_b on BC	Active	Inactive	–	–	–
$T_b = T_a$ on BC	–	Active	Inactive	–	–
$(T_a < Ac_1)$ on AD	–	–	Active	Inactive	–
$(T_b > Ac_1)$ on BC	–	–	Active	Inactive	–

The comparison of the opening angles obtained from the experiments and FEM simulations is shown in Table 5.3. The experimentally observed opening angle after the thermal autofrettage step matches well with the that obtained from the FEM simulation with an error of about 12%. The final configuration of the half section of the cylinder obtained from the FEM analysis is shown in Fig. 5.13. For the heat treated sample, the induced residual stresses are compressive at the inner as well as outer wall. The moment generated due to the release of the compressive stresses at both the inner and outer wall acts to close the faces where the radial cut was made. The closure of the cut faces caused jamming in the blade of the power saw when the cut was being made. When the cut was completed, the cut faces were found to be almost

parallel to each other with almost zero inclination (0.1°) between each other. The final configuration of the half section of the cylinder obtained from the FEM model of the heat treated thermally autofrettaged cylinder is shown in Fig. 5.14. It is observed that the opening angle is negative. This is expected as compressive residual stress causes closure of crack surfaces [182]. However, this is not physically possible as it would mean an overlapping of the faces along AB where the radial cut was made. Hence, the FEM opening angle is assumed as zero. This is in accordance with the mathematical aspect of the effect of compressive residual stress on a crack explained by Perl and Arone [183]. According to them, the opening mode (mode I) stress intensity factor $(K_I)_A$ of a crack due to a compressive residual stress field is negative but is assigned a zero value because a negative value would mean overlapping of the crack faces that is not possible [183].

Table 5.3 Comparison of experimental opening angle with FEM opening angle

Experimental opening angle (°)		FEM opening angle (°)	
After autofrettage	After heat treatment of autofrettaged cylinder	After autofrettage	After heat treatment of autofrettaged cylinder
3	0.1	2.63	0

The distributions of residual stresses in the thermally autofrettaged cylinder before and after conducting the split ring test are shown in Fig. 5.15. Referring to Fig. 5.15(a), the maximum compressive hoop residual stress at the inner wall after thermal autofrettage is 35.2 MPa and the tensile hoop residual stress at the outer wall is 0.2 MPa. Figure 5.15(b) shows that after splitting, the maximum compressive residual stress at the inner wall has reduced to 32.41 MPa and tensile residual stress at the outer wall has become compressive with a magnitude of 0.76 MPa. This is due to relaxation of the residual stresses throughout the cylinder including the compressive hoop residual stress at the inner wall and tensile hoop residual stresses at the outer wall. The redistribution of stresses also causes distortion in the geometry providing the opening angle.

The distributions of residual stresses in the heat treated thermally autofrettaged cylinder before and after conducting the split ring test are shown in Fig. 5.16. The compressive hoop residual stresses at the inner wall and the outer wall after the heat treatment of the cylinder are 30.14 MPa and 140 MPa, respectively as shown in Fig. 5.16(a). After the split ring test, the compressive hoop residual stress at the inner wall increases to 41.08 MPa and that at outer wall decreases to 132.76 MPa as shown in Fig. 5.16(b). This is also due to relaxation of the induced residual stresses in the cylinder, providing an opening angle. The numerical values of the hoop residual stresses are summarized in Table 5.4.

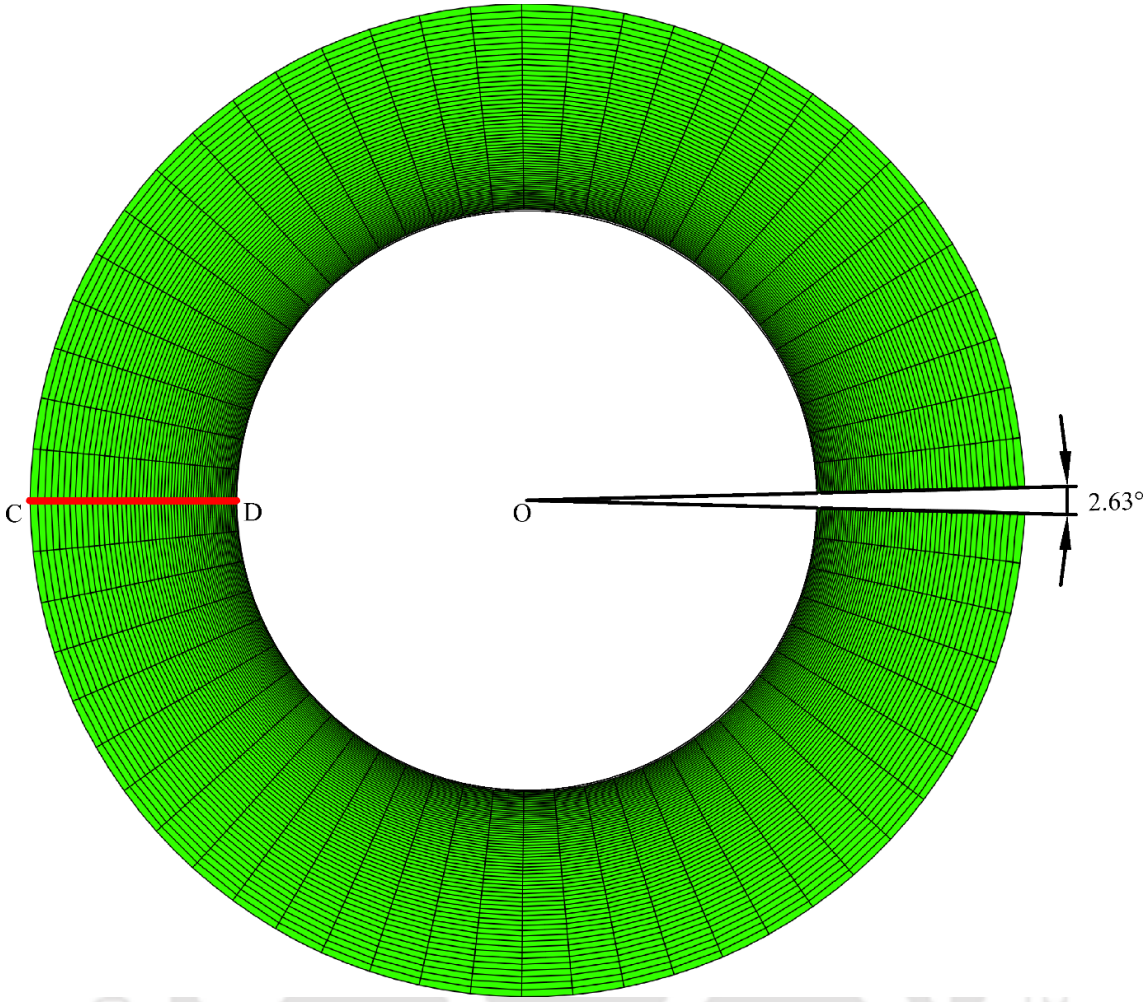

Figure 5.13 Opening angle obtained after the splitting in the FEM model of the thermally autofrettaged cylinder

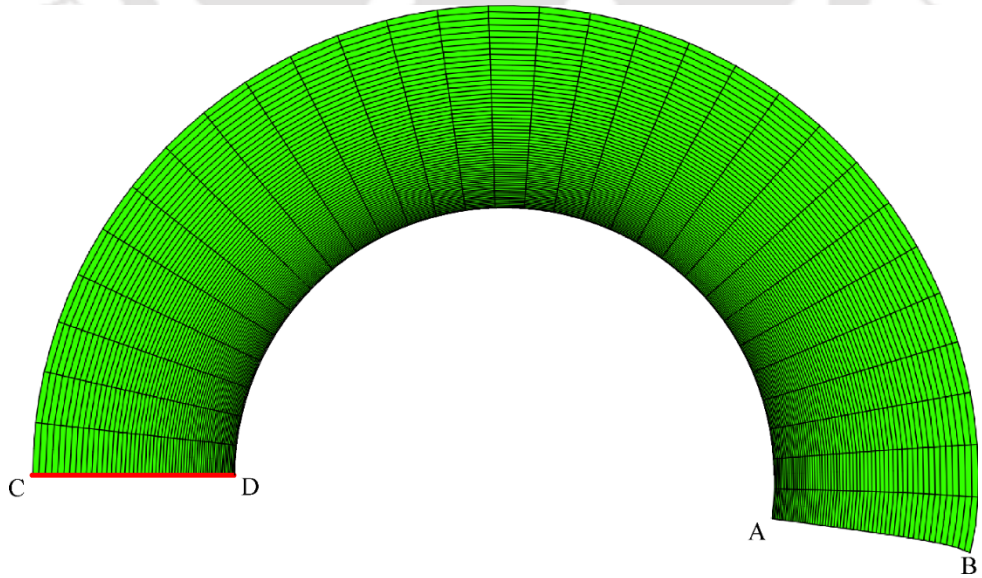

Figure 5.14 Opening angle obtained after the splitting step in FEM model of the heat treated thermally autofrettaged cylinder

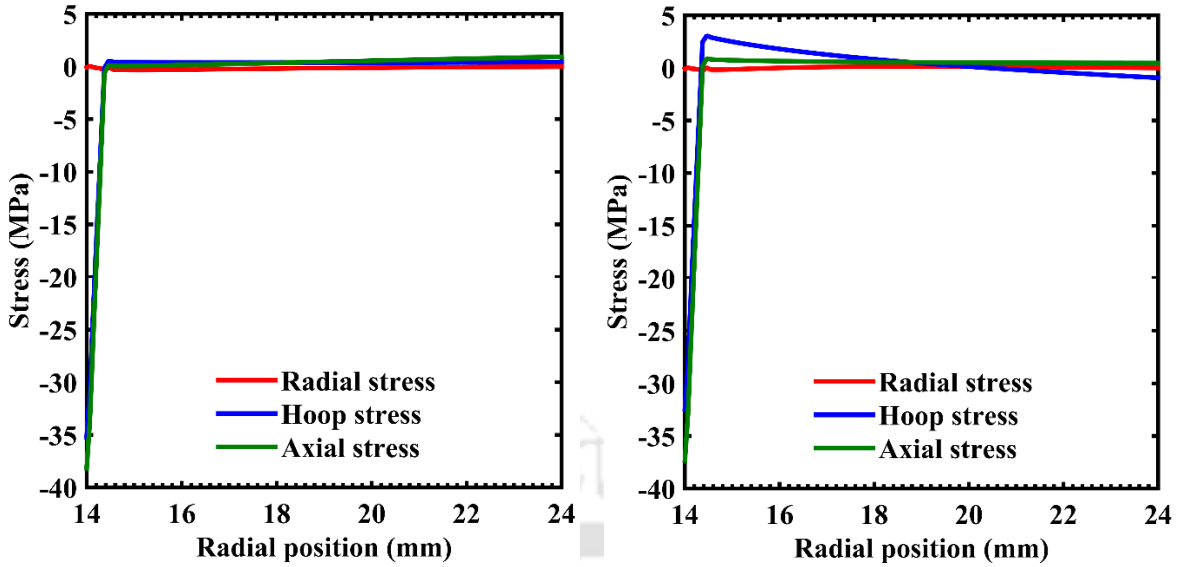

Figure 5.15 Distribution of residual stresses in the thermally autofrettaged cylinder (a) before the split ring test and (b) after the split ring test.

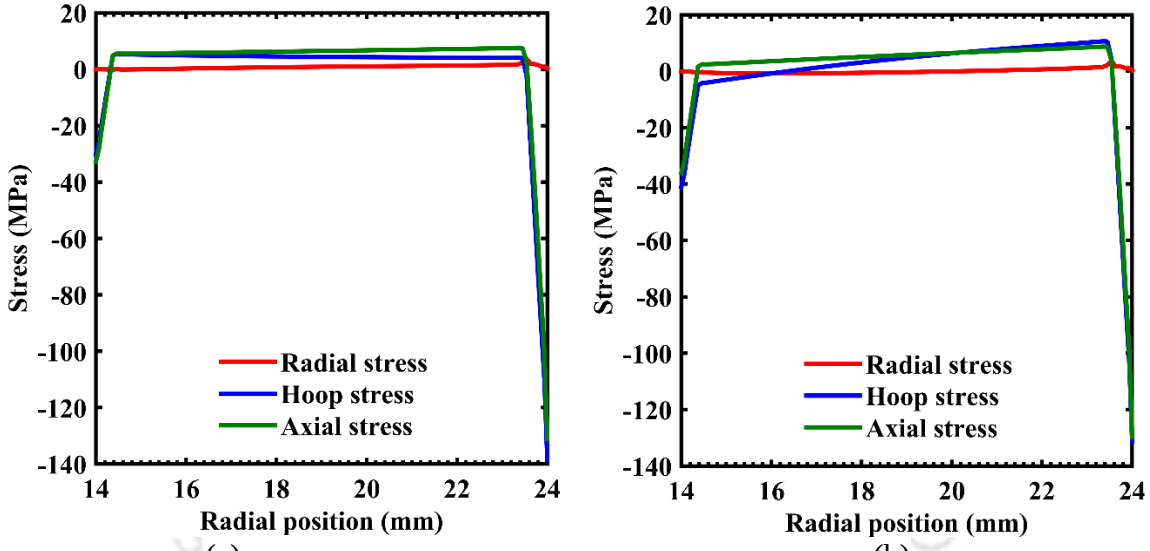

Figure 5.16 Distribution of residual stresses in the heat treated thermally autofrettaged cylinder (a) before the split ring test and (b) after the split ring test

Table 5.4 Hoop residual stress at the inner and outer wall in the autofrettaged cylinder and Heat treated autofrettaged cylinder before and after the FEM split-ring test

Location	Hoop residual stress (MPa)			
	Autofrettaged cylinder		Heat treated autofrettaged cylinder	
	Before splitting	After splitting	Before splitting	After splitting
Inner wall	–35.2	–32.41	–30.14	–41.08
Outer wall	0.2	–0.76	–140	–132.76

5.5 Conclusion

In this work, thermal autofrettage of thick-walled cylinder coupled with heat treatment was carried out experimentally on thick-walled cylinder made of AH36 mild steel. The construction and working of the experimental setup are first explained in detail. It consists of three modules—heating arrangement, cooling arrangement and control system. The measurement of the temperature of the inner wall and outer wall was carried out using a K type thermocouple and MAX6675 module interfaced with an Arduino microcontroller. The temperature gradient was controlled by the switching action of a relay also implemented the Arduino microcontroller. The setup was simple and inexpensive, providing an economic edge to thermal autofrettage. The presence of residual stress in the cylinder after thermal autofrettage and heat treatment was inspected by measuring the microhardness of the inner and outer wall of the cylinder. The measurement was carried out in three samples— non-autofrettaged cylinder, thermally autofrettaged cylinder and heat treated thermally autofrettaged cylinder. The outer wall microhardness of the cylinder after thermal autofrettage was the lowest due to induced tensile residual stresses. It increased after subjecting the thermally autofrettaged cylinder to the subsequent heat treatment process due to induced compressive residual stresses. The inner wall microhardness of thermally autofrettaged cylinder was greater than that of non-autofrettaged cylinder due to presence of compressive residual stresses. The heat treatment slightly reduced the compressive residual stress at the inner wall. This was reflected by a slight reduction of the inner wall microhardness of the thermally autofrettaged cylinder after heat treatment.

A finite element method (FEM) technique was also presented to predict the opening angle due to the release of moment locked generated by the residual stresses in an autofrettaged cylinder. This was validated with experimentally measured angles. The FEM predicted opening angle was in good agreement with the experimentally measured values. The variation of the hoop residual stress at the inner and outer wall in the autofrettaged cylinder and heat treated autofrettaged cylinder after the split-ring test was also analyzed. The phenomenon of stress-relaxation after the cut is clearly depicted, which is responsible for producing an opening angle.

Chapter 6

Heat treatment Design of Hydraulically Autofrettaged Cylinder

6.1 Introduction

A novel heat treatment procedure for inducing compressive residual stresses at the outer wall of a thermally autofrettaged cylinder has been proposed and analyzed in Chapter 4. In the process, the outer wall of the autofrettaged cylinder is locally austenized by heating above the lower critical temperature. The inner wall is maintained at such a temperature that the resulting temperature difference does not cause additional plastic deformation in the cylinder. The cylinder is then quenched subsequently by cooling from both walls to induce compressive residual stresses at the outer wall. Although the method was proposed for a thermally autofrettaged cylinder, it can be applied to any autofrettaged cylinder, be it through hydraulic, swage, explosive or rotational route. This chapter investigates the applicability of the heat treatment procedure in a hydraulic autofrettaged cylinder. An FEM analysis is carried out using a commercial package ABAQUS®. The mechanical and thermal properties of steel alloy AISI 1080 as a function of microstructure and temperature are incorporated in subroutine UMATHT. The rest of the article is ordered as follows. Section 6.2 presents a background of hydraulic autofrettage and the concept of the heat treatment design. Section 6.3 describes the details of the FEM analysis. Section 6.4 presents the detailed procedure for the design of heat treatment of the hydraulic autofrettaged cylinder. Section 6.5 presents the results of the FEM analysis and Section 6.6 concludes the paper.

6.2 Concept of Hydraulic Autofrettage and the Proposed Design of Heat Treatment

In hydraulic autofrettage, the initial plastic deformation of the cylindrical or spherical vessel is achieved by using an ultra-high pressure. As depicted in Fig. 6.1(a), the cylinder or sphere is filled with hydraulic oil. A core is generally inserted to conserve the amount of oil required. The oil is then pressurized at ultra-high-pressure p; if the pressure exceeds the yield pressure i.e., minimum pressure for yielding the cylinder, the applied pressure causes elastic-plastic deformation creating an inner plastic zone and outer elastic zone. This comprises the loading step of the process. When the vessel is depressurized in the unloading step as depicted in Fig. 6.1(b), elastic unloading takes place throughout the cylinder; the outer elastic zone exerts a pressure on the inner plastic zone and residual stresses are induced, which are compressive and tensile in the vicinities of the inner and outer walls, respectively. In the heat treatment procedure, the autofrettaged cylinder is thermally loaded by heating the outer wall as

depicted in Fig. 6.1(c). The inner wall temperature is lower and is governed by the criterion that the corresponding temperature difference does not yield the cylinder. This is followed by a sudden cooling of the cylinder from both the walls as depicted in Fig. 6.1. When the outer wall comes in contact with the quenchant, the surface temperature drops suddenly causing a rapid contraction. The local contraction of the outer wall faces restraint from the rest of material generating high tensile stresses at the surface. This creates an outer plastic zone. With gradual cooling, the remaining portion of the material contracts and exerts an inward pull force on the outer plastic zone. As a result, compressive residual stresses are induced in the vicinity of the outer wall.

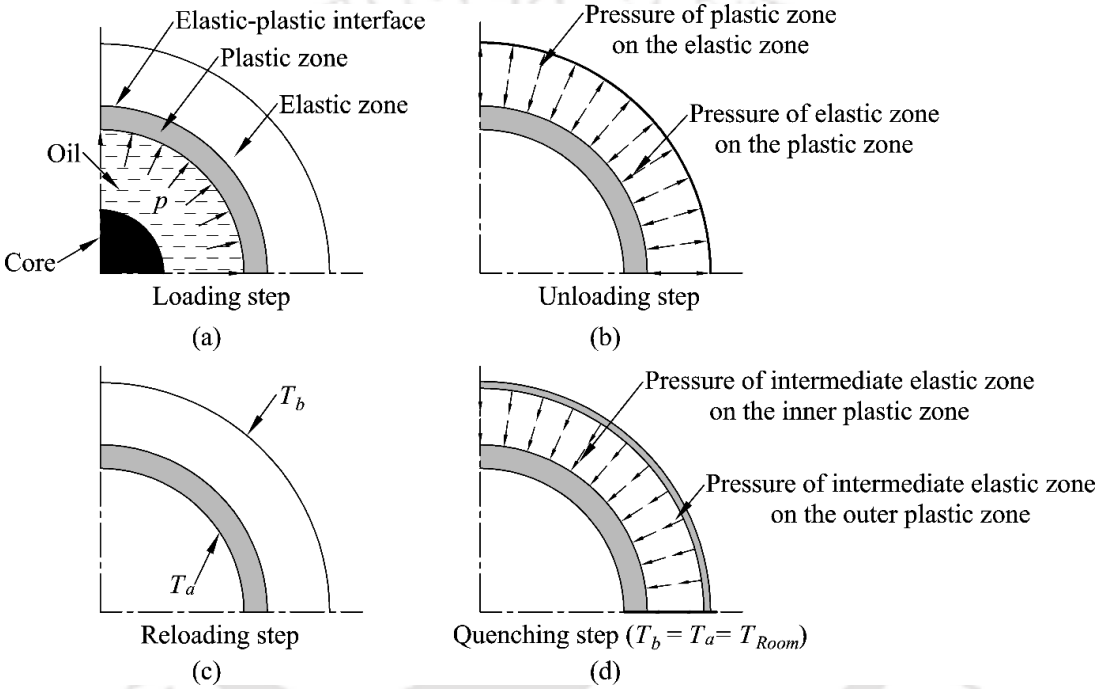

Figure 6.1 Schematic of hydraulic autofrettage process with heat treatment

6.3 FEM Analysis of Hydraulic Autofrettage and Heat Treatment

This section describes the procedure for FEM implementation of hydraulic autofrettage and the heat treatment process. Section 6.3.1 describes the model set-up, analysis steps and boundary conditions and Section 6.3.2 describes the definition of the material model.

6.3.1 Model set-up, Analysis steps, boundary conditions and element type

An open-ended cylinder with inner radius of 10 mm, outer radius 30 mm and length 120 mm is considered in this study. An axisymmetric model is utilized as depicted in Fig 6.2. The FEM model comprises four analysis steps— pressure loading, pressure unloading, thermal reloading and quenching. Since a time dependent phase transformation phenomenon is studied only in the quenching step, the preceding three steps viz. pressure loading, pressure unloading and thermal reloading were analyzed assuming a steady state condition and a transient analysis

was performed only in the quenching step. The pressure and temperature loading conditions in the first three steps were applied incrementally in 100 steps to determine the yield pressure within 1% accuracy. In the quenching step, a minimum increment of 10^{-6} s and a maximum increment of 1 s was used.

The loading and boundary conditions is depicted in Fig. 6.2 in cylindrical coordinate space with r, θ and z representing the radial, angular and axial coordinates, respectively. Referring to Fig. 6.2, q denotes the heat flux from the cylinder walls, h is the coefficient of convective heat transfer, T is the temperature and T_∞=20°C is the ambient temperature at steady state. The subscripts a and b signify the inner wall and the outer wall, respectively. In addition to the boundary conditions shown in Fig. 6.2, an insulation boundary condition was also assigned to the ends AB and CD as initial conditions.

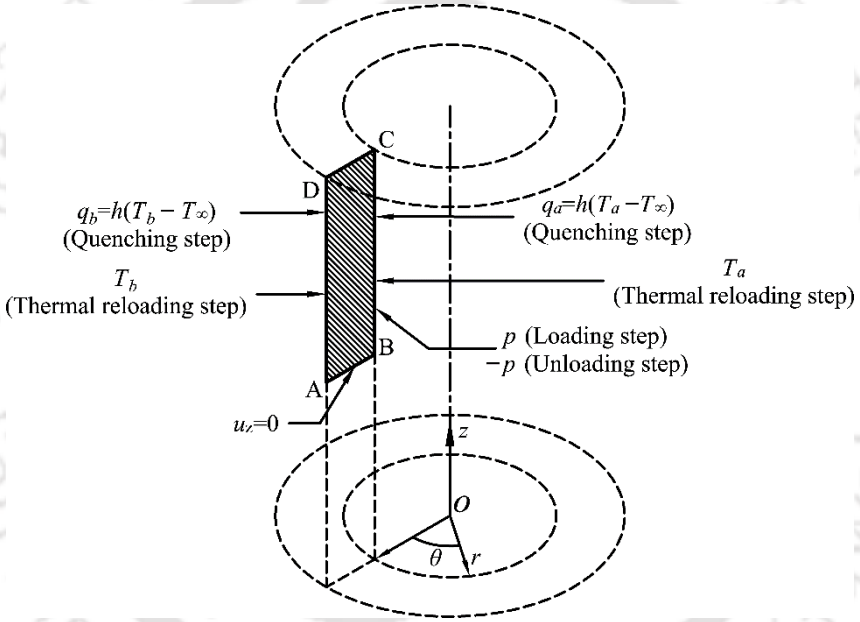

Figure 6.2 Schematic of the axisymmetric model of the cylinder with boundary conditions

The FEM analysis used the axisymmetric eight node quadratic element CAX8T with temperature-displacement coupling. The thickness of the cylinder was partitioned in the ratio of 1:6:1. Based on the results of a mesh sensitivity analysis, the model was meshed with 600 elements comprising 60 divisions along the thickness (15 divisions in the inner and outer partitions, 30 divisions in the intermediate partition) and 10 divisions along the length. A typical mesh is depicted in Fig. 6.3.

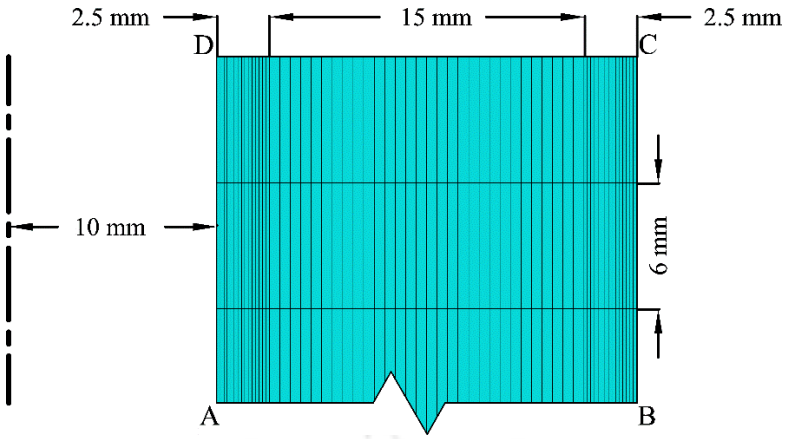

Figure 6.3 Typical mesh used in the FEM model

6.3.2 Material Model

Steel alloy AISI 1080 steel with a eutectoid composition i.e., containing carbon 0.8% by weight, is used in this study. The temperature and microstructure dependent thermal, mechanical and metallurgical properties are taken from [172]. The magnitude of each property at a specific temperature was calculated using the linear combination of the magnitudes due to the individual microstructural constituents, as given in Eq. (4.12). The governing equations for the kinetics of phase transformation were implemented in ABAQUS® through the subroutine UMATHT. The detailed algorithm and the execution have been explained in Section 4.4.3. In essence, the plastic behavior of the material is governed by the von Mises yield criterion and Ziegler's linear kinematic hardening rule [166]. The thermal behavior is based on Fourier's law of heat conduction. The latent heat of formation due to phase change is included in the equation for internal energy change given in Eq. (4.15).

6. 4 Procedure for Heat Treatment Design of Hydraulically Autofrettaged Cylinder

In the heat treatment process, the hydraulically autofrettaged cylinder is to be thermally reloaded by creating a temperature gradient across the thickness of the wall. On the basis of the heat treatment design discussed in Chapter 5, the outer wall of the autofrettaged cylinder must be heated above the lower critical temperature while the inner wall was maintained at a lower temperature such that the cylinder did not yield due to the temperature gradient. In the thermal reloading step, yielding in the autofrettaged cylinder can occur due to two factors, the first of which is yielding due to thermal stresses. When the temperature gradient is created by keeping the inner wall at a lower temperature than the outer wall, thermal stresses are generated, which are tensile at the inner wall and compressive at the outer wall. The autofrettaged cylinder can yield either at the inner or outer wall depending on the percentage of autofrettage. If the percentage of autofrettage is high, the tensile thermal stresses at the inner wall get offset due the large induced compressive residual stresses whereas the compressive

thermal stresses at the outer wall keep on increasing resulting in yielding in the vicinity. If the percentage of autofrettage is low, the tensile thermal stresses at the inner wall reach the local yield stress faster due to low induced compressive residual stresses resulting in yielding.

The second factor is the compressive yielding at the inner wall caused by the autofrettage-induced residual stresses. The plastic zone in the autofrettaged cylinder possesses a reduced compressive yield strength due to the Bauschinger effect. As the temperature of the inner wall increases, the local compressive yield strength of the material further decreases due to thermal softening. Since the maximum compressive residual stress is induced at the inner wall, the autofrettaged cylinder commences yielding when the corresponding equivalent stress becomes equal to the reduced compressive yield strength. This factor is influenced by the percentage of autofrettage carried out in the cylinder because more is the percentage of autofrettage, the more is the induced compressive residual stress and hence more likelihood of the compressive residual stresses causing yielding at the inner wall.

The second factor was not encountered in the heat treatment design proposed in Chapter 4, although it was based on a cylinder with identical dimensions and material used in the present study. This is because it was based on a thermally autofrettaged cylinder whereby the achievable maximum compressive residual stresses at the inner wall were comparatively less than that can be achieved with hydraulic autofrettage. For the present study, both factors must be taken into consideration because the hoop compressive residual stress of 640.53 MPa obtained at 100% autofrettage is significantly high and can cause yielding in the cylinder in the thermal reloading step.

On one hand, lowering the temperature of the inner wall below a threshold will cause yielding due to tensile thermal stresses. On the other hand, increasing the temperature of the inner wall beyond another threshold will cause yielding due to thermal softening. Thus, for a given percentage of autofrettage and a set temperature of the outer wall, the temperature of the inner wall should be chosen judiciously. An algorithm to obtain the lower and upper bound on the inner wall temperature is developed. The steps are as follows:

Step 1. The FEM simulation of the maximum hydraulic autofrettage i.e., 100% autofrettage, is carried out in the cylinder.

Step 2. The temperature of the outer wall of the autofrettaged cylinder is set as T_b = 725 °C (>Ac_1).

Step 3. The temperature of the inner wall is initially set as $T_a = T_b - \Delta T$ where ΔT is the temperature difference. (Initially ΔT is taken as 5°C)

Step 4. The FEM simulation of the thermal reloading of the autofrettaged cylinder is carried out using the current temperature boundary conditions T_a at the inner wall and T_b at the outer

wall. The distributions of the equivalent plastic strain in the autofrettaged cylinder before and after the thermal reloading steps are compared.

Step 5. If yielding occurs at the inner wall due to the compressive residual stresses, then Step 6 is executed else Step 8 is executed.

Step 6. The temperature of the inner wall is reduced by a decrement of ΔT i.e., $T_a \rightarrow T_a - \Delta T$.

Step 7. Deformation condition of the outer wall is checked. If yielding occurs at the outer wall due to compressive thermal stresses, then the temperature of the inner wall cannot be reduced further for the currently set temperature of the outer wall. The procedure may be continued by following one of two approaches (i) reducing the percentage of the autofrettage and going to step 2 (ii) reducing the temperature of the outer wall and going to step 3.

Step 8. The upper bound i.e., maximum permissible temperature of the inner wall has been obtained. Record the temperature of the inner wall.

Step 9. The temperature of the inner wall is reduced by a decrement of ΔT and the temperature of the inner wall is newly set as $T_a \rightarrow T_a - \Delta T$. The FEM simulation of the thermal reloading of the autofrettaged cylinder is carried out using the current temperature boundary conditions T_a at the inner wall and T_b at the outer wall. The distribution of the equivalent plastic strain in the autofrettaged cylinder before and after the thermal reloading steps are compared.

Step 10. If yielding does not occur at the inner wall due to tensile thermal stresses, then Step 9 is executed else Step 11 is executed.

Step 11. The lower bound of the allowable temperature range below which the temperature cannot be reduced further or else tensile yielding will take place at the inner wall. Record the temperature of the inner wall.

The entire procedure is summarized in the flowchart depicted in Fig. 6.5. Two possible types of heat treatment approaches are presented in this study *viz*., one that is carried out above the lower critical temperature and another that is carried out below the lower critical temperature. The design temperature of the inner wall should be in the range of the lower and upper bound temperatures; the exact temperature can be chosen on the basis of the amount of compressive residual stresses desired at the outer surface.

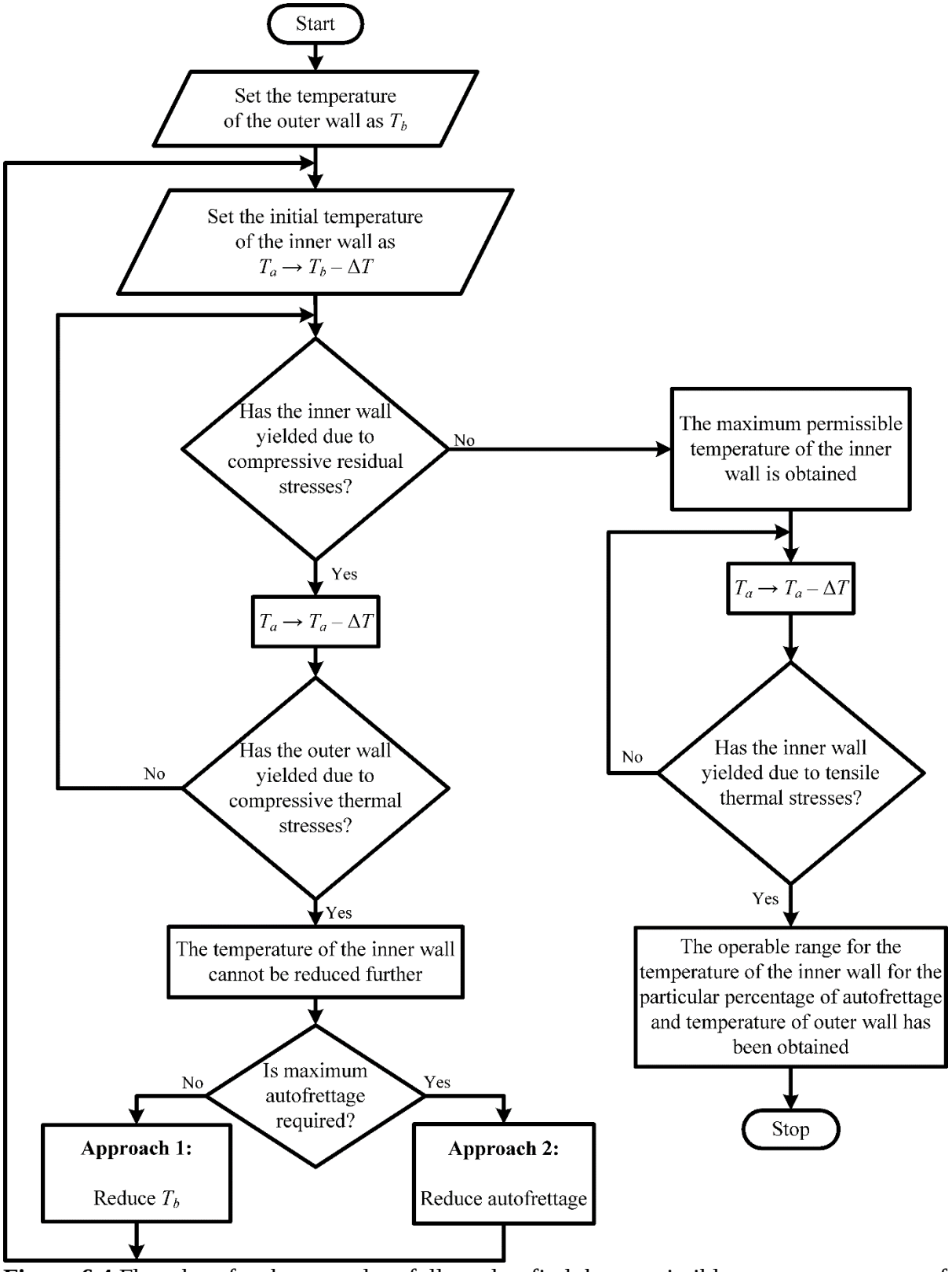

Figure 6.4 Flowchart for the procedure followed to find the permissible temperature range of the inner wall for heat treatment of the hydraulic autofrettaged cylinder

6.5 Results and Discussion

This section describes and discusses the results obtained from the FEM analysis of hydraulic autofrettage and subsequent heat treatment process. The FEM model comprises an interaction of three analysis modules *viz*., mechanical, thermal and metallurgical. The validity of the FEM model used in the present article has been shown in the previous chapters and need not be shown again. The validation based on hydraulic autofrettage has already been carried out in Chapter 3. The hydraulic autofrettage FEM model was validated with the analytical model of Avitzur [21] and the experimental results of Stacey *et al*. [118]. The validation of the heat treatment module in the FEM model based on the experimental study of Wang *et al*. [172] has also been carried out and shown in Chapter 4. Initial FEM analysis is carried out to first determine the hydraulic autofrettage parameters such as the yield pressure and overstrain for 100% autofrettage of the cylinder. These are presented in Section 6.5.1. The results of the subsequent heat treatment of the hydraulic autofrettaged cylinder are shown in Section 6.5.2.

6.5.1 Results of Hydraulic Autofrettage

The yield pressure for initiating the plastic deformation at the inner wall was obtained as 365 MPa at an ambient temperature condition of 20 °C. With further increase in the pressure, autofrettage was achieved and compressive residual stresses were induced. Greater the autofrettage pressure, more was the magnitude of the residual stresses induced at the walls. The maximum permissible autofrettage pressure to avoid compressive reverse yielding during unloading i.e., the pressure for achieving a 100% autofrettage was found to be about 720 MPa. The overstrain and percentage of autofrettage in the cylinder at different autofrettage pressures were computed using Eqs. (1.1) and (1.2). The variation of the residual hoop stresses at the inner wall and outer wall for different autofrettage pressures ranging from the yield pressure 365 MPa to the maximum of 720 MPa is shown in Table 6.1.

Table 6.1 Variation of residual hoop stress at the inner wall and outer wall with the percentage of autofrettage for different autofrettage pressures

Autofrettage pressure (MPa)	Residual hoop stress		Overstrain (%)	Percentage of autofrettage (%)
	Inner wall (MPa)	Outer wall (MPa)		
365	–4.49	0.04	0.83	0.70
400	–74.28	0.51	3.33	11.60
450	–170.16	2.86	5.82	26.57
500	–264.05	7.37	9.97	41.22
550	–355.42	14.33	12.46	55.49
600	–443.76	24.11	17.43	69.28
650	–528.6	37.05	24.90	82.53
720	–640.53	61.35	31.11	100

6.5.2 Results of Heat Treatment

On the basis of the heat treatment design procedure explained in Section 6.4, two types of heat treatment approaches are presented in this study *viz*., one that is carried out above the lower critical temperature and another that is carried out below the lower critical temperature. The results of the first approach are presented in Section 6.5.2.1 and those of the second approach are presented in Section 6.5.2.2.

6.5.2.1 Results of heat treatment carried out above the lower critical temperature

This approach is the same as that proposed in Chapter 4. The outer wall of the hydraulic autofrettaged cylinder is heated above Ac_1 and the temperature of the inner wall is maintained below Ac_1. Starting with a cylinder with 100% autofrettage, the temperature to be kept at the outer wall was set as 725 °C. The permissible temperature of the inner wall was tested by following the procedure depicted in Fig. 6.4. At a temperature of 655 °C, the cylinder commenced yielding simultaneously at both the walls due to thermal stresses. The temperature could not be decreased further, a condition stated in Step 7 of the algorithm explained in Section 6.4. A trade-off was made between the percentage of the hydraulic autofrettage required for inducing the desired residual stresses at the inner wall and that permissible for facilitating the heat treatment procedure.

Following design approach 2 (Refer. Fig. 6.4), the percentage of autofrettage was decreased. A suitable autofrettage pressure was 615 MPa. The variation of stresses after the loading step and the unloading step are depicted in Figs. 6.5(a) and 6.5(b), respectively. Referring to Fig. 6.5(a), the plastic zone radius is 14.5 mm i.e., 22.5% overstrain. The elastic-plastic interface is shown by the vertical dotted line that demarcates the inner plastic zone I and the outer elastic zone II. The maximum compressive hoop residual stress at the inner wall after depressurization is 469.61 MPa as depicted in Fig. 6.5(b). The percentage of autofrettage calculated on the basis of the maximum possible magnitude of 640.53 MPa is 73.33%. The hydraulic autofrettaged cylinder was then thermally loaded by heating the outer wall to 725 °C. The lower bound and upper bound of the inner wall temperature were obtained as 675 °C and 685 ºC, respectively. The thermal reloading was carried out using the lower bound temperature of the inner wall and distribution of stresses is depicted in Fig. 6.6.

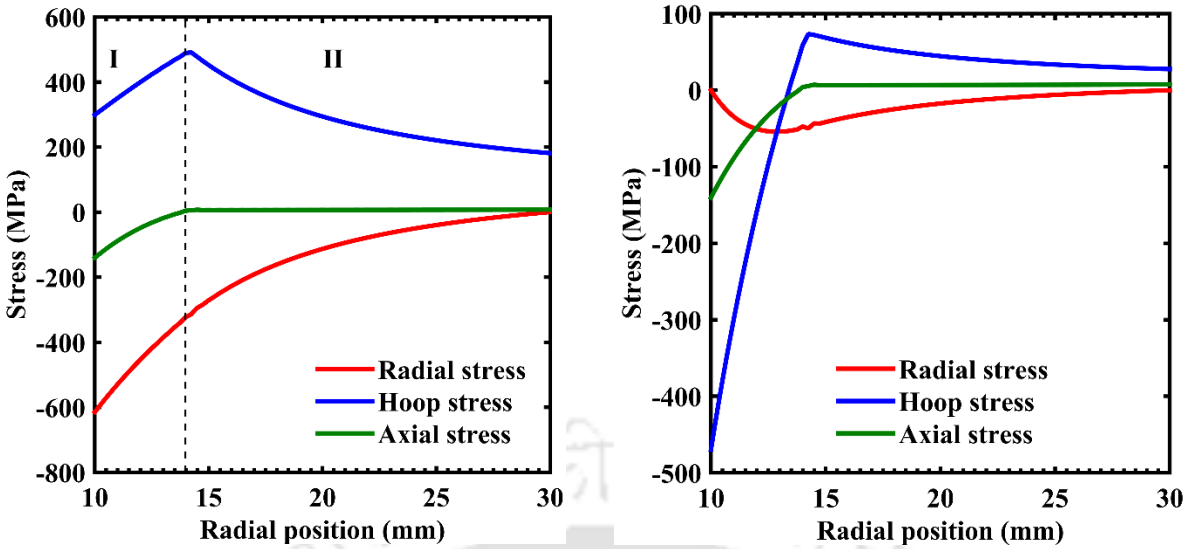

Figure 6.5 Variation of (a) stresses during loading and (b) residual stresses after unloading the cylinder with 615 MPa

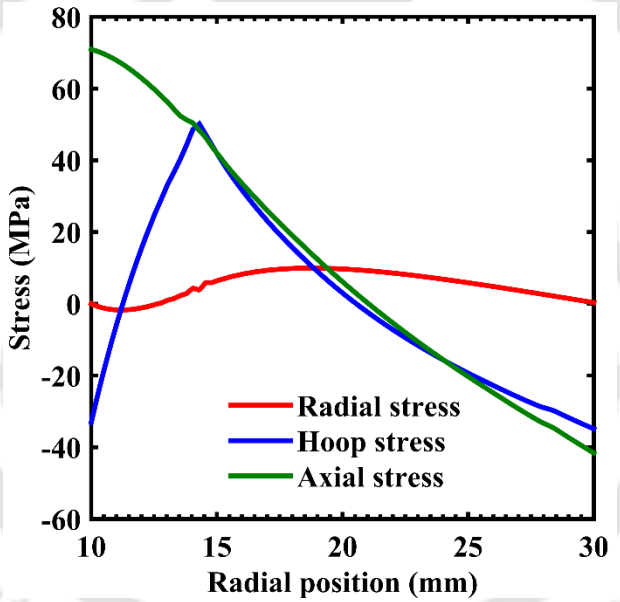

Figure 6.6 Variation of stresses in the hydraulic autofrettaged (73.3%) cylinder due to a temperature gradient resulting from wall temperatures of T_a=675 °C and T_b=725 °C

In the quenching step, the cylinder was cooled using boundary conditions as depicted in Fig. 6.2. It is emphasized here that the temperatures at outer wall as well as the inner wall are significantly high and a rapid cooling rate may cause large plastic deformation in the cylinder during the quenching step. The case of a fast cooling rate was first tested by using water at 20 °C as the quenchant whose temperature dependent heat transfer coefficients were taken from [176]. The coefficient of convective heat transfer averaged between the maximum and minimum values was 6813 W/m^2°C. The variation of the surface temperature and stresses with time at the walls of the cylinder in the quenching step are depicted in Fig. 6.7. Also plotted

in the figures is the evolution of the local yield stress at the wall surface depending on the variation of temperature. When the walls of the cylinder come into contact with the quenchant, the temperature of the walls decrease suddenly leading to rapid contraction. The underlying material having not commenced the contraction at this point resists the contraction of the inner and outer wall, generating very large tensile stresses at the surfaces. If the von Mises equivalent stress at these first few seconds exceed the local yield stress at the temperature, yielding occurs. As can be inferred from Fig. 6.7(a) for the inner wall and Fig. 6.7(b) for the outer wall, there is a spike in the von Mises stresses at the initial stage when the yielding occurs. With gradual cooling, the remaining portion of the material starts contracting. This process exerts an inward pull force on the outer plastic zone and a pressure on the inner plastic zone. This is also evident in Fig. 6.7 as the stresses change from tensile to compressive behaviour with time. When the cylinder attains the room temperature, compressive residual stresses are induced in the vicinity of the walls. The variation of the residual stresses and the microstructural phases along the thickness of the autofrettaged cylinder after the water-based quenching are depicted in Fig 6.8. Referring to Fig. 6.8(a), the cylinder has undergone plastic deformation and compressive stresses are induced at the inner as well as the outer wall. The microstructural state of the outer wall of the cylinder comprising 89.47 % martensite, 10.48% retained austenite, 0.03% pearlite and 0.012% Bainite depicted in Fig. 6.8(b) also demonstrates the effect of rapid cooling.

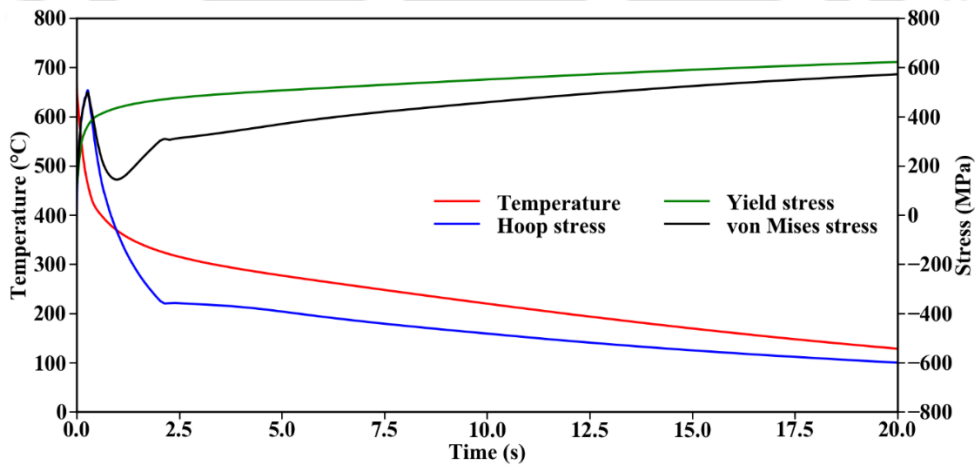

(a)

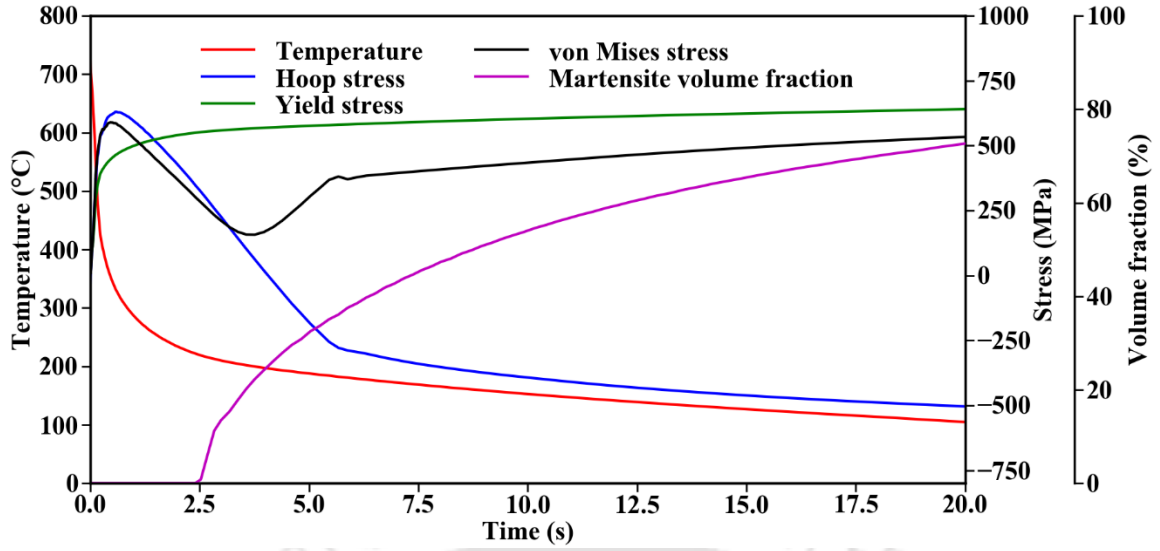

(b)

Figure 6.7 Variation of the surface temperature, hoop stress, axial stress and von Mises stress with time at (a) inner wall and (b) outer wall of the cylinder quenched in water at 20 °C

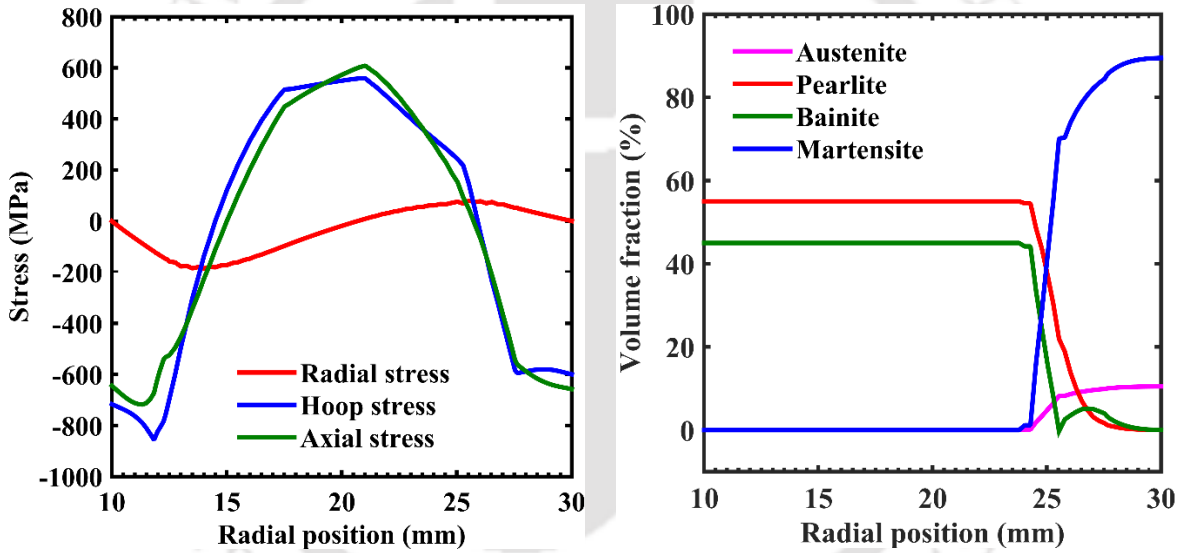

(a) (b)

Figure 6.8 Variation of (a) residual stresses and (b) microstructural phases along the thickness of the cylinder after quenching with water

Further, two different quenchants *viz*. fresh mineral oil MC1 [184] and a 10 bar pressurized nitrogen jet [185] having relatively mild rates of cooling were considered. The coefficient of convective heat transfer averaged between the maximum and minimum values for the mineral oil MC1 was 1143 W/m^2°C whereas that of the pressurized nitrogen jet was 457 W/m^2°C. The variation of the surface temperature and stresses with time at the walls of the cylinder in the quenching step are similar to that already depicted in Fig. 6.7 for the case of fast cooling rate. For briefness, only the variation of the temperature and stresses at the outer wall surface is shown in Fig. 6.9. Referring to Fig. 6.9, the rate of the decrease in temperature in both the cases of the quenchants is less steep compared to that shown in Fig. 6.7(b) because

of a relatively milder coefficient of convective heat transfer. When the walls of the cylinder make contact with the quenchant, the outer wall contracts against the resistance of the underlying material initially generating the large tensile stresses at the surfaces. Yielding occurs when the equivalent stresses exceed the local yield stress. With further cooling of the outer wall, the rate of phase transformation of austenite increases that releases latent heat and causes an increase in the temperature. The increase in temperature slows down the contraction of the outer wall temporarily leads to a decrease of the tensile stresses in the vicinity. This can also be inferred from Fig. 6.9 where the momentary increase in the temperature profile coincides with a decrease in the tensile stresses. With further cooling, the rate of phase transformation decreases with which the contraction of the outer wall resumes and compressive residual stresses are induced in the vicinity of the walls till the cylinder attains the room temperature.

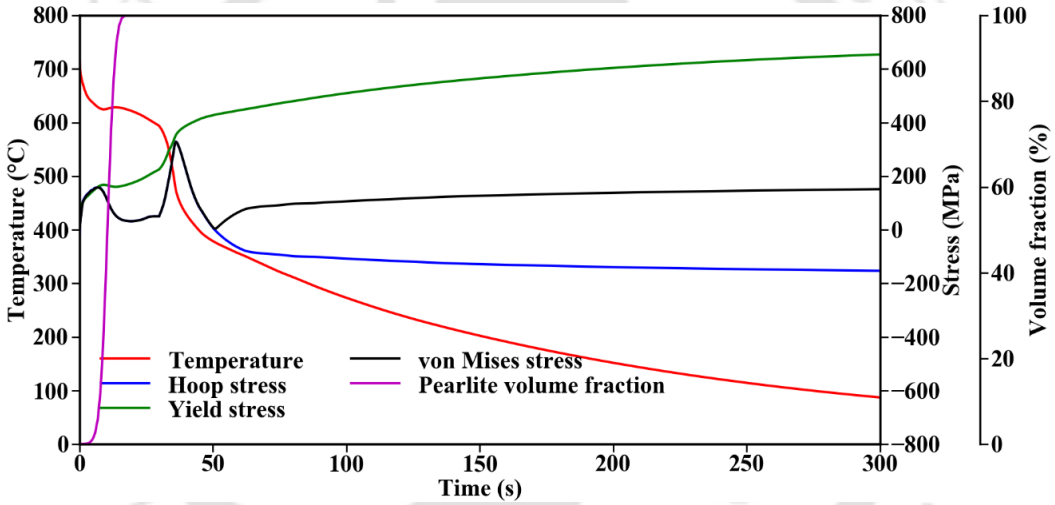

(a)

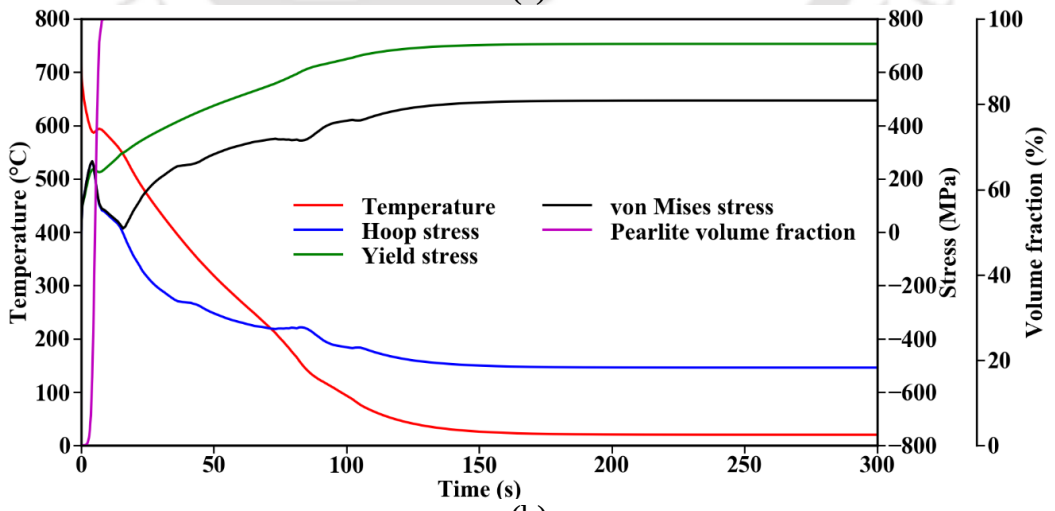

(b)

Figure 6.9 Variation of the surface temperature, hoop stress, yield stress and von Mises stress with time at the outer wall of the cylinder quenched with (a) MC1 mineral oil and (b) nitrogen jet pressurized at 10 bar

The variation of the residual stresses along the thickness of the autofrettaged cylinder after quenching in these two media are depicted in Fig.6.10. In both the cases, residual stresses are induced, which are compressive at both the walls. The cylinder quenched with mineral oil MC1 comprises an inner plastic zone from the inner wall to 10.33 mm, an outer plastic zone III from 27.83 mm to the outer wall and an intermediate elastic zone II. Similarly, the cylinder quenched with pressurized nitrogen comprises an inner plastic zone from the inner wall to 10.83 mm, an outer plastic zone III from 26.5 mm to the outer wall and an intermediate elastic zone II. The magnitude of the residual hoop stresses at walls of the hydraulic autofrettaged cylinder before and after the quenching in the two media are compared in Table 6.2. In both the cases, the inner wall compressive residual stresses decrease due to the quenching at the cost of an increase in the outer wall compressive residual stresses. The variation of the microstructural phases in the autofrettaged cylinder after quenching in fresh mineral oil MC1 and pressurized nitrogen jet are depicted in Fig. 6.11. For both the cases the outer comprises a 100% pearlite from a radius of 25 mm to the outer wall. The remainder of the cylinder from the inner wall to the radius of 25 mm remains in the initial state of 55% pearlite and 45% bainite.

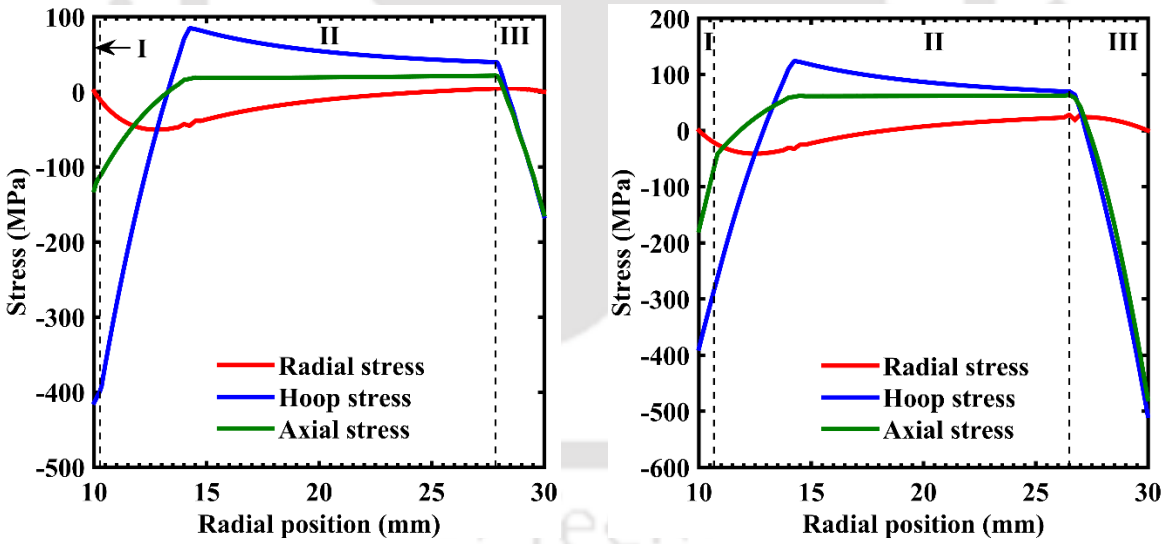

Figure 6.10 Variation of residual stresses along the thickness of the cylinder after quenching with (a) fresh mineral oil MC1 [184] and (b) nitrogen jet pressurized at 10 bar [185]

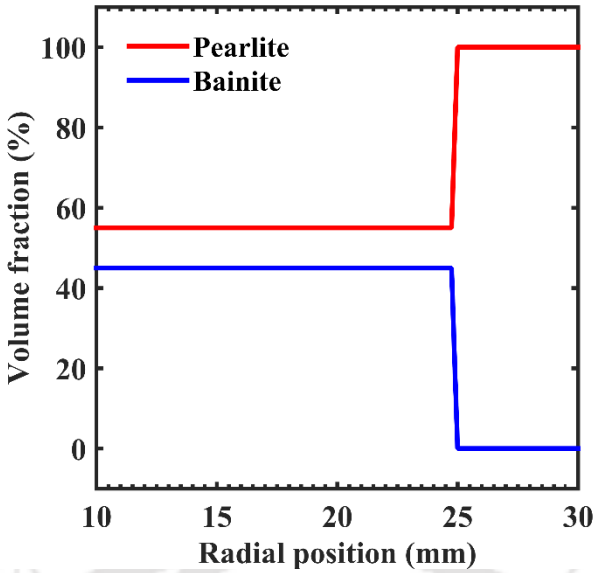

Figure 6.11 Variation of microstructural phases along the thickness of the cylinder after quenching with afresh mineral oil MC1 [184] and nitrogen jet pressurized at 10 bar [185]

Table 6.2 Comparison of residual stresses obtained after quenching with fresh mineral oil MC1 [184] and 10 bar pressurized nitrogen [185]

Quenchant	Hoop residual stresses (MPa)			
	Inner wall		Outer wall	
	After autofrettage	After quenching	After autofrettage	After quenching
Mineral oil MC1	–469.61	–414	27.62	–165.62
10 bar pressurized nitrogen		–388.17		–507.95

6.5.2.2 Results of heat treatment carried out below the lower critical temperature

This is a new approach investigated in this study where the outer wall of the autofrettaged cylinder is kept below the lower critical temperature in the thermal reloading step. A 100% autofrettage is considered in this approach, which was achieved with an autofrettage pressure of 720 MPa at room temperature. The variation of stresses during loading and that of the residual stresses after unloading the cylinder are depicted in Figs. 6.12(a) and 6.12(b), respectively. Referring to Fig. 6.12(a), the plastic zone radius of the cylinder is 16.22 mm i.e., 31.11% overstrain. The elastic-plastic interface is shown by the vertical dotted line that demarcates the inner plastic zone I and the outer elastic zone II. The compressive hoop residual stress at the inner wall is 640.53 MPa and the tensile hoop residual stress at the outer wall is 61.35 MPa. The wall temperatures that must be maintained in the thermal reloading step was investigated by following the procedure for design approach 1 depicted in Fig. 6.4. Feasible combinations wall temperatures that can be used for thermally loading the autofrettaged cylinder without yielding were obtained.

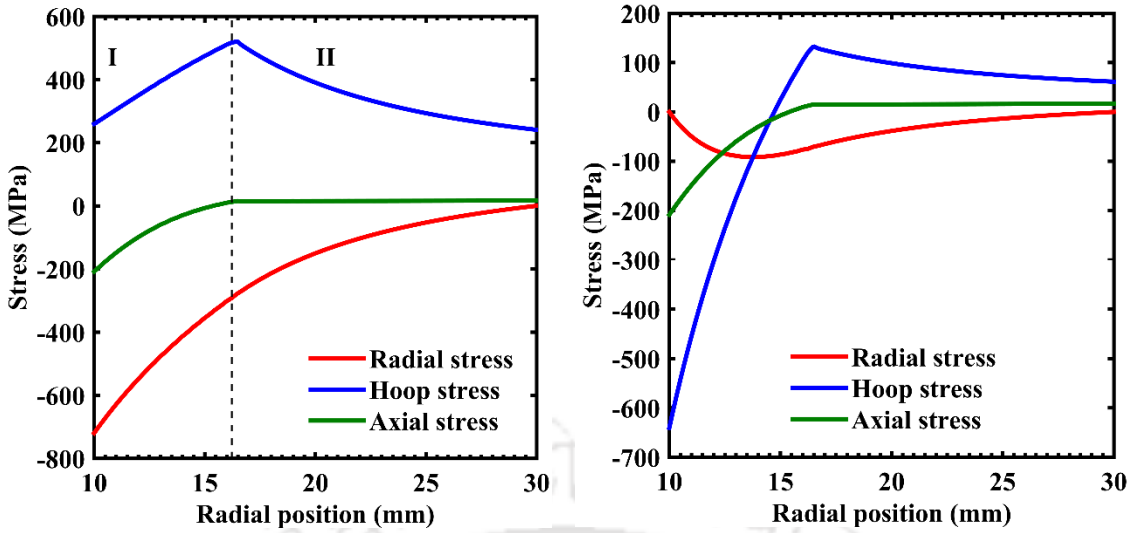

Figure 6.12 Variation of (a) stresses during loading and (b) residual stresses after unloading the cylinder with 100% autofrettage using a pressure of 720 MPa

The quenching simulation of the autofrettaged cylinder for each case of the thermal reloading condition was carried out using the temperature dependent heat transfer coefficient of water at 20 °C that was taken from [176]. The hoop residual stresses after quenching the cylinder from various cases of thermal reloading conditions are tabulated in Table 6.3. For each temperature of the outer wall, the lower and upper bound temperatures allowable at the inner wall for avoiding yielding are indicated in bold. For temperatures of the outer wall above the maximum of 600 °C, no possible temperature combination was obtained that avoided yielding in the cylinder. Below 500 °C, the temperature of the outer wall was insufficient to cause plastic deformation of the outer wall during the quenching process. It is worth noting that the quenching operation decreases the tensile hoop residual stress at the outer wall even if in some cases it is not compressive. For outer wall temperatures of 500 °C, 525°C, 550 °C and 600°C, the compressive hoop residual stress at the outer wall was maximum when quenched from a thermally loaded state with inner wall temperatures of 425 °C, 445 °C, 460 °C and 475 °C, respectively as shown in Table. 6.3.

For the sake of brevity, the variation of residual stresses in the cylinder has been shown only for the cases with those combination of the inner and outer wall temperatures in the thermal reloading step that provides the maximum compressive residual stresses after quenching. The variation of residual stresses in the autofrettaged cylinder after quenching in water at 20 °C from a thermally loaded state with inner and outer wall temperature combinations of (T_a =425 °C, T_b = 500 °C), (T_a =445 °C, T_b = 525 °C), (T_a =460 °C, T_b = 550 °C) and (T_a =500 °C, T_b = 600 °C) is depicted in Figs. 6.13(a), 6.13(b), 6.13(c) and 6.13(d), respectively. Referring to Figs. 12(a–c), the quenched cylinder comprises two zones, *viz*., an

inner material zone I obtained just after the initial autofrettage and an outer plastic zone II obtained after the quenching. For quenching after thermal reloading with T_a =500 °C and T_b = 600 °C, the cylinder comprises an inner plastic zone I and an outer plastic zone III caused by yielding in the quenching step and an intermediate material zone II from the initial autofrettage. As a typical case, the variation of the surface temperature and stresses with time at the walls of the cylinder after quenching in water at 20 °C from a thermally loaded state with T_a =460 °C, T_b = 550 °C is depicted in Fig. 6.14. The explanation of the evolution of stresses with temperature is similar to that already described in Sections 6.5.2.1 and will not be repeated. In essence, the quenching process initially yields the outer wall due to tensile stresses at the outer wall. With gradual cooling till room temperature changes compressive residual stresses are induced due to the interaction of the plastic zones with the intermediate elastic zone.

Table 6.3 Comparison of residual stresses obtained after quenching from various cases of thermal reloading states. The upper and lower bound temperatures of the inner wall are shown in bold.

Thermal reloading step			Hoop residual stress after quenching	
T_a (°C)	T_b (°C)	$T_b - T_a = \Delta T$ (°C)	Inner wall (MPa)	Outer wall (MPa)
215		285	–640.51	61.35
300		200	–640.35	38.96
350	500	150	–638.79	–12.97
400		100	–635.47	–67.34
425		75	–632.86	–94.90
260		265	–640.50	58.4
300		225	–639.86	15.13
350	525	175	–637.55	–39.3
400		125	–633.48	–94.71
445		80	–628.26	–145.17
310		240	–638.57	–22.07
350	550	200	–636	–66.40
400		150	–631.19	–122.66
460		90	–622.84	–197.07
475		125	–610.61	–301.60
485	600	115	–608.23	–317.91
500		100	–604.68	–344.37

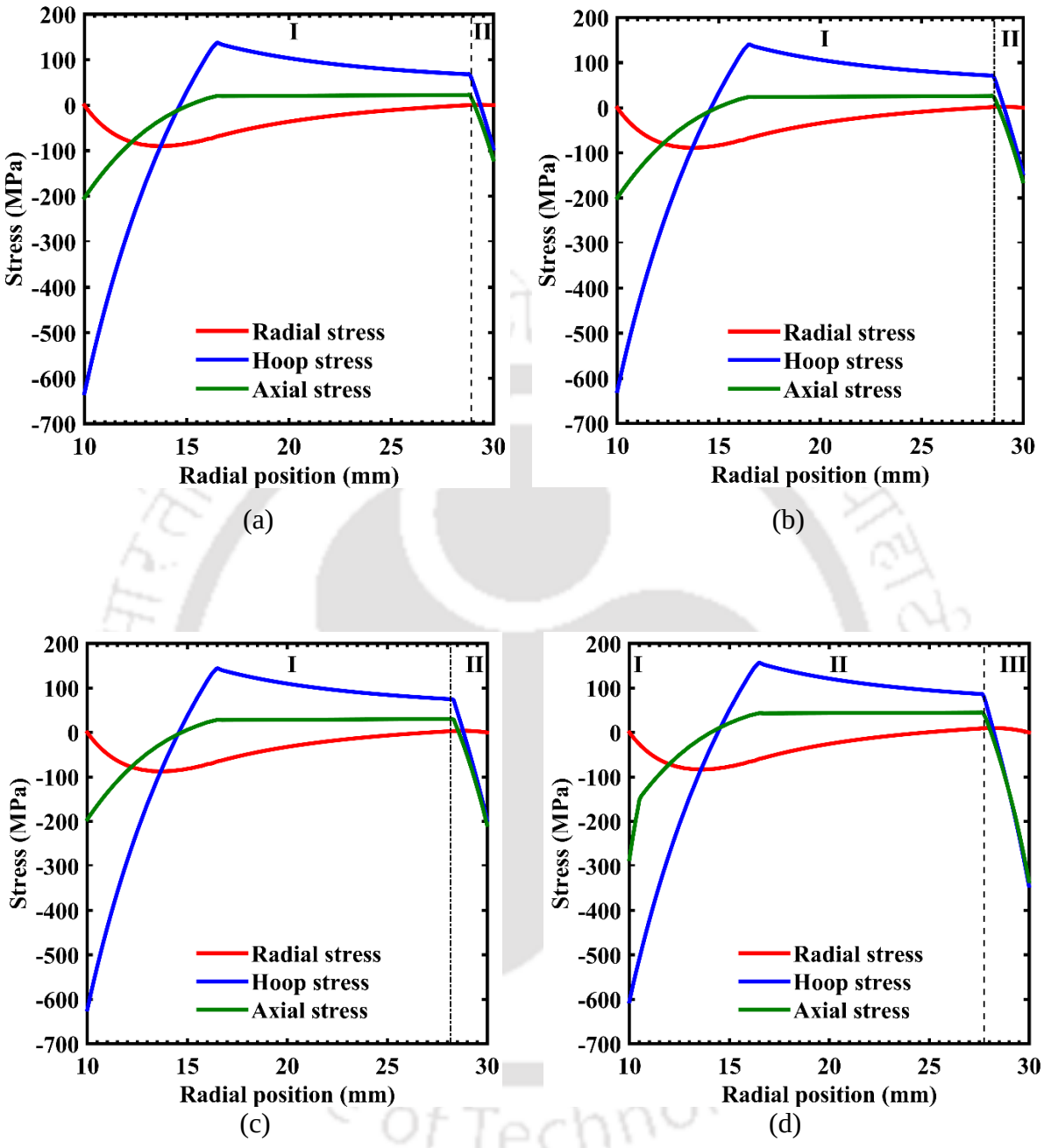

Figure 6.13 Variation of residual stresses in the 100% autofrettaged cylinder after quenching in water at 20 °C from a thermally loaded state with inner and outer wall temperature combinations of (a) T_a =425 °C, T_b = 500 °C (b) T_a =445 °C, T_b = 525 °C (c) T_a =460 °C, T_b = 550 °C and (d) T_a =500 °C, T_b = 600 °C

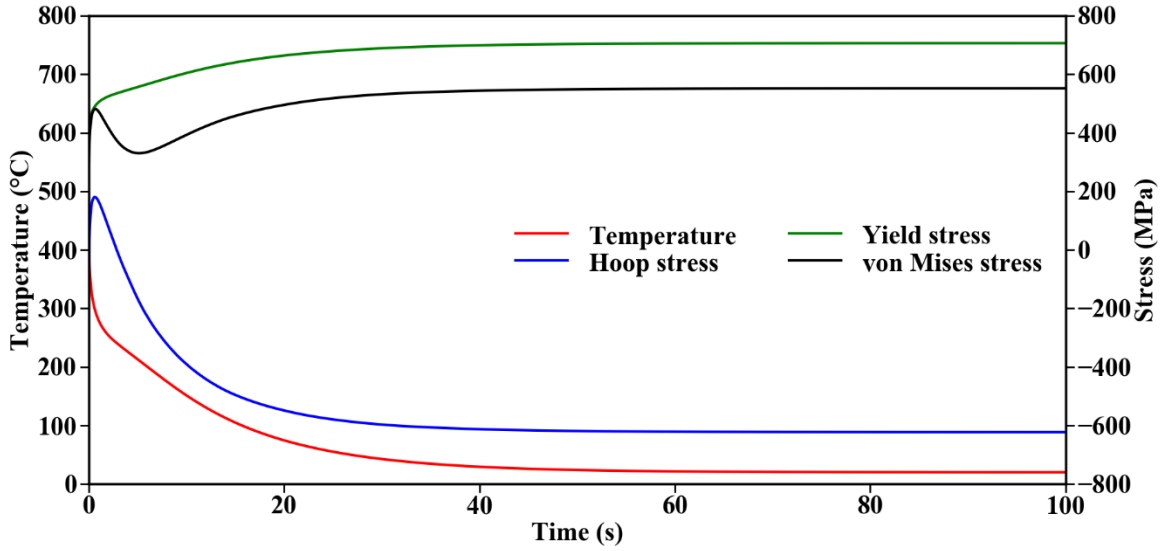

(a)

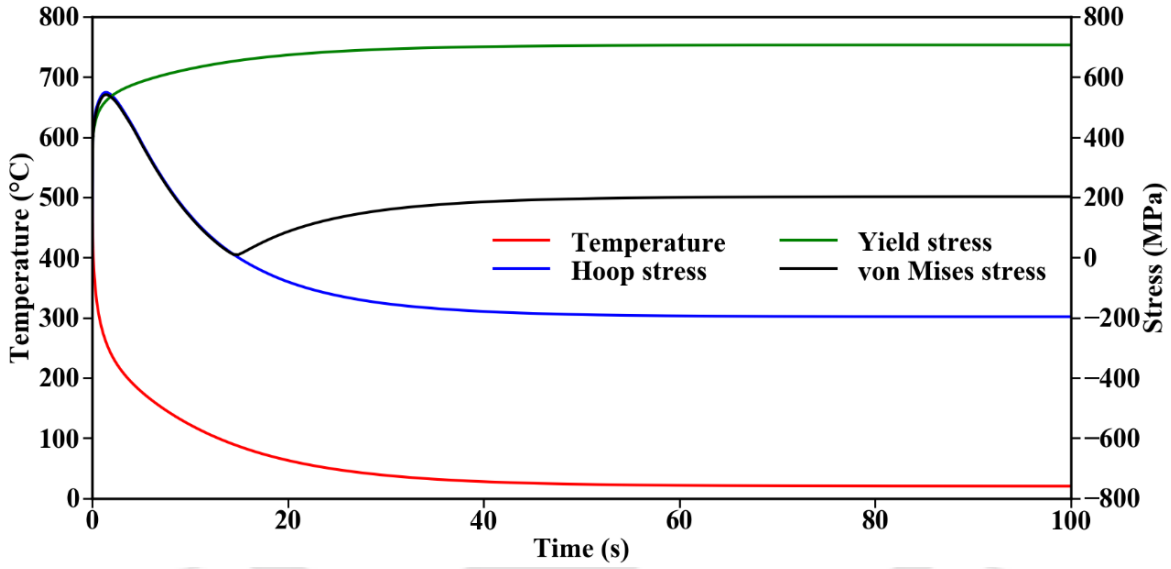

(b)

Figure 6.14 Variation of the surface temperature, hoop stress, yield stress and von Mises stress with time at (a) inner wall and (b) outer wall of the cylinder after quenching in water at 20 °C from a thermally loaded state with T_a= 460 °C and T_b = 550 °C

6.6 Conclusion

This work proposed the design of a heat treatment process for eliminating tensile residual stresses induced at the outer wall of a hydraulic autofrettaged cylinder. In this method, a hydraulic autofrettaged cylinder was first thermally reloaded with a temperature gradient where the outer wall was kept at a higher temperature than that at the inner wall without yielding the autofrettaged cylinder. Finally, the autofrettaged cylinder was quenched from the walls after which compressive residual stresses were induced at the surfaces of the cylinder. Two types of heat treatment approaches were presented. One was a novel technique, which involved temperatures below the lower critical temperature and the other was based on an

existing technique proposed for a thermally autofrettaged cylinder that involved temperatures above the lower critical temperature. Both methods induce compressive residual stresses at the outer wall of the hydraulically autofrettaged cylinder but the novel approach has two advantages. It requires less energy because the cylinder is heated well-below the lower critical temperature. It is also applicable to cylinder with low as well as large percentage of autofrettage.

Chapter 7

Epilogue

7.1 Introduction

Autofrettage is a widely practiced metal working process for enhancing the pressure carrying capacity, fatigue life, creep resistance and stress corrosion resistance of thick-walled cylindrical and spherical vessels. The basic principle of the process is to load the vessel and cause partial or full plastic deformation prior to its service condition. When the vessel is subsequently unloaded, compressive residual stresses are induced in the vicinity of the inner wall whereas tensile residual stresses are induced in the vicinity of the outer wall. On the basis of the type of load used for the plastic deformation, autofrettage can be classified into five types such as hydraulic, swage, explosive, thermal and rotational autofrettage.

Significant researches have been carried out in the different types of autofrettage processes encompassing various theoretical models and carried out experimental studies. A review of the works available in the literature reveals that the hydraulic autofrettage is the most popular and widely accepted type of autofrettage process but the requirement of very high pressure makes the process costly. On the other hand, the thermal autofrettage is very simple but limited in its efficacy. Another detrimental feature common to all types of autofrettage processes is that while the compressive residual stresses induced in the vicinity of the inner wall benefit the vessel for strengthening, the tensile residual stresses in the vicinity of the outer wall weaken the autofrettaged cylinder or sphere. This condition gets aggravated in the presence of external surface flaws like cracks or wears as the tensile stresses cause the cracks to open up. These two aspects of autofrettage have not been investigated in that much detail. The focus of the thesis is the design of a special class of autofrettage processes that could be called as “thermally assisted autofrettage processes” where a conventional autofrettage process is augmented by a thermal load. The scope of the thesis is limited to hydraulic and thermal autofrettage processes.

7.2 Overall Conclusions

The salient conclusions that can be drawn from the present thesis can be listed as follows:

- A combined hydraulic and thermal autofrettage process is studied. The study indicates that the combined hydraulic and thermal autofrettage can economize a hydraulic autofrettage process. A desirable increase in pressure carrying capacity in a particular cylinder can be

achieved with a lesser pressure by combining with a thermal load. The same increase in pressure carrying capacity would have required a higher pressure using a conventional hydraulic autofrettage process carried out at room temperature.

- A thermal autofrettage with a coupled heat treatment process is studied wherein the outer wall of a thermally autofrettaged cylinder is locally austenized by heating above the lower critical temperature while the temperature of the inner wall is kept below it. After the cylinder is quenched, residual stresses are induced in the cylinder that are compressive in the vicinity of the inner as well as the outer wall. This technique mitigates the harmful autofrettage-induced tensile residual stresses in the vicinity of the outer wall.
- An experimental set up is developed for the proposed heat treatment coupled thermal autofrettage process. The presence of compressive residual stresses at the outer wall is confirmed by measuring the microhardness and opening angle due to a longitudinal cut in the autofrettaged cylinder. The microhardness of the outer wall decreased after the thermal autofrettage due to tensile residual stresses but it increased after the heat treatment due to compressive residual stresses.
- The feasibility of the heat treatment design for inducing compressive residual stresses at the outer wall of an autofrettaged cylinder is also investigated in a cylinder autofrettaged by hydraulic pressure. The results indicate that the proposed heat treatment design can also be adapted for a hydraulic autofrettaged cylinder. The study also reveals that the same procedure can be implemented by limiting the maximum temperature to well below the lower critical temperature. This is advantageous in terms of energy economy.

7.3 Scope for Future Work

Based on the review and work carried out in this thesis, some of the key challenges and areas where future researches can be directed are as follows:

- Further detailed experiments are needed to quantitatively measure the compressive residual stresses induced by the heat treatment procedure proposed in this work.
- Although the beneficial aspect of autofrettage in improving the fatigue life of thick cylinders is well established, Sills and Marmur [186] pointed out that it reduced the fracture toughness of thick cylinders made of gun steel. It is a worth investigating aspect for various materials.
- The scope of the present thesis is limited to hydraulic and thermal autofrettages. The proposed heat treatment technique for inducing compressive residual stresses at the

walls of an autofrettaged cylinder can be studied for a cylinder autofrettaged through swage, explosive or rotational route.

- Similar theoretical and experimental studies can be carried out for thick-walled spheres.
- The aspects related to stress corrosion cracking of autofrettaged vessels can be explored.

References

[1] Bastable, M. J., 1992, "From Breechloaders to Monster Guns: Sir William Armstrong and the Invention of Modern Artillery, 1854-1880," Technology and Culture, **33**(2), pp. 213–247.

[2] Faupel, J. H., 1955, "Residual Stresses in Heavy-Wall Cylinders," Journal of the Franklin Institute, **259**(5), pp. 405–419.

[3] Hu, C., Yang, F., Zhao, Z., and Zeng, F., 2017, "An Alternative Design Method for the Double-Layer Combined Die Using Autofrettage Theory," Mechanical Sciences, **8**(2), pp. 267–276.

[4] ASME Pressure Vessel and Piping Design Code, 2007, "Design Using Autofrettage," **Division 3, Section 8, Article KD-5**, pp. 71–73.

[5] Jacob, L., 1907, "La Résistance et L'équilibre Élastique Des Tubes Frettés," Memorial de L'artillerie Navale, **1**(1907), pp. 43–155.

[6] Chakrabarty, J., 2006, *Theory of Plasticity*, Butterworth-Heinemann, Amsterdam.

[7] Crossland, B., and Bones, J. A., 1958, "Behaviour of Thick-Walled Steel Cylinders Subjected to Internal Pressure," Proceedings of the Institution of Mechanical Engineers, **172**(1), pp. 777–804.

[8] Davidson, T. E., Barton, C. S., Reiner, A. N., and Kendall, D. P., 1962, "New Approach to the Autofrettage of High-Strength Cylinders," Experimental Mechanics, **2**(2), pp. 33–40.

[9] Chen, P. C., 1988, *A Simple Analysis of the Swage Autofrettage Process*, Army Armament Research Development and Engineering Center, Benet Weapons Lab, NY.

[10] Parker, A. P., O'Hara, G. P., and Underwood, J. H., 2003, "Hydraulic Versus Swage Autofrettage and Implications of the Bauschinger Effect," ASME Journal of Pressure Vessel Technology, **125**(3), pp. 309–314.

[11] Mote, J. D., Ching, L. K., Knight, R. E., Fay, R. J., and Kaplan, M. A., 1971, *Explosive Autofrettage of Cannon Barrels*, AMMRC CR 70-25, Army Materials and Research Center, Watertown, Massachusetts.

[12] Kamal, S. M., 2016, "A Theoretical and Experimental Study of Thermal Autofrettage Process," Ph.D. Thesis, IIT Guwahati.

[13] Wen, E., Barbero, E., and Tygielski, P., 2002, "Autofrettage to Offset CTE Mismatch in Metal-Lined Composite Cryogenic Feed Lines," *43rd AIAA/ASME/ASCE/AHS/ASC Structures, Structural Dynamics, and Materials Conference*, American Institute of Aeronautics and Astronautics, pp. 1–9.

[14] Kamal, S. M., and Dixit, U. S., 2015, "Feasibility Study of Thermal Autofrettage of Thick-Walled Cylinders," ASME Journal of Pressure Vessel Technology, **137**(6), pp. 061207-061207–18.

[15] Kamal, S. M., Borsaikia, A. C., and Dixit, U. S., 2016, "Experimental Assessment of Residual Stresses Induced by the Thermal Autofrettage of Thick-Walled Cylinders," The Journal of Strain Analysis for, **51**(2), pp. 144–160.

[16] Kamal, S. M., and Dixit, U. S., 2016, "A Comparative Study of Thermal and Hydraulic Autofrettage," J Mech Sci Technol, **30**(6), pp. 2483–2496.

[17] Zare, H. R., and Darijani, H., 2016, "A Novel Autofrettage Method for Strengthening and Design of Thick-Walled Cylinders," Materials & Design, **105**, pp. 366–374.

[18] Parker, A. P., 1981, "Stress Intensity and Fatigue Crack Growth in Multiply-Cracked, Pressurized, Partially Autofrettaged Thick Cylinders," Fatigue & Fracture of Engineering Materials & Structures, **4**(4), pp. 321–330.

[19] Malik, M. A., Khushnood, S., Khan, M., Rashid, B., and Khan, M., 2008, "Hydraulic Autofrettage Technology: A Review," ASME, Orlando, Florida, US, pp. 195–206.

[20] Malik, M. A., and Khushnood, S., 2003, "A Review of Swage - Autofrettage Process," Japan Society of Mechanical Engineers, Tokyo, Japan, p. 3610.
[21] Avitzur, B., 1994, "Autofrettage—Stress Distribution under Load and Retained Stresses after Depressurization," International Journal of Pressure Vessels and Piping, **57**(3), pp. 271–287.
[22] Chen, P. C. T., 1973, "A Comparison of Flow and Deformation Theories in a Radially Stressed Annular Plate," J. Appl. Mech, **40**(1), pp. 283–287.
[23] Lu, W. Y., and Hsu, Y. C., 1977, "Elastic-Plastic Analysis of a Flat Ring Subject to Internal Pressure," Acta Mechanica, **27**(1–4), pp. 155–172.
[24] Perry, J., and Aboudi, J., 2003, "Elasto-Plastic Stresses in Thick Walled Cylinders," ASME Journal of Pressure Vessel Technology, **125**(3), pp. 248–252.
[25] Rees, D. W. A., 1990, "Autofrettage Theory and Fatigue Life of Open-Ended Cylinders," The Journal of Strain Analysis for, **25**(2), pp. 109–121.
[26] Li, G., Zeng, X., Li, J., and Huang, L., 1988, "Elastoplastic Analysis of an Open-Ended Cylinder from the Twelve Polygonal Yield Condition," International Journal of Pressure Vessels and Piping, **33**(2), pp. 143–152.
[27] Zeng, X., Li, J., Li, J., Li, G., Yang, Z., and Li, J., 1993, "The Application of the Twelve-Angled Polygonal Yield Criterion to Pressure Vessel Problems," International Journal of Pressure Vessels and Piping, **55**(3), pp. 385–393.
[28] Parker, A. P., 2000, "Autofrettage of Open-End Tubes—Pressures, Stresses, Strains, and Code Comparisons," ASME Journal of Pressure Vessel Technology, **123**(3), pp. 271–281.
[29] Thomas, D. G. B., 1953, "The Autofrettage of Thick Tubes with Free Ends," Journal of the Mechanics and Physics of Solids, **1**(2), pp. 124–133.
[30] Gao, X., 1992, "An Exact Elasto-Plastic Solution for an Open-Ended Thick-Walled Cylinder of a Strain-Hardening Material," International Journal of Pressure Vessels and Piping, **52**(1), pp. 129–144.
[31] Chen, P., 1980, *Generalized Plane-Strain Problems in an Elastic-Plastic Thick-Walled Cylinder*, ARLCB-TR-80028, Army Armament Research and Development Center, Watervliet, New York.
[32] MacGregor, C. W., L.F. Coffin, Jr., and Fisher, J. C., 1948, "Partially Plastic Thick-Walled Tubes," Journal of the Franklin Institute, **245**(2), pp. 135–158.
[33] Allen, D. N. de G., and Sopwith, D. G., 1951, "The Stresses and Strains in a Partly Plastic Thick Tube under Internal Pressure and End-Load," Proceedings of the Royal Society of London A: Mathematical, Physical and Engineering Sciences, **205**(1080), pp. 69–83.
[34] Koiter, W., 1953, "On Partially Plastic Thick-Walled Tubes," Biezeno Anniversary Volume, pp. 232–251.
[35] Mendelson, A., 1968, *Plasticity, Theory and Application*, Macmillan, New York.
[36] Chen, P. C. T., 1986, "The Bauschinger and Hardening Effect on Residual Stresses in an Autofrettaged Thick-Walled Cylinder," ASME Journal of Pressure Vessel Technology, **108**(1), pp. 108–112.
[37] Bland, D. R., 1956, "Elastoplastic Thick-Walled Tubes of Work-Hardening Material Subject to Internal and External Pressures and to Temperature Gradients," Journal of the Mechanics and Physics of Solids, **4**(4), pp. 209–229.
[38] Davidson, T., Barton, C., Reiner, A., and Kendall, D., 2013, "Overstrain of High Strength, Open End Cylinders of Intermediate Diameter Ratio," pp. 335–352.
[39] Chu, S.-C., 1972, "A More Rational Approach to the Problem of an Elastoplastic Thick-Walled Cylinder," Journal of the Franklin Institute, **294**(1), pp. 57–65.

[40] Elder, A. S., Tomkins, R., and Mann, T. L., 1975, "Generalized Plane Strain in an Elastic, Perfectly Plastic Cylinder, With Reference to the Hydraulic Autofrettage Process," pp. 623–659.

[41] Marcal, P. V., 1965, "A Note on the Elastic-Plastic Thick Cylinder with Internal Pressure in the Open and Closed-End Condition," International Journal of Mechanical Sciences, **7**(12), pp. 841–845.

[42] Gao, X.-L., 1993, "An Exact Elasto-Plastic Solution for a Closed-End Thick-Walled Cylinder of Elastic Linear-Hardening Material with Large Strains," International Journal of Pressure Vessels and Piping, **56**(3), pp. 331–350.

[43] Livieri, P., and Lazzarin, P., 2001, "Autofrettaged Cylindrical Vessels and Bauschinger Effect: An Analytical Frame for Evaluating Residual Stress Distributions," ASME Journal of Pressure Vessel Technology, **124**(1), pp. 38–46.

[44] Lazzarin, P., and Livieri, P., 1997, "Different Solutions for Stress and Strain Fields in Autofrettaged Thick-Walled Cylinders," International Journal of Pressure Vessels and Piping, **71**(3), pp. 231–238.

[45] Loghman, A., and Wahab, M. A., 1994, "Loading and Unloading of Thick-Walled Cylindrical Pressure Vessels of Strain-Hardening Material," ASME Journal of Pressure Vessel Technology, **116**(2), pp. 105–109.

[46] Perl, M., and Perry, J., 2005, "An Experimental-Numerical Determination of the Three-Dimensional Autofrettage Residual Stress Field Incorporating Bauschinger Effects," ASME Journal of Pressure Vessel Technology, **128**(2), pp. 173–178.

[47] Marcal, P. V., 1965, "A Stiffness Method for Elastic-Plastic Problems," International Journal of Mechanical Sciences, **7**(4), pp. 229–238.

[48] Alexandrov, S., Jeong, W., and Chung, K., 2015, "Descriptions of Reversed Yielding in Internally Pressurized Tubes," ASME Journal of Pressure Vessel Technology, **138**(1), pp. 011204-1-011204–10.

[49] Hill, R., Lee, E. H., and Tupper, S. J., 1947, "The Theory of Combined Plastic and Elastic Deformation with Particular Reference to a Thick Tube under Internal Pressure," Proceedings of the Royal Society of London A: Mathematical, Physical and Engineering Sciences, **191**(1026), pp. 278–303.

[50] Wang, G. S., 1988, "An Elastic-Plastic Solution for a Normally Loaded Center Hole in a Finite Circular Body," International Journal of Pressure Vessels and Piping, **33**(4), pp. 269–284.

[51] Nádai, A., 1950, *Theory Of Flow And Fracture Of Solids Vol-1*, McGraw-Hill, New York,.

[52] Huang, X. P., 2005, "A General Autofrettage Model of a Thick-Walled Cylinder Based on Tensile-Compressive Stress-Strain Curve of a Material," The Journal of Strain Analysis for, **40**(6), pp. 599–607.

[53] Huang, X. P., and Cui, W., 2004, "Autofrettage Analysis of Thick-Walled Cylinder Based on Tensile-Compressive Curve of Material," Key Engineering Materials, **274–276**, pp. 1035–1040.

[54] Huang, X. P., and Cui, W. C., 2005, "Effect of Bauschinger Effect and Yield Criterion on Residual Stress Distribution of Autofrettaged Tube," ASME Journal of Pressure Vessel Technology, **128**(2), pp. 212–216.

[55] Huang, X., and Moan, T., 2009, "Residual Stress in an Autofrettaged Tube Taking Bauschinger Effect as a Function of the Prior Plastic Strain," ASME Journal of Pressure Vessel Technology, **131**(2), pp. 021207-021207–7.

[56] Hosseinian, E., Farrahi, G. H., and Movahhedy, M. R., 2009, "An Analytical Framework for the Solution of Autofrettaged Tubes Under Constant Axial Strain

Condition," ASME Journal of Pressure Vessel Technology, **131**(6), pp. 061201-061201–8.

[57] Gao, X.-L., 2003, "Elasto-Plastic Analysis of an Internally Pressurized Thick-Walled Cylinder Using a Strain Gradient Plasticity Theory," International Journal of Solids and Structures, **40**(23), pp. 6445–6455.

[58] Gao, X.-L., 2007, "Strain Gradient Plasticity Solution for an Internally Pressurized Thick-Walled Cylinder of an Elastic Linear-Hardening Material," Z. angew. Math. Phys., **58**(1), pp. 161–173.

[59] Gao, X.-L., Wen, J.-F., Xuan, F.-Z., and Tu, S.-T., 2015, "Autofrettage and Shakedown Analyses of an Internally Pressurized Thick-Walled Cylinder Based on Strain Gradient Plasticity Solutions," J. Appl. Mech, **82**(4), pp. 041010-041010–12.

[60] Durban, D., and Kubi, M., 1992, "A General Solution for the Pressurized Elastoplastic Tube," J. Appl. Mech, **59**(1), pp. 20–26.

[61] Gibson, M. C., Hameed, A., Parker, A. P., and Hetherington, J. G., 2005, "A Comparison of Methods for Predicting Residual Stresses in Strain-Hardening, Autofrettaged Thick Cylinders, Including the Bauschinger Effect," ASME Journal of Pressure Vessel Technology, **128**(2), pp. 217–222.

[62] Dixit, P. M., and Dixit, U. S., 2014, *Plasticity: Fundamentals and Applications*, CRC Press, Boca Raton.

[63] Milligan, R. V., Koo, W. H., and Davidson, T. E., 1966, "The Bauschinger Effect in a High-Strength Steel," J. Basic Eng, **88**(2), pp. 480–488.

[64] Bastun, V., and Podil'chuk, I., 2017, "Bauschinger Effect Prediction in Thick-Walled Autofrettaged Cylindrical Pressure Vessels," ASME Journal of Pressure Vessel Technology, **139**(4), pp. 041404-041404–6.

[65] Prager, W., 1955, "The Theory of Plasticity: A Survey of Recent Achievements," Proceedings of the Institution of Mechanical Engineers, **169**(1), pp. 41–57.

[66] Ziegler, H., 1959, "A Modification of Prager's Hardening Rule," Quarterly of Applied mathematics, **17**(1), pp. 55–65.

[67] Jahed, H., Sethuraman, R., and Dubey, R. N., 1997, "A Variable Material Property Approach for Solving Elastic-Plastic Problems," International Journal of Pressure Vessels and Piping, **71**(3), pp. 285–291.

[68] Jahed, H., and Dubey, R. N., 1997, "An Axisymmetric Method of Elastic-Plastic Analysis Capable of Predicting Residual Stress Field," ASME Journal of Pressure Vessel Technology, **119**(3), pp. 264–273.

[69] Sedighi, M., and Jabbari, A. H., 2013, "Investigation of Residual Stresses in Thick-Walled Vessels with Combination of Autofrettage and Wire-Winding," International Journal of Pressure Vessels and Piping, **111–112**, pp. 295–301.

[70] Song, J., Tang, C. Y., Xu, B. Y., and Lee, W. B., 1994, "Strain Rate Effects on Medium Carbon Steel and Its Effects on Autofrettage," Scripta Metallurgica et Materialia, **30**(2), pp. 139–144.

[71] Marcal, P. V., and King, I. P., 1967, "Elastic-Plastic Analysis of Two-Dimensional Stress Systems by the Finite Element Method," International Journal of Mechanical Sciences, **9**(3), pp. 143–155.

[72] Chen, P., and O'Hara, G., 1983, *Finite Element Results of Pressurized Thick Tubes Based on Two Elastic-Plastic Material Models*, ARLCB-TR-83047, Army Armament Research Development and Engineering Center, Benet Weapons Lab, NY.

[73] Alegre, J. M., Bravo, P., and Preciado, M., 2006, "Design of an Autofrettaged High-Pressure Vessel, Considering the Bauschinger Effect," Proceedings of the IMechE, **220**(1), pp. 7–16.

[74] Gibson, M. C., Parker, A. P., Hameed, A., and Hetherington, J. G., 2012, "Implementing Realistic, Nonlinear, Material Stress–Strain Behavior in ANSYS for the Autofrettage of Thick-Walled Cylinders," ASME Journal of Pressure Vessel Technology, **134**(5), pp. 051202-051202–7.

[75] Feng, H., Mughrabi, H., and Donth, B., 1998, "Finite-Element Modelling of Low-Temperature Autofrettage of Thick-Walled Tubes of the Austenitic Stainless Steel AISI 304 L: Part I. Smooth Thick-Walled Tubes," Modelling Simul. Mater. Sci. Eng., **6**(1), p. 51.

[76] Feng, H., Donth, B., and Mughrabi, H., 1998, "Finite-Element Modelling of Low-Temperature Autofrettage of Thick-Walled Tubes of the Austenitic Stainless Steel AISI 304 L: Part II. Thick-Walled Tube with Cross-Bore," Modelling Simul. Mater. Sci. Eng., **6**(1), p. 71.

[77] Ayob, A., Tamin, M., and Elbasheer, M. K., 2009, "Pressure Limits of Thick-Walled Cylinders," pp. 1–4.

[78] Farrahi, G. H., Voyiadjis, G. Z., Hoseini, S. H., and Hosseinian, E., 2013, "Residual Stress Analysis of the Autofrettaged Thick-Walled Tube Using Nonlinear Kinematic Hardening," ASME Journal of Pressure Vessel Technology, **135**(2), pp. 021204-021204–8.

[79] Hojjati, M. H., and Hassani, A., 2007, "Theoretical and Finite-Element Modeling of Autofrettage Process in Strain-Hardening Thick-Walled Cylinders," International Journal of Pressure Vessels and Piping, **84**(5), pp. 310–319.

[80] Wahi, N., Ayob, A., and Elbasheer, M. K., 2011, "Effect of Optimum Autofrettage on Pressure Limits OfThick-Walled Cylinder," International Journal of Environmental Science and Development, **2**(4), pp. 329–333.

[81] Trojnacki, A., and Krasiński, M., 2014, "Numerical Verification of Analytical Solution for Autofrettaged High-Pressure Vessels," Journal of Theoretical and Applied Mechanics, **52**(3), pp. 731–744.

[82] Tuba, I. S., 1965, "Elastic Plastic Analysis for Hollow Spherical Media under Uniform Radial Loading," Journal of the Franklin Institute, **280**(4), pp. 343–355.

[83] Gao, X.-L., 1994, "An Exact Elasto-Plastic Solution for a Thick-Walled Spherical Shell of Elastic Linear-Hardening Material with Finite Deformations," International Journal of Pressure Vessels and Piping, **57**(1), pp. 45–56.

[84] Gao, X.-L., 2003, "Strain Gradient Plasticity Solution for an Internally Pressurized Thick-Walled Spherical Shell of an Elastic–Plastic Material," Mechanics Research Communications, **30**(5), pp. 411–420.

[85] Wen, J.-F., Gao, X.-L., Xuan, F.-Z., and Tu, S.-T., 2017, "Autofrettage and Shakedown Analyses of an Internally Pressurized Thick-Walled Spherical Shell Based on Two Strain Gradient Plasticity Solutions," Acta Mech, **228**(1), pp. 89–105.

[86] Chadwick, P., 1963, "Compression of a Spherical Shell of Work-Hardening Material," International Journal of Mechanical Sciences, **5**(2), pp. 165–182.

[87] Adibi-Asl, R., and Livieri, P., 2006, "Analytical Approach in Autofrettaged Spherical Pressure Vessels Considering the Bauschinger Effect," ASME Journal of Pressure Vessel Technology, **129**(3), pp. 411–419.

[88] Partom, Y., 1970, "Large Elastoplastic Deformation of a Thick-Walled Spherical Shell," International Journal of Non-Linear Mechanics, **5**(3), pp. 475–490.

[89] Hrudey, T. M., and Haddow, J. B., 1973, "Elastic-Plastic Expansion of a Thick Spherical Shell with Finite Elastic Strain," Acta Mechanica, **18**(1–2), pp. 21–34.

[90] Carroll, M. M., 1985, "Radial Expansion of Hollow Spheres of Elastic-Plastic Hardening Material," International Journal of Solids and Structures, **21**(7), pp. 645–670.

[91] Gamer, U., 1988, "The Expansion of the Elastic-Plastic Spherical Shell with Nonlinear Hardening," International Journal of Mechanical Sciences, **30**(6), pp. 415–426.
[92] Parker, A. P., and Huang, X., 2006, "Autofrettage and Reautofrettage of a Spherical Pressure Vessel," ASME Journal of Pressure Vessel Technology, **129**(1), pp. 83–88.
[93] Parker, A. P., and Huang, X., 2007, "Autofrettage of a Spherical Pressure Vessel," *Proceedings of ASME Pressure Vessels and Piping*, San Antonio, pp. 1–6.
[94] Maleki, M., Farrahi, G. H., Haghpanah Jahromi, B., and Hosseinian, E., 2010, "Residual Stress Analysis of Autofrettaged Thick-Walled Spherical Pressure Vessel," International Journal of Pressure Vessels and Piping, **87**(7), pp. 396–401.
[95] Durban, D., and Baruch, M., 1974, "Behaviour of an Incrementally Elastic Thick Walled Sphere under Internal and External Pressure," International Journal of Non-Linear Mechanics, **9**(2), pp. 105–119.
[96] Durban, D., and Baruch, M., 1977, "Analysis of an Elasto-Plastic Thick Walled Sphere Loaded by Internal and External Pressure," International Journal of Non-Linear Mechanics, **12**(1), pp. 9–22.
[97] Rupali, and Mondal, S., 2015, "Finite Element Analysis for Predicting Residual Stresses of Autofrettaged Spherical Vessels Considering Bauschinger Effect," International Journal of Scientific & Engineering Research, **6**(8), pp. 912–919.
[98] Hencky, H., 1924, "Zur Theorie Plastischer Deformationen Und Der Hierdurch Im Material Hervorgerufenen Nachspannungen," Z. angew. Math. Mech., **4**(4), pp. 323–334.
[99] Hill, R., 1998, *The Mathematical Theory of Plasticity*, Oxford university press.
[100] Jones, R. M., 2009, *Deformation Theory of Plasticity*, Bull Ridge Publishing.
[101] Rees, D. W. A., 1987, "A Theory of Autofrettage with Applications to Creep and Fatigue," International Journal of Pressure Vessels and Piping, **30**(1), pp. 57–76.
[102] Niitsu, Y, and Ikegami, K., 1990, "Effect of Temperature Variation on Cyclic Elastic-Plastic Behavior of SUS 304 Stainless Steel," ASME Journal of Pressure Vessel Technology, **112**(2), pp. 152–157.
[103] Haghpanah Jahromi, B., Farrahi, G. H., Maleki, M., Nayeb-Hashemi, H., and Vaziri, A., 2009, "Residual Stresses in Autofrettaged Vessel Made of Functionally Graded Material," Engineering Structures, **31**(12), pp. 2930–2935.
[104] Parker, A. P., and Farrow, J. R., 1980, "Technical Note: On the Equivalence of Axisymmetric Bending, Thermal, and Autofrettage Residual Stress Fields," The Journal of Strain Analysis for, **15**(1), pp. 51–52.
[105] Parker, A. P., and Farrow, J. R.., 1980, "Technical Note: On the Equivalence of Axisymmetric Bending, Thermal, and Autofrettage Residual Stress Fields," The Journal of Strain Analysis for Engineering Design, **15**(1), pp. 51–52.
[106] Perl, M., 1998, "An Improved Split-Ring Method for Measuring the Level of Autofrettage in Thick-Walled Cylinders," ASME Journal of Pressure Vessel Technology, **120**(1), pp. 69–73.
[107] Perl, M., and Aroné, R., 1994, "An Axisymmetric Stress Release Method for Measuring the Autofrettage Level in Thick-Walled Cylinders—Part I: Basic Concept and Numerical Simulation," ASME Journal of Pressure Vessel Technology, **116**(4), pp. 384–388.
[108] Prime, M. B., 1999, "Residual Stress Measurement by Successive Extension of a Slot: The Crack Compliance Method," Appl. Mech. Rev, **52**(2), pp. 75–96.
[109] Perl, M., and Aroné, R., 1994, "An Axisymmetric Stress Release Method for Measuring the Autofrettage Level in Thick-Walled Cylinders—Part II: Experimental Validation," ASME Journal of Pressure Vessel Technology, **116**(4), pp. 389–395.

[110] Stacey, A., and Webster, G. A., 1988, "Determination of Residual Stress Distributions in Autofrettaged Tubing," International Journal of Pressure Vessels and Piping, **31**(3), pp. 205–220.
[111] Jahed, H., Faritus, M. R., and Jahed, Z., 2012, "Residual Stress Measurements in an Autofrettage Tube Using Hole Drilling Method," ASME Journal of Pressure Vessel Technology, **134**(5), pp. 051501-051501–7.
[112] George, D., and Smith, D., 2000, "The Application of the Deep Hole Technique for Measuring Residual Stresses in an Autofrettaged Tube," *Proceedings of ASME Pressure Vessels and Piping*, pp. 25–32.
[113] Sachs, G., 1927, "Evidence of Residual Stresses in Rods and Tubes," Feitschriff fur Metallkunde, **19**, pp. 352–357.
[114] Cheng, W., and Finnie, I., 1985, "A Method for Measurement of Axisymmetric Axial Residual Stresses in Circumferentially Welded Thin-Walled Cylinders," ASME Journal of Engineering Materials and Technology, **107**(3), pp. 181–185.
[115] James, M., and Cohen, J., 1978, "The Measurement of Residual Stresses by X-Ray Diffraction Techniques," *Treatise on Materials Science and Technology*, pp. 1–62.
[116] Bacon, G. E., 1975, *Neutron Diffraction 3 Edition*, Clarendon Press, United Kingdom.
[117] Franklin, G. J., and Morrison, J. L. M., 1960, "Autofrettage of Cylinders: Prediction of Pressure/External Expansion Curves and Calculation of Residual Stresses," Proceedings of the Institution of Mechanical Engineers, **174**(1), pp. 947–974.
[118] Stacey, A., MacGillivary, H. J., Webster, G. A., Webster, P. J., and Ziebeck, K. R. A., 1985, "Measurement of Residual Stresses by Neutron Diffraction," The Journal of Strain Analysis for, **20**(2), pp. 93–100.
[119] Parker, A. P., Underwood, J. H., and Kendall, D. P., 1999, "Bauschinger Effect Design Procedures for Autofrettaged Tubes Including Material Removal and Sachs' Method," J. Pressure Vessel Technology, **121**(4), pp. 430–437.
[120] Parker, A. P., 2004, "A Critical Examination of Sachs' Material-Removal Method for Determination of Residual Stress," ASME Journal of Pressure Vessel Technology, **126**(2), pp. 234–236.
[121] Cheng, W., and Finnie, I., 1986, "Measurement of Residual Hoop Stresses in Cylinders Using the Compliance Method," ASME Journal of Engineering Materials and Technology **108**(2), pp. 87–92.
[122] Venter, A. M., de Swardt, R. R., and Kyriacou, S., 2000, "Comparative Measurements on Autofrettaged Cylinders with Large Bauschinger Reverse Yielding Zones," The Journal of Strain Analysis for, **35**(6), pp. 459–469.
[123] Zerari, N., Saidouni, T., and Benretem, A., 2013, "Determination of Residuals Stresses Induced by the Autofrettage Treatment by the X-Rays Diffraction Method," Modern Mechanical Engineering, **03**(03), pp. 121–126.
[124] Çandar, H., and Filiz, İ. H., 2017, "Experimental Study on Residual Stresses in Autofrettaged Thick-Walled High Pressure Cylinders," High Pressure Research, **37**(4), pp. 516–528.
[125] Underwood, J. H., DeSwardt, R. R., Venter, A. M., Troiano, E., Hyland, E. J., and Parker, A. P., 2007, "Hill Stress Calculations for Autofrettaged Tubes Compared With Neutron Diffraction Residual Stresses and Measured Yield Pressure and Fatigue Life," *Proceedings of ASME Pressure Vessels and Piping*, pp. 47–52.
[126] Ma, Y., Zhang, S. Y., Goodway, C., Done, R., Evans, B., Kirichek, O., and Bowden, Z., 2012, "A Non-Destructive Experimental Investigation of Elastic Plastic Interfaces of Autofrettaged Thick-Walled Cylindrical Aluminium High Pressure Vessels," High Pressure Research, **32**(3), pp. 364–375.

[127] Langer, B. F., 1971, "Design-Stress Basis for Pressure Vessels," Experimental Mechanics, **11**(1), pp. 1–11.
[128] Majzoobi, G. H., Farrahi, G. H., and Mahmoudi, A. H., 2003, "A Finite Element Simulation and an Experimental Study of Autofrettage for Strain Hardened Thick-Walled Cylinders," Materials Science and Engineering: A, **359**(1–2), pp. 326–331.
[129] Seifi, R., and Babalhavaeji, M., 2012, "Bursting Pressure of Autofrettaged Cylinders with Inclined External Cracks," International Journal of Pressure Vessels and Piping, **89**, pp. 112–119.
[130] Chen, P. C., 1988, *A Simple Analysis of the Swage Autofrettage Process*, ARCCB-TR-88037, Army Armament Research Development and Engineering Center, Benet Weapons Lab, NY.
[131] Rees, D. W. A., 2011, "A Theory for Swaging of Discs and Lugs," Meccanica, **46**(6), pp. 1213–1237.
[132] Parker, A. P., O'Hara, G. P., and Underwood, J. H., 2003, "Hydraulic Versus Swage Autofrettage and Implications of the Bauschinger Effect," ASME Journal of Pressure Vessel Technology, **125**(3), pp. 309–314.
[133] Perry, J., and Perl, M., 2008, "A 3-D Model for Evaluating the Residual Stress Field Due to Swage Autofrettage," ASME Journal of Pressure Vessel Technology, **130**(4), pp. 041211-041211–6.
[134] Iremonger, M. J., and Kalsi, G. S., 2003, "A Numerical Study of Swage Autofrettage," ASME Journal of Pressure Vessel Technology, **125**(3), pp. 347–351.
[135] Till, E. T., and Rammerstorfer, F. G., 1983, "Nonlinear Finite Element Analysis of an Autofrettage Process," Computers & Structures, **17**(5), pp. 857–864.
[136] Bihamta, R., Movahhedy, M. R., and Mashreghi, A. R., 2007, "A Numerical Study of Swage Autofrettage of Thick-Walled Tubes," Materials & Design, **28**(3), pp. 804–815.
[137] C. Gibson, M., Hameed, A., and Hetherington, J. G., 2012, "Investigation of Driving Force Variation During Swage Autofrettage, Using Finite Element Analysis," ASME Journal of Pressure Vessel Technology, **134**(5), pp. 051203-051203–7.
[138] Gibson, M. C., Hameed, A., and Hetherington, J. G., 2014, "Investigation of Residual Stress Development During Swage Autofrettage, Using Finite Element Analysis," ASME Journal of Pressure Vessel Technology, **136**(2), pp. 021206-021206–7.
[139] O'Hara, G. P., 1992, *Analysis of the Swage Autofrettage Process*, ARCCB-TR-92016, Army Armament Research Development and Engineering Center, Benet Weapons Lab, NY.
[140] Chen, P. C., 1988, *Finite Element Analysis of the Swage Autofrettage Process*, ARCCB-TR-88037, Army Armament Research Development and Engineering Center, Benet Weapons Lab, NY.
[141] Barbachano, H., Alegre, J. M., and Cuesta, I. I., "FEM Simulation of the Swage Tube Forming (STF) in Cylinders Subjected to Internal Pressure," Anales de Mecanica de la Fractura, **28**(2), pp. 481–486.
[142] Hua, Z., and Penumarthy, C., 2014, "Computer Modeling and Optimization of Swage Autofrettage Process of a Thick-Walled Cylinder Incorporating Bauschinger Effect," American Transactions on Engineering & Applied Sciences, **3**, pp. 31–63.
[143] Chang, L., Pan, Y., and Ma, X., 2013, "Residual Stress Calculation of Swage Autofrettage Gun Barrel," International Journal of Computer Science Issues, **10**(2), pp. 52–59.
[144] S Jin, C., and S Yuan, R., 2018, "Design and Analysis of the Swage for Swage Autofrettage with a Center Hole," IOP Conference Series: Materials Science and Engineering, **392**, p. 062041.

[145] Hu, Z., 2019, "Design of Two-Pass Swage Autofrettage Processes of Thick-Walled Cylinders by Computer Modeling," Proceedings of the Institution of Mechanical Engineers, Part C: Journal of Mechanical Engineering Science, **233**(4), pp. 1312–1333.

[146] Chaboche, J. L., 2008, "A Review of Some Plasticity and Viscoplasticity Constitutive Theories," International Journal of Plasticity, **24**(10), pp. 1642–1693.

[147] Davidson, T. E., Kendall, D. P., and Reiner, A. N., 1963, "Residual Stresses in Thick-Walled Cylinders Resulting from Mechanically Induced Overstrain," Experimental Mechanics, **3**(11), pp. 253–262.

[148] Clark, G., 1982, *Residual Stresses in Swage-Autofrettaged Thick-Walled Cylinders*, MRL-R-847, Materials Research Labs, Ascot Vale, Australia.

[149] Clark, G., 1984, "Fatigue Crack Growth through Residual Stress Fields—Theoretical and Experimental Studies on Thick-Walled Cylinders," Theoretical and Applied Fracture Mechanics, **2**(2), pp. 111–125.

[150] Lee, S., O'Hara, G., Olmstead, V., and Capsimalis, G., 1992, *Characterization of Residual Stresses in an Eccentric Swage Autofrettaged Thick-Walled Steel Cylinder*, ARCCB-TR-92017, Army Armament Research Development and Engineering Center, Benet Weapons Lab, NY.

[151] Zare, H. R., and Darijani, H., 2017, "Strengthening and Design of the Linear Hardening Thick-Walled Cylinders Using the New Method of Rotational Autofrettage," International Journal of Mechanical Sciences, **124–125**(Supplement C), pp. 1–8.

[152] Kamal, S. M., 2017, "An Analytical Study of Rotational Autofrettage of Thick-Walled Disks," Tezpur, Assam, pp. 69–74.

[153] Kamal, S. M., 2018, "Analysis of Residual Stress in the Rotational Autofrettage of Thick-Walled Disks," ASME Journal of Pressure Vessel Technology, **140**(6).

[154] Kamal, S. M., Perl, M., and Bharali, D., 2019, "Generalized Plane Strain Study of Rotational Autofrettage of Thick-Walled Cylinders—Part I: Theoretical Analysis," ASME Journal of Pressure Vessel Technology, **141**(5).

[155] Kamal, S. M., and Perl, M., 2019, "Generalized Plane Strain Study of Rotational Autofrettage of Thick-Walled Cylinders—Part II: Numerical Evaluation," ASME Journal of Pressure Vessel Technology, **141**(5).

[156] Chakrabarty, J., 2006, *Theory of Plasticity*, Butterworth-Heinemann, Amsterdam.

[157] Morrison, J. L. M., Crossland, B., and Parry, J. S. C., 1960, "Strength of Thick Cylinders Subjected to Repeated Internal Pressure," Proceedings of the Institution of Mechanical Engineers, **174**(1), pp. 95–117.

[158] Parker, A. P., 2004, "A Re-Autofrettage Procedure for Mitigation of Bauschinger Effect in Thick Cylinders," ASME Journal of Pressure Vessel Technology, **126**(4), pp. 451–454.

[159] Varga, L., 1991, "Design of Optimum High-Pressure Monobloc Vessels," International Journal of Pressure Vessels and Piping, **48**(1), pp. 93–110.

[160] Zhu, R., and Yang, J., 1998, "Autofrettage of Thick Cylinders," International Journal of Pressure Vessels and Piping, **75**(6), pp. 443–446.

[161] Darijani, H., Kargarnovin, M. H., and Naghdabadi, R., 2009, "Design of Thick-Walled Cylindrical Vessels under Internal Pressure Based on Elasto-Plastic Approach," Materials & Design, **30**(9), pp. 3537–3544.

[162] Çandar, H., and Filiz, İ. H., 2017, "Optimum Autofrettage Pressure for a High Pressure Cylinder of a Waterjet Intensifier Pump," Universal Journal of Engineering Science, **5**(3), pp. 44–55.

[163] Perl, M., and Perry, J., 2010, "The Beneficial Contribution of Realistic Autofrettage to the Load-Carrying Capacity of Thick-Walled Spherical Pressure Vessels," ASME Journal of Pressure Vessel Technology, **132**(1), pp. 011204-011204–6.
[164] Koh, S. K., and Stephens, R. I., 1991, "Stress Analysis of an Autofrettaged Thick-Walled Pressure Vessel Containing an External Groove," International Journal of Pressure Vessels and Piping, **46**(1), pp. 95–111.
[165] Hashmi, S., 2016, *Comprehensive Materials Finishing*, Elsevier.
[166] Dixit, P. M., and Dixit, U. S., 2008, *Modeling of Metal Forming and Machining Processes: By Finite Element and Soft Computing Methods*, Springer, London.
[167] Barbáchano, H., Alegre, J., and Cuesta, I., 2011, "FEM Simulation of the Swage Tube Forming (STF) in Cylinders Subjected to Internal Pressure," **2**(28), pp. 481–486.
[168] De Oliveira, W. P., Savi, M. A., Pacheco, P. M. C. L., and De Souza, L. F. G., 2010, "Thermomechanical Analysis of Steel Cylinders Quenching Using a Constitutive Model with Diffusional and Non-Diffusional Phase Transformations," Mechanics of Materials, **42**(1), pp. 31–43.
[169] Phadke, S., Pauskar, P., and Shivpuri, R., 2004, "Computational Modeling of Phase Transformations and Mechanical Properties during the Cooling of Hot Rolled Rod," Journal of Materials Processing Technology, **150**(1), pp. 107–115.
[170] Callister, W. D., and Rethwisch, D. G., 2009, *Materials Science and Engineering: An Introduction*, John Wiley and Sons, Hoboken, NJ.
[171] Kamal, S. M., Dixit, U. S., Roy, A., Liu, Q., and Silberschmidt, V. V., 2017, "Comparison of Plane-Stress, Generalized-Plane-Strain and 3D FEM Elastic–Plastic Analyses of Thick-Walled Cylinders Subjected to Radial Thermal Gradient," International Journal of Mechanical Sciences, **131–132**(Supplement C), pp. 744–752.
[173] Wang, K. F., Chandrasekar, S., and Yang, H. T. Y., 1997, "Experimental and Computational Study of the Quenching of Carbon Steel," ASME Journal of Manufacturing Science and Engineering, **119**(3), pp. 257–265.
[174] Denis, S., Sjöström, S., and Simon, A., 1987, "Coupled Temperature, Stress, Phase Transformation Calculation," MTA, **18**(7), pp. 1203–1212.
[175] Incropera, F. P., DeWitt, D. P., Bergman, T. L., and Lavine, A. S., 2006, *Fundamentals of Heat and Mass Transfer*, John Wiley & Sons, Hoboken, NJ.
[175] Zhang, L., Reutzel, E. W., and Michaleris, P., 2004, "Finite Element Modeling Discretization Requirements for the Laser Forming Process," International Journal of Mechanical Sciences, **46**(4), pp. 623–637.
[176] Gür, C. H., and Tekkaya, A. E., 2001, "Numerical Investigation of Non-Homogeneous Plastic Deformation in Quenching Process," Materials Science and Engineering: A, **319–321**, pp. 164–169.
[177] "Geekcreit® 1000W 20A ZVS Induction Heating Machine Cooling Fan PCB Copper Tube 12-36V," accessed: 12-Mar-2019, https://www.banggood.in/1000W-20A-ZVS-Induction-Heating-Machine-Cooling-Fan-PCB-Copper-Tube-12-36V-p-1089662.html.
[178] H. B. Dwight, 1918, "Skin Effect in Tubular and Flat Conductors," Transactions of the American Institute of Electrical Engineers, **37**(2), pp. 1379–1403.
[179] "MAX6675 Cold-Junction-Compensated K-Thermocouple-to-Digital Converter (0°C to +1024°C)-Maxim" accessed: 16-Feb-2019, https://www.maximintegrated.com/en/products/sensors/MAX6675.html.
[180] Pharr, G. M., Tsui, T. Y., Bolshakov, A., and Oliver, W. C., 1994, "Effects of Residual Stress on the Measurement of Hardness and Elastic Modulus Using Nanoindentation," MRS Online Proceedings Library Archive, **338**.
[181] Tosha, K., 2002, "Influence of Residual Stresses on the Hardness Number," p. 7.

[182] Parker, A. P., and Farrow, J. R., 1981, "Stress Intensity Factors for Multiple Radial Cracks Emanating from the Bore of an Autofrettaged or Thermally Stressed, Thick Cylinder," Engineering Fracture Mechanics, **14**(1), pp. 237–241.
[183] Perl, M., and Aroné, R., 1988, "Stress Intensity Factors for a Radially Multicracked Partially Autofrettaged Pressurized Thick-Walled Cylinder," ASME Journal of Pressure Vessel Technology, **110**(2), pp. 147–154.
[184] Canale, L. de C. F., Sarmiento, G. S., Totten, G. E., and Penha, R. N., "Effect of Vegetable Oil Oxidation on the Ability to Harden AISI 4140 Steel," pp. 3209–3217.
[185] Cheng, H., Xie, J., and Li, J., 2004, "Determination of Surface Heat-Transfer Coefficients of Steel Cylinder with Phase Transformation during Gas Quenching with High Pressures," Computational Materials Science, **29**(4), pp. 453–458.
[186] Banks-Sills, L., and Marmur, I., 1989, "Influence of Autofrettage on Fracture Toughness," Int J Fract, **40**(2), pp. 143–155.
[187] Loflin, L., 2015, "Simple 3-Wire MAX6675 Thermocouple ADC Arduino Interface" accessed: 14-Feb-2020: http://www.bristolwatch.com/ele2/therc.htm.

Appendix A

Basics of FEM in ABAQUS®

This Appendix describes the basic equations for displacement based finite element analysis. The finite element method (FEM) may be considered as a technique for solving differential equations by converting them to algebraic equation. The main window of ABAQUS® graphical user interface (GUI) is shown in Fig. A1. The procedure for carrying out a typical FEM analysis in ABAQUS may be divided into three steps— preprocessing, simulation and post processing. These steps are explained in the following subsections.

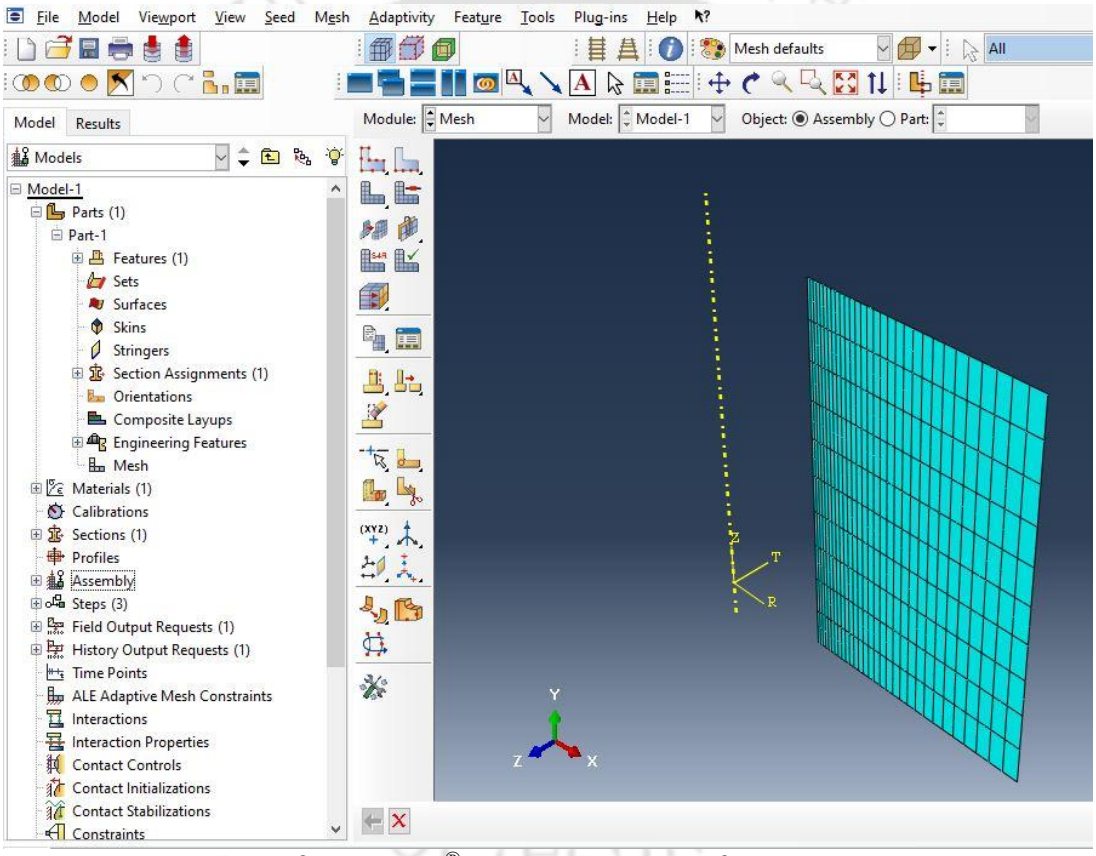

Figure A1 Main window of ABAQUS® graphical user interface (GUI)

A1. Preprocessing

In this stage geometric model of the problem is created as an input file. The model may be created using the ABAQUS® GUI, imported from a computer aided design (CAD) software or by programming the input file through a text editor. The pre-processing module in carried out in the model tree labelled as Model-1. The part model is created in the Parts module. The material behavior is defined in the Materials module. The Section module is used to assign a particular material behavior to the desired part created in the Parts module. The Assembly

module assigns the part or parts being created to an assembly. The Steps module defines the number of analysis steps required. The step module is usually used for changing the type of loading. In Fig. A1, there are three steps such as the initial step, Step 1 and Step 2. In autofrettage modeling, the Step 1 can be for loading and the Step 2 can be for unloading. The Load module is used to define the loading conditions and the Boundary Conditions module is used to define the boundary conditions. The model is discretized into finite number of elements using the mesh tool in the Parts module. Elements may be in the form of different shapes and sizes. The cost and time of the computation increase with increase in the number of elements and is usually decided by a mesh sensitivity analysis. In this study, an 8-node axisymmetric quadrilateral element is used as shown in in Fig. A2.

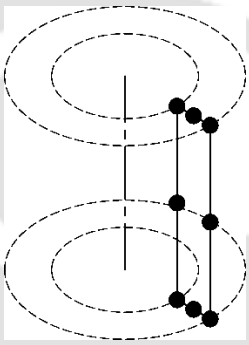

Figure A2 Schematic of an 8-node axisymmetric quadrilateral element

In preprocessing step, the elemental equations are developed in the background. There are various approaches for obtaining the elemental equations in FEM some of which are the direct stiffness method, virtual work method, principle of minimum energy method and the Galerkin's method. The virtual work method has been briefly described in the Theory Guide of ABAQUS®. Here it is explained in detail.

Virtual work is the work done by a real force acting through a virtual displacement or a virtual force acting through a real displacement. The principle of virtual work states that in equilibrium condition of a domain, the total work done by the forces due to a virtual displacement is zero. It is required that the virtual displacement must satisfy the boundary conditions at the supports.

Let δu be a virtual displacement field in a domain that vanishes on the part of the boundary where the actual displacement field is prescribed, i.e., $\delta u = 0$ on S_u. The external work done due to the virtual displacement is

$$\delta W = \int_V b_i \delta u_i \mathrm{d}V + \int_S t_i \delta u_i \mathrm{d}S \tag{A3}$$

where b_i is the i^{th} component of the body force per unit volume, t_i is the i-th traction component, V is the domain with boundary S. The entire boundary S for the integral term in Equation A4 can divided into two parts:

- S_u : The part of the boundary where the incremental displacement du is specified
- S_t : The part of the boundary where the traction t_i is specified

Since $\delta u = 0$ at the part of the boundary where the incremental displacement du is prescribed, the surface integral term in over S_u reduces to 0. Hence, only the integral over the surface S_t remains. In absence of body forces, Eqn. (A3) reduces to

$$\delta W = \int_{S_t} t_i \delta u_i \mathrm{d}S \tag{A4}$$

The total internal work δU is given by

$$\delta U = \int_{V} \sigma_{ij} \delta \varepsilon_{ij} \mathrm{d}V \tag{A5}$$

where σ_{ij} are the components of the stress tensor and $\delta\varepsilon_{ij}$ is the virtual strain field resulting from the virtual displacement field given by

$$\delta \varepsilon_{ij} = \frac{1}{2}\left(\frac{\partial \delta u_i}{\partial x_j} + \frac{\partial \delta u_j}{\partial x_i} \right) \tag{A6}$$

The principle of virtual work requires that that the stress, body force and traction are in equilibrium if and only if the total internal virtual work equals the external virtual work for every virtual displacement field. Therefore,

$$\delta W = \delta U \tag{A7}$$

$$\int_{V} \sigma_{ij} \delta \varepsilon_{ij} \mathrm{d}V = \int_{S_t} t_i \delta u_i \mathrm{d}S \tag{A8}$$

To begin the FEM formulation of Equation (A8), it is first converted into array representation as follows [166]:

$$\int_{V} \left\{\delta \varepsilon_{ij}\right\}^{\mathrm{T}} \left\{\sigma_{ij}\right\} \mathrm{d}V = \int_{S_t} \left\{\delta u_i\right\}^{\mathrm{T}} \left\{t_i\right\} \mathrm{d}S, \tag{A9}$$

where

$$\left\{\delta \varepsilon_{ij}\right\} = \begin{Bmatrix} \delta\varepsilon_{xx} \\ \delta\varepsilon_{yy} \\ \delta\varepsilon_{zz} \\ 2\delta\varepsilon_{xy} \\ 2\delta\varepsilon_{yz} \\ 2\delta\varepsilon_{zx} \end{Bmatrix}, \quad \left\{\sigma_{ij}\right\} = \begin{Bmatrix} \sigma_{xx} \\ \sigma_{yy} \\ \sigma_{zz} \\ \sigma_{xy} \\ \sigma_{yz} \\ \sigma_{zx} \end{Bmatrix}, \quad \left\{t_i\right\} = \begin{Bmatrix} t_x \\ t_y \\ t_z \end{Bmatrix}, \quad \left\{\delta u_i\right\} = \begin{Bmatrix} \delta u_x \\ \delta u_y \\ \delta u_z \end{Bmatrix}. \tag{A10}$$

The incremental displacement vector $\{\Delta u\}$ for a volume element is given by

$$\{\Delta u\} = \begin{Bmatrix} \Delta u_x \\ \Delta u_y \\ \Delta u_z \end{Bmatrix} = [\phi]\{\Delta u\}^e, \tag{A11}$$

where $[\phi]$ is the shape function matrix

$$[\phi] = \begin{bmatrix} \{\phi_1\}^{\mathrm{T}} \\ \{\phi_2\}^{\mathrm{T}} \\ \{\phi_3\}^{\mathrm{T}} \end{bmatrix} \tag{A12}$$

shown in expanded form as

$$\begin{aligned} {}^t\{\phi_1\}^{\mathrm{T}} &= \{N_1,\ 0,\ 0\ ,N_2,\ 0,\ 0\ ,N_3,\ 0,\ 0\ ,...N_n,\ 0,\ 0\ \}, \\ {}^t\{\phi_2\}^{\mathrm{T}} &= \{\ 0,\ N_1,\ 0\ ,\ 0,\ N_2,\ 0\ ,\ 0,\ N_3,\ 0\ ,...,\ 0,\ N_n,\ 0\ \}, \\ {}^t\{\phi_3\}^{\mathrm{T}} &= \{\ 0,\ 0,\ N_1,\ 0,\ 0,\ N_2,\ 0,\ 0,\ N_3,...,\ 0,\ 0,\ N_n\}, \end{aligned} \tag{A13}$$

where N_i are the shape functions for the n-noded element and $\{\Delta u\}^e$ is the incremental displacement vector at the specific nodes for the n-noded element and is expressed as follows:

$$\{\Delta u\}^{e\mathrm{T}} = \{\Delta u_x^1, \Delta u_y^1, \Delta u_z^1, ...\Delta u_x^n, \Delta u_y^n, \Delta u_z^n\}. \tag{A14}$$

When the volume domain V is discretized into volume elements, the surface domain S_t at the boundary is automatically discretized into area elements. For example, if the domain V is discretized with 8-node brick elements as shown in Fig. A3(b), then the surface domain S is discretized into 4-node quadrilateral elements. Following this, the elemental equations are derived from Equation A9.

Since, the virtual displacement field must be compatible with all the kinematic constrains, the shape functions also govern the spatial variation of the virtual displacement field. Therefore,

$$\{\delta u\} = \begin{Bmatrix} \delta u_x \\ \delta u_y \\ \delta u_z \end{Bmatrix} = [\phi]\{\delta u\}^e, \tag{A15}$$

where $\{\Delta\delta u\}^e$ is the virtual displacement vector at the specific nodes for the n-noded brick element e and is given as

$$\{\delta u\}^{e\mathrm{T}} = \{\delta u_x^1,\ \delta u_y^1\ ,\delta u_z^1,..., \delta u_x^n\ ,\delta u_y^n\ ,\delta u_z^n\}. \tag{A16}$$

The term $\delta\varepsilon_{ij}$ can be written as

$$\{\delta\varepsilon\} = [B_L]\{\delta u\}^e, \tag{A17}$$

where

$$[B_L] = \begin{bmatrix} \{\phi_1\},_x^{\mathrm{T}} \\ \{\phi_2\},_x^{\mathrm{T}} \\ \{\phi_3\},_x^{\mathrm{T}} \\ \{\phi_2\},_x^{\mathrm{T}} + \{\phi_1\},_y^{\mathrm{T}} \\ \{\phi_3\},_y^{\mathrm{T}} + \{\phi_2\},_z^{\mathrm{T}} \\ \{\phi_3\},_x^{\mathrm{T}} + \{\phi_1\},_z^{\mathrm{T}} \end{bmatrix}. \tag{A18}$$

Similarly, for the term on the right hand side of Equation (A12), the approximation for the area element is given as

$$\{\delta u_i\} = \begin{Bmatrix} \delta u_x \\ \delta u_y \\ \delta u_z \end{Bmatrix} = [\phi]^b \{\delta u\}^e, \tag{A19}$$

where

$$[\phi]^b = \begin{bmatrix} \{\phi_1\}^{b\mathrm{T}} \\ \{\phi_2\}^{b\mathrm{T}} \\ \{\phi_3\}^{b\mathrm{T}} \end{bmatrix}, \tag{A20}$$

The shape function matrix $[\phi]^b$ for the area element shown in expanded form as

$$\begin{aligned} \{\phi_1\}^{b\mathrm{T}} &= \{N_1^b,\ 0,\ 0,\ N_2^b,\ 0,\ 0,\ N_3^b,\ 0,\ 0,\ldots, N_{nb}^b,\ 0,\ 0\}, \\ \{\phi_2\}^{b\mathrm{T}} &= \{0,\ N_1^b,\ 0,\ 0,\ N_2^b,\ 0,\ 0,\ N_3^b,\ 0,\ldots,\ 0,\ N_{nb}^b,\ 0\}, \\ \{\phi_3\}^{b\mathrm{T}} &= \{0,\ 0,\ N_1^b,\ 0,\ 0,\ N_2^b,\ 0,\ 0,\ N_3^b,\ldots,\ 0,\ 0,\ N_{nb}^b\}, \end{aligned} \tag{A21}$$

where N_i^b are the shape functions for the boundary. The vector $\{\delta u\}^b$ of a surface element at the boundary is given as

$$\{\delta u_i\}^{b\mathrm{T}} = \{\delta u_x^{b1},\ \delta u_y^{b1},\ \delta u_z^{b1},\ldots,\delta u_x^{bn_b},\ \delta u_y^{bn_b},\ \delta u_z^{bn_b}\}. \tag{A22}$$

If the total number of elements used is N_e, using Equations A17 and A19 in Equation A9 and following the elemental assembly procedure for FEM provides

$$\sum_{e=1}^{N_e}\{w_i\}^{eT}\{f_i\}_{in}^{e}=\sum_{b=1}^{N_b}\{w_i\}^{bT}\{f_i\}_{ex}^{e}, \tag{A23}$$

where

$$\{f_i\}_{in}^{e}=\int_{V^e}[B_L]^{T}\{\sigma_{ij}\}dV, \tag{A24}$$

and

$$\{f\}_{ex}^{b}=\int_{S_t^b}[\phi]^{bT}\{t\}dS. \tag{A25}$$

where $\{f_i\}_{in}^{e}$ is the elemental internal force vector and $\{f_i\}_{ex}^{b}$ is the elemental force vector. The summation symbol Σ represents the assembling operation of the elements. The representation of Equation A23 in the assembled form is given by

$$\{\delta u\}^{T}\{F\}_{in}=\{\delta u\}^{T}\{F\}_{ex}, \tag{A26}$$

where $\{F_{in}\}$ is the global internal force vector, $\{F_{ex}\}$ is the global external force vector and $\{\delta u\}$ is the global virtual displacement vector. Since $\{\delta u\}$ is arbitrary, Equation A26 reduces to

$$\{F\}_{ex}-\{F\}_{in}=\{0\}. \tag{A27}$$

A2. Simulation

The simulation, is the stage in which ABAQUS® solves the numerical problem defined in the model. The simulation is carried out in the Analysis module shown in Fig A1. After the problem has been correctly defined, a job is created and then submitted. The problem is solved in the background.

The discretized equilibrium equation given in Equation A27 solved using the numerical method of Newton Raphson using an iterative procedure. It is implemented by using the following equation:

$$\{F\}_{in}^{i}=\{F\}_{in}^{i-1}\left.\frac{\partial\{F_{in}\}}{\partial\{\Delta U\}}\right|_{\{\Delta U\}=\{\Delta U\}^{(i-1)}}\left(\{\Delta U\}^{(i)}-\{\Delta U\}^{(i-1)}\right), \tag{A28}$$

where $\{U\}^{(i-1)}$ is the global incremental displacement vector in the previous iteration and $\{U\}^{(i)}$ is the corresponding vector in the current iteration. The above equation can be rearranged in the following form:

$$[K]^{(i-1)}\left(\{\Delta U\}^{(i)}-\{\Delta U\}^{(i-1)}\right)=\{R\}^{(i-1)}, \tag{A29}$$

where $[K]^{(i-1)}$ is the global stiffness matrix given by

$$ {}^{t+\Delta t}[K]^{(i-1)} = \left. \frac{\partial^{t+\Delta t}\{F_{in}\}}{\partial_t\{U\}} \right|_{{}_t\{\Delta U\}={}_t\{\Delta U\}^{(i-1)}}, \tag{A30} $$

and the vector $\{R\}^{(i-1)}$ denotes the unbalanced force between the external force vector $\{F_{ex}\}$and the internal force vector $\{F\}_{in}^{(i-1)}$calculated in the $(i-1)^{\text{th}}$ iteration. Therefore,

$$ \{R\}^{(i-1)} = \{F\}_{ex} - \{F\}_{in}^{(i-1)}. \tag{A31} $$

The Newton-Raphson equation given by Equation A28 is for the assumption that the internal force vector $\{F_{in}\}$is a function of $\{\Delta U\}$ and independent of the external force vector $\{F_{ex}\}$ If $\{F_{in}\}$is instead a function of $\{F_{ex}\}$, then Equation A28 is applied with the slight modification that$\{U\}$is replaced with $\{F_{ex}\}$.

The solution procedure is initiated using a guess solution of $\{\Delta U\}$ which is obtained by solving the following equation:

$$ [K]\{\Delta U\} = \{F\}_{ex}. \tag{A32} $$

The iterative method is implemented in the following way—the global displacement vector $\{\Delta U\}^{(i-1)}$ in the $(i-1)^{\text{th}}$ iteration is used to update the domain to $V^{(i-1)}$. Corresponding to the domain $V^{(i-1)}$, the shape function matrix $[\phi]^{(i-1)}$ is calculated. Using the elemental equations and of FEM, the incremental displacement vector is approximated for an element e as

$$ {}_t\{\Delta u\} = {}^{t+\Delta t}[\phi]^{(i-1)}\ {}_t\{\Delta u\}^{e(i-1)}, \tag{A33} $$

where $\{\Delta u\}^{e(i-1)}$ is the incremental displacement vector for the element in the $(i-1)^{\text{th}}$ iteration. Using the approximation of $\{\Delta u\}$, the strain is calculated. Subsequently the incremental stress $\sigma^{(i-1)}$ is determined. Then finally the internal force vector is calculated as

$$ \{f\}_{in}^{e(i-1)} = \int_{V^{e(i-1)}} [B_L]^{(i\text{-}1)\mathrm{T}} \{\sigma\}^{(i-1)} \mathrm{d}V, \tag{A36} $$

During the implementation of the solution, the global internal force vector $\{F\}_{in}^{(i-1)}$, it is assumed that the external force vector $\{F_{ex}\}$ is independent of $\{\Delta U\}$. The iterative equation A28 is to be solved until the unbalanced force vector $\{R\}^{(i-1)}$ converges to a very small value. The convergence of the procedure can be provided using a tolerance criterion as follows:

$$ \frac{\left\| {}^{t+\Delta t}\{R\}^{(i-1)} \right\|}{\left\| {}^{t+\Delta t}\{F\}_{ex} \right\|} \le tol, \tag{A37} $$

where *tol* is a tolerance parameter and $\|\{a_i\}\|$ denotes the norm of an array defined as

$$ \left\|\{a_i\}\right\| = \sum a_i^2. \tag{A38} $$

The Newton Raphson method given by Equation A28 is called the full Newton Raphson iterative scheme. In this scheme, the global stiffness matrix $[K]^{(i-1)}$ is updated in each iteration. This process takes a lot of computational time. To overcome this, a modified Newton Raphson scheme is sometimes used in which the global stiffness is kept as a constant $[K]$ matrix for every iteration.

A3. Post processing

After the simulation has been completed the field variables such as displacements, stresses can be obtained interactively using the Visualization module. The Visualization module has a various option for displaying the results in the form of coloured contour plots, animations, deformed shape plots, and *X*–*Y* plots. The typical graphical contour showing the variation of the von Mises stress on the axisymmetric model of a hydraulic autofrettage model after the simulation has been shown in Fig. A3. The (Avg: 75%) in the contour box signifies that if the values of the von Mises stresses between two adjacent nodes are within 75% of each other, then they will be averaged and then displayed.

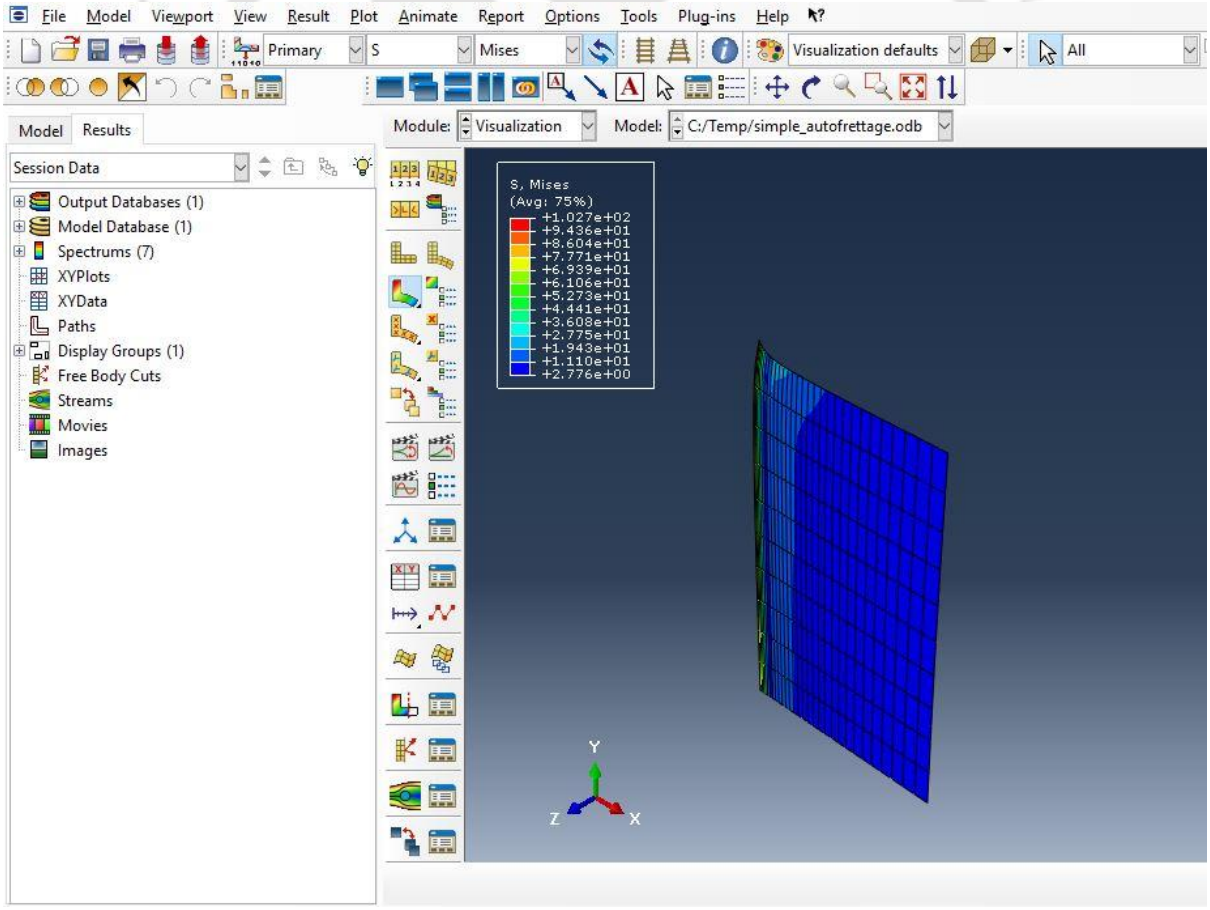

Figure A3 A typical contour plot in the ABAQUS® GUI

Appendix B

Subroutine for Phase Transformation Kinetics

This Appendix the SDVINI and UMATHT subroutine for implementing the phase transformation kinetics in ABAQUS®. Both subroutines are written in the same FORTRAN file. The SDVINI subroutine is called only once whereas the UMATHT subroutine is called in each increment.

```
      SUBROUTINE SDVINI(STATEV,COORDS,NSTATV,NCRDS,NOEL,NPT,LAYER,KSPT)
C
      INCLUDE 'ABA_PARAM.INC'
C
      DIMENSION STATEV(NSTATV),COORDS(NCRDS)
C
      WRITE(6,*)'SDVINI CALLED'

      STATEV(1)=0             ! Austenite fraction
      STATEV(2)=0.55          ! Pearlite fraction
      STATEV(3)=0.45          ! Bainite fraction

      STATEV(4)=0             ! Martensite fraction
      STATEV(5)=0             ! Incremental Pearlite fraction
      STATEV(6)=0             ! Incremental Bainite fraction
      STATEV(7)=0             ! Incremental Martensite fraction

      RETURN
      END

      SUBROUTINE UMATHT(U,DUDT,DUDG,FLUX,DFDT,DFDG,STATEV,TEMP,
      1 DTEMP,DTEMDX,TIME,DTIME,PREDEF,DPRED,CMNAME,NTGRD,NSTATV,
      2 PROPS,NPROPS,COORDS,PNEWDT,NOEL,NPT,LAYER,KSPT,KSTEP,KINC)
C
      INCLUDE 'ABA_PARAM.INC'
C
      CHARACTER*80 CMNAME
C
      DIMENSION DUDG(NTGRD),FLUX(NTGRD),DFDT(NTGRD),
      1 DFDG(NTGRD,NTGRD),STATEV(NSTATV),DTEMDX(NTGRD),TIME(2),
      2 PREDEF(1),DPRED(1),PROPS(NPROPS),COORDS(3)

      DOUBLE PRECISION ETAK,BK,TAU,TEMP,DTEMP
      DOUBLE PRECISION XAUS,XPER,XBAIN,XMAR,NMZTEMP,TSTART,TFINISH
      INTEGER :: AE1=715,TBN=540,TMS=225,ONE=1.0D0
      PARAMETER (TOLER=1.D-6)

C----------------------------- AUSTENITIZATION CHECK ----------------------
      IF (TEMP.GE.AE1) THEN
          STATEV(1)=1
          STATEV(2)=0
          STATEV(3)=0
          STATEV(4)=0
      END IF
```

```
C----------------------- LOCAL VARIABLES ASSINGMENT -----------------------

    XAUS=STATEV(1)
    XPER=STATEV(2)
    XBAIN=STATEV(3)
    XMAR=STATEV(4)

    DXPER=STATEV(5)
    DXBAIN=STATEV(6)
    DXMAR=STATEV(7)

    IF (XAUS.GT.TOLER) THEN         ! Check available Austenite fraction

C----------------- CHECK TEMPERATURE IN THE PEARLITIC RANGE---------------

    IF (TEMP.LT.AE1 .AND. TEMP.GT.TBN) THEN

C   START TIME POLYNOMIAL INTERPOLATION FROM TTT DIAGRAM

        NMZTEMP=(TEMP-566.1)/158.8

        TSTART = 6.98E10*EXP(-((NMZTEMP-1.359)/0.08374)**2)
        TSTART = TSTART + 3.03E4*EXP(-((NMZTEMP - 77.72)/32.91)**2)
        TSTART = TSTART + 33.86*EXP(-((NMZTEMP - 1.633)/0.4003)**2)
        TSTART = TSTART - 154.9*EXP(-((NMZTEMP - 4.217)/7.652)**2)
        TSTART = TSTART + 2.741*EXP(-((NMZTEMP + 2.195)/1.27)**2)
        TSTART = TSTART + 0.3828*EXP(-((NMZTEMP + 1.681)/0.2824)**2)
        TSTART = TSTART - 7.761*EXP(-((NMZTEMP + 2.754)/1.637)**2)
        TSTART =10**TSTART

C       FINISHING TIME POLYNOMIAL INTERPOLATION FROM TTT DIAGRAM

        NMZTEMP=(TEMP-538.8)/154.2

        TFINISH = 2.469E6*EXP(-((NMZTEMP-2.93)/0.5094)**2)
        TFINISH = TFINISH + 176.1*EXP(-((NMZTEMP+4.457)/0.939)**2)
        TFINISH = TFINISH - 0.01039*EXP(-((NMZTEMP+1.835)/0.06161)**2)
        TFINISH = TFINISH - 13.4*EXP(-((NMZTEMP+1.826)/1.038)**2)
        TFINISH = TFINISH + 17.2*EXP(-((NMZTEMP+1.897)/1.148)**2)
        TFINISH = TFINISH + 2.204E4*EXP(-((NMZTEMP-8.61)/2.543)**2)
        TFINISH = 10**TFINISH

        ETAK=LOG(TSTART/TFINISH)
        ETAK=-6.1273/ETAK

        BK=(TSTART**ETAK)
        BK=0.01005/BK

        TAU=-LOG(1 - XPER)
        TAU=TAU/BK
        TAU=TAU**(1/ETAK)
        TAU=TAU+DTIME

        XPER=1 - EXP(-BK*(TAU**ETAK))
        IF (XPER.LT.STATEV(2)) XPER=STATEV(2)
        DXPER=XPER-STATEV(2)
        XAUS=(1-XPER)

        STATEV(1)=XAUS
        STATEV(2)=XPER
        STATEV(5)=DXPER
```

```
C----------------- CHECK TEMPERATURE IN THE BAINITIC RANGE--------------

    ELSE IF (TEMP.LE.TBN .AND. TEMP.GT.TMS) THEN

C   START TIME POLYNOMIAL INTERPOLATION FROM TTT DIAGRAM

        NMZTEMP=(TEMP-566.1)/158.8

        TSTART = 6.98E10*EXP(-((NMZTEMP-1.359)/0.08374)**2)
        TSTART = TSTART + 3.03E4*EXP(-((NMZTEMP - 77.72)/32.91)**2)
        TSTART = TSTART + 33.86*EXP(-((NMZTEMP - 1.633)/0.4003)**2)
        TSTART = TSTART - 154.9*EXP(-((NMZTEMP - 4.217)/7.652)**2)
        TSTART = TSTART + 2.741*EXP(-((NMZTEMP + 2.195)/1.27)**2)
        TSTART = TSTART + 0.3828*EXP(-((NMZTEMP + 1.681)/0.2824)**2)
        TSTART = TSTART - 7.761*EXP(-((NMZTEMP + 2.754)/1.637)**2)
        TSTART =10**TSTART

C       FINISHING TIME POLYNOMIAL INTERPOLATION FROM TTT DIAGRAM

        NMZTEMP=(TEMP-538.8)/154.2

        TFINISH = 2.469E6*EXP(-((NMZTEMP-2.93)/0.5094)**2)
        TFINISH = TFINISH + 176.1*EXP(-((NMZTEMP+4.457)/0.939)**2)
        TFINISH = TFINISH - 0.01039*EXP(-((NMZTEMP+1.835)/0.06161)**2)
        TFINISH = TFINISH - 13.4*EXP(-((NMZTEMP+1.826)/1.038)**2)
        TFINISH = TFINISH + 17.2*EXP(-((NMZTEMP+1.897)/1.148)**2)
        TFINISH = TFINISH + 2.204E4*EXP(-((NMZTEMP-8.61)/2.543)**2)
        TFINISH = 10**TFINISH

        ETAK=LOG(TSTART/TFINISH)
        ETAK=-6.1273/ETAK

        BK=(TSTART**ETAK)
        BK=0.01005/BK

        TAU=-LOG(1 - XBAIN)
        TAU=TAU/BK
        TAU=TAU**(1/ETAK)
        TAU=TAU+DTIME

        XP=1-XPER
        XBAIN=1 - EXP(-BK*(TAU**ETAK))
        XBAIN=XP*XBAIN
        IF (XBAIN.LT.STATEV(3)) XBAIN=STATEV(3)
        DXBAIN=XBAIN-STATEV(3)
        XAUS=(1-XPER-XBAIN)

        STATEV(1)=XAUS
        STATEV(3)=XBAIN
        STATEV(5)=0
        STATEV(6)=DXBAIN

C---------------- CHECK TEMPERATURE IN THE MARTENSITIC RANGE--------------

    ELSE IF (TEMP.LE.TMS) THEN

        XP=1-XPER-XBAIN
        XMAR=1 - EXP(-0.011*(TMS-TEMP))
```

```
        XMAR=XP*XMAR
        IF (XMAR.LT.STATEV(4)) XMAR=STATEV(4)
        DXMAR=XMAR-STATEV(4)
        XAUS=1-XMAR-XPER-XBAIN

        STATEV(1)=XAUS
        STATEV(4)=XMAR
        STATEV(6)=0
        STATEV(7)=DXMAR

    END IF
    END IF

    IF (XAUS.LE.TOLER) STATEV(7)=0
    STATEV(8)=66*(XMAR) + 39*(XPER+XBAIN)

C------------------------ CONDUCTIVITY ------------------------

    IF (TEMP.LE.13) THEN
        KAUS=PROPS(1)
    ELSE IF (TEMP.GE.13 .AND. TEMP.LE.1199) THEN
        KAUS=(1199-TEMP)*PROPS(1)/1186
        KAUS=KAUS + (TEMP-13)*PROPS(2)/1186
    ELSE IF (TEMP.GE.1199) THEN
        KAUS=PROPS(2)
    END IF

    IF (TEMP.LE.16) THEN
        KPB=PROPS(3)
    ELSE IF (TEMP.GE.16 .AND. TEMP.LE.788) THEN
        KPB=(788-TEMP)*PROPS(3)/772
        KPB=KPB + (TEMP-16)*PROPS(4)/772
    ELSE IF (TEMP.GE.788) THEN
        KPB=PROPS(4)
    END IF

    KMAR = PROPS(5)

    COND = (XAUS*KAUS) + (XMAR*KMAR) + (XPER+XBAIN)*KPB

C------------------------ SPECIFIC HEAT ------------------------

    IF (TEMP.LE.10) THEN
        SPMAR=PROPS(6)
    ELSE IF (TEMP.GE.10 .AND. TEMP.LE.626) THEN
        SPMAR =(626-TEMP)*PROPS(6)/616
        SPMAR=SPMAR + (TEMP-10)*PROPS(7)/616
    ELSE IF (TEMP.GE.626 .AND. TEMP.LE.1195) THEN
        SPMAR =(1195-TEMP)*PROPS(7)/569
        SPMAR =SPMAR + (TEMP-626)*PROPS(8)/569
    ELSE IF (TEMP.GE.1195) THEN
        SPMAR=PROPS(8)
    END IF

    IF (TEMP.LE.10) THEN
        SPPB=PROPS(9)
    ELSE IF (TEMP.GE.10 .AND. TEMP.LE.689) THEN
        SPPB = (TEMP-388)*(TEMP-689)*PROPS(9)/256662
        SPPB = SPPB + (TEMP-10)*(689-TEMP)*PROPS(10)/113778
        SPPB = SPPB + (TEMP-10)*(TEMP-388)*PROPS(11)/204379
    ELSE IF (TEMP.GE.689) THEN
```

```
        SPPB=PROPS(11)
    END IF

    SPECHT=SPMAR*(XMAR+XAUS) + SPPB*(XPER+XBAIN)

C------------------------ DENSITY -------------------------


    IF (TEMP.LE.10) THEN
        RHO=7929
    ELSE IF (TEMP.GE.10 .AND. TEMP.LE.810) THEN
        RHO =(810-TEMP)*7929/800 + (TEMP-10)*7596/800
    ELSE IF (TEMP.GE.810 .AND. TEMP.LE.1210) THEN
        RHO =(1210-TEMP)*7596/400 + (TEMP-810)*7495/400
    ELSE IF (TEMP.GT.1210) THEN
        RHO=7495
    END IF

    LATHT=0

    IF (DXPER.NE.0) LATHT=DXPER*(1.56E9 - TEMP*1.5E6)/RHO
    IF (DXMAR.NE.0) LATHT=DXMAR*640E6/RHO
    IF (DTEMP.GT.0) THEN
        PAR=ONE
    ELSE PAR=-ONE
    END IF

C********************** INPUT SPECIFIC HEAT ********************
    DUDT = SPECHT
    DU = DUDT*DTEMP + PAR*LATHT
    U = U+DU

C****************** INPUT FLUX = -[K]*{DTEMDX} ******************

    DO I=1, NTGRD
         FLUX(I) = -COND*DTEMDX(I)
    END DO

C***************** INPUT ISOTROPIC CONDUCTIVITY *****************

    DO I=1, NTGRD
         DFDG(I,I) = -COND
    END DO
    IF (TEMP.LT.21 .AND. TEMP.GT.20.5) CALL XIT
    RETURN
    END
```

Appendix C

Arduino Code for the Control Module

This Appendix provides the Arduino code that was used in the control module of the experimental set up explained in Section 5.3.3. This code has been written according to the pin diagram provided in Fig.5.9. The part of the code for interfacing the two thermocouples with the MAX6675 modules was modified from that given in Ref. [187] for a single thermocouple.

```
#include <SoftwareSerial.h>
// Library for serial communication in the digital pins

int D1=3;
// Define digital pin D1 as D1 and assign integer 3

int v1=0,SO1=5,CS1=6,SCK1=7;
int v2=0,SO2=9,CS2=10,SCK2=11;

// Initialize v1=0
// MAX6675 module 1
// Define global variable SO and assign value 5 (MAX6675 SO to pin 5)
// Define global varial CS and assign value 6 (MAX6675 CS to pin 6)
// Define global varial SCK and assign value 7 (MAX6675 SCK to pin 7)

// Initialize v2=0
// MAX6675 module 2
// Define global variable SO2 and assign value 9 (MAX6675 SO to pin 9)
// Define global variable CS2 and assign value 10 (MAX6675 SO to pin 10)
// Define global variable SCK2 and assign value 11 (MAX6675 SO to pin 11)


float Ctemp1,Ctemp2,dtemp;
// Ctemp1=temperature of inner wall
// Ctemp1=temperature of outer wall
// dtemp=Ctemp2-Ctemp1

//---------- Digital pin Input output setting ----------

void setup()   {
  Serial.begin(9600);
  pinMode(D1,OUTPUT);

  pinMode(SCK1, OUTPUT);
  pinMode(SO1, INPUT);
  pinMode(CS1, OUTPUT);
  digitalWrite(CS1, HIGH);
  digitalWrite(SCK1, LOW);

  pinMode(SCK2, OUTPUT);
  pinMode(SO2, INPUT);
  pinMode(CS2, OUTPUT);
  digitalWrite(CS2, HIGH);
  digitalWrite(SCK2, LOW);
}
//-------------------- Loop module --------------------
void loop()   {
```

```
  v1 = spiRead(SO1,CS1,SCK1);
  v2 = spiRead(SO2,CS2,SCK2);
  if (v1 == -1 || v2 == -1)   {
    Serial.print("No sensor \n");
  }
  else   {
    Ctemp1 =  v1 * 0.25;
    Ctemp2 =  v2 * 0.25;
    dtemp= abs(Ctemp2-Ctemp1);

  Serial.print("Deg C= ");
  Serial.print(Ctemp1);
  Serial.print("\t Deg C= ");
  Serial.print(Ctemp2);
  Serial.print("\t Deg C= ");
  Serial.print(dtemp);
  Serial.println();

  }
  delay(100);
  if (dtemp < 50) {
    digitalWrite(D1, HIGH);
  }
  else {
    digitalWrite(D1, LOW);
  }
}

// SpiRead function for thermocouple

  int spiRead(int SO,int CS, int SCK)   {
  int value = 0;
  digitalWrite(CS,LOW);
  delay(2);
  digitalWrite(CS,HIGH);
  delay(220);
  digitalWrite(CS,LOW);
  /* Cycle the clock for dummy bit 15 */
  digitalWrite(SCK,HIGH);
  delay(1);
  digitalWrite(SCK,LOW);

  /*
   Read bits 14-3 from MAX6675 for the Temp. Loop for each bit reading
   the value and storing the final value in 'temp'
   */

  for (int i=14; i>=0; i--) {
    digitalWrite(SCK,HIGH);
    value += digitalRead(SO) << i;
    digitalWrite(SCK,LOW);
  }
  // check bit D2 if HIGH no sensor
  if ((value & 0x04) == 0x04) return -1;

  // shift right three places
  return value >> 3;
}
```

List of Publications from the Thesis

Journal papers

- Shufen, R., and Dixit, U. S., 2017, "A Finite Element Method Study of Combined Hydraulic and Thermal Autofrettage Process," ASME Journal of Pressure Vessel Technology, 139(4), pp. 041204-041204–9.

- Shufen, R., and Dixit, U. S., 2018, "A Review of Theoretical and Experimental Research on Various Autofrettage Processes," ASME Journal of Pressure Vessel Technology, 140(5), pp. 050802-050802–15.

- Shufen, R., and Dixit, U. S., 2018, "An Analysis of Thermal Autofrettage Process with Heat Treatment," International Journal of Mechanical Sciences, 144, pp. 134–145.

- Shufen, R., Mahanta, N., and Dixit, U. S., 2019, "Development of a Thermal Autofrettage Setup to Generate Compressive Residual Stresses on the Surfaces of a Cylinder," ASME Journal of Pressure Vessel Technology, 141(5), pp 051403–051403-12.

Book Chapter

- Shufen, R., and Dixit, 2020, "Finite-element modeling of hydraulic and thermal autofrettage processes", *Mechanics of Materials in Modern Manufacturing Methods and Processing Techniques*, Ed. V.V. Silberschmidt, Elsevier, London.

Book (Partial contribution as co-author)

- Dixit, U.S, Kamal, S.M and Shufen, R., 2019, *Autofrettage Processes: Technology and Modelling*, CRC Press.